University of Warsaw
Faculty of Physics

UNIVERSITY
OF WARSAW

FACULTY OF
PHYSICS

Marcin Muszyński

Dissertation

Self-Organizing Photonic Potentials of Different Dimensions in Liquid Crystal Microcavities with Spin-Orbit and Light-Matter Couplings

Samoorganizujące się potencjały fotoniczne o różnej wymiarowości
w ciekłokrystalicznych mikrownękach ze sprzężeniem spin-orbita
oraz światło-materia

Supervised by:
dr hab. Jacek Szczytko, prof. UW

Warsaw, 2025

Abstract

This dissertation is devoted to the study of planar liquid crystal optical microcavities, a unique platform in which an optical resonator is filled with a highly birefringent liquid-crystalline material. This configuration provides dynamic control over the properties of the confined light, such as its energy and polarization. The work focuses on two main goals: investigating nonlinear optical phenomena in both the weak and strong light–matter coupling regimes, and implementing spatially varying photonic potentials of different dimensions.

In the weak coupling regime, the results demonstrate tunable photon lasing in a nematic liquid crystal microcavity. This tunability enables lasing in the Rashba–Dresselhaus spin–orbit coupling regime, in which oppositely circularly polarized beams are emitted at different angles. Their interference leads to the formation of an optical persistent optical spin helix under nonlinear conditions.

In the strong coupling regime, a room-temperature Bose–Einstein condensate of exciton-polaritons is realized, with its energy and polarization tunable by an external electric field and the polarization of the excitation beam. Spin–orbit interaction in this system gives rise to a polariton spin current and a periodic modulation of condensate density in real space, known as the *stripe phase*. The mechanism of spontaneous symmetry breaking, together with the observation of quantized vortices in single-shot experiments, provides evidence of superfluidity. The coexistence of the stripe phase and superfluidity constitutes the first full demonstration of a supersolid phase of exciton-polariton condensates and the first such realization at room temperature.

The following chapters explore self-organized, spatially varying photonic potentials. In the case of zero-dimensional photonic traps with spatially modulated birefringence, the system can be regarded as an optical analogue of an atom in a synthetic magnetic field. In this context, the confined ground state of light within the trap is interpreted as an optical analogue of the Landau level. Lasing from this state exhibits distinct polarization characteristics and carries non-zero orbital angular momentum.

One- and two-dimensional photonic lattices give rise to photonic energy bands. In the one-dimensional case, two independent band structures corresponding to orthogonal linear polarizations of light can be tuned using an external electric field. The introduction of molecular tilt leads to interband spin–orbit coupling, which mixes photonic bands with specific symmetries.

In the case of a three-dimensional, self-organized photonic crystal, lasing is associated with specific diffraction directions that have been experimentally mapped. The polarization and angular distribution of the emitted light strongly depend on the geometry of the excitation relative to the crystal structure.

The presented research represents a significant step toward simulating spin-related solid-state physics phenomena using light, as well as observing quantum effects at room temperature. The proposed platform exhibits a high degree of adaptability, scalability, and tunability, making it a promising tool for both fundamental studies and practical applications.

Streszczenie

Niniejsza rozprawa poświęcona jest badaniom planarnych ciekłokrystalicznych mikrownęk optycznych, stanowiących wyjątkową platformę, w której rezonator optyczny wypełniony jest silnie dwójłomnym materiałem ciekłokrystalicznym. Dzięki temu możliwa jest dynamiczna kontrola własności światła uwięzionego w mikrownęce, takich jak energia czy polaryzacja. Praca koncentruje się na dwóch głównych celach: badaniu nieliniowych zjawisk optycznych w reżimach słabego i silnego sprzężenia światło–materia oraz wprowadzeniu przestrzennie zmiennych potencjałów fotonicznych o różnej wymiarowości.

W reżimie słabego sprzężenia zaprezentowano wyniki dotyczące przestrajalnego laserowania fotonowego w nematycznej mikrownęce ciekłokrystalicznej. Przestrajalność ta pozwoliła uzyskać laserowanie fotonowe w reżimie sprzężenia spin-orbita Rashba-Dresselhaus, w którym przeciwnie kołowo spolaryzowane wiązki emitowane są pod różnymi kątami. Ich interferencja prowadzi do powstania optycznej trwałej spinowej helisy w warunkach nieliniowych.

W reżimie silnego sprzężenia uzyskano kondensat Bosego–Einstaina polarytonów ekscytonowych w temperaturze pokojowej, którego energia oraz polaryzacja mogą być kontrolowane za pomocą zewnętrznego pola elektrycznego oraz polaryzacji wiązki pobudzającej. Oddziaływanie spin–orbita prowadzi do pojawienia się polarytonowego prądu spinowego oraz modulacji gęstości kondensatu w przestrzeni – tak zwanej *fazy prążkowanej*. Przedstawiony mechanizm spontanicznego złamania symetrii oraz obserwacja wirów kwantowych w eksperymentach pojedynczych impulsów stanowią dowód na nadciekłość kondensatu. Współwystępowanie fazy prążkowanej i nadciekłości stanowi pierwszą pełną demonstrację fazy nadstałej (nadkrystalicznej) kondensatów polarytonów ekscytonowych oraz pierwszą jej demonstrację w temperaturze pokojowej w ogóle.

Dalsza część pracy poświęcona jest samoorganizującym się, przestrzennie zmiennym potencjałom fotonicznym. Dla zerowymiarowych pułapek fotonicznych z przestrzennie zmienną dwójłomnością układ ten może być traktowany jako optyczny analog atomu w syntetycznym polu magnetycznym. W tym ujęciu związany w pułapce stan podstawowy światła interpretowany jest jako optyczny analog poziomu Landaua. Laserowanie z tego stanu cechuje się charakterystycznymi właściwościami polaryzacyjnymi i niesie niezerowy orbitalny moment pędu.

Jedno- i dwuwymiarowe sieci fotoniczne prowadzą do powstania pasm energetycznych. W przypadku jednowymiarowej sieci, dwie niezależne struktury pasmowe dla ortogonalnych liniowych polaryzacji światła mogą być przestrajane za pomocą napięcia elekrycznego. Wprowadzenie pochylenia molekuł skutkuje międzypasmowym sprzężeniem spin–orbita, które miesza pasma o odpowiednich symetriach.

W przypadku trójwymiarowego, samoorganizującego się kryształu fotonicznego, uzyskane laserowanie jest związane z określonymi kierunkami dyfrakcji, które zostały zmapowane eksperymentalnie. Własności polaryzacyjne oraz kątowe tego laserowania silnie zależą od geometrii pobudzenia względem struktury krystalicznej.

Przedstawione badania stanowią istotny krok w kierunku symulowania zjawisk fizyki ciała stałego z udziałem spinu przy użyciu światła, jak również obserwacji zjawisk kwantowych w temperaturze pokojowej. Zaproponowana platforma charakteryzuje się wysokim stopniem adaptowalności, skalowalności i przestrajalności, co czyni ją obiecującym narzędziem zarówno dla badań podstawowych, jak i zastosowań aplikacyjnych.

Acknowledgments

First and foremost, I would like to express my deepest gratitude to my supervisor, Prof. Jacek Szczytko, for his guidance throughout my PhD and for the opportunity to work on the exceptional platform of liquid crystal microcavities. The trust and independence I have received over the past five years have shaped me as a researcher.

I am sincerely grateful to the members of the Polariton group at the University of Warsaw, with whom I had the pleasure of working and from whom I learned a lot: Przemek Oliwa, Piotr Kapuściński, Kasia Rechcińska, Karolina Łempicka-Mirek, Mateusz Król, Rafał Mirek, Helgi Sigurðsson, Prof. Barbara Piętka, Joachim Czapliński, and Wiktoria Solarska–thank you all.

Experimental research would not be possible without the samples we study. I am grateful to the team at the Military University of Technology for their remarkable work in fabricating the microcavities and for the discussions that helped improve their quality. In particular, I thank Prof. Wiktor Piecek and his group: Dr. Eng. Przemysław Morawiak, Dr. Eng. Rafał Mazur, and Dr. Eva Oton, as well as Prof. Przemysław Kula and Natan Rychłowicz.

I express my special appreciation to Dr. Pavel Kokhanchik, Dr. Daniel Bobylev, and especially to Prof. Dmitry Solnyshkov and Prof. Guillaume Malpuech from Institut Pascal, CNRS, Clermont-Ferrand. Their theoretical insight, ideas, and critical discussions were invaluable and often defined the direction of the research presented in this thesis.

I am also thankful for the collaboration with the group at IBM Research Zurich, led by Prof. Thilo Stöferle and Prof. Rainer Mahrt–Dr. Darius Urbonas, Dr. Ioannis Georgakilas, and Pietro Tassan–with whom I worked on the supersolid phase project. Although working with these samples posed a real challenge, the satisfaction of the results made it well worth the effort.

Warm thanks go to Dr. Dmitriy Dovzhenko and Dr. Krzysztof Sawicki for their kind hospitality during my two research visits to the University of Southampton.

I would also like to thank my colleagues from the Solid State Physics Division at the Faculty of Physics, University of Warsaw, especially Maciek and Kuba, for many stimulating discussions, not always strictly work-related.

To my brother: I know that you are a role model for your daughter, just as you have always been to me.

Dziękuję Ci mamo za wiarę we mnie i wspieranie moich nawet najgłupszych decyzji.

Finally, Magda–thank you. I am still impressed by how you managed to survive all these years. I hope your incredible enthusiasm never fades.

This work is dedicated to the memory of my father,
Bogdan Muszyński (1964–2023).

Contents

1 Introduction I: Motivations

Over the past few years, the platform of liquid crystal optical microcavities (LCMCs) has proven to be exceptionally rich in fascinating phenomena at the intersection of photonics and solid-state physics [1–22]. Embedding highly birefringent liquid crystals inside microcavities has expanded their functionality in two significant ways. First, the ability to control the orientation of liquid crystal molecules using an external electric field enables precise and convenient tuning of the optical properties of the cavity. Second, it strongly enhances the effects related to the polarization of confined light.

Polarization can be treated as a pseudospin of light [23,24]. Consequently, phenomena that couple the direction of light propagation to its polarization are known as spin-orbit interactions for photons. Remarkably, such spin-orbit effects become particularly pronounced in LCMCs. When described using the mathematical framework of synthetic Hamiltonians [2], these effects reveal that LCMC platforms can serve as optical analogues of electronic systems with spin, enabling the exploration of spin-dependent phenomena in a photonic context.

Before the start of this PhD project, aside from the initial efforts of my predecessors Katarzyna Rechcińska, who worked with laser dyes and luminescent proteins (work which I directly continued) and Karolina Łempicka-Mirek, who studied perovskites, all research on LCMCs had been done in the linear regime, without considering gain of the active material. The microcavities were translationally invariant in the plane, and the studied liquid crystal phases were mainly nematic, with some attempts at cholesteric phases, although the results of the latter were never published.

Other research groups working on lasing from cavities combined with liquid crystals focused exclusively on application-oriented studies [25], without exploring the underlying physics accessible through synthetic Hamiltonian descriptions, spin-orbit interactions, or photonic potential engineering.

Therefore, in this doctoral project, I set myself two main goals, which I am pleased to say have been successfully achieved and are documented in this dissertation. The first was to investigate the nonlinear properties of LCMCs in both the weak and strong light-matter coupling regimes. The second was to introduce tunable photonic potentials of different dimensionalities into the system. Achieving these goals led to the discovery of several novel physical phenomena, which are summarized in the second part of this chapter.

The main motivation behind both goals was, above all, scientific curiosity. I believe that the proposed platform offers exceptional versatility in the design of experiments that reveals many remarkable phenomena. This potential stems from the numerous available degrees of freedom, including polarization, tunability of the confined photon energy, and the possibility to engineer photonic potentials.

The light–matter coupling offered by this platform not only allows exploration of fundamental phenomena, such as those associated with Bose–Einstein condensation, but also opens promising avenues for practical applications. One of the driving motivations was to develop a tunable microlaser that, owing to spin–orbit coupling, would demonstrate distinctive polarization and angular emission characteristics. These features make it a promising candidate for applications in light sources, quantum communication, metrology, sensing, and even biomedical diagnostics [26]. Furthermore, it was anticipated that, in the strong coupling regime, the threshold for achieving coherent nonlinear emission would be significantly lower than in the weak coupling (conventional lasing) regime. Integration with a self-organized liquid crystal structure further endowed the microlaser with nonzero orbital angular momentum, a desirable property in fields such as optical micromanipulation [27] and quantum information [28].

It is important to emphasize that all experiments presented in this thesis were performed at room

temperature. This represents a significant advancement, particularly in the context of one of the key findings of this work: the observation of the supersolid phase, which combines crystalline order with superfluidity. Until now, such phenomena have been observed exclusively in ultracold atomic gases at temperatures in the nanokelvin range. Demonstrating analogous behavior under ambient conditions may provide a major impetus for future studies in this field. Furthermore, the fact that all of the experiments were performed in the visible spectral range, which can be relatively easily adapted to the telecom band [29, 30], further enhances the application potential of the findings, particularly for the engineering of photonic devices, optical communication, and quantum optics.

The motivation behind integrating photonic potentials of varying dimensionalities with LCMCs in the subsequent chapters of this thesis was to take a step further toward the simulation of solid-state phenomena using light. In the case of zero-dimensional optical traps, the system can be regarded as an analogue of a particle with spin confined within a single atom. For one- and two-dimensional periodic photonic potentials, the emergent photonic band structures act as optical analogues of electronic band structures found in crystalline solids. Because of the use of birefringent liquid crystals, these photonic lattices can be tuned in ways that are inaccessible to other fabrication methods, and each self-assembled liquid crystal structure offers unique tuning capabilities. Compared to traditional fabrication techniques, this approach stands out because of its simplicity, lower cost, and large scale of the resulting lattices. Furthermore, spin–orbit interactions emerging from birefringence lift the degeneracy of photonic orbitals and bands, which could open exciting avenues for future investigations at the intersection of topological photonics and non-Hermitian physics.

As I mentioned earlier, when I began this PhD five years ago, research on the integration of LCMCs with light–matter coupling and spatially varying photonic potentials was only explored in the Polariton group at the University of Warsaw. Today, as I complete this dissertation, a growing number of research teams are reporting exciting discoveries related to strong light–matter coupling in this system [9, 13, 16, 17, 19, 22]. Furthermore, I expect that structured LCMCs will soon become a topic of greater interest (at the time of writing, I am aware of one such study that is already underway [18]. This demonstrates that the research direction I undertook was not only innovative but also carries significant potential that is now increasingly acknowledged by the wider scientific community.

After this introduction, the rest of the dissertation is ordered as follows:

Chapter 2 introduces the key concepts necessary to understand the experimental results presented in the following chapters. It begins with the fundamentals of liquid crystals and their self-organization into various phases. The chapter then covers the principles of Bragg mirrors and optical microcavities, including the concept of a photon confined within the cavity behaving as a massive particle. The influence of birefringent materials on the polarization properties of light inside such cavities is discussed along with spin-orbit coupling and the physical phenomena that arise from the distinct symmetries of LCMC. Next, both the weak and strong light-matter coupling regimes are considered, including related nonlinear processes, namely photon lasing and Bose-Einstein condensation. The chapter concludes by presenting common methods for fabricating spatially varying photonic potentials and discusses their physical implications depending on the dimensionality.

Chapter 3 focuses on the experimental methods employed throughout this work. It provides a detailed description of the studied samples and the optical spectroscopy techniques used, with particular emphasis on spatially and momentum-resolved spectroscopy. In addition, two simulation approaches utilized to model the investigated phenomena are briefly introduced. The chapter concludes by outlining the specific contributions of the author and collaborators to the results presented in the thesis.

Chapter 4 presents the results obtained for the nematic LCMC in the weak light-matter coupling regime. Tunable spontaneous emission and photon lasing are demonstrated. The lasing regime

is explored in the Rashba-Dresselhaus spin-orbit coupling regime, where two oppositely circularly polarized beams are emitted at different angles. The interference between these beams leads to the formation of an optical persistent spin helix in the nonlinear regime.

Chapter 5 focuses on the strong light-matter coupling regime. The existence of exciton-polaritons in the nematic LCMC is experimentally demonstrated. The process of Bose-Einstein condensation is presented, along with a detailed characterization of its spatial and temporal coherence. Furthermore, the tunability of the condensate's energy and polarization are shown.

Next, the formation of a condensate in the Rashba–Dresselhaus regime is demonstrated. This regime leads to the generation of polariton spin current and interference that produce a periodic modulation of the polariton density in real space, known as the stripe phase. Evidence for superfluidity is presented based on the observation of spontaneous symmetry breaking in disordered photonic potential, as well as the emergence of quantized vortices in single-shot measurements. Together, these findings confirm the realization of a supersolid state of exciton-polaritons at room temperature.

Chapter 6 presents results obtained with a self-organized one-dimensional periodic photonic potential based on the uniform lying helix (ULH) liquid crystal phase. The chapter demonstrates the formation of two independent photonic band structures corresponding to two orthogonal light polarizations and their tunability by an external electric field.

The introduction of molecular tilt enables coupling between photonic bands with specific symmetries, giving rise to what is referred to as interband spin–orbit coupling. Lasing from these photonic bands is demonstrated, preserving both their polarization and angular characteristics.

This chapter also covers different types of defects in the ULH structure, with particular focus on the uniform lying helix spiral.

Chapter 7 focuses on a different class of liquid crystal defects, torons embdedded within LCMC, in which the spatially varying orientation of the liquid crystal gives rise to a synthetic gauge field. The chapter presents an unusual ladder of quantized energy states in a single toron along with a detailed analysis of the polarization properties of these states.

Two independent methods of tuning the toron size are presented: by external electric fields and by changing the position on the sample, allowing the study of nontrivial dependence of the ground and first excited states as a function of trap size, with a possible topological phase transition.

Next, lasing from the ground state of the toron is demonstrated, where the emission carries nonzero orbital angular momentum. These observations support the interpretation of the toron ground state as an optical analogue of a Landau level.

The chapter concludes with the realization of a two-dimensional triangular lattice of interacting torons, opening avenues for future studies of many-body physics in synthetic photonic gauge fields.

Chapter 8 presents results on the blue phase (I) liquid crystal phase as an example of a self-organized three-dimensional photonic crystal, investigated in the absence of an optical cavity. Optical tomography of this structure is demonstrated, enabling the reconstruction of a three-dimensional map of Kossel patterns and providing insight into the spatial arrangement of the phase.

Blue phase lasing is demonstrated, exhibiting a strong dependence on the excitation beam geometry. Notably, the emitted polarization can match or oppose the intrinsic chirality of the blue phase. Furthermore, an attempt to integrate the blue phase with an LCMC is presented, resulting in the splitting of cavity eigenstates and the observation of dual-threshold lasing.

Chapter 9 provides a general summary and conclusions of the thesis.

The Appendix A presents results on patterned nematic LCMCs fabricated using focused ion beam techniques. Several effects observed in these devices are shown to resemble phenomena found in self-assembled LCMCs. Examples of one- and two-dimensional photonic lattices are provided for two distinct LCMC regimes, offering complementary insights into photonic potential engineering

within this platform.

I believe that an important step forward and a natural future direction and outcome of this work is the integration of exciton-polariton Bose–Einstein condensates with spatially varying photonic potentials in LCMC systems. This goal now appears to be within reach, and the combination of the unique features of both approaches holds the promise of uncovering a wide range of fascinating physical phenomena that remain to be explored.

2 Introduction II: Useful Concepts

This chapter introduces the key concepts necessary for understanding the results presented later in the thesis. The first section focuses on liquid crystals and their optical properties. The following section discusses Bragg mirrors and optical microcavities, with particular stress on spin-orbit coupling and cavities filled with highly birefringent materials. It also introduces the concept of standing electromagnetic waves confined within a cavity as analogues of massive particles. The third section explores light–matter coupling, distinguishing between the weak and strong coupling regimes. Nonlinear processes occurring in both regimes are also discussed, with special attention given to the Bose–Einstein condensation of exciton-polaritons. The final section addresses periodic photonic potentials of various dimensionalities within optical cavities, as well as their influence on confined 'massive photons'.

2.1 Liquid Crystals

Liquid crystals (LCs) are state of matter that simultaneously exhibit properties of both liquids (flow) and crystalline solids (molecular order). They belong to a larger class of materials known as *soft matter*. Due to their dual nature, LCs exhibit phenomena such as long-range order, birefringence, and anisotropic viscosity.

Liquid crystals can exist in a variety of phases, distinguished by their degree of positional and orientational order, as well as their optical and mechanical properties. Transitions between these phases are sensitive to external parameters such as temperature, chemical composition, and applied stimuli, and may result in the coexistence of domains with different local molecular alignments within a single phase.

Although liquid crystals are widely used in laboratory and industrial applications, they also occur naturally. In inorganic systems, examples include solutions of soaps, detergents, and clays [31]. In biological systems, many macromolecules, such as proteins [32], DNA [33], cell membranes [34], and even the tobacco mosaic virus [35], exhibit liquid crystalline behavior.

One of the most remarkable features of liquid crystals (and of nature in general) is their ability to self-organize. During non-equilibrium processes such as phase transitions, LC molecules spontaneously assemble into well-defined supramolecular structures with higher degrees of order. This occurs through collective interactions among individual molecules, without the need for external control, provided the system's available energy exceeds the entropy-driven disorder. As a result, the ensemble may exhibit emergent properties that are not present at the level of individual molecules. This self-organization is dynamic and can evolve over time, often observable in real time in LC systems. The self-organization is common in nature, from fundamental physical processes like crystal growth, superconductivity, Bose-Einstein condensation, and oscillatory chemical reactions, to macroscopic collective behavior observed in flocks of birds, swarms of insects, and even economic systems.

Liquid crystals are generally classified into three main categories based on the mechanism of phase transition:

- Thermotropic LCs: phase transitions are driven by temperature changes.
- Lyotropic LCs: phases depend on both the concentration of the molecules and the temperature.
- Metallotropic LCs: composed of organic and inorganic components, with phase behavior governed by their relative composition.

Despite substantial differences in chemical composition, most common liquid crystal phases belong to a few primary categories, classified according to the molecular arrangement of the liquid crystal molecules. Many compounds can exhibit one or more LC phases. Among thermotropic LCs, discotic (disk-like) and conical (bowl-like) molecules tend to self-assemble into two-dimensional columnar phases. However, all investigations in this dissertation will be focused on the *rod-like molecule*. These molecules have elongated anisotropic shapes, with a typical length of 2–6 nm (with a lower bound of approximately 1.3 nm, often due to the presence of long alkyl side chains) and a width of 0.5–1 nm.

LC phases are dense systems with strong many-body interactions and correlations. Their microscopic behavior, characterized by anisotropic viscosity and orientational order, is very complex. To address this problem, simplified theoretical models such as the *Landau–de Gennes theory* are used, which allow one to predict the global behavior of LCs, including phase transitions and optical properties. For rod-like molecules, a common simplification is to represent the molecule as a uniaxial object with cylindrical symmetry, defined by a long molecular axis. The *director* $\mathbf{n}$ is introduced as the preferred average orientation of these axes over a given volume and time. Importantly, $\mathbf{n}$ and $-\mathbf{n}$ are considered equivalent, making the director an apolar vector.

The optical properties of liquid crystals are directly linked to their shape and molecular orientation. This relationship is described using the *dielectric tensor* $\boldsymbol{\varepsilon}$, which depends on the molecular orientation relative to the propagation direction and wavelength λ of light. Two key optical phenomena relevant to this thesis are *birefringence* and *optical activity*.

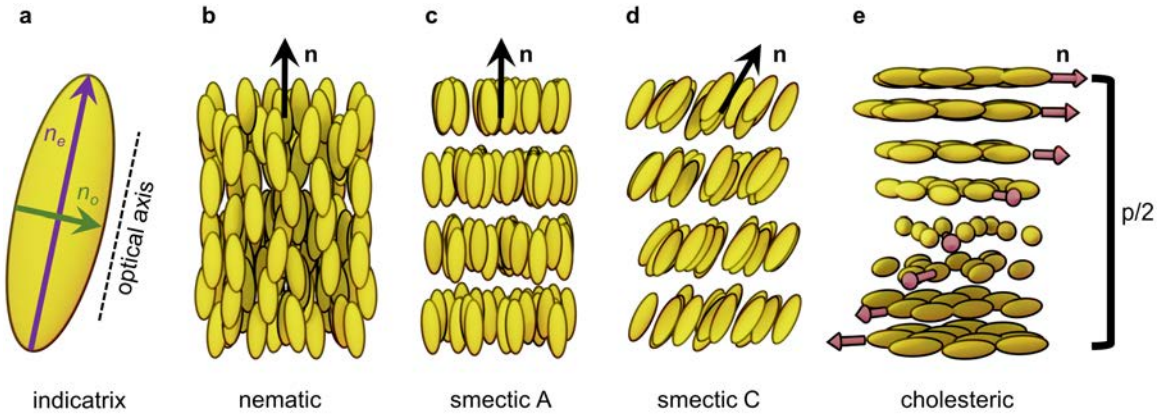

Figure 2.1: **Liquid Crystal Phases.** (a) Schematic illustration of the liquid crystal indicatrix, with the ordinary (green arrow), extraordinary (purple arrow) and optical axes marked. (b–e) Schematic representations of various liquid crystal phases: nematic, smectic A, smectic C, and cholesteric, respectively. The directors $\mathbf{n}$ are indicated with arrows.

Materials in which the refractive index depends on the polarization and propagation direction of light are *birefringent*. In such materials, light splits into two rays with orthogonal polarizations and different propagation velocities: the *ordinary* (o) and *extraordinary* (e) rays. The optical anisotropy is defined by birefringence $\Delta n = n_e - n_o$, where n_e and n_o are the refractive indices of the extraordinary and ordinary rays, respectively. These correspond to the long and short axes of the optical indicatrix, a geometric representation of the optical anisotropy of the material (see Fig. 2.1(a)).

In uniaxial materials (which are the focus of this thesis), a single optical axis exists along which the refractive index is independent of polarization. For materials with $\Delta n > 0$ (optically positive,

such as typical nematic LCs), the long molecular axis is the same as the optical axis.

Chiral liquid crystals lacking mirror symmetry exhibit *optical activity*, where the polarization plane of transmitted light is rotated. This phenomenon is similar to, but distinct from, the Faraday effect, which also rotates polarization, but is non-reciprocal (dependent on light's propagation direction relative to an involved static magnetic field), whereas optical activity is reciprocal (independent on propagation direction).

Liquid crystals can exist in a variety of ordered phases, defined by their *positional order* (periodicity, as in crystals) and *orientational order* (alignment of molecular axes). At high temperatures, thermotropic LCs typically exhibit an *isotropic phase*, where molecules are randomly oriented with no long-range order, resembling conventional fluids.

Upon cooling, LCs may undergo phase transitions into more ordered phases, each characterized by different types and degrees of anisotropy or lower symmetry. For many compounds, further cooling eventually leads to the formation of conventional crystals.

The simplest LC phase is the *nematic phase*, where rod-like molecules exhibit long-range orientational order but no positional periodicity (Fig. 2.1(b)). Molecular centers of mass are randomly distributed, yet their long axes tend to align along a common direction. Nematic LCs retain fluidity and respond to external electric or magnetic fields, allowing dynamic control of optical properties. Nematic-like ordering is also observed in some inorganic systems, such as charge-density waves in high magnetic fields [36]. The nametic phase will be of particular relevance in Chapters 4, 5, and Appendix A.

At lower temperatures, LCs may form *smectic phases*. Here, molecules are organized into well-defined layers, showing one-dimensional positional order. In *Smectic A* (SmA), molecules are perpendicular to the layers (Fig. 2.1(c)), while in *Smectic C* (SmC), they are tilted with respect to the layer normal (Fig. 2.1(d)).

Another important phase is the *chiral nematic* or *cholesteric* phase, named after its initial discovery in cholesterol derivatives. This phase incorporates chiral molecules into a nematic host, causing the director to twist helically along one axis (Fig. 2.1(e)). For simplicity, the gradual change can be represented as a structure composed of layers with uniformly aligned directors, each twisted slightly relative to the next, resulting in a helical superstructure. The chiral pitch p is defined as the distance over which the director completes a 360° rotation. Due to the apolar nature of the director, the structure repeats every half-pitch $p/2$. The pitch can be tuned by adjusting the temperature or concentration of the chiral dopants. If the helical pitch matches the wavelength of incident light according to Bragg's law, a selective Bragg reflection occurs for the circularly polarized light that matches the handedness of the helix. This phenomenon is used in devices such as liquid crystal lasers [37].

Although the phases discussed above are the most common, the landscape of the LC phase is much richer, with new phases still being discovered [38]. Additionally, LCs can exhibit a variety of topological defects, which significantly influence their physical and optical properties [39, 40]. This thesis, in addition to the nematic phase, will focus on particular LC phases and defect structures, including the *uniform lying helix* (Chapter 6), *torons* (Chapter 7), and *blue phases* (Chapter 8).

In nematic LC cells (the cell formed by two parallel glass substrates), two main alignment geometries are typically used [41]:

- **Homogeneous alignment**: The director align parallel to the substrate surface (see Fig. 2.2(a)). This alignment can be achieved through surface rubbing, photoalignment, or chemical coatings. Mechanical antiparallel rubbing (where both substrates are rubbed in opposite directions) is commonly used to minimize elastic deformations, such as splay.

- **Homeotropic alignment**: The director align perpendicular to the substrate surface (see

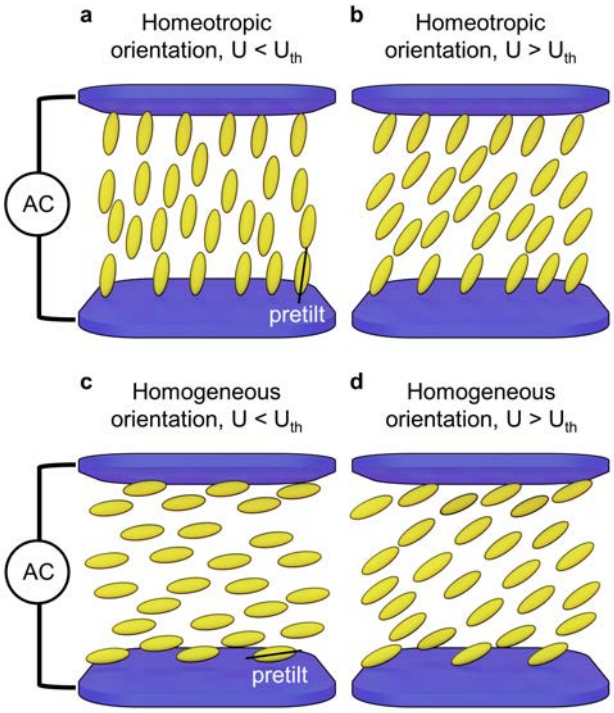

Figure 2.2: **Orientations of Nematic Liquid Crystals.** Schematic illustrations of molecular alignment in (a,b) homeotropic and (c,d) homogeneous configurations in LC cells. Panels (a,c) show the alignment in the absence of an applied voltage, while panels (b,d) show the response under applied AC voltage (when $\Delta\varepsilon > 0$ and $\Delta\varepsilon < 0$, respectively). A small pretilt angle is indicated schematically.

Fig. 2.2(c)). This configuration is induced through surface treatment with specific alignment layers or surfactants.

Hybrid alignments are also possible. In both geometries, a small *pretilt angle* (typically a few degrees) is often introduced, which affects the electro-optic response of the LC (marked in Fig. 2.2(a,c)).

As previously mentioned, the application of an electric field can induce reorientation of the LC director. In homogeneous cells containing LC with *positive dielectric anisotropy* $\Delta\varepsilon > 0$, an electric field applied perpendicular to the substrate causes the director to tilt toward the field direction once the *Fréedericksz threshold* voltage U_{th} is exceeded [42, 43] (Fig. 2.2(b)). Initially, the reorientation occurs in the center of the LC cell, where the anchoring is weakest. At higher voltages, molecules throughout the cell align homeotropically. A similar effect can be observed in homeotropic cells containing LCs with *negative dielectric anisotropy* $\Delta\varepsilon < 0$ (Fig. 2.2(d)). Interestingly, some LC mixtures allow the dielectric anisotropy to be switched between positive and negative values by tuning the frequency of the applied electric field (see the section Dual-frequency LC in the Supplementary Information of [1]). The use of an alternating current (voltage) instead of a direct current is a commonly employed technique, also used in this thesis, as it prevents the accumulation of static charge on the electrodes, reduces performance degradation, and helps maintain a more uniform electric field within the cell.

One of the key advantages of liquid crystals is their compatibility with a wide range of organic

and inorganic materials with desirable room-temperature optical properties. These include light emitters (e.g., organic laser dyes) and selective absorbers (e.g., chiral nanoparticles).

Due to their remarkable optical properties and tunability, LCs have found numerous technological applications. The most prominent are liquid crystal displays (LCDs), which were very popular in a wide range of electronic devices in the 1990s and remain a well-understood and accessible technology. The principles of LCD are also used in modern spatial light modulators. Other applications include smart windows that control light transmission [44], optical filters [45], sensors for temperature, humidity, or chemical substances [46–50], emerging fields like microrobotics [51] and many more.

2.2 Optical Microcavities, LCMC, Spin-Orbit Coupling

2.2.1 Distributed Bragg Reflectors

Photonic crystals (PhCs) are periodic structures that exhibit spatial modulation of the refractive index on the scale of the wavelength of light. This periodicity leads to the emergence of photonic band gaps (PBGs), frequency ranges within which light propagation is prohibited because of destructive interference. The term photonic crystal was introduced in the late 1980s by Yablonovitch [52], who proposed that such structures can inhibit spontaneous emission by modifying the electromagnetic density of states, and by John [53], who worked on its acceleration. The underlying concept is analogous to the electronic band structure in crystals, where the periodic atomic potential leads to electronic band gaps. In PhCs, the periodic dielectric function plays an analogous role.

An important one-dimensional (1D) microstructure in photonic and laser physics is the distributed Bragg reflector (DBR). DBRs are multilayer structures composed of alternating layers of low and high refractive index materials with low optical absorption, designed to achieve high reflectivity in a specific spectral range. Each interface partially reflects incident light, and constructive (destructive) interference for reflection (transmission) is ensured when the quarter-wave condition is met:

$$n_1 d_1 = n_2 d_2 = \frac{\lambda_0}{4}, \tag{1}$$

where n_1 and n_2 are the refractive indices and d_1, d_2 the respective thicknesses of the alternating layers. λ_0 is the central wavelength of the DBR.

Figure 2.3(a) shows transfer matrix simulations (more on this in the next chapter) of the reflectance spectra of DBRs under normal incidence, for varying numbers of layer pairs N, using $\lambda_0 = 550$ nm and refractive indices $n_1 = 1.46$ and $n_2 = 2.2$, representative of SiO_2 and TiO_2 at room temperature. These materials are commonly used, including this thesis, for the fabrication of DBRs. As N increases, the reflectivity in the spectrally broad high-reflectivity region centered at λ_0, termed the stopband or photonic bandgap, approaches unity. The stopband also narrows and becomes steeper with increasing N.

Figure 2.3(b) illustrates the effect of increasing the refractive index contrast $\Delta n = n_2 - n_1$ on the DBR reflectance for $N = 10$ pairs. As Δn increases, the stopband becomes wider and the peak reflectance increases. Oscillatory features outside the stopband are called Bragg modes. Notably, the mechanism for selective reflection in cholesteric liquid crystals has a similar origin, stemming from periodic modulation of the refractive index.

2.2.2 Optical Microcavities and Cavity Modes

A defect introduced into a periodic DBR structure, such as a layer of thickness L_c and refractive index n_c between two DBRs, forms a photonic resonator, commonly referred to as an optical microcavity,

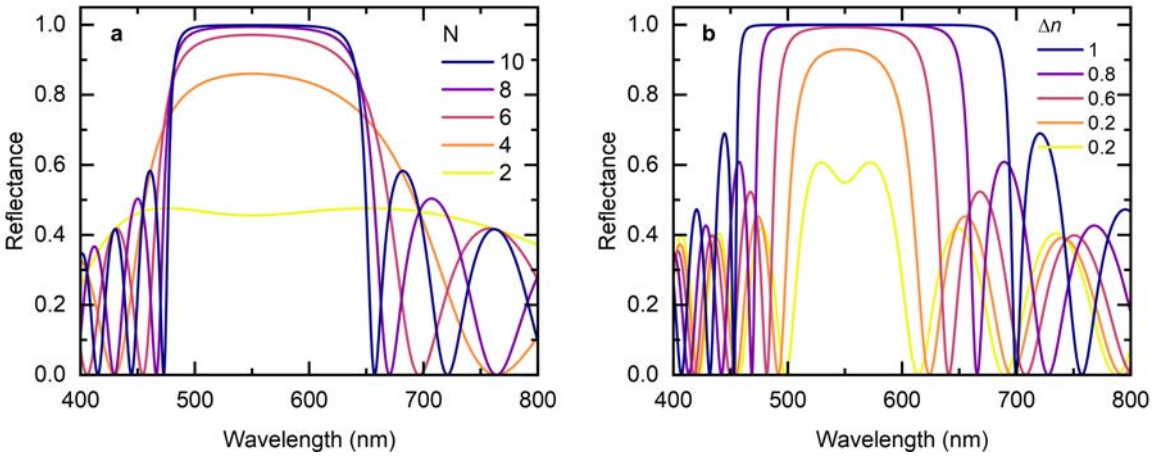

Figure 2.3: **Distributed Bragg Reflectors.** Calculated reflectance spectra of a dielectric multilayer stack centered at $\lambda_0 = 550$ nm with: (a) fixed refractive index contrast between layers, $\Delta n = 0.74$, and varying number of layer pairs N; and (b) fixed number of layer pairs $N = 10$, and varying refractive index contrast Δn.

which is a type of Fabry–Pérot resonator (see Figure 2.4(a)).

The term 'micro' applies when the cavity size is comparable to the wavelength of confined light λ in at least one dimension [54]. Such a configuration provides cavity modes, where light confined between the mirrors forms a standing wave satisfying:

$$n_c L_c = \frac{N\lambda}{2}, \tag{2}$$

with N denoting the *mode number*, corresponding to the number of antinodes in the standing wave. The product $n_c L_c$ is known as optical length or the optical cavity thickness and determines the resonant condition. Figure 2.4(b) schematically illustrates the electric field distribution for three cavity modes with lowest N. Modes with odd N exhibit even, centrosymmetric field distribution, whereas even N modes show antisymmetric profiles. For DBRs with the top layer made of the high-index material, the electric field nodes are located at the interfaces. These simplified considerations neglect penetration of light into the DBRs.

The presence of resonant states leads to enhanced light transmission at their corresponding energies. Figure 2.4(c) shows normal-incidence reflectivity spectra calculated using the transfer matrix method for a cavity with $n_{\text{low}} = 1.46$, $n_{\text{high}} = 2.2$, $n_c = 1$ (air), and $L_c = 275$ nm (a so-called single-mode $\lambda/2$ cavity, meaning that only the $N = 1$ mode lies within the energy range of the stopband), for different 3, 4 and 6 pairs of dielectric layer. A pronounced dip appears at the resonance of the fundamental $N = 1$ mode. As the number of DBR pairs increases, this dip narrows, corresponding to an increase in the quality factor Q, defined as:

$$Q = \frac{\omega_c}{\delta\omega_c}, \tag{3}$$

where ω_c is the resonant angular frequency and $\delta\omega_c$ is the full width at half maximum (FWHM). The Q-factor quantifies the rate at which optical energy decays from the cavity due to absorption, scattering, or leakage through imperfect mirrors. The inverse, Q^{-1}, represents the fractional energy

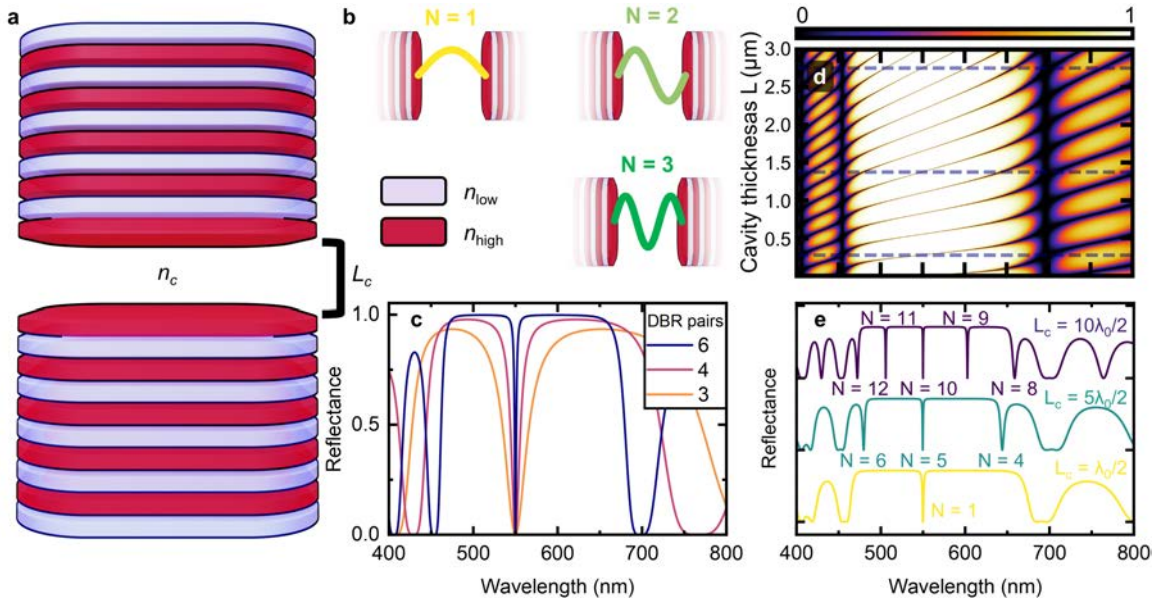

Figure 2.4: **Optical Microcavity.** (a) Schematic illustration of a planar optical microcavity formed by two distributed Bragg reflectors separated by a distance L_c and filled with air. (b) Spatial profiles of the three lowest-order cavity modes, corresponding to standing waves of the confined electromagnetic field. (c–e) Calculated reflectance spectra of the optical cavity. (c) As the number of DBR layer pairs increases, the spectral width of the cavity mode narrows. (d) Reflectance map as a function of wavelength and cavity thickness L_c. (e) Cross-sections of the map shown in (d), with corresponding cavity thicknesses and mode numbers labeled. As L_c increases, the free spectral range decreases, resulting in a greater number of cavity modes within the DBR stopband.

loss per cavity round-trip, while the cavity photon lifetime is given by $\tau = 1/\delta\omega_c$. The photon lifetime, optical length, and quality factor are related by the equation:

$$\tau = \frac{Q n_c L_c}{\pi c} \tag{4}$$

where c is the speed of light. This implies that a longer cavity length or a higher refractive index n_c results in a longer photon lifetime within the resonator.

Increasing L_c leads to the emergence of multiple cavity modes within the stopband; such structures are known as multimode cavities. Figure 2.4(d) shows a waterfall plot of reflectivity spectra for various cavity widths L_c, filled with air ($n_c = 1$), illustrating how additional modes with higher N appear within the stopband, while lower-N modes shift out. The free spectral range (FSR) is the mode spacing in optical frequency or wavelength and is decreases with increasing L_c. Note that, for clarity in illustrating the relationship between cavity thickness and photon wavelength, Figs 2.4(c–e) are plotted as a function of wavelength, resulting in an apparent asymmetry. If instead the horizontal axis was converted to energy, the spectra would become approximately symmetric with respect to the center of the stopband, and the FSR between successive pairs of modes would appear constant.

2.2.3 In-Plane Dispersion and Effective Mass

The previous consideration focused on the normal incidence, where the in-plane wavevector $k_{\|}$ vanishes. However, light in a planar cavity can freely propagate in the in-plane directions.

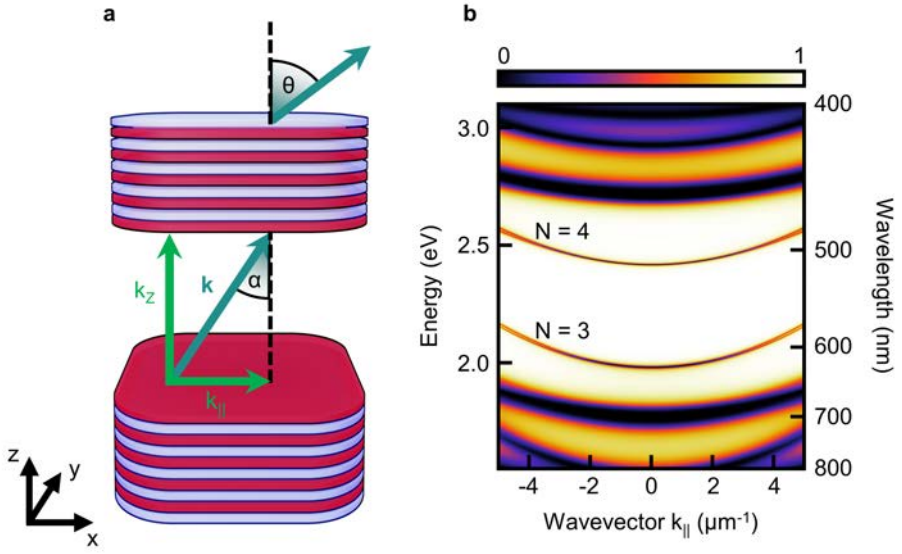

Figure 2.5: **Wavevector of a Confined Photon.** (a) Scheme of the optical cavity, showing the photon wavevector $\vec{k}$ decomposed into its in-plane component $k_{\|}$ and vertical component k_z. The angles α and θ illustrate the correspondence between the wavevector direction and the angle measured in experiment at which the photon exits the cavity. Note that if the refractive indices inside and outside the cavity are equal, then $\alpha = \theta$. (b) Calculated momentum-resolved reflectivity spectrum of an air-filled cavity with thickness $L_c = 1\,\mu\text{m}$.

The total wavevector $\vec{k} = (k_x, k_y, k_z) = (k_{||}, k_z)$, where the directions (x, y) correspond to the plane of the cavity and z is the confinement direction (see Figure 2.5(a)), can be decomposed into a longitudinal component $k_z = 2\pi n_c/\lambda$ and an in-plane component $k_{\|}$. In this form, the condition for photonic modes inside the resonator becomes $N\pi = k_z L_c$. For small $k_{\|}$, the photonic dispersion relation can be expanded as:

$$E(\vec{k}) = \frac{\hbar c}{n_c}|\vec{k}| = \frac{\hbar c}{n_c}\sqrt{k_z^2 + k_{\|}^2} \approx \frac{\hbar c}{n_c}\left(k_z + \frac{k_{\|}^2}{2k_z}\right) = \frac{\hbar c N\pi}{n_c L_c} + \frac{\hbar c L_c}{2n_c N\pi}k_{\|}^2. \tag{5}$$

In this approximation, the photonic dispersion relation inside the cavity exhibits a quadratic character, in contrast to free photons which have a linear dispersion. This results from the confinement in the z direction and the formation of a standing wave inside the resonator. By defining an effective mass of the cavity photon as:

$$m_c^* = \frac{\hbar n_c N\pi}{cL_c}, \tag{6}$$

the dispersion relation can be written in the form typical for a massive particle:

$$E(k_{\|}) = E_0 + \frac{\hbar^2 k_{\|}^2}{2m_c^*}. \tag{7}$$

Thus, the photon in the cavity can be treated as an optical analogue of a massive particle [54].

Based on Eq. (5), for two known mode energies E_{0,N_1} and E_{0,N_2} corresponding to any two consecutive modes N_1 and N_2, the slope a_0 can be determined as:

$$\Delta E_0 = E_{0,N_1} - E_{0,N_2} = \frac{\hbar c \pi}{n_c L_c} (N_1 - N_2) = a_0 (N_1 - N_2), \tag{8}$$

which in turn allows for the determination of any mode number N_m corresponding to a known energy $E_{0,m}$ as $N_m = E_{0,m}/a_0$.

Because $k_\parallel$ is continuous, angle-resolved measurements of photons that exit the sample (for example, in transmission or photoluminescence experiment) provide access to the in-plane momentum via:

$$k_\parallel = \frac{E_{\text{ph}}}{\hbar c} \sin\theta, \tag{9}$$

where θ is the emission angle in air relative to the surface normal (see Figure 2.5(a)) and E_{ph} is the photon energy. To visualize this dispersion relation, Figure 2.5(b) presents a calculated momentum-resolved reflectivity spectrum for a cavity of thickness $L_c = 1000$ nm, over a broad spectral range, so that two subsequent modes, $N = 3$ and $N = 4$, are shown.

2.2.4 Polarization and Spin-Orbit Coupling

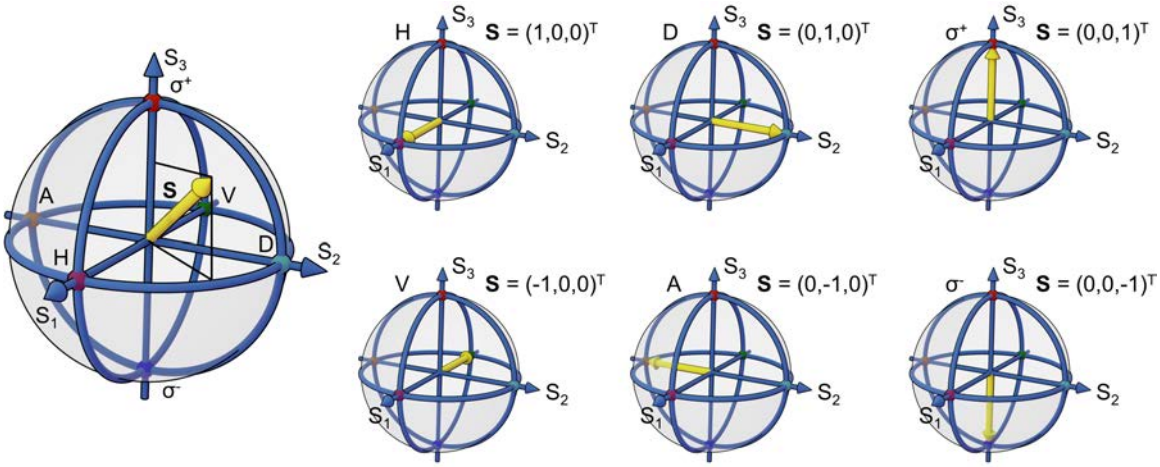

Figure 2.6: **Poincaré (Bloch) Sphere.** Schematic representation of the Poincaré sphere, where the orthogonal axes correspond to the Stokes parameters S_1, S_2, and S_3. The yellow vector $\vec{S}$ represents an arbitrary polarization state (or spin) on the sphere. Additionally, the six basis polarizations are indicated.

The polarization state of confined light, defined by the orientation of its electric field, plays a key role in cavity physics. A convenient description is given by the Stokes parameters (degree of polarization):

$$S_1 = \frac{I_H - I_V}{I_H + I_V}, \quad S_2 = \frac{I_D - I_A}{I_D + I_A}, \quad S_3 = \frac{I_{\sigma^+} - I_{\sigma^-}}{I_{\sigma^+} + I_{\sigma^-}}, \tag{10}$$

with S_0 representing the total intensity. The I values denote measured intensities in horizontal (H), vertical (V), diagonal (D), antidiagonal (A), right- (σ^+) and left-circular (σ^-) polarizations. The vector $\vec{S} = (S_1, S_2, S_3)^T$ maps onto the Poincaré sphere (see Figure 2.6), analogous to the Bloch sphere for spin-$\frac{1}{2}$ particles. Circularly polarized photons carry so-called spin angular momentum (SAM) of $\pm\hbar$ [23, 24]. Due to the conservation of angular momentum, light can be generated (or absorbed) in a medium with an excitonic (or exciton-polariton) state of the same spin. Therefore, studying the polarization of the emitted light also provides information about the spin of the particle in the cavity that emitted or absorbed it. The analogy between the Bloch sphere (representing particle spin) and the Poincaré sphere (representing polarization, i.e., spin of light), despite some differences (e.g., fermion spin is $\pm 1/2$, whereas light pseudospin is ± 1), allows one to interpret massive photons with spin in the cavity as quasiparticle analogs of electronic systems.

A crucial mechanism for controlling photonic spin is spin-orbit coupling (SOC) [23], arising in inhomogeneous or anisotropic media where polarization and spatial degrees of freedom are coupled, such that changing one affects the other. This leads to phenomena in which polarization influences the propagation path, or conversely, the shape or spatial structure of the beam affects its polarization. SOC leads to phenomena such as the optical spin Hall effect (OSHE) [55, 56], spin-to-orbital angular momentum conversion via q-plates or metasurfaces [57], and emulation of magnetic monopoles [58].

Several mechanisms can induce SOC in optical cavities. The most common is the TE-TM splitting. Since the transverse-electric (in-plane, TE) and transverse-magnetic (out-of-plane, TM) modes interact differently with an anisotropic medium (e.g., at the interface between layers in DBRs, where they satisfy different boundary conditions for the electric field), their energies split for $k_\parallel > 0$. For the TE mode, the electric field is perpendicular to the plane of incidence (that is, it is entirely within the cavity plane), whereas for the TM mode, it lies in the plane of incidence and therefore includes a longitudinal (z) component. The $k_\parallel$-dependent splitting between the dispersions of the TE and TM modes is quadratic in $k_\parallel$. As a result, the TE and TM modes have different effective masses and are degenerate only at $k_\parallel = 0$ (normal incidence), where no polarization is favored. This splitting can be modeled using an effective Hamiltonian with an in-plane synthetic (effective) magnetic field acting on the pseudospin of photons, leading, for example, to spin precession [59].

Strong birefringence, such as that offered by nematic liquid crystals, can significantly enhance and introduce other types of SOC beyond the conventional TE-TM splitting. For example, cavities that incorporate birefringent perovskites exhibit a substantial increase in TE-TM splitting and additional polarization splitting that from the point of view of an effective Hamiltonian can be interpreted as an artificial Zeeman field [60]. In this perspective, liquid crystals are excellent candidates for integration into such cavities to enhance spin-orbit interactions. Devices that combine liquid crystals and microcavities are called liquid crystal optical microcavities (LCMCs).

To briefly illustrate the concept of a nematic LCMC, Figure 2.7 presents simplified schematics of a typical device with homogeneous alignment, shown both without applied voltage (left) and with applied voltage (right). In the following chapters, this core device structure will be further modified. The liquid crystal matrix (which, in different chapters, may refer to phases other than the nematic) is embedded between the DBRs and aligned using specific orienting layers on both sides. ITO electrodes are also deposited on both sides (including the top surface) to provide electrical contacts. A detailed description of each component of the device is provided in the *Samples* section of the next chapter.

Since various conventions are used to denote linear polarizations (e.g., TE and TM, X and Y, H and V), which may represent opposite definitions across different works, it is necessary to clearly define the notation adopted in this thesis. Here, I primarily use the notation of horizontal (H) and vertical (V) polarization, defined in the laboratory frame. For the nematic LCMC, H polarization corresponds to the direction perpendicular to the spectrometer slit and is aligned with the long

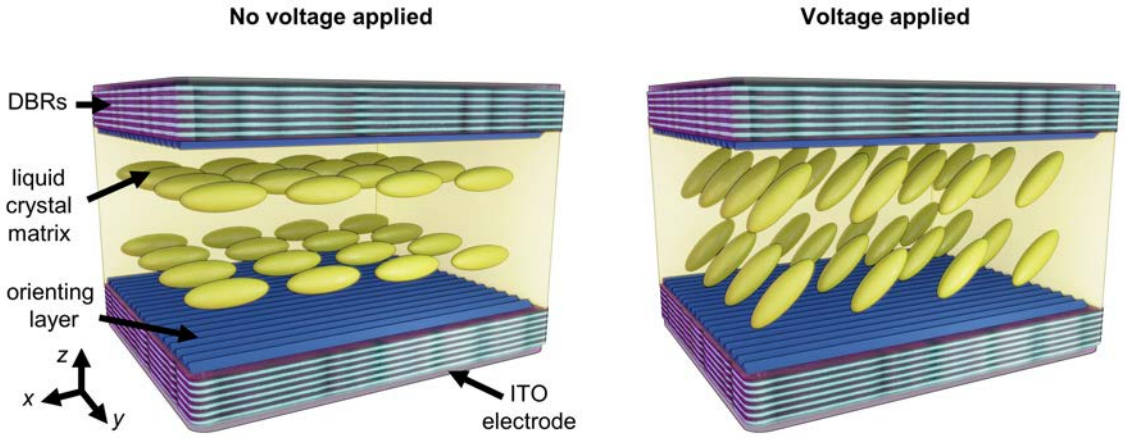

Figure 2.7: **Liquid Crystal Optical Microcavity.** Schematic illustration of an LCMC in two configurations: (left) without applied voltage, and (right) with an external voltage applied to the cavity.

axis of the molecules (or more precisely, with the rubbing direction, the x-direction in Fig. 2.7). V polarization corresponds to the direction along the slit (the y-direction in Fig. 2.7).

In the following, based on Figure 2.8 adapted from [2], I will discuss the key features of a nematic LCMC in the context of SOC.

The three-dimensional dispersion of photonic cavity modes is approximately paraboloidal (see Figures 2.8(A,D,G)). Figures 2.8(B,C) present momentum-resolved reflectivity spectra along the k_y direction, expressed in terms of S_0 (total intensity) and S_1 (degree of linear polarization between horizontal and vertical modes, here labeled as Y and X), respectively [2]. The homogeneous alignment of the nematic liquid crystal in the LCMC, combined with the high birefringence of the LC material ($\Delta n \approx 0.41$ [61]), leads to the splitting of the cavity modes into two eigenstates with orthogonal polarizations: horizontal (H, along the long axis of the molecules) and vertical (V, along the short axis). This splitting can be interpreted as a giant artificial Zeeman effect (on the order of hundreds of meV, though not shown explicitly in the figure).

A key advantage of such a system is the large range of dynamic tunability of the anisotropy of the medium, particularly through the use of an external electric field, as discussed in the previous section, which is difficult or even impossible to achieve in other systems. By rotating the LC molecules by applied voltage, the energy of the H-polarized mode can be tuned (due to a change in the effective optical cavity thickness for this polarization as the molecules align from homogeneous to homeotropic orientation). Consequently, the splitting of polarized optical modes, the analogue of the Zeeman splitting in electronic systems, can also be controlled or even switched off [2].

When the two modes have the same energy and parity, a large effective TE-TM splitting can easily be seen. Due to strong birefringence, this splitting can be up to two orders of magnitude larger than in typical anisotropic microcavities [1]. This effect is clearly visible in Figures 2.8(E,F), which show a strong difference in the effective masses of the H and V modes.

When H and V modes with different parities have the same energy, another type of spin-orbit interaction becomes prominent: the Rashba–Dresselhaus spin-orbit coupling (RDSOC). In this regime, the polarization of both modes acquires a strong and opposite circular component, and the modes

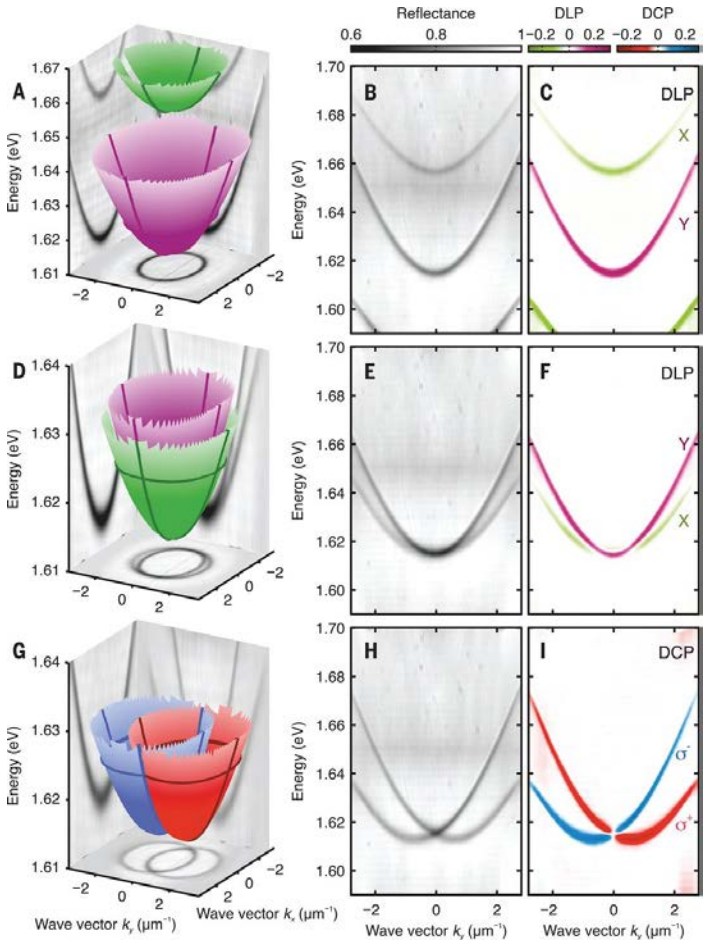

Figure 2.8: **Dispersion Engineering in a Tunable Liquid Crystal–Filled Optical Cavity.** (A, D, and G) Experimental 2D polarization-resolved reciprocal space tomography of reflectance at 0.0 (A), 1.38 (D), and 2.48 V (G). (B, E, and H) Reflectance dispersion at the $k_x = 0$ cross section. (C and F) The dispersion of the DLP at the kx = 0 cross section of the respective 2D dispersions for modes of the same parity. The two orthogonal modes correspond to the main axes of the LC indicatrix. (I) The dispersion of the DCP at the $k_x = 0$ cross section of the 2D dispersion, realizing the solution of the Rashba-Dresselhaus Hamiltonian. The figure and figure caption reproduced from [2].

are symmetrically shifted in the momentum space along the k_y direction. Unlike quadratic TE-TM splitting, this effect is proportional to k_y. This arises from a change of symmetry due to the different parities of the modes, which leads to the emergence of SU(2) symmetry in the resulting effective Hamiltonian [2]. The name comes from the electronic Rashba–Dresselhaus spin-orbit interaction, since the resulting dispersion relations, and the effective Hamiltonian describing the system, closely resemble those found for electrons. This is another example of how optical microcavities can be used to emulate phenomena known from solid-state physics.

2.2.5 Effective Hamiltonian and Spin-Orbit Phenomena in LCMCs

After the most relevant phenomena observed in liquid crystal microcavities are described, an effective Hamiltonian that captures their key features can be introduced. Using the Pauli matrix formalism:

$$\sigma_0 = \begin{pmatrix} 1 & 0 \\ 0 & 1 \end{pmatrix}, \tag{11}$$

$$\sigma_1 = \sigma_x = \begin{pmatrix} 0 & 1 \\ 1 & 0 \end{pmatrix}, \tag{12}$$

$$\sigma_2 = \sigma_y = \begin{pmatrix} 0 & -i \\ i & 0 \end{pmatrix}, \tag{13}$$

$$\sigma_3 = \sigma_z = \begin{pmatrix} 1 & 0 \\ 0 & -1 \end{pmatrix}, \tag{14}$$

we define a 2×2 effective Hamiltonian describing the coupling between H and V polarized cavity modes, incorporating RDSOC [2] and written in the circular polarization basis:

$$H_{\mathrm{RDSOC}} = \frac{\hbar^2 k_{||}^2}{2M} I + (\Delta_{HV} + \gamma k_{||}^2)\sigma_x + 2\alpha k_y \sigma_z, \tag{15}$$

where:

- I is the identity matrix,
- $\frac{\hbar^2 k_{||}^2}{2M}$ is the kinetic energy of the photon, where the effective mass is given by $M = \frac{2m_H m_V}{m_H + m_V}$. Here, m_H and m_V denote the effective masses of the H and V modes, respectively.
- $\Delta_{HV} = E_V - E_H$ is the $H - V$ detuning, corresponding to an effective Zeeman splitting,
- $\gamma = \frac{\hbar^2}{2m}$ with $m = \frac{2m_H m_V}{m_H - m_V}$ is the TE–TM splitting term,
- α is the RDSOC constant.

2.2.6 Mode Parity and Resonant Regimes

As mentioned above, the parity of LCMC modes plays a crucial role in the observation of many phenomena. Figure 2.9(a-e) presents schematic representations of the electromagnetic field distribution inside the cavity for H-polarized (purple curves) and V-polarized (green curves) modes, corresponding to different mode numbers indicated in the $(N_{\mathrm{V}}, N_{\mathrm{H}})$ notation above each panel. For clarity, the V-mode number is fixed at 3, while the H-mode number is varied; the inverse case is analogous. These different combinations of mode numbers will be referred to as *regimes* throughout this thesis.

Below each scheme of the regime, the corresponding momentum-resolved reflectivity spectra are presented, expressed by the Stokes parameters: S_0 (top row), S_1 (middle row) and S_3 (bottom row). These spectra were simulated using the Berreman matrix method (described in detail in the following chapter). The simulations assume a fixed cavity thickness of $L_c = 3450$ µm and a highly birefringent LC with $\Delta n = 0.41$, consistent with the material used in Chapters 4 and 5. This configuration ensures that the energy of the vertical mode remains constant, while different regimes are achieved by rotating the LC molecules, effectively tuning the energy of the horizontal mode [1].

The angle of orientation of the LC θ was chosen such that the energies of the H- and V-polarized modes at $k_{||} = 0$ were always degenerate ($\Delta_{HV} = 0$). The selected orientation angles (defined from the cavity normal) were: 0°, 30°, 51.15°, 65.15°, and 80°.

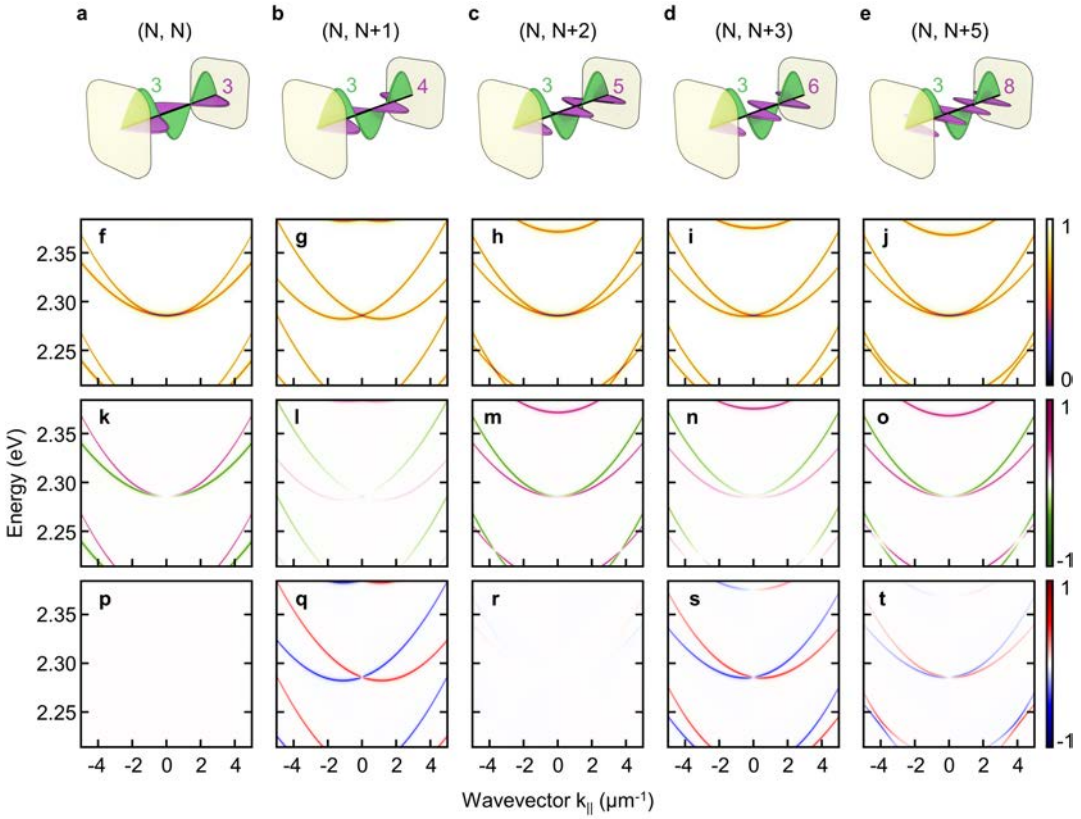

Figure 2.9: **LCMC Regimes.** (a–e) Schematic representations of the electric field distributions for H- (violet) and V-polarized (green) modes in selected LCMC regimes, labeled above each panel. Corresponding Berreman matrix method simulations of the momentum-resolved reflectivity spectra are shown as: (f–j) S_0 (total intensity), (k–o) S_1 (degree of linear polarization), and (p–t) S_3 (degree of circular polarization) Stokes parameters. In regimes where the H- and V-polarized modes exhibit opposite parity, the characteristic Rashba–Dresselhaus spin–orbit coupling is strongly pronounced in the S_3 spectra.

In the homeotropic configuration ($\theta = 0°$, Figures 2.9(a,f,k,p)), $N_V = N_H$. The spectra for total intensity (S_0, Fig. 2.9(f)) and linear polarization (S_1, Fig. 2.9(k)) reveal a large TE-TM splitting. The modes are fully linearly polarized, as indicated by the absence of a circular polarization component in S_3 (Fig. 2.9(p)).

The tilt of the LC molecules breaks the rotational symmetry of the cavity, giving rise to RDSOC. In the $(N, N{+}1)$ regime, illustrated in Figures 2.9(b,g,l,q), when the modes are in resonance, RDSOC is most pronounced, similar to what is observed in Figures 2.8(G,H,I). A strong elliptical polarization, predominantly circular, is visible for both parabolic branches (valleys), along with a significant valley separation $Q \propto \alpha$, where α is the RDSOC constant defined in Hamiltonian (15).

According to the waveguide approximation (see Supplementary Information in Ref. [2]), α is

given by:

$$\alpha = \frac{-\hbar^2}{m_c^* L_c} \frac{MN}{M^2 - N^2} \left(\frac{n_e^2 - n_o^2}{n_e n_o^2} \right) \frac{\sin\theta\cos\theta}{\sqrt{n_o^2 \sin^2\theta + n_e^2 \cos^2\theta}}, \tag{16}$$

where m_c^* is the effective mass of the cavity modes, L_c is the cavity thickness, M and N are the mode numbers of two modes with orthogonal polarizations (H or V), n_e and n_o are the extraordinary and ordinary refractive indices of the LC, respectively, and θ denotes the LC tilt angle.

Several implications can be drawn from this expression. First, the SOC strength α increases when the LC birefringence Δn also increases. Second, the term $\sin\theta\cos\theta$ reaches its maximum at $\theta = 45°$ and vanishes at $\theta = 0°$ and $\theta = 90°$. This indicates that LC molecules must be tilted to observe RDSOC. Furthermore, as the thickness of the cavity L_c increases, α decreases. However, when the cavity becomes too thin, achieving the $(N, N+1)$ resonance regime may become impossible. Such a situation, where the sample turned out to be too thin, required the fabrication of a new device.

Due to the term $M^2 - N^2$, the strongest coupling occurs when the mode numbers differ by one. Although not directly evident from the equation, α is nonzero only when the two modes have opposite parity. If both modes are either odd or even, RDSOC vanishes.

This effect is clearly visible in Figures 2.9(c,h,m,r) for the $(N, N+2)$ regime, similarly to Figures 2.8(E,F). Here, although the modes have different numbers, their identical parity leads to almost completely linear polarization (Fig. 2.9(m)), with only a very weak elliptical component appearing at higher wavevectors (Fig. 2.9(r)). The same applies to other regimes of the same parity, such as $(N, N+4)$ and $(N, N+6)$ (not shown).

Figures 2.9(d,i,n,s) and Figures 2.9(e,j,o,t) show the corresponding spectra for the $(N, N+3)$ and $(N, N+5)$ regimes, respectively. As predicted by Eq. (16), increasing the difference between the mode numbers N_V and N_H reduces the RDSOC strength. This manifests itself in a smaller valley separation Q (defined as the distance between the minima of the RDSOC valleys in reciprocal space) and stronger linear polarizations (Figs. 2.9(l,n,o)), at the cost of circular polarizations (Figs. 2.9(q,s,t)).

2.2.7 Spin-Orbit Coupled Phenomena in LCMCs

Although the integration of optical microcavities with liquid crystals had previously been used in tunable VCSELs [25], it is only with the recent approach employed effective Hamiltonians and the concept of *massive photons with spin* that their rich potential has been discovered. In the following, I present a brief overview of works that demonstrate the versatility of this system.

Due to mode tunability and strong TE–TM splitting, an externally controllable spin current has been demonstrated by the optical spin Hall effect (OSHE) [1].

Another notable phenomenon that can emulate an electronic system is the *optical persistent spin helix* (PSH) [4]. In spin–orbit coupled systems, spin-rotation symmetry is generally broken. However, when Rashba and Dresselhaus couplings are equal, an SU(2) spin symmetry arises that is robust to spin-independent disorder and interactions. This leads to infinite spin lifetimes for selected wavevectors and the emergence of PSH for electrons [62, 63]. This state was recently demonstrated for photons in LCMCs in the linear regime [4], and this thesis extends the study to nonlinear regimes, including both weak and strong light–matter coupling (Chapters 4 and 5, respectively).

Other types of spin patterns appearing in an electromagnetic field, second-order merons and antimerons, have been observed in LCMCs [3]. These half-skyrmion spin textures, which carry a topological charge of $\pm 1/2$, emerge in real space due to artificial gauge fields induced by spin–orbit coupling. Depending on the LCMC regime (from (N, N) to $(N, N+2)$), different types of merons with varying vorticities and topological charges form.

In momentum space, similar polarization singularities, referred to as *C-points*, have been demonstrated [21], forming Möbius strip-like structures in polarization pattern. Their number, position in reciprocal space and symmetry can be tuned via the non-Hermitian effects arising from coupling to higher-order and Bragg modes, as well as externally applied electric field.

These phenomena are closely related to the Berry curvature, which captures the local geometric structure of photonic bands and connects to global topological invariants such as the Chern number. When the nematic phase is twisted between mirrors (by a relative rotation of 45 degrees between rubbing layers), a diagonal–antidiagonal polarization splitting is introduced [7]. This symmetry breaking opens a gap in the RDSOC dispersion, leading to a highly localized, electrically tunable Berry curvature dipole.

Differences in the lifetimes of the H and V modes, due to polarization-dependent optical path lengths and scattering losses, give rise to non-Hermitian physics. This can be tuned by changing the H-V detuning Δ_{HV}. In the $(N, N+2)$ regime, for small positive Δ_{HV}, exceptional points (EPs) form at the crossing of the two branches in the momentum space. These EPs can be precisely controlled by continous change of the detuning and eventually annihilated [6].

These examples show only a part of the rich spin–orbit phenomena accessible in LCMCs. Remarkably, with the exception of [7], all of these results were achieved in nematic LCMCs without embedded light emitters. The integration of LCMCs with other liquid crystal phases in weak and strong light–matter coupling regimes, the subject of this thesis, remains a largely unexplored but highly promising field.

2.3 Light-Matter Coupling and Non-equilibrium Bose-Einstein Condensate

2.3.1 Interaction of Light with Matter

Light interacts with matter through various physical mechanisms, including reflection, absorption, spontaneous and stimulated emission, transmission, refraction, scattering, phase delay, changes in polarization, and many others. Each of these processes depends on both the properties of the incident light and the material involved.

When light is absorbed by a material, its energy is transferred to the matter. Matter can also emit light. This occurs, for example, when electrons in atoms or molecules are excited, typically via dipole transitions induced by incident photons, and subsequently return to their ground states, releasing energy in the form of photons. This emission underlies phenomena such as fluorescence and phosphorescence, which are classified as forms of photoluminescence (PL).

A particularly important concept in the context of optical transitions and light emission is a quasiparticle known as *exciton*. This is a bound states of an electron and a hole, which are attracted to each other because of their opposite electric charges via Coulomb electrostatic interaction. Excitons are electrically neutral bosons and are treated as elementary excitations in condensed matter physics.

Excitons are generally classified into two main types. The first type is the *Wannier–Mott exciton*. In semiconductors, the dielectric constant is typically large, which reduces the strength of the Coulomb interaction because of the screening of the electric field. In addition, the effective masses of electrons in such materials are usually relatively small. When the bandgap is narrow, the resulting Wannier–Mott excitons exhibit radii significantly larger than the lattice constant. This also leads to small binding energies compared to that of the hydrogen atom, typically on the order of 10 meV. As a consequence, such excitons are most commonly observed at cryogenic temperatures, where the thermal energy $k_B T$ is lower than the exciton binding energy.

The second type of exciton is the *Frenkel exciton*, which occurs in materials with relatively low dielectric constants, often organic molecular crystals. In such materials, Coulomb interactions can be strong, resulting in excitons with spatial dimensions on the order of the lattice constant. In molecular systems, excitons can even be fully localized on a single molecule. Their binding energies are significantly higher than those of Wannier–Mott excitons, typically ranging from 100 meV up to 1 eV. As a result, Frenkel excitons can be observed at room temperature.

2.3.2 Weak and Strong Coupling Regimes

Placing a material with a dipole-allowed transition (an emitter) inside an optical cavity resonant with that transition leads to coupling between the emitter and the eigenmodes of the cavity. This is typically achieved by positioning the emitter at an antinode of the electromagnetic field to maximize the interaction. The coupling to the oscillating electromagnetic field results in a periodic exchange of energy in a two-level system (for example, between the ground and excited electronic states), described by the Rabi frequency Ω. Depending on the ratio of the Rabi frequency to the dissipation rate of the cavity, two primary regimes of light–matter interaction can be distinguished: the weak coupling regime and the strong coupling regime.

In the weak coupling regime, the Rabi oscillation frequency is smaller than the rate at which the system loses energy or decoheres. Mathematically, for a single-mode cavity and a two-level emitter, weak coupling occurs when:

$$\Omega < \frac{1}{2}(\gamma_{\mathrm{ph}} + \gamma_{\mathrm{Ex}})$$

where γ_{ph} is the cavity loss rate (inversely proportional to the photon lifetime τ), and γ_{Ex} is the emitter decoherence rate, which includes both spontaneous emission and dephasing processes.

In this regime, a prominent phenomenon is the *Purcell effect*, which modifies the spontaneous emission rate of an emitter. Since the cavity enhances the density of optical states at the emitter's transition frequency, the emitter becomes more likely to emit into the cavity mode. The enhancement factor is quantified by the *Purcell factor* F_p, which depends on the quality factor of the cavity Q and mode volume V (i.e., the spatial confinement of the mode):

$$F_p = \frac{3}{4\pi^2}\left(\frac{\lambda}{n_c}\right)^3 \frac{Q}{V}$$

where n_c is the refractive index of the medium. This effect has important implications in various applications, such as laser design, where it allows for reduced lasing thresholds, as well as improved efficiencies in LEDs and solar cells. In quantum optics, it is used to enhance photon emission rates from single-photon sources.

In the weak coupling regime, light–matter interaction modifies the decay rate of the emitter rather than the energy levels of the cavity photons. As a result, in the energy–wavevector plot of typical planar cavities with an embedded light emitter (dashed lines in Figure 2.10), where the main emission mechanism is exciton recombination, the dispersion relations of the cavity photon (parabolic due to its effective mass) and the exciton (nearly flat due to its much larger effective mass) remain unaffected by each other. The two curves intersect directly without an *anticrossing*, indicating the absence of any significant interaction.

Light-emitting devices such as LEDs, lasers, and VCSELs typically operate in the weak coupling regime. When an externally pumped system (e.g., optically or electrically) exceeds a threshold value P_{th}, required to achieve population inversion, the system enters a non-equilibrium state in which stimulated emission dominates, leading to *photon lasing*. This results in a superlinear increase in

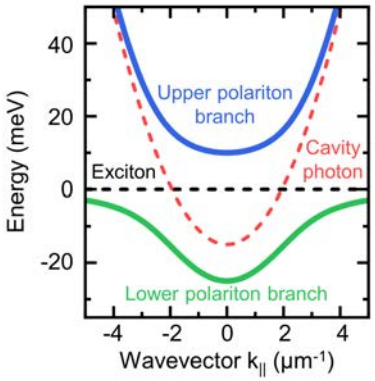

Figure 2.10: **Weak and Strong Coupling Dispersion Relations.** Momentum-resolved spectra for the photon and exciton in the weak coupling regime (dashed red and black lines, respectively), and for the upper and lower polariton branches in the strong coupling regime (solid blue and green lines, respectively), calculated using the Hamiltonian (17). The characteristic anti-crossing of the polariton branches is a signature of the strong light–matter coupling regime.

emission intensity with excitation power, accompanied by spectral linewidth narrowing. Due to Kerr nonlinearities, the lasing energy may redshift, although this is not a general rule [64].

When the interaction rate exceeds the sum of the photon and exciton decay rates, that is $\Omega > \frac{1}{2}(\gamma_{\mathrm{ph}} + \gamma_{\mathrm{Ex}})$, the system enters the *strong light–matter coupling regime*. In this regime, due to the hybridization of the exciton and cavity photon wavefunctions, new eigenstates are formed, referred to as *exciton-polaritons* (for simplicity they will be called polaritons). The system can be described by the model of two coupled oscillators with the effective non-Hermitian Hamiltonian:

$$H = \begin{pmatrix} E_{\mathrm{ph}} + i\hbar\gamma_{\mathrm{ph}} & \hbar\Omega/2 \\ \hbar\Omega/2 & E_{\mathrm{Ex}} + i\hbar\gamma_{\mathrm{Ex}} \end{pmatrix} \tag{17}$$

where E_{ph} and E_{Ex} represent the bare photon and exciton energies, respectively, and $\hbar$ is the reduced Planck constant.

Diagonalization of the above 2×2 Hamiltonian leads to the following eigenvalues:

$$E_{\mathrm{LPB,UPB}} = \frac{E_{\mathrm{ph}} + E_{\mathrm{Ex}} + i\hbar(\gamma_{\mathrm{ph}} + \gamma_{\mathrm{Ex}})}{2} \pm \frac{1}{2}\sqrt{(E_{\mathrm{ph}} - E_{\mathrm{Ex}})^2 + \left(i\hbar(\gamma_{\mathrm{ph}} - \gamma_{\mathrm{Ex}})\right)^2 + (\hbar\Omega)^2} \tag{18}$$

where E_{LPB} and E_{UPB} denote the energies of the lower and upper polariton branches, respectively. These are schematically plotted as solid lines in Figure 2.10.

Compared with the dispersion observed in the weak coupling regime, a characteristic anticrossing appears here, indicating strong coupling between the modes. Exciton-polaritons are referred to as hybrid quasiparticles because they inherit properties from both their constituent exciton and photon components. Due to their photonic character, they are extremely light: Their effective mass is approximately four orders of magnitude smaller than that of a free electron in vacuum and about three orders of magnitude smaller than the typical exciton mass in semiconductor quantum wells [65]. This ultralow mass enables long-range spatial coherence, with propagation distances that reach even several millimeters in certain cases [66]. Furthermore, the small effective mass allows quantum phenomena to be observed in these systems at much higher temperatures than

those required for cold atomic gases. The excitonic component, on the other hand, provides strong nonlinear interactions, several orders of magnitude higher than those of bare photons in conventional optical materials [67], as well as spin-selective interaction mechanisms.

The properties of exciton-polaritons depend on the relative contributions of their photonic and excitonic components. This composition can be tuned by the polariton detuning, defined as

$$\Delta_{\mathrm{pol}} = E_{\mathrm{ph}} - E_{\mathrm{Ex}},$$

where E_{ph} and E_{Ex} denote the energies of the bare cavity photon and exciton, respectively.

In typical semiconductor microcavities grown using molecular beam epitaxy, fixing the substrate holder during the growth process leads to the formation of so-called *wedge cavities*. In these structures, the cavity length L_c, and consequently the photon mode energy, varies continuously across the sample surface, allowing spatial control of Δ_{pol} simply by selecting different positions on the wafer.

As discussed in the previous section, two main mechanisms for detuning control are available in the LCMC system. The first involves wedge cavities (more details will be given in next chapter), similar to the semiconductor case, and affects both photonic modes H and V. The second utilizes an external electric field to modify the refractive index n_c in the nematic LCMC, thus affecting only the H-polarized mode. These approaches allow for precise tuning of the polariton detuning, and hence control over the photonic and excitonic fractions in the lower and upper polariton branches.

The excitonic fraction $|\chi(k_{||})|^2$ and the photonic fraction $|C(k_{||})|^2$ are described by the Hopfield coefficients [68]:

$$|\chi(k_{||})|^2 = \frac{1}{2}\left(1 + \frac{E_{\mathrm{Ex}}(k_{||}) - E_{\mathrm{ph}}(k_{||})}{\sqrt{\left(E_{\mathrm{Ex}}(k_{||}) - E_{\mathrm{ph}}(k_{||})\right)^2 + (\hbar\Omega)^2}}\right), \tag{19}$$

$$|C(k_{||})|^2 = \frac{1}{2}\left(1 - \frac{E_{\mathrm{Ex}}(k_{||}) - E_{\mathrm{ph}}(k_{||})}{\sqrt{\left(E_{\mathrm{Ex}}(k_{||}) - E_{\mathrm{ph}}(k_{||})\right)^2 + (\hbar\Omega)^2}}\right). \tag{20}$$

Figure 2.11 shows typical dispersion relations of exciton-polaritons for positive (Fig. 2.11(a)), zero (Fig. 2.11(b)), and negative (Fig. 2.11(c)) detuning, along with the corresponding Hopfield coefficients (Fig. 2.11(d–f), respectively).

At positive detuning, the lower and upper polariton branches closely resemble the dispersions of the exciton and photon, respectively, reflecting their dominant excitonic and photonic character. As detuning decreases, the effective mass of the lower polariton branch also decreases. At zero detuning, the excitonic and photonic components of both polariton branches are equally mixed at zero in-plane wavevector. However, as the wavevector increases, the lower polariton acquires a more excitonic character, while the upper polariton becomes increasingly photonic. Importantly, at zero detuning, the light–matter coupling strength $\hbar\Omega$ can be directly extracted from the energy splitting between the lower and upper polariton branches at $k_{||} = 0$.

In the case of negative detuning, the bare exciton dispersion intersects the photon dispersion at two distinct in-plane wavevectors (along one direction of $k_{||}$). At these points, the energy separation between the polariton branches again reflects the coupling strength. Between these intersections, the lower polariton exhibits a predominantly photonic character. This figure thus highlights how the effective masses of the polariton branches are modified by the light–matter interaction, and how their evolution can be systematically studied through detuning control.

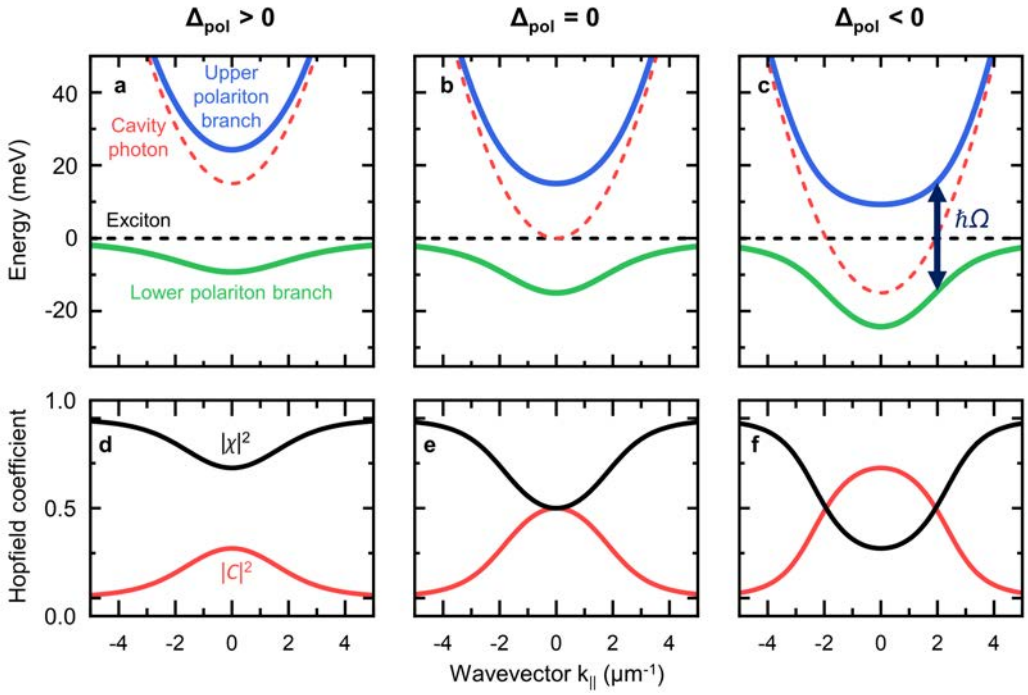

Figure 2.11: **Polariton Dispersion Dependence on Detuning.** (a–c) Momentum-resolved spectra calculated using Hamiltonian (17) for positive ($\Delta_{\mathrm{pol}} = 15$ meV), zero ($\Delta_{\mathrm{pol}} = 0$ meV), and negative ($\Delta_{\mathrm{pol}} = -15$ meV) polariton detuning. The bare exciton and cavity photon dispersions are shown as dashed lines. Simulation parameters: $\hbar\Omega = 30$ meV and $\hbar\gamma_{\mathrm{ph}} = \gamma_{\mathrm{Ex}} = 0$. In panel (c), the arrow indicates the in-plane wavevector at which the uncoupled photon and exciton intersect; at this point, the energy splitting between the upper and lower polariton branches corresponds to $\hbar\Omega$. (d–f) Corresponding Hopfield coefficients for the lower polariton branch: excitonic fraction $|\chi(k_{||})|^2$ (black) and photonic fraction $|C(k_{||})|^2$ (red).

Among the phenomena in which exciton-polaritons play a crucial role are, for example, polariton-mediated energy transfer [69], the modification of chemical reaction dynamics (polariton chemistry) [70], and polarization multistability [71, 72]. One of the most prominent examples is the Bose–Einstein condensation (BEC) of exciton-polaritons.

In contrast to photon lasing, polariton condensation does not require population inversion. Instead, the mechanism is governed by relaxation: above a critical density, polaritons macroscopically occupy the same quantum state in the form of a coherent matter wave. Because the polariton lifetime, limited by radiative leakage from the cavity, is comparable to or shorter than thermalization times, polariton BEC is classified as a non-equilibrium condensate (nBEC) and requires continuous external pumping. Despite its non-equilibrium nature, it exhibits many hallmarks of equilibrium BECs.

It is worth mentioning that BEC is a well-established phenomenon in a variety of bosonic systems. The first and most prominent realizations were in ultracold atomic gases such as rubidium [73] and sodium [74], which, however, require temperatures of the order of nanokelvins. Other examples include magnon BECs in antiferromagnets [75], exciton condensates in semiconductors [76], and

photon condensates in optical cavities [77].

Due to the extremely small effective mass of polaritons, BEC in this system can occur at temperatures much higher than those in atomic systems, even up to room temperature. Intuitively, condensation occurs when the density of bosons is sufficiently high for their wavefunctions to overlap. Using the expression for the de Broglie wavelength,

$$\lambda_D = \sqrt{\frac{2\pi\hbar^2}{mk_BT}},$$

where m is the particle mass, k_B is the Boltzmann constant, and T is the temperature, it is clear that the smaller the mass, the more easily this condition is satisfied.

The driven-dissipative nature of polariton BEC leads to unique properties, such as spontaneous coherence of many particles in the ground state [78], long-range order [79], quantized vortices [80], and superfluid behavior [81]. Furthermore, nontrivial condensate phases are expected to exhibit Berezinskii–Kosterlitz–Thouless and Bardeen–Cooper–Schrieffer physics [82].

The condensation process is illustrated in the momentum-resolved emission shown in Figure 2.12, based on the work of Kasprzak et al. [83], where exciton-polariton BEC was demonstrated for the first time in the CdTe-based microcavity.

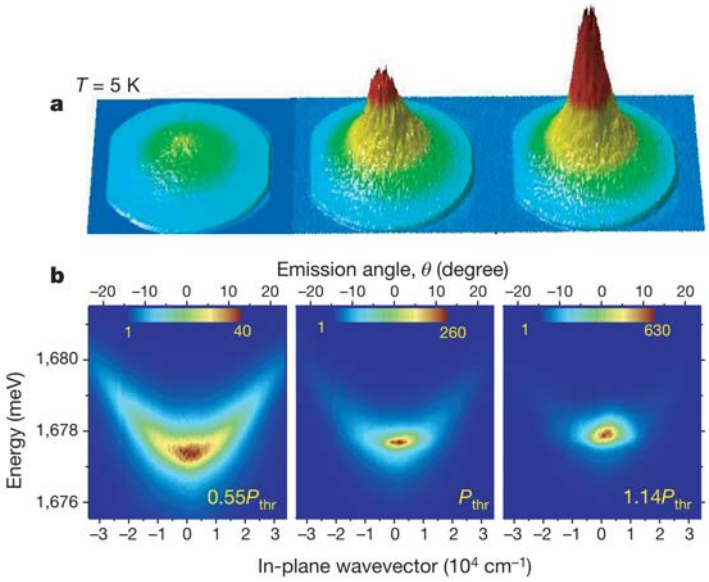

Figure 2.12: **Nonequilibrium Bose-Einstein Condensation of Exciton-Polaritons.** (a) Angle-resolved emission and (b) in-plane wavevector-resolved spectra as a function of excitation power. As the polariton density increases, relaxation toward the minimum of the lower polariton branch leads to nonlinear emission accompanied by a slight blueshift due to polariton-polariton interactions. As they thermalize, polaritons macroscopically occupy the ground state and spontaneously synchronize, resulting in the formation of a nonequilibrium Bose-Einstein condensate. Adopted from [83].

Below the condensation threshold (left panel), non-resonant excitation creates a hot cloud of polaritons, which predominantly occupy the lower polariton branch. The momentum space emission

exhibits a smooth distribution centered around $\theta_x = \theta_y = 0$. These polaritons undergo scattering with the crystal lattice, loss of energy through interactions with phonons, and relaxation toward the lowest energy state. As the excitation power increases and approaches the condensation threshold (middle panel), polaritons accumulate near $k_{\parallel} = 0$, and the emission from this state begins to dominate. Eventually, above the threshold (right panel), a strong peak emerges at $k_{\parallel} = 0$, signaling the macroscopic occupation of the ground state. In the momentum-resolved spectra, a distinct spectral narrowing and a blueshift of the emission line are observed above the condensation threshold. This blueshift results from polariton–polariton interactions. Although a moderate blueshift of the order of a few meV is often interpreted as an indicator of strong coupling, an excessively large blueshift may suggest a reduction in the light–matter coupling strength, potentially caused by sample heating and partial loss of strong coupling.

An important issue to address is the fundamental difference between photon lasing, polariton lasing, and Bose–Einstein condensation. A planar microcavity corresponds structurally to a vertical-cavity surface-emitting laser (VCSEL), which is well known for photon lasing involving population inversion and stimulated emission. In this regime, coherent emission results from the recombination of electron-hole pairs in weak light–matter coupling. The particles responsible for building coherence are the photons in stimulated emission process, and not the gain medium itself [82].

In the case of the polariton BEC, the first crucial distinction is the presence of strong coupling. Here, coherence is built by polaritons, which undergo a stimulated scattering into the $k_{\parallel} = 0$ mode during thermalization. Thus, even though both systems emit coherent light, the underlying mechanisms are fundamentally different: stimulated emission in photon lasing versus stimulated cooling in BEC.

The above considerations hold under the assumption that the system undergoes thermalization. On one end of the spectrum lies the polariton BEC, discussed earlier, where, ideally, the polariton lifetime is long enough for thermal equilibrium to be reached. In this case, the particle distribution is expected to follow the Bose–Einstein statistics. On the opposite end, if the polariton lifetime is too short or if there are additional dephasing mechanisms, strong coupling is lost, and the system behaves as a conventional photon laser.

The intermediate case occurs when strong coupling and macroscopic occupation of the ground state are preserved, but thermalization does not occur. This regime is referred to as polariton lasing. The term *polariton condensate* is often used as a broader classification that encompasses both polariton BEC and polariton lasing [82]. For a more detailed comparison of these three regimes, see [82].

BEC of exciton-polaritons is being extensively studied from both the perspective of fundamental physics (e.g., emergent phases of matter such as supersolidity) and potential applications (e.g., optical switches and spin-dependent propagation devices). More on this topic will be discussed in Chapter 5. However, it is worth emphasizing that room-temperature polariton condensation is most commonly demonstrated under conditions of very photonic detuning (as is also the case in this dissertation), where the excitonic fraction of BEC generally does not exceed 10%.

There is a substantial body of literature on polariton BEC reporting a wide range of physical phenomena. However, if a given effect does not inherently rely on interactions, such as polariton–exciton reservoir or polariton–polariton interactions (as required, for example, in superfluidity), its origin is often purely photonic. Such phenomena could be equally well demonstrated in the weak coupling regime using photons and conventional photon lasing. In this context, in my opinion, the use of polaritons and the BEC to present these effects, rather than photons and photon lasing, often appears to serve more of a promotional or "marketing" role, rather than reflecting a fundamental need for strong light–matter coupling or condensate physics.

2.4 Periodic Photonic Potentials

2.4.1 Fabrication of Photonic Potentials

As mentioned at the beginning of this chapter, photonic crystals represent a broad field of physics with a wide range of applications, including optical communication, solar cells, optical fibers, anti-reflective and reflective coatings, lasers, amplifiers, and many others. Interestingly, various forms of photonic crystals also occur in nature, notably in the wings of certain butterfly species [84] and in beetles (see Figure 2.13). Their vivid and metallic colors do not result from pigments, but rather from the reflective properties of photonic crystal structures arising from light interference within periodically ordered material layers.

Figure 2.13: **Adult Scarab Beetle – Chrysina Limbata.** The metallic sheen of the beetle's wings arises from a chirped photonic crystal structure composed of approximately 70 layers of chitin, each exhibiting slightly different refractive indices. Source: Wikimedia Commons, licensed under CC BY-SA 4.0.

From the perspective of this dissertation, the photonic crystal structure is employed in the context of photonic potentials confined within a planar optical microcavity. The microcavity itself acts as a one-dimensional photonic crystal, providing vertical confinement. In this work, several types of photonic potentials are explored: a flat, translationally invariant potential in nematic LCMCs (Chapters 4 and 5); a self-organized, periodic potential based on different liquid crystal phases (Chapters 6, 7, and 8); and an artificially microstructured periodic potential fabricated via focused ion beam (FIB) lithography (Appendix A).

Typical methods for fabricating spatially varying photonic potentials (such as single traps and lattices) can be broadly classified into subtractive (top-down), where material is removed, and additive (bottom-up), where material is deposited. One of the most widely adopted strategies involves lithographic techniques, which rely on transferring geometric patterns onto a substrate. Among these, scanning probe lithography employs a physical probe, similar to those used in atomic force microscopy (AFM), to transfer molecules to or from the substrate via mechanical, diffusive, electrical, or thermal interactions. Another well-established method is photolithography in which a light-sensitive photoresist layer is applied to the substrate. After patterning, typically by exposure to light through a photomask, subsequent etching processes are used to remove the material and define the microstructures. Etching can be performed using either wet techniques (chemical solutions) or dry methods (plasma-based processes).

A widely used approach in microcavity physics is direct-writing scanning beam lithography

(SBL). In this method, patterns are written onto a resist layer using one or more scanning beams of photons, electrons, or ions. Notably, the resist does not necessarily serve as an etch-resistant layer but rather as a medium that is directly modified. In typical implementations, the microstructure is defined on a resist layer (e.g., PMMA) deposited onto one of the cavity mirrors. After processing, the second mirror is deposited to enclose the cavity. Alternatively, in techniques such as focused ion beam (FIB) milling, microstructuring is performed directly on the grown microcavity by locally removing atoms from specific regions of the sample, thereby creating a potential barier at the sample–air interface. Due to the serial nature of SBL, fabrication times are relatively long, often requiring several hours to produce structures with lateral dimensions on the order of hundreds of micrometers squared. However, these methods offer exceptionally high spatial resolution and patterning precision.

Soft lithography involves the use of elastomeric stamps, typically made from polydimethylsiloxane (PDMS), to replicate micro- and nanoscale patterns. This method is advantageous because of its low cost, simplicity, and compatibility with a wide range of materials. Recently, such techniques have gained increasing popularity, particularly due to their ability to directly structure the active material (the emitter) on top of the DBRs [20, 85]. Other related techniques include nanoimprinting, which similarly allows for the replication of nanostructures through mechanical deformation of a resist layer [86].

These are just some of the possible techniques that can be employed to engineer a photonic landscape. Other methods include direct laser writing [87], optical lattices based on the excitonic reservoir [88,89], or even naturally occurring photonic disorder traps [90]. One particularly intriguing approach, already employed in general photonics [91, 92], but, to the best of my knowledge, not yet explored in the context of microcavities and massive photons, is the self-organization of periodic photonic potentials. In this dissertation, this method is investigated in the context of self-organizing liquid crystals.

This approach presents several advantages over conventional lithographic techniques, which will be discussed in more detail in Chapter 6. However, some of the key benefits may be briefly highlighted here: relatively fast, simple, and low-cost preparation of macroscopic photonic structures; the possibility of dynamic tuning, including electrical control; high birefringence, which can be spatially modulated; and the resulting remarkable polarization-dependent band splitting and strong spin-orbit interaction mechanisms, including previously not observed ones.

2.4.2 Types and Dimensions of Photonic Potentials

In the case of a flat photonic potential (nematic LCMC), massive photons are not additionally confined in the plane of the microcavity and are therefore free to propagate in the lateral directions.

Zero-dimensional photonic potentials (0D traps) are typically realized in the form of mesas (etched holes, for example, in the DBRs or substrate) [93] or micropillars [94]. In both cases, a refractive index contrast between the inside and outside of the trap leads to lateral confinement of the cavity modes, while vertical confinement is provided by the cavity. The dispersion relation of the confined photonic modes no longer follows the typical parabolic shape associated with massive photons but instead exhibits a ladder of flat, discrete resonances with approximately uniform energy separation. Such structures can be regarded as photonic artificial analogues of atoms or quantum dots. Similarly to electronic orbitals in atoms, the photonic states in these traps form a shell-like structure with ground and excited states (e.g., exhibiting commonly called *s*-, *p*-, or *d*-like symmetries), whose properties depend on trap parameters such as depth, width, and potential shape.

In addition, a single trap can serve as a building block for more complex potential landscapes. For instance, coupling two such traps may result in the formation of a *photonic molecule* [18, 95],

where hybridization of localized modes gives rise to bonding and antibonding states with controllable inter-site coupling. Arranging six traps in a hexagonal 'benzene-like' geometry can even lead to the emergence of spin-orbit coupling effects [96].

One-dimensional photonic potentials are most commonly realized through chains of laterally coupled pillars/mesas or photonic slabs. A periodic arrangement of multiple pillars, with spacing small enough to allow the wavefunctions of confined states to overlap, leads to the formation of photonic bands, analogous to electronic bands in solid-state physics. This effectively increases the dimensionality of the system by one. Instead of a dispersionless ladder of discrete states, the periodic modulation of the potential in one direction gives rise to energy bands with finite curvature, allowing the particles to acquire either positive or negative effective mass depending on the band structure.

By introducing a second sublattice, thus forming a so-called dimer chain, and tuning its parameters, including the coupling strengths between neighboring sites, one can realize the Su–Schrieffer–Heeger (SSH) model. In this configuration, edge states acquire nontrivial topological properties, which protect them against local perturbations [97, 98]. The coupling constants can also be controlled through spin-orbit interactions, such as TE–TM splitting [99]. Furthermore, theoretical proposals have suggested controlling the SSH chain topology using RDSOC [8].

A currently prominent effect that arises in photonic slab arrays embedded within microcavities is the formation of bound states in the continuum (BICs) [100], which exhibit exceptionally high quality factors. Other related phenomena include the realization of photonic waveguides [101] and subwavelength grating-based lasers [102].

Extending the photonic lattice into two dimensions offers a broad range of opportunities for engineering band dispersion and simulating many-body phenomena. For example, square lattices enable the realization of BEC in higher orbital modes [103] and facilitate the implementation of analog quantum simulators for XY Hamiltonians [104]. Triangular and honeycomb lattices provide access to Dirac point physics [105, 106], where linear dispersions emerge, while Lieb and Kagome lattices provide a versatile platform for studying flat-band physics [107–109].

Two-dimensional photonic lattices can also support topologically nontrivial states. This allows for the realization of photonic topological insulators [110–112], featuring robust unidirectional edge states whose propagation is protected against disorder and backscattering.

Due to their challenging implementation and limited spatial dimensions, to the best of my knowledge, no realizations of three-dimensional photonic lattices in microcavities have been reported. By a three-dimensional lattice, I refer to a structure that imposes a periodic modulation of the refractive index also along the vertical axis, that is, the direction in which the planar cavity confines light. For such a configuration to exhibit lattice interaction effects and to minimize boundary artifacts near the mirrors, the cavity would need to host at least several lattice periods along the vertical direction. This implies that the cavity thickness must span multiple wavelengths of confined light. Although technically demanding, such a device could be of significant interest for optical simulations of condensed matter phenomena in truly three-dimensional geometries.

The examples discussed above represent only selected phenomena from the broad and rapidly developing field of translationally invariant photonic potentials in optical microcavities.

3 Exprimental Methods

This chapter introduces and describes the samples investigated in this thesis, the experimental techniques used during the studies, as well as a brief overview of the data analysis and the simulation methods employed to model the observed phenomena. The chapter concludes with a statement outlining my contribution to the research.

3.1 Samples

The samples investigated in this thesis are planar liquid crystal optical microcavities, featuring either a uniform photonic potential (compare to the spectral linewidth, Chapters 4 and 5) or a periodic photonic potential, either self-assembled (Chapters 6, 7, and 8) or artificially fabricated (Appendix A). All samples were assembled by members of Prof. Wiktor Piecek's group at the Military University of Technology (MUT). Various types of samples were studied: six in total, one for each of the five experimental chapters and one for the Appendix A. Over the five years of research, each sample type was fabricated into several devices, either to improve the technological performance or to replace devices that had degraded.

Despite their differences, the core structure of all devices followed a similar design:

- The main component is a liquid crystal microcavity, as illustrated in Figure 2.7, which consists of indium-tin oxide (ITO) electrodes, DBRs, alignment layers, a liquid crystal layer in a particular phase, and an embedded light emitter. Each experimental chapter begins with a description of this part of the structure.
- Two parallel quartz or glass substrates were glued together to form what is referred to as a 'cell' or 'LC cell'. The photonic structure described above is enclosed within this cell.
- Silica spacers of varying thicknesses, mixed with glue, were placed along the edges of the cell to define the desired cavity thickness.
- The wires were soldered to the ITO electrodes to establish an electrical connection.

The exceptions were the samples discussed in Sections 8.1 and 8.2, which did not include Bragg mirrors, but were sandwiched within an LC cell or exfoliated as freestanding films.

Figure 3.1 shows a photograph of typical assembled devices. Above each sample, the number of the chapter in which it was primarily studied is indicated.

The sample labeled as "1" is mounted in the holder in a manner typical for experiments in Polariton Group Organic Laboratory. Most of the studied devices were fabricated on less expensive glass substrates polished to a flatness of $\lambda/4$(@633 nm), with a thickness of 1.1 mm (see sample "1"). In the strong-coupling LCMC project, one of the suspected reasons for the issues with achieving Bose–Einstein condensation (discussed further in Chapter 5) was the quality of the substrates. Due to various forces acting on the substrates (e.g., elastic, capillary, mechanical, and thermal expansion), they tend to bend slightly, which leads to local decreasing of the cavity quality factor.

The proposed solution was to use higher quality quartz substrates with a thickness of 3 mm and an improved flatness of $\lambda/20$ (see sample "2"). However, based on my observations $\lambda/4$-polished substrates performed equally well in any kind of experiment related to this thesis. Any potential bending was far less evident in the spectroscopic measurements than, for instance, the cavity wedge effect discussed below. Furthermore, within the typical experimental spot size, any bending-induced variations were negligible. Nevertheless, most LCMCs studied in Chapter 5 were sandwiched between one or two 3 mm quartz substrates, as shown in sample "2".

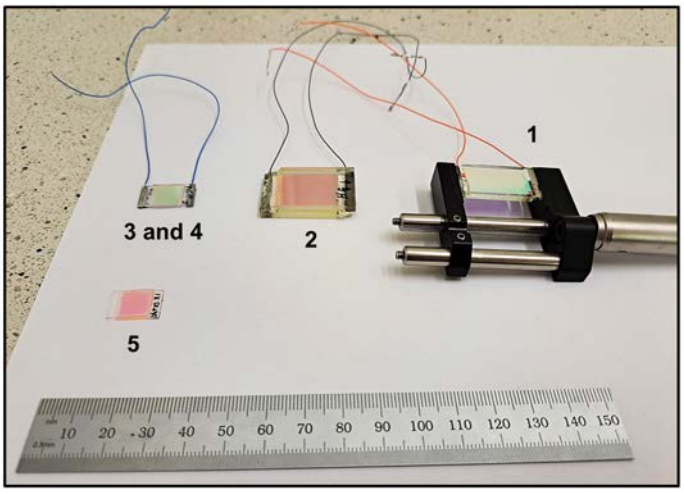

Figure 3.1: **Photograph of representative samples of various sizes studied in this dissertation.** The numbers correspond to the chapters in which the samples with the given geometries were investigated. From right to left: (1) A typical dye-doped liquid crystal microcavity mounted in a sample holder. (2) An LCMC with MeLPPP placed between 3 mm-thick glass substrates. (3 and 4) LCMC with self-organizing ULH and toron structures in a smaller cell. The wires are soldered to the ITO electrodes. (5) A liquid crystal cell without mirrors, containing monocrystalline blue phase (I). A centimeter ruler for scale.

Samples with self-organized photonic structures ("3 and 4", "5") were typically fabricated on smaller substrates (both in-plane dimensions and thickness, with 0.7 mm being standard), which made it easier to maintain a uniform temperature across the surface during fabrication. Additionally, blue phase samples (sample "5") did not include DBRs. Their color, unlike that of the other samples, did not originate from DBRs stopbands but from the photonic stopband of the blue phase crystal itself (more on this in Chapter 8).

Using spacers to define the cavity thickness seems, in principle, to be a good idea. Unfortunately, since the assembly is performed manually and the required precision is often in the range of 1 to 2 micrometers, the actual thickness occasionally differed significantly from the target value. Sporadically, the assembled cavities ended up being either too wide or too narrow, indicating that the spacers had likely been crushed. This was one of the reasons why multiple devices had to be fabricated for each sample type. This issue is now expected to be solved thanks to the recent purchase of equipment at MUT specifically designed for assembling LC cells, which will hopefully ease the work of future PhD students.

Many of the devices were intentionally fabricated with spacers of different thicknesses at opposite edges of the sample (e.g., 1.5 μm and 2.5 μm). This design, used in nematic LCMC samples (Chapters 4, 5, and the Appendix A), allows independent tuning of the energies of the two cavity modes. By moving along the wedge-type sample, the effective cavity thickness, and thus the energy of both horizontal and vertical modes, changes. However, applying a voltage only affects the horizontal mode energy. This provides remarkable and precise tunability, allowing one to reach desired cavity regimes, for example, at the energy of the exciton resonance of the active material. For samples with self-organizing photonic potentials (Chapters 6, 7, and 8), the cavity thickness plays a crucial role in determining the periodicity and size of the formed photonic structures. Thanks to the wedge, for

example, the experiment in Chapter 7 was possible: by changing the position on the sample in one direction, the photonic traps based on LC torons gradually decreased in diameter.

The ITO electrode layers (the material that is nearly transparent to visible light) was typically 20–30 nm thick. For samples with the P580 emitter (Chapters 4, 6, 7, 8, and the Appendix A), symmetric cavities were assembled using DBRs composed of 6 pairs of SiO_2/TiO_2 layers (12 layers total), centered at 550 nm. The samples with MeLPPP (Chapter 5) were asymmetric cavities with DBRs consisting of 15 and 13 SiO_2/Ta_2O_5 layers, with a central wavelength of 490 nm. Such cavities, where an additional scattering from the LC medium occurs, typically achieved a Q-factor in the range of 600 to 1800.

Various methods for orienting LCs have been developed [113–116]. The results presented in this thesis were obtained using samples with orienting layers that provided either homogeneous alignment, achieved by mechanical rubbing in an antiparallel configuration (used in nematic LCMCs and blue phase cells), or homeotropic anchoring, induced by surface chemistry (used in other self-organizing LCMCs). Different materials were tested for the orienting layers; in the case of nematic LCMCs, SE-130 was most commonly used, while in later samples incorporating MeLPPP, PMMA was used.

The cavities were filled with the LC mixtures by capillary action. For the nematic LCMCs, a high birefringence mixture, LC2091* (with refractive indices $n_o \approx 1.57$ and $n_e \approx 1.98$ at the sodium line 589 nm), was used. This mixture was developed in the group of Prof. Przemysław Kula at MUT. Different batches of LC2091* occasionally exhibited slight variations, for example, in light scattering efficiency, which influenced the Q-factor of the cavities. In the case of self-organizing structures, one type of sample used commercial LC, E7 ($n_o = 1.522$, $n_e = 1.737$ at $\lambda = 600$ nm). The blue phase mixture is described in detail in [117].

The results presented in this thesis are based on measurements from the following samples: Chapter 4 — three nominally identical samples; Chapter 5 — three nominally identical samples; Chapter 6 — two samples with different liquid crystals; Chapter 7 — two samples with different liquid crystals; Chapter 8 — eight different samples; Appendix A — two nominally identical samples. Differences between the samples are described in the respective chapters.

By nominally identical samples, I refer to devices that were designed to have the same parameters (orienting layers, DBRs, concentration of light emitter, etc.) but which are physically different objects, in some cases, assembled even years apart. This list does not include samples used only in the introduction paragraphs, such as self-organizing structures without DBRs shown in Fig. 6.18, or damaged MeLPPP samples shown in Fig. 5.3.

The results included in this thesis are limited to the representative samples and coherent body of work closely tied to the core goals of my PhD. However, the actual path to obtaining these results involved a significantly larger number of devices, either due to the need to explore alternative technological approaches (various LCs, emitters, orientation or self-assembly techniques, etc.), or due to some samples that did not meet the required quality, degraded over time, or were used in projects not covered in this thesis (e.g., projects that were unsuccessful, still ongoing, or managed by my collaborators).

In total, over the course of five years, I measured or at least preliminarily characterized at least 224 samples, including: planar nematic LCMCs in the weak coupling regime (with various emitters or none): 39; MeLPPP samples: 34; ULH samples: 19; toron samples: 21; blue phase samples: 63; FIB-fabricated structures: 6; mCherry protein samples: 20; LCMCs with chiral nanoparticle for non-Hermitian skin effect project: 7; LCMCs designed at 810 nm for PSH in the single-photon regime: 6; other: 9.

At this point, I would like to express my deep appreciation once again for the tremendous effort of Prof. Wiktor Piecek's group in preparing all of these samples.

3.2 Experimental Techniques

In the study of photonic crystals, including optical microcavities, two parameter spaces are typically of interest: the real space, defined by spatial coordinates and corresponding to the physical surface of the sample, and the reciprocal space, which relates to the angles at which light exits the sample. As shown in Chapter 2, Figure 2.5, these angles carry information about the in-plane wavevectors of the cavity modes. Therefore, the possibility of imaging both spaces provides a powerful tool for investigating the eigenstates of the cavity.

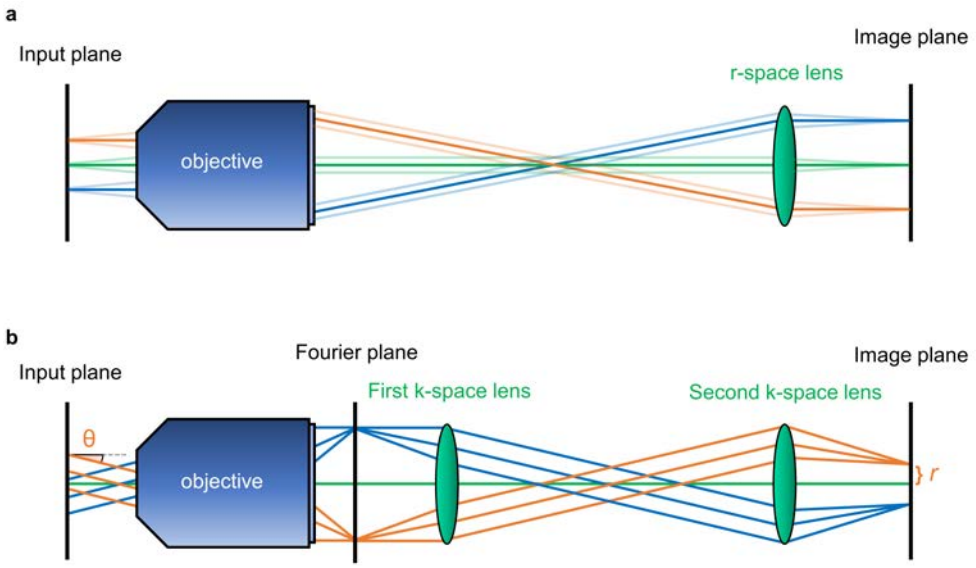

Figure 3.2: **The Scheme of Imaging in (a) Real Space and (b) Reciprocal Space.** Colors indicate light rays that (a) originate from the same spatial positions, and (b) initially propagate at identical angles.

Figure 3.2 presents the scheme of optical methods used to image both spaces. Figure 3.2(a) shows the setup for real-space imaging using a microscope objective and a single (ocular) lens. This configuration allows the input plane to be transmitted through the optical system and projected onto the image plane. Light rays originating from the same points in the input plane are marked with the same color. The magnification of the image is determined by the magnification of the microscope objective and the focal length of the lens.

Figure 3.2(b) presents a scheme of the reciprocal-space imaging setup. Here, light rays that initially propagate at the same angle θ are marked with the same color. Behind the microscope objective, initially parallel rays of light intersect in a plane known as the back focal plane (BFP). For infinity-corrected objectives, this plane contains the optically performed Fourier transform of the input plane. It can also be interpreted as the image of the sample as seen from infinity. In physical optical systems, the BFP is typically located directly behind the objective, close to its rear aperture (see Figure 3.2(b)).

By using two lenses (referred to here as "k-space lenses"), one can propagate the Fourier plane through the optical setup and project it onto the image plane. Knowing the numerical aperture NA of the microscope objective, this configuration allows the determination of the relationship between θ and the radial distance r from the optical axis:

$$\sin\theta = \frac{r}{r_{\max}}\mathrm{NA} \tag{21}$$

where $r_{\max}$ is the radius of the image. The exact positions of the lenses for a given focal length and desired magnification can be determined using the standard lens formula. Further details can be found in section 12.3.5 of [118].

Images collected using the setup shown in Figure 3.2(a) will be referred to as real-space or spatially-resolved images. Those obtained using the configuration in Figure 3.2(b) will be referred to as Fourier-space, reciprocal-space, momentum-space, momentum-resolved, or, in the case of samples without a cavity, angle-resolved images.

In principle, the objective in both setups can be replaced with a single lens. However, microscope objectives offer several advantages: flat-field imaging, high magnification, large NA, and correction of spherical and chromatic aberrations. In the classical 4f configuration [118], the r-space lens can also serve as one of the two k-space lenses. However, separating them into distinct elements provides more flexibility in designing the optical setup. It should also be noted that the ray paths shown in both schemes have been simplified and exaggerated to emphasize the core concepts of each technique.

The image plane contains spatially resolved information in both real and reciprocal space. A narrow stripe of this image is selected at the entrance slit of the spectrometer and then resolved spectrally. This results in maps of wavelength (or energy) as a function of position on the sample in real space, or as a function of angle θ (or wavevector k) in reciprocal space, both along the direction defined by the spectrometer slit. In LCMCs, the spectrally resolved real-space image is mainly determined by the photonic potential, whereas the reciprocal-space image typically shows a parabolic dispersion, as discussed in Chapter 2.

Because the spectrometer slit is vertically oriented relative to the laboratory frame, the thesis adopts the convention that this direction (also associated with vertical linear polarization V), is defined as the y-axis. This may initially cause confusion, as in both real- and reciprocal-space maps, the horizontal axis is typically labeled 'Position y' or 'Wavevector k_y', respectively.

The imaging geometry allows access to only a narrow part of the beam (usually a few tens of micrometers wide, depending on the slit width) because narrower slits provide higher spectral resolution (narrower spectral lines). The experimental setup is typically aligned so that the center of the detected beam is projected on the slit, corresponding in reciprocal space to $\theta_x = 0$.

To collect the full energy dependence as a function of position or wavevector in two dimensions, multiple measurements can be taken, each imaging a different part of the detected beam onto the slit. These individual slices can then be combined into a three-dimensional map. This technique, known as optical tomography, is typically implemented by mounting the final lens of the detection setup on an automated translation stage. By moving this lens, the detected beam is scanned across the slit, allowing different parts of the image to be probed.

This technique is extremely useful, as cross-sections of the resulting 3D maps provide access to isoenergetic planes or spectra along arbitrary directions in parameter space. However, the main drawback is acquisition time. When signals are weak, resolution requirements are high, and multiple polarizations must be collected separately, obtaining a complete single 3D map can take several tens of minutes to a few hours.

The experimental setups used to perform the main results presented in this thesis, which are based on the real-space and reciprocal-space imaging techniques discussed above, were built in two laboratories: the Polariton Group Organic Laboratory led by Prof. Jacek Szczytko (all experimental chapters except Chapter 5) and the Ultrafast Phenomena Laboratory (UPL) led by Prof. Piotr Fita (Chapter 5). Both setups are very similar; the second one was built to excite samples in the strong light–matter coupling regime using a femtosecond laser, not available in the Polariton Laboratory,

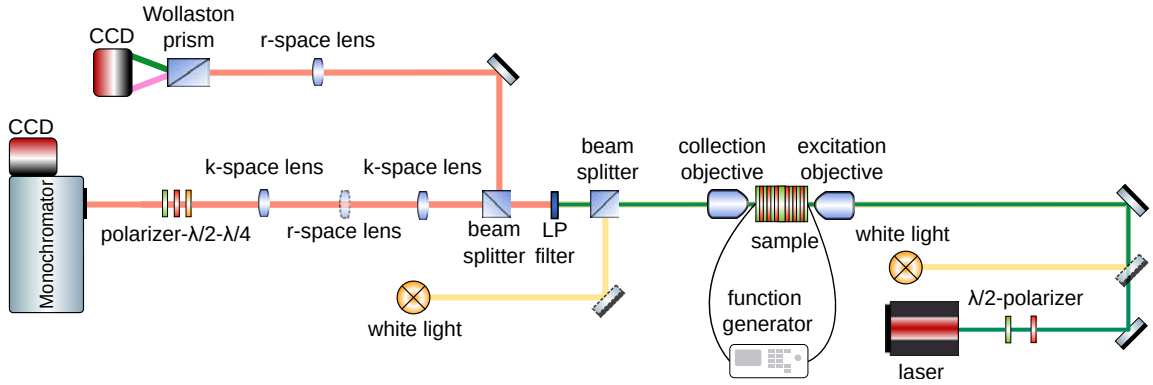

Figure 3.3: **Scheme of the Basic Experimental Setup.** Straight lines help trace the optical path of different beams (green – excitation laser, yellow – white light, red – detected signal).

with the aim of generating Bose–Einstein condensates. Figure 3.3 shows the scheme of the key components of both systems. Differences specific to the UPL setup, compared to the Polariton setup, will be noted in parentheses. Dashed lines indicate removable or optional components (e.g., the r-space lens is removed during reciprocal-space measurements, or the white light source is blocked during emission measurements).

At the heart of the system is a Czerny–Turner Andor Shamrock 750 spectrograph (Princeton Instruments IsoPlane SCT 320), equipped with an Andor Newton DU940P (ProEM-HS 1024) 2D-CCD camera. The image plane is projected onto the entrance slit of the spectrograph (left side of the diagram), providing the possibility of acquisition of angle- or spatially resolved spectra.

Let us now follow the configuration from the transmission and excitation side on the right of the scheme. For emission measurements, the sample is excited using a Q-switched diode-pumped laser Cobolt Tor XS, 532.1 nm center wavelength, 2-ns pulse duration, from 1000 Hz to single-shot repetition rate (a femtosecond laser system Light Conversion Orpheus-F OPA pumped by Carbide, tunable emission wavelength, typically set to 426 nm in Chapter 5 experiments, 181-fs pulse duration, 2 MHz to single-shot). A half-wave plate mounted on a motorized rotation stage and a fixed polarizer are used to control the excitation energy. As the white light source on the transmission side, a Thorlabs SLS302 tungsten–halogen lamp is used with a short-pass filter to eliminate IR radiation.

The sample is excited using objectives selected depending on the experiment: 5X Nikon CFI60 TU Plan Epi (NA = 0.15), 20X Nikon CFI60 TU Plan Epi ELWD (NA = 0.4), or 60XC CFI S Plan Fluor ELWD (NA = 0.7). The diameter of the laser spot on the sample surface ranged from 2 to 10 µm depending on the experiment. In the UPL setup, the excitation objective was replaced with a lens (f = 100 mm) to focus the laser to a 20 µm spot.

To tune the dispersion relation of the cavity modes, the nematic LCMCs were driven with a Rigol DG2041A AC waveform generator, providing a 1010 Hz square wave with peak to peak amplitude in the range of 0–20 V.

On the detection side, a 60XC CFI S Plan Fluor ELWD (NA = 0.7, with compensation for cover glass thickness) was used (50X Mitutoyo Plan Apo NIR HR in UPL). All objectives were infinity corrected. The first 30:70 (R:T) non-polarizing beam splitter allows for an additional white light source (IKEA lamp) used for reflectivity measurements. This configuration provides an easy way to focus the sample with the detection objective, which helps aligning in transmission-mode

experiments. A 532-nm long-pass (LP) filter blocks the excitation laser to protect the detectors.

A second 50:50 non-polarizing beam splitter directs the beam toward two detectors simultaneously. The lower arm includes AB coated imaging lenses with focal lengths f: k-space – 1000 and 500 mm, r-space – 750 mm. A polarization detection setup ($\lambda/4$-$\lambda/2$-polarizer) allows for the selection of one of six polarization states: horizontal H (x direction), vertical V (y direction, along the spectrometer slit), diagonal D, antidiagonal A, and both circular σ^+ and σ^-, as defined in Chapter 2. The polarizer is fixed in orientation to match the spectrometer grating axis, whereas the waveplates are mounted on motorized rotation stages. Proper rotation angles were calibrated using a Thorlabs PAX PAN5710VIS polarimeter at $\lambda = 532$ nm.

The other half of the beam, reflected by the 50:50 beam splitter, is independently focused by an f = 500 mm lens on a Thorlabs 8050M-USB monochrome 2D-CCD camera (CMOS ZWO ASI 178MM-Cool) through a Wollaston prism that spatially separates the H and V polarization components on the camera sensor. This configuration enables simultaneous acquisition of spectra (via spectrometer) and real-space imaging in both linear polarizations. It is not only very convenient for photonic structure measurements, but also essential for experiments such as single-shot lasing to observe PSH and supersolidity phenomena discussed in Chapters 4 and 5.

In principle, additional lenses could be integrated into the upper detection arm to enable energy-integrated momentum imaging. However, since such measurements could also be performed in the zeroth-order diffraction mode of the spectrometer, I never found it necessary to implement this extension.

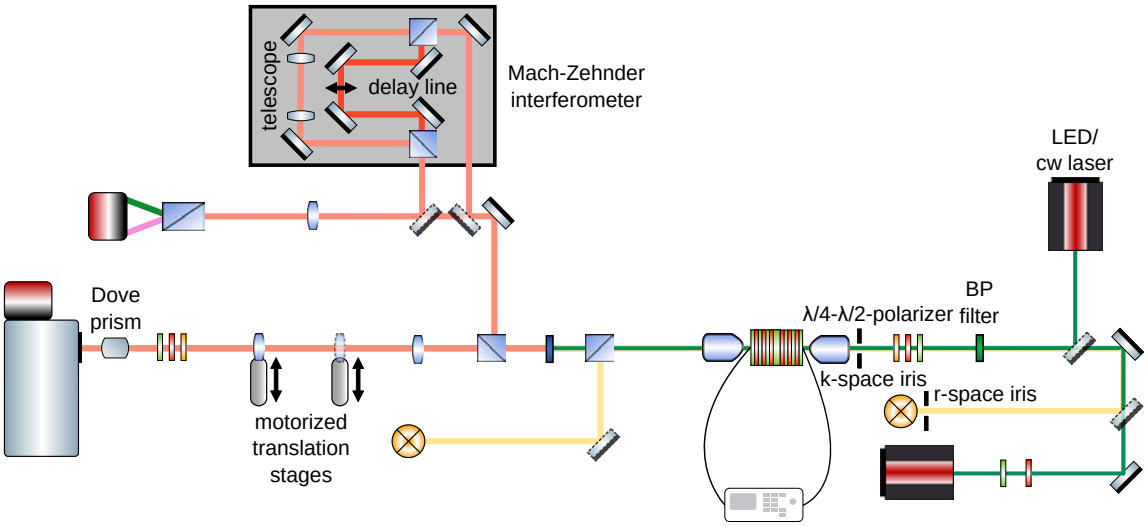

Figure 3.4: **Scheme of the Extended Experimental Setup.** For clarity, only newly introduced optical elements are labeled.

The part of the setup described above contains the core of most of the experiments presented in this thesis. However, the setup was frequently adapted for specific experiments. Figure 3.4 shows its extended version with additional components. Starting from the right side: the r-space iris, mounted at the output of the white light source fiber, allows for easy adjustment of the illuminated area, from covering the full field of view of the detection objective (hundreds of square microns) to a spot with a diameter on the order of several microns. Although the textbook solution would be to use a telescope, this method is much more practical when frequently changing the spot size is needed,

and I did not observe any visible diffraction-related artifacts for white light in the experiment.

Additional light sources, such as LEDs or *cw* lasers at 405 and 532 nm, can also be introduced into the setup in either transmission or reflectivity (not shown) geometry. In this thesis, they were used for the *in situ* formation of 0D photonic traps (Chapter 6) and the characterization of Kossel patterns (Chapter 8).

Because LCMCs are sensitive to temperature changes, results from long spectroscopic measurements (such as polarization- and angle-resolved optical tomography or a scan as a function of voltage) may exhibit fluctuations in the energy of the modes. To minimize this effect, during such measurements, the excitation beams were blocked using an automated optical beam shutter when data was not being acquired, and a set of band-pass filters matched to the spectrometer window (approximately 60 nm range) was inserted into the beam path.

In measurements where well-defined polarization of the incident beam was essential (e.g., Chapter 5, Fig. 5.9), the second polarization setup was used on the excitation side, operating on the same principle as the detection-side polarization setup, but arranged in reverse order (the beam first passes through a polarizer and then through the waveplates).

An k-space iris, placed in the back focal plane of the excitation objective, allows the angular range of the incident light to be limited on demand without replacing the objective. This is useful in real-space transmission experiments (narrowing the line width), but it also remarkably enhanced the visibility of photonic structures in LCMCs. Discovering this trick significantly improved the comfort of my measurements.

Mounting the r-space lens and the second k-space lens on motorized translation stages allows for optical tomography measurements described previously, which was used in Chapters 7, 8, and the Appendix A.

Rotating the Dove prism results in a rotated image. This is useful in experiments where the system geometry is essential (e.g., due to RDSOC direction or the shape of photonic structures—see Chapter 6 or the Appendix A), although properly aligning it is time-consuming and challenging. Note that rotation with a Dove prism does not preserve light polarization, so it must be placed after the polarization detection setup.

For interference measurements (Chapter 8, Fig. 7.10), a Mach–Zehnder interferometer was built with a manually controlled delay line (a black arrow indicates the direction of movement of two mirrors) and the telescope in one of the arms. The interfered image from both arms was detected on the upper CCD camera.

At this point, a more in-depth comment on polarization detection is necessary. Since polarization plays a major role in the study of LCMCs, the entire detection side of the optical setup (from the point where light exits the sample to the spectrometer slit) is kept in a single straight line, without reflections (as mirror reflections can depolarize the signal). This is quite an unusual configuration for spectroscopy setups, and requires that the sample be mounted perpendicular to the optical table. Moreover, the precise alignment of the sample with respect to the optical axis (i.e. how perpendicular it is to the propagated beam) has a significant effect on detecting subtle polarization phenomena, and so sensitive measurements required patient alignment of the sample placed between two short working distance objectives. Despite these efforts and the use of achromatic optics, light undergoes slight depolarization ($\approx$2–4%) after passing through the detection side. A natural solution would be to place the polarization detection immediately after the detection objective. In fact, this approach was used in the orbital angular momentum measurements in Chapter 8, Fig. 7.10, because the circular polarization state of light reflected from multiple mirrors in the interferometer was almost completely lost.

However, for the main (lower) optical axis, this approach is unfortunately not suitable. Placing the polarization optics far from the spectrometer introduces a small beam shift that depends on the

waveplates orientation. Although this shift is negligible or compensable when polarization is selected just before the spectrometer, it becomes unacceptable if introduced before the lenses on motorized stages. Therefore, in the vast majority of experiments, the polarization detection setup was placed directly in front of the spectrometer.

It is also worth emphasizing that the spectrometer itself preferred one linear polarization, so it is good practice to make the final optical element a polarizer with fixed orientation.

Most emission experiments were performed in a low repetition rate regime, where it is difficult to accurately determine the pulse energy using the power meters available in the laboratory. Instead of permanently placing a power meter in the setup, a calibration curve of the pulse energy as a function of the angle of the motorized half-wave plate used to control excitation power was recorded. For this purpose, the power meter was placed in the sample position and the calibration was performed at a repetition rate of 1000 Hz. The spectrometer, top-arm camera, beam shutter, and laser are synchronized and can be triggered simultaneously on demand. Other instruments, including the function generator, polarization setups, and motorized stages, are also controlled via custom in-house software.

For clarity, the schemes do not show elements such as neutral density filters, collimating lenses for light sources, laser line clean-up filters, additional alignment mirrors, and irises. For the curious reader, photographs of the optical setup used in the Polariton Group Organic Laboratory are included in the Appendix B in Figure 9.11. To preserve realism, the device cables were not disconnected.

There are several methods for calibrating detector pixels to positions in real space and angles in reciprocal space. In real space, if the optical magnification of the system is known (based on the parameters of the optical elements used) and the pixel size of the detector is specified, one can calculate how many micrometers in the image correspond to a single camera pixel. An alternative approach is to identify a distinctive feature in the image (e.g., a dirt on the sample surface) and trace how its position changes as the sample is moved by a known distance using a micrometer screw. For reciprocal space calibration, one can use Eq. 21. I prefer to use calibration samples with well-defined properties.

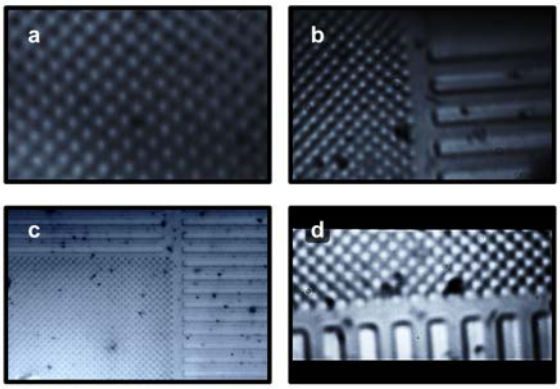

Figure 3.5: **Real-Space Calibration.** Photographs of the real-space calibration sample taken at various positions and with different imaging setups: (a, b) real-space imaging camera equipped with a Wollaston prism, (c) automated microscope, and (d) spectrometer using the 0-th diffraction order. The black stripes at the top and bottom in panel (d) correspond to the spectrometer slit.

The calibration sample for real-space scaling consists of lithographically fabricated structures

with precision higher than the resolution of typical optical systems. These structures have well-defined sizes and spacings. Figure 3.5 shows real-space images of this sample taken using different detectors. The sample contains etched dot arrays with diameters of 1 µm, arranged in a regular square lattice with a center-to-center distance of 2 µm (see Fig. 3.5(a)). It also contains rows of etched stripes, each 2 µm wide, with a spacing of 4 µm between their centers (Fig. 3.5(b-d)).

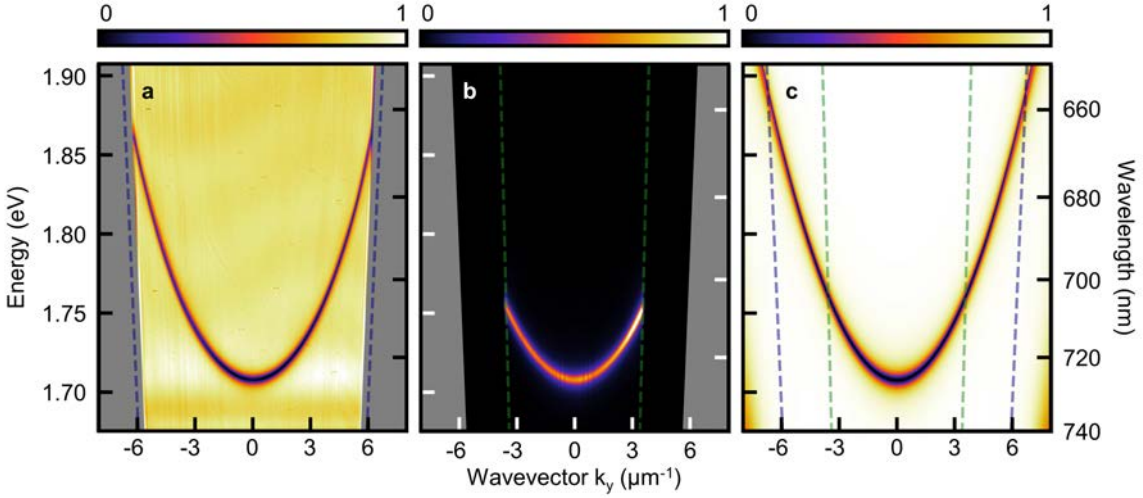

Figure 3.6: **Wavevector Calibration.** (a) Normalized momentum-resolved reflectivity spectra measured on a reciprocal space calibration sample using a collection microscope objective with a numerical aperture NA = 0.7. (b) Normalized momentum-resolved transmission spectra obtained using an excitation objective with NA = 0.4. Gray regions indicate areas outside the range of collection objective accessibility. (c) Simulated momentum-resolved reflectivity spectra for the same dielectric stack, calculated using the 4×4 Berreman matrix method. Half-transparent navy and forest green dashed lines indicate the theoretical maximum wavevector values accessible with the two objectives.

The sample used for reciprocal-space calibration consists of a known stack of 9 SiO_2/TiO_2 dielectric layers per Bragg mirror, forming a $\lambda_0/2$ microcavity centered at 726 nm. Using the setup shown in Figure 3.3, reflectivity (Figure 3.6(a)) and transmission (Figure 3.6(b)) measurements of white light were performed and compared with a simulation using the Berreman 4×4 matrix method (Fig. 3.6(c)), which will be described in the next section. The good agreement between the measured and simulated energies at k_y=0, allows to compare the cutoff energy and thereby determine the maximum observable in-plane wavevector, and extract the calibration scale for the horizontal axis.

Since the in-plane wavevector in y direction k_y and the detection angle θ_y are related to Eq. 9, the transformed image will take a trapezoidal shape. Furthermore, the range of observable k_y can be compared with the theoretically accessible maximum derived from the relation $\mathrm{NA} = n\sin(\theta_{\max})$, where the refractive index of the medium $n = 1$ because the angles are detected in the air.

In Fig. 3.6, $\theta_{\max}$ converted to the corresponding maximum in-plane wavevector $k_{y,\max}$ is indicated with dashed lines. In reflectivity measurements, $\theta_{\max}$ is limited by the collection objective, here with $\mathrm{NA}_{\mathrm{det}} = 0.7$, which corresponds to $\theta_{\max,\mathrm{det}} = 44.4°$. Compared with the simulation, it turns out that the maximum angle actually observed is 41.4°, meaning that the remaining 3° are lost due to

apertures of other optical elements.

In transmission measurements, the excitation objective with $\mathrm{NA_{exc}} = 0.4$ was used, corresponding to $\theta_{\mathrm{max,exc}} = 23.6°$. Since $\mathrm{NA_{det}} > \mathrm{NA_{exc}}$, the maximum detectable signal in this case is limited by the excitation objective and perfectly matches the experimental data.

Both of the calibration methods described above were used in the analysis of the results presented in this thesis.

3.3 Modelling Approaches

This thesis presents simulation results of different types of LCMCs, obtained using several numerical methods, either performed by me or by my collaborators. In the following, I briefly introduce two numerical approaches that I used.

3.3.1 Berreman 4×4 Matrix Method

The first approach used to calculate the nematic LCMCs spectra is the Berreman 4×4 matrix method [119], a numerical technique used to model light propagation through stratified anisotropic media. It is based on the well-known, though less general, transfer-matrix method, which is commonly used for isotropic media.

Reflection at a single interface between two media is described by the Fresnel equations. However, when light encounters multiple interfaces, as in photonic structures like Bragg mirrors, the partially reflected and transmitted beams can interfere constructively or destructively. As a result, the total transmission and reflection of light through such a structure is the sum of multiple interference contributions.

In the matrix formalism of wave propagation, light propagation through a single layer can be expressed as:

$$\begin{pmatrix} E_r^{(2)} \\ E_l^{(2)} \end{pmatrix} = \hat{\mathbf{M}} \begin{pmatrix} E_r^{(1)} \\ E_l^{(1)} \end{pmatrix},$$

where $\hat{\mathbf{M}}$ is a 2×2 wave transfer matrix:

$$\hat{\mathbf{M}} = \begin{pmatrix} M_{11} & M_{12} \\ M_{21} & M_{22} \end{pmatrix}.$$

The matrix elements M_{ij} depend on the optical properties of the medium, such as layer thickness and refractive index. The amplitudes $E_r^{(1)}$, $E_l^{(1)}$, $E_r^{(2)}$, and $E_l^{(2)}$ correspond to the electric field amplitudes of the incident, reflected, transmitted and incident from the back waves, respectively. For a multilayer structure, the total transfer matrix $\hat{\mathbf{M}}_{\mathbf{total}}$ is given by the product of the individual transfer matrices of each layer:

$$\hat{\mathbf{M}}_{\mathbf{total}} = \hat{\mathbf{M}}_N \cdot \hat{\mathbf{M}}_{N-1} \cdot \cdots \cdot \hat{\mathbf{M}}_1.$$

This total matrix allows one to calculate the overall transmission and reflection coefficients of the entire photonic structure.

The 4×4 Berreman matrix method is a generalization of the transfer-matrix method for anisotropic media, in which the optical properties are described by a 3×3 dielectric tensor $\hat{\varepsilon}$. A comprehensive description of the method and derivation of the relevant coefficients can be found in [119]; here, I present only the key results.

The generalized 4×4 transfer matrix equation for TE and TM waves takes the form:

$$\begin{pmatrix} A_{\mathrm{TE}} \\ B_{\mathrm{TE}} \\ A_{\mathrm{TM}} \\ B_{\mathrm{TM}} \end{pmatrix} = \hat{\mathbf{T}} \begin{pmatrix} C_{\mathrm{TE}} \\ D_{\mathrm{TE}} \\ C_{\mathrm{TM}} \\ D_{\mathrm{TM}} \end{pmatrix}, \tag{22}$$

where A, B, C, D are the amplitudes of electric field amplitudes of the incident, reflected, transmitted, and back-incident waves, respectively, for both TE and TM linear polarizations.

Each layer of the structure is described by a partial transfer matrix $\hat{\mathbf{T}}_i$, given by:

$$\hat{\mathbf{T}}_i = \exp\left(-\mathrm{i}\frac{2\pi}{\lambda}\hat{\Delta}_i d_i\right), \tag{23}$$

where λ is the wavelength of light, d_i is the thickness of the layer, and $\hat{\Delta}_i$ is the propagation matrix:

$$\hat{\Delta}_i = \begin{pmatrix} -k_x\frac{\varepsilon_{31}}{\varepsilon_{33}} & -k_x\frac{\varepsilon_{32}}{\varepsilon_{33}} & 0 & 1-\frac{k_x^2}{\varepsilon_{33}} \\ 0 & 0 & -1 & 0 \\ \varepsilon_{23}\frac{\varepsilon_{31}}{\varepsilon_{33}} - \varepsilon_{21} & k_x^2 - \varepsilon_{22} - \varepsilon_{23}\frac{\varepsilon_{32}}{\varepsilon_{33}} & 0 & k_x\frac{\varepsilon_{23}}{\varepsilon_{33}} \\ \varepsilon_{11} - \varepsilon_{13}\frac{\varepsilon_{31}}{\varepsilon_{33}} & \varepsilon_{12} - \varepsilon_{13}\frac{\varepsilon_{32}}{\varepsilon_{33}} & 0 & -k_x\frac{\varepsilon_{13}}{\varepsilon_{33}} \end{pmatrix}, \tag{24}$$

where $k_x = n_a \sin\theta_a$, with θ_a being the angle of incidence and n_a the refractive index of the incident medium.

The formulation in [119] assumes that the incident wave lies in the xz-plane (i.e., $k_y = 0$). To achieve results for an arbitrary incident angle ϕ (including components along k_y), one can rotate the dielectric tensors of each layer according to:

$$\hat{\varepsilon}' = \hat{\mathbf{R}}(\phi)\hat{\varepsilon}\hat{\mathbf{R}}(-\phi) \tag{25}$$

where $\hat{\mathbf{R}}$ is rotation matrix.

The total transfer matrix $\hat{\mathbf{T}}$ is then calculated as the product of the individual layer matrices:

$$\hat{\mathbf{T}} = \hat{\mathbf{L}}_a^{-1}\left(\prod_{i=1}^{N}\hat{\mathbf{T}}_i\right)\hat{\mathbf{L}}_f, \tag{26}$$

where $\hat{\mathbf{L}}_a^{-1}$ and $\hat{\mathbf{L}}_f$ are the input and output matrices, respectively, given by:

$$\hat{\mathbf{L}}_a^{-1} = \frac{1}{2}\begin{pmatrix} 0 & 1 & -1/n_a\cos\theta_a & 0 \\ 0 & 1 & 1/n_a\cos\theta_a & 0 \\ 1/\cos\theta_a & 0 & 0 & 1/n_a \\ -1/\cos\theta_a & 0 & 0 & 1/n_a \end{pmatrix}, \tag{27}$$

$$\hat{\mathbf{L}}_f = \begin{pmatrix} 0 & 1 & -n_f\cos\theta_f & 0 \\ 0 & 0 & 0 & 0 \\ \cos\theta_f & 0 & 0 & n_f \\ 0 & 0 & 0 & 0 \end{pmatrix}. \tag{28}$$

Here, θ_f is the exit angle of the light in the final medium. For typical symmetric configurations where both input and output media are vacuum ($n_a = n_f = 1$), $\theta_f = \theta_a$.

Once the full transfer matrix $\hat{\mathbf{T}}$ is calculated, and assuming no back-incident light ($D_{\mathrm{TE}} = D_{\mathrm{TM}} = 0$), the equation simplifies to:

$$\begin{pmatrix} A_{\mathrm{TE}} \\ B_{\mathrm{TE}} \\ A_{\mathrm{TM}} \\ B_{\mathrm{TM}} \end{pmatrix} = \hat{\mathbf{T}} \begin{pmatrix} C_{\mathrm{TE}} \\ 0 \\ C_{\mathrm{TM}} \\ 0 \end{pmatrix}, \tag{29}$$

which, with known incident amplitudes A_{TE} and A_{TM}, reduces to four linear equations for the reflected and transmitted light $B_{\mathrm{TE}}, B_{\mathrm{TM}}, C_{\mathrm{TE}}, C_{\mathrm{TM}}$:

$$B_{\mathrm{TE}} = -\frac{A_{\mathrm{TM}}(T_{13}T_{21} - T_{11}T_{23}) + A_{\mathrm{TE}}(T_{23}T_{31} - T_{21}T_{33})}{-T_{13}T_{31} + T_{11}T_{33}}, \tag{30}$$

$$B_{\mathrm{TM}} = -\frac{A_{\mathrm{TM}}(T_{13}T_{41} - T_{11}T_{43}) + A_{\mathrm{TE}}(T_{31}T_{43} - T_{33}T_{41})}{-T_{13}T_{31} + T_{11}T_{33}}, \tag{31}$$

$$C_{\mathrm{TE}} = -\frac{-A_{\mathrm{TM}}T_{13} + A_{\mathrm{TE}}T_{33}}{T_{13}T_{31} - T_{11}T_{33}}, \tag{32}$$

$$C_{\mathrm{TM}} = -\frac{-A_{\mathrm{TM}}T_{11} + A_{\mathrm{TE}}T_{31}}{-T_{13}T_{31} + T_{11}T_{33}}. \tag{33}$$

This method is extremely useful for planar LCMCs with translationally invariant photonic potentials in the xy-plane, as it enables the calculation of momentum- and polarization-resolved spectra. It also allows for the introduction of absorption effects and thus the impact of light–matter interaction, including in the strong coupling regime.

3.3.2 Finite Difference Method

The second method used is based on the finite difference method. In the case where the dielectric tensor $\hat{\varepsilon}$ is position-dependent in the x and y directions, the Berreman matrix method becomes significantly harder to generalize. An alternative, instead of solving Maxwell's equations numerically, as in the FDTD method, is to reduce the problem to a 1D Schrödinger-like equation. The effective two-mode Hamiltonian $\hat{\mathcal{H}}$ written in a linear basis is time-independent but spatially dependent:

$$\hat{\mathcal{H}}(x)\psi(x) = E\psi(x) \tag{34}$$

where E is the eigenvalue corresponding to energy and ψ is the 2D wave function, in this case $\psi = [\psi_H, \psi_V]^{\mathrm{T}}$, where ψ_H, ψ_V denote the electric field for horizontally and vertically polarized mode, respectively.

Typically, the above eigenvalue problem is not solvable analytically. Instead, the space is discretized so that

$$\hat{\mathcal{H}}(x_i)\psi(x_i) = E\psi(x_i) \tag{35}$$

where x_i are points on the grid in the discretized 1D space, with distance between neighouring points equal to h, and n is a number of points.

Since the Hamiltonians proposed in Chapters 6 and Appendix A contain both first- and second-order derivative terms (e.g. $\partial/\partial x$ and $\partial^2/\partial x^2$), the set of $2n$ differential equations are not independent. This dependence can be found by using Taylor expansions, one can approximate the central derivatives as follows:

$$\left.\frac{\partial\psi}{\partial x}\right|_{x=x_i} \approx \frac{\psi(x_{i+1}) - \psi(x_{i-1})}{2h} \tag{36}$$

$$\left.\frac{\partial^2\psi}{\partial x^2}\right|_{x=x_i} \approx \frac{\psi(x_{i+1}) - 2\psi(x_i) + \psi(x_{i-1})}{h^2} \tag{37}$$

In this way, the problem is transformed into a system of algebraic equations. For a one-dimensional grid with n points, this leads to the problem of the $2n \times 2n$ matrix eigenvalue. For a two-dimensional grid with $n \times m$ points, the Hamiltonian becomes a $2nm \times 2nm$ matrix.

This matrix eigenvalue problem can be solved numerically using standard diagonalization techniques to obtain the energy spectrum.

3.4 Author Contributions

Since the results presented in this thesis are the outcome of collaborative work involving many researchers from different scientific institutions, I find it appropriate to acknowledge the contributions of my collaborators and to clearly distinguish which results are of my own authorship.

In all projects described in the following five chapters and Appendix A, I acted as the Principal Investigator under the supervision of Prof. Jacek Szczytko.

The assembly and orientation of the cells described throughout the thesis were performed by Dr. Eng. Przemysław Morawiak (MUT). All dielectric mirrors for LCMCs, except those used in Chapter 5, were fabricated by Dr. Eng. Rafał Mazur (MUT). The mirrors, MeLPPP layers, and Al_2O_3 protective coatings in Chapter 5 were prepared at IBM Research, mostly by Darius Urbonas. The self-organizing samples (Chapters 6, 7, 8) were prepared by Dr. Eva Oton (MUT). The FIB-structured substrates (Appendix A) and their AFM characterization were performed by myself. The high-birefringence liquid crystal LC2091* was synthesized in the group of Prof. Przemysław Kula (MUT).

All experimental measurements not explicitly attributed to others were performed by me, sometimes with the assistance of Polariton Group members (postdoc, PhD students, MSc and BSc students, all chapters), and IBM Research group members (coherence and single-shot measurements in Chapter 5). I used three experimental setups for these measurements. Most of the data (excluding Chapter 5) were acquired using the experimental setup in the Polariton Group Organic Laboratory. This setup was originally built by previous PhD students but was significantly expanded and adapted by me for LCMC photonic structures studies. I also co-developed the automation software used in this laboratory. The setup in UPL (used for most of the Chapter 5 results) was built from scratch by me. The coherence and single-shot measurements of Chapter 5 were carried out by me at IBM Research.

Theoretical models presented in this thesis were proposed by Prof. Guillaume Malpuech and Prof. Dmitry Solnyshkov and their collaborators Dr. Pavel Kokhanchik and Dr. Daniel Bobylev (Institute Pascal, CNRS, Clermont-Ferrand), as well as by Przemysław Oliwa and Prof. Witold Bardyszewski (UW). All simulations not explicitly attributed to others were performed by me. This includes the Berreman method and finite difference simulations, which were performed using software kindly shared by Przemysław Oliwa.

All data analysis and visualization, unless explicitly attributed to other authors, were performed by me.

Interpretation of the results was the outcome of discussions among my collaborators in the TopoLight project, particularly Prof. Jacek Szczytko (Polariton Group, UW), Prof. Guillaume

Malpuech and Prof. Dmitry Solnyshkov (CNRS), Prof. Wiktor Piecek (MUT), and Prof. Thilo Stöferle and Prof. Rainer Mahrt (IBM Research Zurich).

4 Nematic Planar Liquid Crystal Optical Microcavity in the Weak Coupling Regime

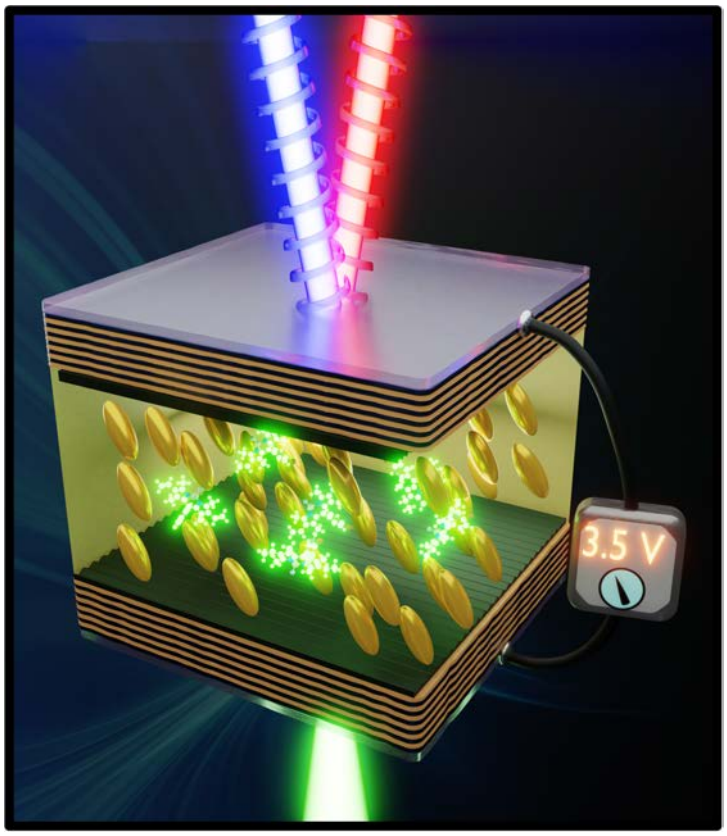

The results presented in this chapter have been published in:

M. Muszyński, et al. Realizing persistent-spin-helix lasing in the regime of Rashba-Dresselhaus spin-orbit coupling in a dye-filled liquid-crystal optical microcavity. *Phys. Rev. Appl.* **17**, 014041 (2022). [5]

This chapter introduces the optical properties of a dye-doped planar nematic liquid crystal microcavity in the weak coupling regime. It begins with the characterization of tunable photonic modes and the demonstration of tunable spontaneous emission. Subsequently, the nonlinear regime with tunable photonic lasing is presented. This tunability enables lasing in the Rashba-Dresselhaus spin-orbit coupling regime, where laser action occurs from the bottoms of two oppositely polarized valleys shifted apart in reciprocal space. The interference between these two beams leads to the formation of a Persistent Spin-Helix lasing on the surface of the sample.

4.1 Tunable Photonic Modes and Tunable Spontaneous Emission

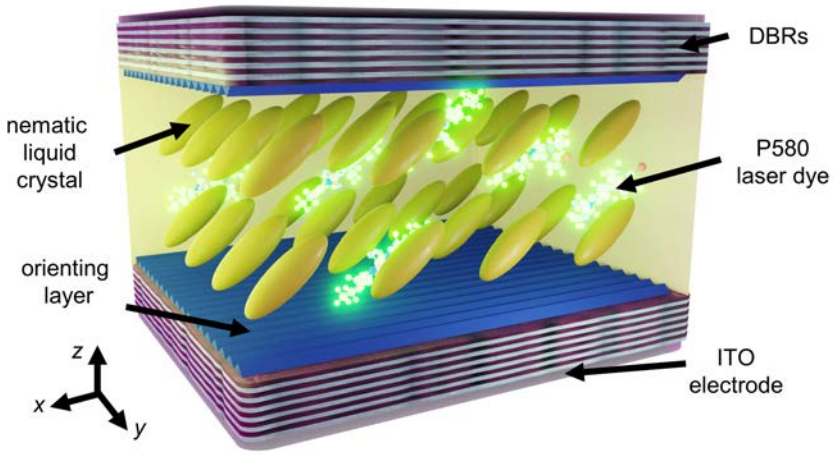

Figure 4.1: **Scheme of the Dye-Doped Planar Nematic Liquid Crystal Optical Microcavity.** The Figure illustrates the scenario when a voltage is applied to the sample, causing the liquid crystal molecules to rotate at a non-zero angle.

The scheme of the dye-doped LCMC device is presented in Figure 4.1. Its design is similar to the LCMC described in the Introduction chapter, where the LC molecules have a homogeneous orientation without applied voltage. To introduce gain into the system, an organic laser dye, pyrromethene P580, is dispersed within the LC matrix.

The choice of emitter is dictated by the desired lasing characteristics. To achieve Bose-Einstein condensation of exciton-polaritons (strong light-matter coupling regime), characterized by condensation thresholds approximately two orders of magnitude lower than for photonic lasing [120, 121] and strong polariton-polariton interactions, materials with narrow excitonic transision lines (on the order of a few meV) and minimal Stokes shift (significant overlap between absorption and emission spectra) are required. However, such a narrow spectral gain profile limits the tunability of the lasing wavelength. Therefore, achieving a broadly tunable laser source necessitates an emitter with a wide gain spectrum [122, 123].

The two primary criteria were taken into account in the choice of the active material: efficient room-temperature emission (quantum yield) and compatibility with liquid crystals inside the optical microcavity. In addition, selection was restricted by the experimental capabilities available in the laboratories. Ideally, the emitter should operate in the visible or near-infrared range (detectable by silicon detectors), efficiently emit light when excited by the available lasers described in the

Experimental Methods chapter (especially avoiding UV excitation, which would be absorbed by the liquid crystal), not chemically react with the liquid crystal, and remain stable under long optical excitation. Furthermore, the material thickness along the growth axis (z-axis) should not exceed a few hundred nanometers. The larger the effective cavity thickness (a combination of the active layer width and the required thickness of the liquid crystal), the narrower the free spectral range, leading to the distribution of the gain profile across multiple modes simultaneously (e.g. this issue we encountered with perovskite crystals in different project).

Active media in planar microcavities in a strong light-matter coupling regime and room temperature include inorganic [124, 125] and hybrid organic-inorganic perovskites [126, 127], transition metal dichalcogenides (TMDCs) [127–131], bulk and quantum wells of inorganic materials, e.g. GaN [132, 133], ZnO [134, 135], GaAs [136], as well as organic fluorescent materials such as anthracene [137], fluorene [138], conjugated polymers [139] and BODIPY [122, 140]. In addition, many inorganic and organic compounds are used for lasing in the weak coupling regime, such as GaAs in VCSEL geometries [141] or rhodamine for photon condensates [77].

Within this research and previous doctoral theses [142, 143] in the Polariton group, various active materials were tested, both commercially available (e.g. DCM 640, Coumarin 540, Coumarin 522) and synthesized at MUT (light-emitting liquid crystals), the Faculty of Biology at the UW (luminescent proteins mCherry and tdTomato), and the Faculty of Physics at the UW (perovskites). After numerous experiments, the materials that best met the outlined criteria for broadband lasing in the weak coupling regime discussed in this chapter were pyrromethene P580 (see Figures 4.2(a,b) for chemical sctructure), and for strong coupling and Bose-Einstein condensation, which will be presented in the following chapter, polymer MeLPPP.

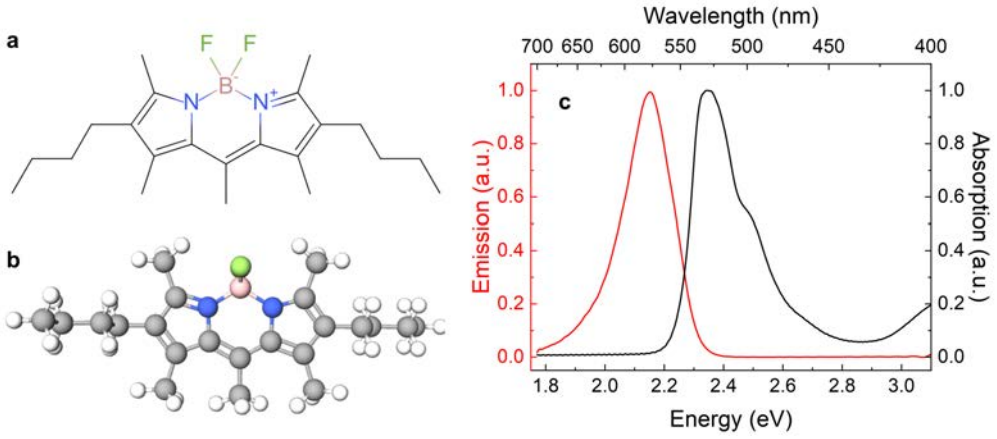

Figure 4.2: **Pyrromethene 580 (P580) dispersed in the LC2091* mixture.** (a,b) Chemical structure of the molecule. (c) Emission (red) and absorption (black) spectra, data measured by Natan Rychłowicz.

The absorption and emission spectra of P580 dispersed in the highly birefringent liquid crystal LC2091* are shown in Figure 4.2(c). Organic materials typically exhibit a solvatochromic effect [144, 145], which means that their spectra shift depending on the solvent. Comparison of the spectra in Figure 4.2 with the P580 data sheet for methanol [146] reveals a redshift of approximately 20 nm in the LC2091* mixture. The absorption peak in the LC mixture occurs at 2.34 eV (529 nm), almost perfectly matching the second harmonic Nd:YAG laser line available in the Polariton Laboratory

(532.1 nm). The emission maximum appears at 2.15 eV (576 nm), with a broad emission range exceeding 400 meV. Combined with a relatively high quantum yield (over 80% [147]), these properties led to the choice of this dye as the active material for the experiments in this chapter and in Chapters 6, 7, and 8. However, this does not imply that it is the best possible choice; other materials, such as the widely used rhodamine 6G [77, 148–150] with a quantum yield greater than 95% [151], may perform even better. Nevertheless, after a stable and effective compound was identified for the weak-coupling regime, it was consistently used in subsequent experiments.

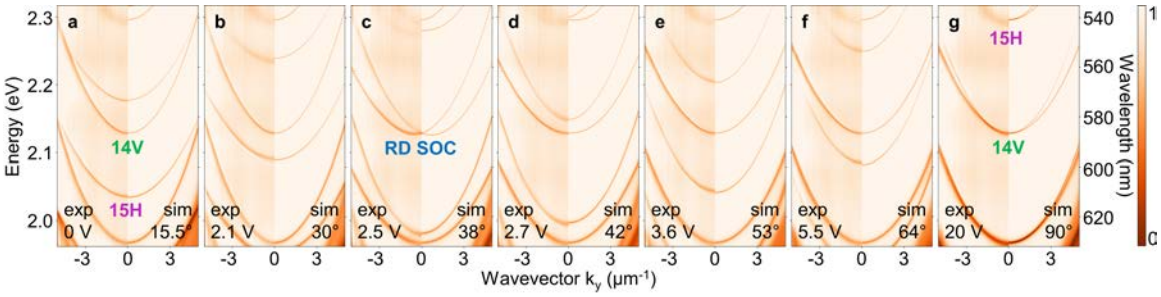

Figure 4.3: **Photonic modes of LCMC.** Momentum-resolved reflectivity spectra measured for different voltages applied to the sample. The left side of each panel corresponds to the experimental data (voltages are indicated in the bottom left corners), while the right side shows the simulation using Berreman's 4×4 matrix method (angles of rotation of LC molecules are indicated in the bottom right corners).

The evolution of the momentum-resolved reflectivity spectra of dye-doped LCMC measured at different voltages applied to the sample is shown in Figure 4.3. The left panels display experimentally obtained normalized spectra, while the right panels present Berreman 4x4 matrix method simulations for LC molecule rotation angles that closely match the experimental results. The simulation parameters assume an 1880 nm thick rotating LC layer sandwiched between two 250 nm thick isotropic layers.

Based on the formula presented in the Experimental Methods chapter, the calculated mode numbers for the 15th horizontal mode and the 14th vertical mode are indicated below these modes in Figures 4.3(a,f). As discussed in Section 2.3 of the Introduction, the energy of vertical modes in a nematic LCMC remains unchanged with applied voltage, whereas the energy of horizontal modes can be precisely tuned.

Initially, at low voltage, there is a negative Δ_{HV} detuning between the 15H and 14V modes (Figs.4.3(a,b)). As the voltage increases, at 2.5 V, Δ_{HV} reaches zero, bringing these two modes into RDSOC resonance in the $(N, N+1)$ regime. This results in two well-separated valleys in momentum space (Fig.4.3(c)). Further increasing the voltage weakens the interaction, causing the modes to return to their initial linearly polarized states with their original effective masses (positive Δ_{HV}, Fig. 4.3(d-f)). At 20 V, the two modes with different parity are well separated in energy. At this point, the LC directors are perpendicular to the cavity plane (homeotropic alignment), meaning that the H and V modes with the same parity are now in resonance (N, N) regime, Fig. 4.3(g)). Since there is no interaction between modes of the same parity, the only difference between 14H and 14V is their effective mass, influenced by the strong TE-TM splitting. It is also worth noting that even without any applied voltage, this sample exhibits an intrinsic LC pretilt angle of approximately 15 degrees.

The tunability of the photonic modes in the LCMC is presented in Figure 4.4. Figure 4.4(a)

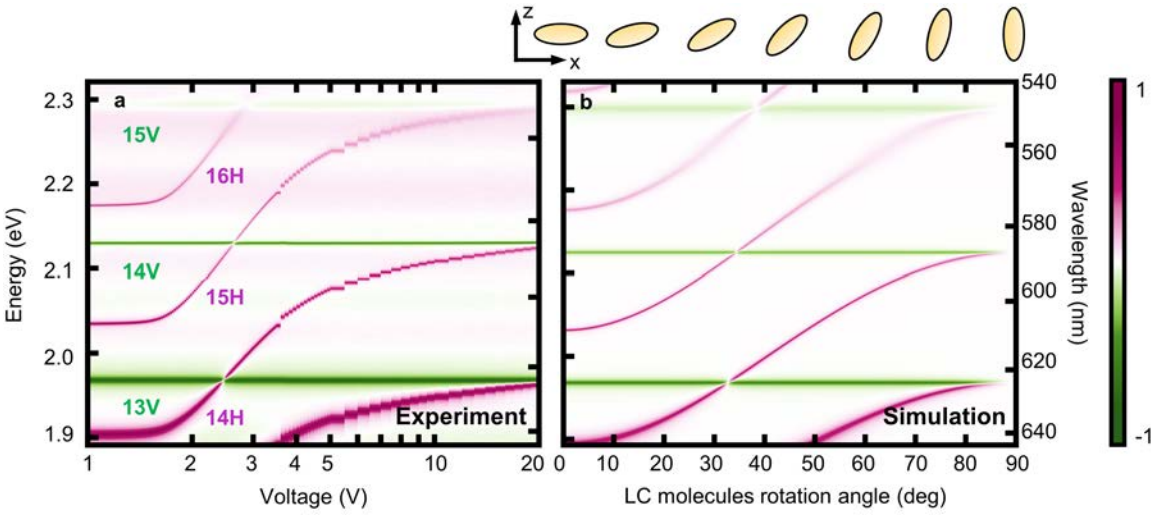

Figure 4.4: **Tunability of LCMC Photonic Modes.** (a) Reflectivity spectra measured at normal incidence as a function of voltage, plotted on a logarithmic scale and expressed by the S_1 Stokes parameter. Purple and green labels indicate the number of horizontal and vertical photonic modes, respectively. (b) Corresponding simulation based on the Berreman 4x4 matrix method as a function of the rotation angle of nematic LC molecules, schematically illustrated in the inset at the top.

shows a voltage scan from 1 V to 20 V, measured independently at normal incidence in H and V polarizations, expressed by the S_1 Stokes parameter. A comparison with Berreman method simulations, corresponding to different LC molecule rotation angles and maintaining the same cavity parameters as in Figure 4.3, is presented in Figure 4.4(b).

For voltages up to approximately 1.8 V—below the Fréedericksz transition threshold—the spectra remain unaffected [42, 43]. Above this threshold, and considering the previously mentioned pretilt, the agreement between the experimental data and the simulations is quite satisfactory, despite differences in spectral curves shapes due to the complex dependence of the LC director rotation on the applied voltage, which deviates from a simple logarithmic relation [152, 153].

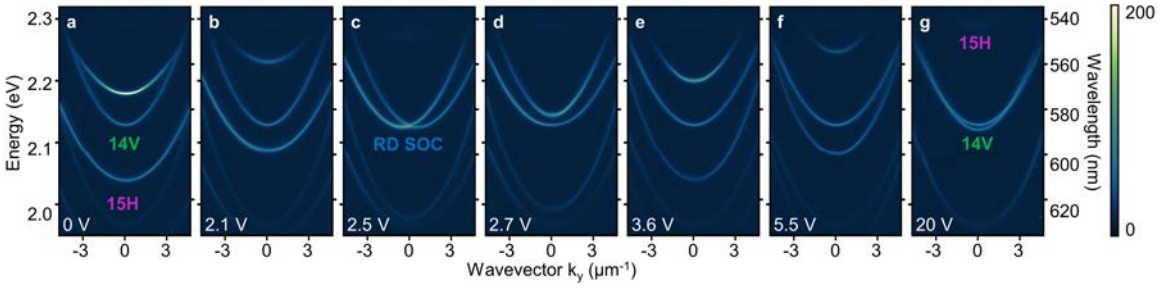

Figure 4.5: **Tunable spontaneous emission**. Momentum-resolved photoluminescence spectra measured for different voltages applied to the sample. Voltages are indicated in the bottom left corners.

In contrast to the simulations presented in Figure 4.3, where for clarity the refractive index was chosen as in the Experimental Methods chapter, to better match the experimental results the simulations in Figure 4.4(b) include the absorption of the dye. The refractive index was assumed to be same as in the Lorentz oscillator model:

$$\varepsilon(E) = \varepsilon_\infty + \sum_{j=1}^{N} \frac{\mathrm{OS}_j}{E^2 - E_j^2 - iE\gamma_j}$$

where ε_∞ is the dielectric constant at infinite energy of electromagnetic radiation, OS_j, E_j and γ_j are the oscillator strength, resonant energy and losses for the j-th oscillator present in the system, respectively. Here, N denotes the total number of oscillators.

Due to birefringence, two different dependencies of the refractive index is assume:

$$n_e(E) = \sqrt{n_{e,\infty}^2 + \sum_{j=1}^{2} \frac{\mathrm{OS}_j}{E^2 - E_j^2 - iE\gamma_j}}$$

$$n_o(E) = \sqrt{n_{o,\infty}^2 + \sum_{j=1}^{2} \frac{\mathrm{OS}_j}{E^2 - E_j^2 - iE\gamma_j}}$$

The final dielectric tensor for any angle of the molecule is given by:

$$\boldsymbol{\varepsilon}(\theta, \lambda) = \mathbf{R}_y(\theta) \begin{bmatrix} n_e^2(E) & 0 & 0 \\ 0 & n_o^2(E) & 0 \\ 0 & 0 & n_o^2(E) \end{bmatrix} \mathbf{R}_y(-\theta)$$

where $\mathbf{R}_y(\theta)$ is the rotation matrix along y axis.

Compared to bare LCMC (without an emitter), the strong absorption of the dye broadens the linewidth of the cavity modes (see experimental panels in Figures 4.3 and 4.4 for energies above 2.3 eV). At high dye concentrations (above approximately 0.5%), cavity modes within the high absorption spectral range essentially disappear, often making it difficult to achieve resonant excitation laser injection into a cavity mode or even a Bragg mode in wedge-type dye-doped LCMC. Strong absorption not only broadens lines in reflectivity measurents but also reduces the emitted photoluminescence signal. This is the reason why in strong light-matter coupling regime the upper polariton branch is difficult to observe in organic materials [20], as will be discussed in next chapter.

Figure 4.5 presents momentum-resolved spontaneous emission spectra measured at the same voltages as in Figure 4.3. The repetition rate f_{rep} of excitation laser was set to 50 Hz and an energy density (fluence F) to 9 mJ/cm^2. Here, the strong absorption is clearly visible for energies above 2.3 eV. It is evident that the effects observed in reflectivity spectra (such as photonic mode tunability and RDSOC) are also present in spontaneous emission spectra. In this case, the microcavity acts as a tunable spectral and angular filter for the light emitted by the excited dye molecules embedded inside. The reflectivity and PL spectra are complementary; however, a notable difference is visible in Figure 4.5(g). At 20 V, resonance in (N, N) regime has not yet been achieved, as there is still a small splitting of $\Delta_{HV} = 8$ meV for modes of the same parity, compared to 6 meV in the reflectivity spectra. Since these spectra are snapshots from a voltage scan series, a possible explanation could be heating induced by laser spot that increase disorder of LC molecules, as they are sensitive to temperature fluctuations [154, 155].

4.2 Tunable Lasing

The emission results presented in the previous section were obtained in the low-fluence excitation regime, below the lasing threshold. Figure 4.6 shows the influence of pump energy density on the PL spectra of dye-doped LCMC. Figures 4.6(a-c) show momentum-resolved emission spectra measured at different pump energy densities, as indicated in the upper right corner. The spectra are not normalized to allow for easy comparison of maximum emission intensity. The pump spot diameter was 5 µm. Since the peak energy of excitation beam determines if the lasing threshold is reached, as long as the excited state lifetime is shorter than the interval between successive pulses, single-shot and multi-shot experiments have similar impact on lasing. Increasing f_{rep} only improves the signal-to-noise ratio or reduces the measurement time. The lifetime of the excited state in organic materials is typically on the order of a several picoseconds [156], so for the nanosecond laser used in the experiment (maximum repetition rate of 1 kHz), changing the f_{rep} does not affect the lasing threshold. To prevent sample degradation, f_{rep} was set to 5 Hz.

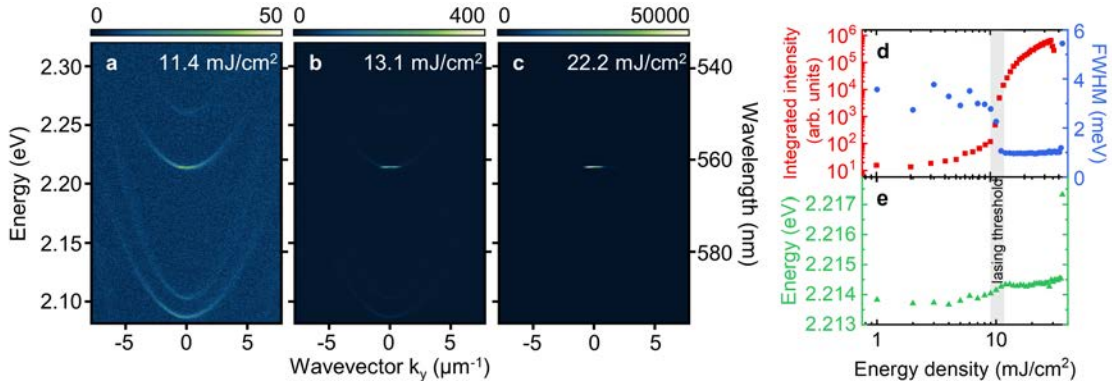

Figure 4.6: **Lasing in dye-doped LCMC.** Emission spectra: (a) below and (b, c) above the lasing threshold. (d) Emission intensity (red squares), linewidth (blue dots), and (e) peak position (green triangles) as a function of the excitation pulse energy density. The lasing threshold is marked with a gray rectangle.

Figure 4.6(a) was collected just below the lasing threshold, showing spontaneous emission from the microcavity modes with a maximum count not exceeding 50. Figure 4.6(b) presents the spectrum just above the lasing threshold, where a strong, spectrally and angularly narrow lasing line appears at the bottom of the mode at 2.215 eV. Figure 4.6(c) shows the spectrum collected at a pump energy density of $F = 2F_{\mathrm{th}}$. With an approximately twofold increase in pump fluence between Fig. 4.6(b) and Fig. 4.6(c), the emission intensity increases by a factor of 100.

The emission intensity (red squares), full-width at half-maximum (blue circles), and lasing peak energy (green triangles), determined by fitting a Lorentzian curve at normal emission, are plotted as a function of excitation energy density in Figures 4.6(d,e). The gray rectangle marks the pump fluence range where strong nonlinear intensity increase and spectral line narrowing occur, indicating the lasing threshold. For high fluence, the lasing emission saturates, followed by a quenching of the emission above approximately 25 mJ/cm^2 due to photobleaching. The plateau in linewidth above the lasing threshold is due to the limited spectral resolution of the detection setup (measurements with higher resolution are shown in Figure 4.9).

The lasing peak energy exhibits a slight blueshift (approximately 0.7 meV) above the threshold. It is worth noting that in noncrystalline organic microcavities, where excitons are localized

on individual chromophores or molecules, energy blueshifts of nonlinear emission with increasing excitation density do not necessarily indicate strong coupling [64, 140]. The localized nature of excitons precludes repulsive exchange interactions and the associated blueshifts observed with increasing polariton density in crystalline semiconductors. Studies have shown that even in strongly coupled dye-filled microcavities, the observed blueshift at the condensation threshold is primarily driven by a renormalization of the intracavity refractive index and, to a lesser extent, by a quenching of the Rabi splitting [64].

Therefore, one should be cautious when attributing nonlinear emission blueshifts at the lasing threshold to strong coupling without considering other mechanisms. Claims of strong coupling should be supported by spectroscopic evidence of anticrossing or comparisons with non-strongly coupled reference samples [157]. In this work, no evidence of strong coupling is identified, and the observed emission energy shifts are attributed to excitation-density-induced changes in the intracavity refractive index, including thermal effects.

If the relaxation process to the lasing state in non-resonantly pumped cavities is faster than depolarization mechanisms, the lasing polarization can be inherited by the polarization of the excitation beam (more on this in the next chapter). In the case of the P580-doped LCMC, I did not observe such a dependence either for linear or circular polarization in the majority of samples. However, very locally, in high-quality samples, this effect can be observed for linearly polarized excitation (a study on this is currently in progress in collaboration with group from the University of Southampton). Nevertheless, in most cases, regardless of the pump polarization, lasing occurs on the tunable H mode.

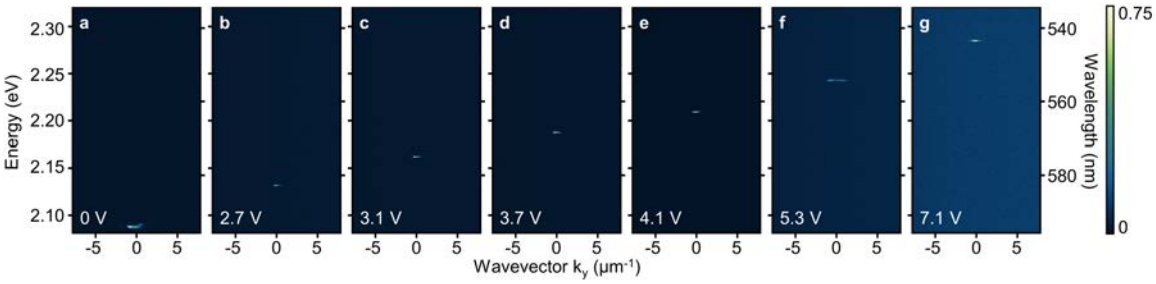

Figure 4.7: **Tunable lasing emission.** (a-g) Normalized emission spectra measured above the lasing threshold for different voltages, as indicated in the bottom left corners.

Normalized momentum-resolved emission spectra for different applied voltages are presented in Figure 4.7. The tunability of single H mode lasing under applied voltage is clearly visible. According to Berreman simulations and the formula for the photon lifetime in the cavity (Equation (4)), the H mode has a higher Q-factor than V mode. Since photons of both polarizations are reflected the same number of times within the resonator, the optical length $d = n_c L_c$ of the H mode is longer due to the higher refractive index in y direction. However, experimental observations indicate the opposite trend—due to intracavity scattering, V modes exhibit a higher Q-factor when voltage is applied [1]. This suggests that the dominant factor influencing preferential lasing on the H mode is not the photon lifetime but rather the partial alignment of dye molecules (and thus their electric dipole moments) along the liquid crystal director [145, 158].

The dependence of lasing peak energy on applied voltage is shown in Figure 4.8(a). The tuning curve for the H mode lasing follows a similar trend as in Figure 4.4.

If the cavity is too thick, the small free spectral range leads to competition between different

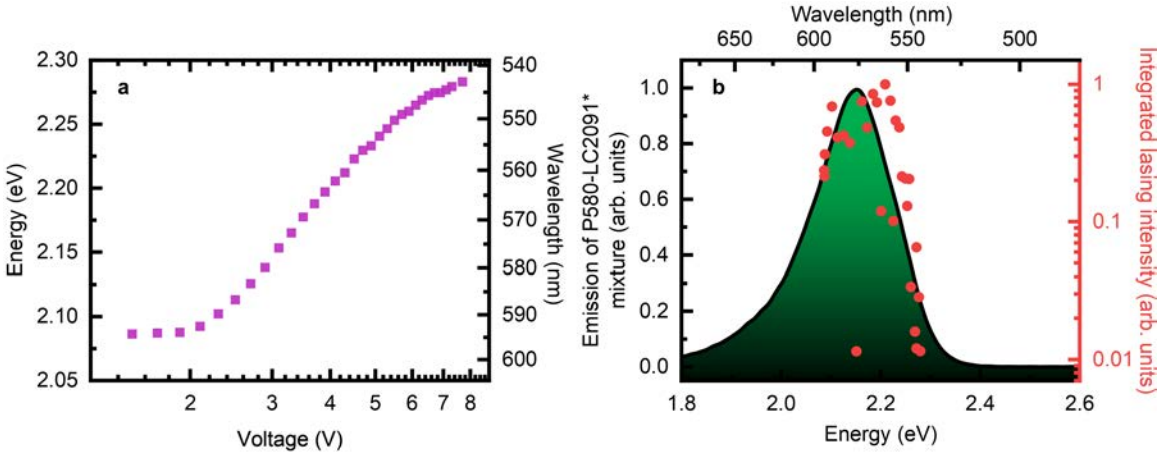

Figure 4.8: **Spectral range of a tunable laser based on LCMC doped with P580.** (a) Lasing peak position as a function of the voltage applied to the sample. (b) Emission spectra from Fig. 4.2 overlapped with extracted lasing peak intensity maxima (red dots, plotted on a logarithmic scale).

modes, resulting in either multimode lasing or lasing mode switching (as seen around 1.5 V and 3.5 V in [5]). To achieve a wide tuning range and ensuring that for all voltages only a single horizontal mode overlaps with the spectral region of strong gain, a relatively thin cavity of approximately 1.2 μm was chosen. This allowed for tunable lasing over a spectral range from 2.086 eV (594.4 nm) to 2.283 eV (543.0 nm).

Figure 4.8(b) shows the emission spectrum of the P580 dispersed in LC2091* from Figure 4.2, with overlapped points representing the normalized integrated lasing intensity on a logarithmic scale extracted from the voltage scan in Figure 4.8(a). Apart from a blueshift, there is good agreement between the two curves, suggesting that lasing efficiency can be well estimated based on the dye emission spectrum.

Due to the highly nonlinear nature of the system mention previously, even small fluctuations of the excitation laser power introduce high intensity fluctuation. This is probably the reason why the intensity of a single measurement at 2.149 eV is two orders of magnitude weaker than neighboring measurements. However, all measurements, even those with a normalized emission value around 0.01, remained above the lasing threshold. Additionally, the dye emission remains relatively strong between 2.0 eV and the lasing scan range, suggesting that for sufficiently thin LCMCs (of around 0.8 μm, which are experimentally accessible), the spectral tuning range of lasing could be extended to nearly 300 meV.

To demonstrate that the energy tunability of the dye-doped LCMC laser has a truly continuous nature, Figure 4.9(a) presents a combined map of normalized momentum-resolved spectra for wavevector values of ± 1 μm^{-1} as a function of applied voltage. The scan was performed with a step size of 20 mV (still far from the lower limit of typical function generator of order of 1 mV), and the energy resolution was enhanced using a 1800 grooves/mm diffraction grating. This voltage step size ensures that at each successive spectrum energy of the lasing peak shifts by less than it linewidth.

Figure 4.9(b) shows spectra collected at normal emission for selected voltages. Compared to the spectrum at 1.30 V (before the Fréedericksz threshold), the spectral lines broaden and become

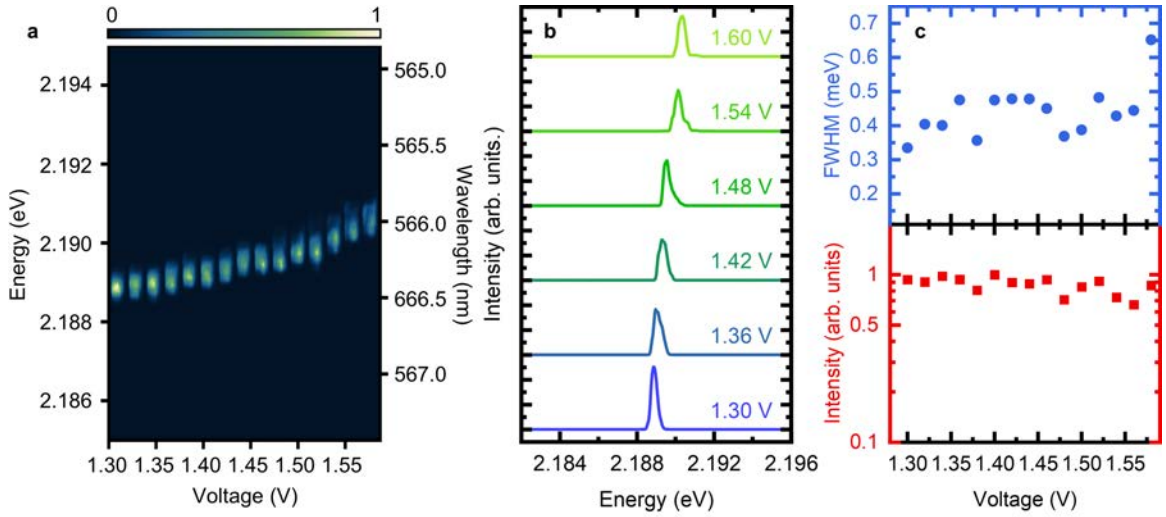

Figure 4.9: **Precise Control of Lasing** (a) Combined map of normalized momentum-resolved spectra for low momentum ($\pm$ 1 μm^{-1}) measured at different voltages, with a small step size of 20 mV. (b) Selected spectra at the normal emission. (c) Linewidth (top) and intensity (bottom) as a function of voltage, extracted from Lorentzian fits to the lasing peaks.

asymmetric, which is attributed to inhomogeneities in the liquid crystal potential. However, these broadening remain within the linewidth of a single mode.

Figure 4.9(c) presents the FWHM (blue circles) and emission intensity (red squares) extracted from Lorentzian fits. The linewidths remain around 0.5 meV, while the emission intensity fluctuates up to 60% of its maximum value. Since the device is intended to serve as a proof of concept rather than a fully functional product and has not been optimized for practical applications, its parameters are far from commercially available lasers. Nevertheless, by improving the stability of the excitation, the cavity Q-factor, and the homogeneity of the LC, I believe there is significant room for further improvements. Nevertheless, the results show that the device indeed can work as a tunable laser, with a tuning step that can be arbitrarily small, limited only by the stability of the function generator.

4.3 Rashba-Dresselhaus Resonance and Persistent Spin-Helix Lasing

The precise tunability over a broad spectral range demonstrated in the previous section allows achieving RDSOC lasing. This effect is presented in Figure 4.10. Figures 4.10(a-e) show normalized momentum-resolved emission spectra collected above the lasing threshold.

In Figure 4.10(a), the signal was measured in horizontal polarization. Lasing occurs at the bottom of both valleys and is separated in reciprocal space at $Q = 3.1\,\mu m^{-1}$. Performing this measurement for σ^- and σ^+ polarization detection (Figures 4.10(b) and 4.10(c), respectively), it is evident that lasing inherits the valley circular polarizations.

Figure 4.10(d) presents these results expressed by the Stokes parameter S_3. The spectrum is modeled using the Hamiltonian (15), represented by a solid line. The modeling parameters are $\Delta_{HV} = 1$ meV, $\alpha = 319\ \mu eV \cdot \mu m$, $m_H = 1.5 \times 10^{-5} m_0$, and $m_V = 1.0 \times 10^{-5} m_0$. To better visualize the strong circular emission from both valleys, Figure 4.10(e) presents the non-normalized difference of both polarizations.

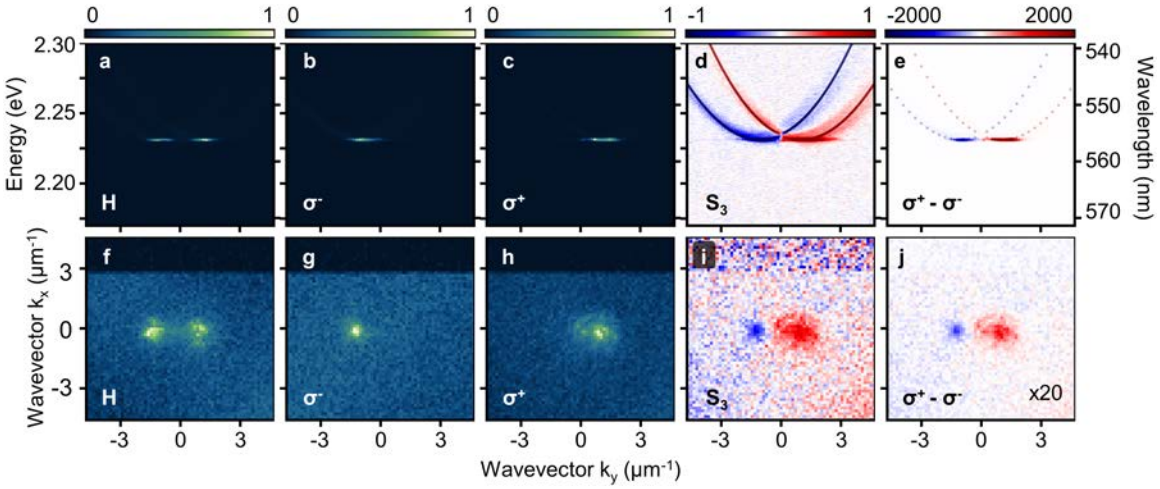

Figure 4.10: **Lasing in Rashba-Dresselhaus Resonance.** Momentum-resolved emission spectra above the lasing threshold measured for (a) H polarization, (b) σ^- polarization, (c) σ^+ polarization, (d) S_3 Stokes component, and (e) the difference between the emission intensities of both circular polarizations. Continuous and dashed lines show the modeling (d,e) using Hamiltonian (15) (f-j) Corresponding momentum-space images.

The lower panel Figures 4.10(f-j) shows the corresponding momentum-resolved images. The dark stripe at the top of the maps is related to the spectrometer slit aperture. The signal in Figure 4.10(f) has been multiplied by a factor of 20 to maintain the same intensity scale as Figure 4.10(e). These results demonstrate that in the RDSOC regime, lasing occurs simultaneously from two valleys separated in reciprocal space. The lasing signal inherits the valley polarization, leading to the emission of two orthogonally circularly polarized beams at different angles of about ± 8 degrees for 2.23 eV in $(N, N+1)$ regime.

It is worth noting that the lasing threshold in the RDSOC regime is approximately twice as high as outside the resonance. This is because no mechanism favors either σ^+ or σ^- polarization, meaning the threshold is reached simultaneously for both valleys. However, this requires higher excitation energy to reach the thresholds. We utilized this in [20] for the electrical on-and-off switching of a perovskite polariton laser.

The light emitted in the RDSOC resonance can be described as two beams of equal intensity with circular polarization, defined by the polarization basis vectors $\{\vec{\sigma}_-, \vec{\sigma}_+\}$ and momentum states $\{-\vec{Q}, +\vec{Q}\}$ [4]. In the far field, this means that the beam direction determines the polarization state, and vice versa. Thus, the emission pattern in Fig. 4.10 can be decomposed into the pairs $\{-\vec{Q}, \vec{\sigma}_+\}$ and $\{+\vec{Q}, \vec{\sigma}_-\}$. However, in the near field, the coherent superposition of emissions from both spin valleys leads to an interference pattern of a linearly polarized Persistent Spin-Helix (PSH) [4]. This interference arises because of both circular polarization contributions, resulting in a non-separable state where all basis vectors are mixed in both momentum and polarization spaces.

At the RDSOC regime, the electric field at the cavity surface (real space, near field image) is described by the normalized Stokes vector components [4]:

$$
\begin{aligned}
S_1(\vec{r}) &= \cos\left(\vec{Q}\cdot\vec{r}+2\Theta\right),\\
S_2(\vec{r}) &= -\sin\left(\vec{Q}\cdot\vec{r}+2\Theta\right),\\
S_3(\vec{r}) &= 0,
\end{aligned}
\tag{38}
$$

where Θ defines the position of the maxima and minima in the PSH linear polarization interference pattern.

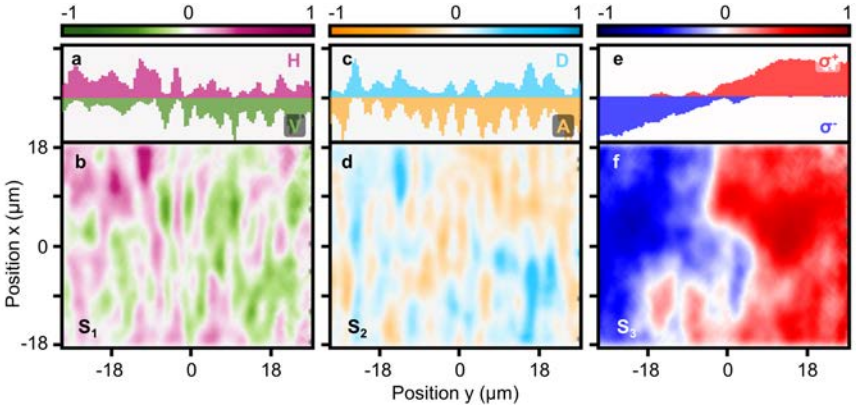

Figure 4.11: **The Persistent Spin-Helix Laser.** The Stokes parameters (a) S_1, (b) S_2, and (c) S_3 for real-space imaging. The histograms in the insets at the top correspond to the positive and negative values along the y-direction.

The bottom panel of Figure 4.11 presents real-space distributions of the Stokes parameters S_1, S_2, and S_3 (Fig. 4.11(b), (d), and (f), respectively). The maps of $S_1(\vec{r})$ and $S_2(\vec{r})$ exhibit longitudinal stripe patterns along the x-axis, an indication of the PSH state, that confirms the presence of spin coherence in the system [4]. To better illustrate the PSH pattern, the top panel of Fig. 4.11 shows histograms of the positive and negative Stokes parameter values along the y-axis.

The maxima of the histogram in Fig. 4.11(a) for H polarization correspond to the minima of the V polarization, and vice versa. This effect becomes even more pronounced for the orthogonal linear polarizations D and A (Fig. 4.11(c)), which, as predicted by Eq. (38), should be phase-shifted by $\pi/2$ relative to the H and V polarization texture. In fact, according to Eq. (38), any pair of orthogonal linear polarizations should generate the PSH pattern with an appropriate phase shift relative to the given basis.

Unlike Eq. (38), the $S_3(\vec{r})$ map in Fig. 4.11(f) reveals a distinct spatial separation of circular polarization components. The histogram along the y-axis shows that the absolute value of $S_3(\vec{r})$ increases with distance from the excitation spot, where $S_3(0) \approx 0$. As demonstrated in [4], the spatial profile of $S_3(\vec{r})$ arises due to the optical Stern-Gerlach effect and serves as an effective measure of the inseparability between orbital and polarization degrees of freedom.

When $S_3^2 = 0$, the system is maximally inseparable, whereas for $S_3^2 = 1$, the spin and valley degrees of freedom are fully separable [4, 159]. At the center of the excitation spot, $S_3(0) \approx 0$, while $S_1(\vec{r})$ and $S_2(\vec{r})$ exhibit the periodic modulation described by Eq. (38) (Fig. 4.11(a,b)). At larger distances, photons become predominantly circularly polarized, as expected from the non-zero momentum emission seen in Fig. 4.10. Consequently, the polarization and momentum degrees of freedom become fully separable, resulting in $S_3^2 \approx 1$ (Fig. 4.11(f)).

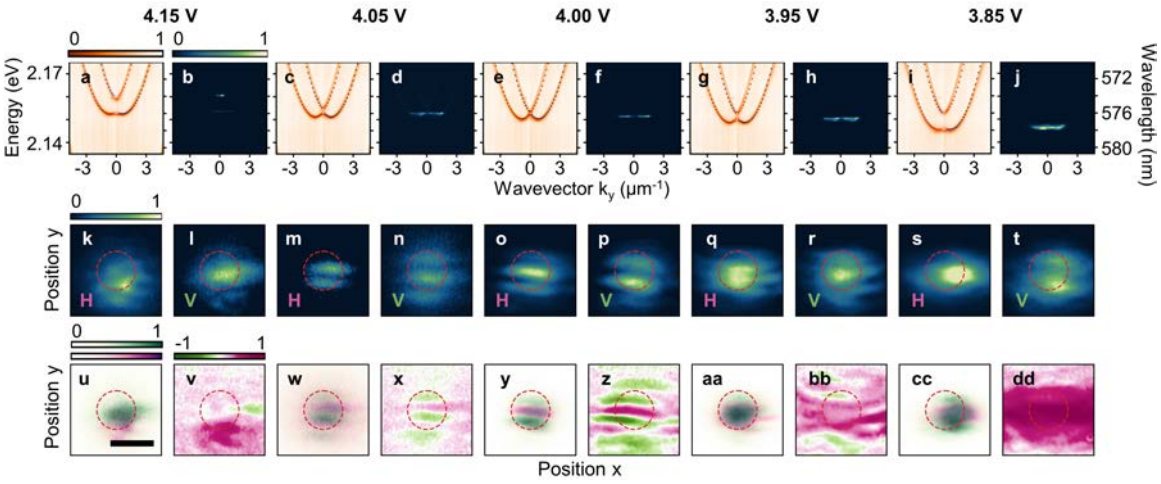

Figure 4.12: **Voltage Dependence on Persistent Spin-Helix.** (a) Normalized momentum-resolved reflectivity spectrum near the RDSOC resonance measured at 4.15 V. Dashed curves show the fitting using (15). (b) Corresponding normalized momentum-resolved emission spectrum above the lasing threshold. (c-j) Reflectivity and emission spectra measured at different voltages, as labeled above. (k,m,o,q,s) Corresponding real-space emission in horizontal, and (l,n,p,r,t) in vertical polarization. (u,w,y,aa,cc) Overlapping signals of horizontally (purple) and vertically (green) polarized emission. (v,x,z,bb,dd) S_1 Stokes parameter in real space. The red dashed circle marks the excitation spot. Scale bar: 5 μm.

Figure 4.12 illustrates the influence of detuning Δ_{HV} on the PSH pattern. The figure is vertically divided into five panels, each corresponding to a different voltage applied to the sample, ranging from 4.15 V to 3.85 V, as indicated at the top. This voltage range modifies Δ_{HV} from positive to negative values.

Figures 4.12(a,c,e,g,i) show the experimental normalized momentum-resolved reflectivity spectra, modeled using Hamiltonian (15), represented by a dashed line. The modeling parameters are $E_V = 2.1528$ eV, $\alpha = 290$ μeV · μm, $m_H = 1.57 \times 10^{-5} m_0$, and $m_V = 1.0 \times 10^{-5} m_0$. The corresponding Δ_{HV} value from left to right are: 7.2 meV, 2.0 meV, 0.0 meV, -3.0 meV, and -7.2 meV.

Figures 4.12(b,d,f,h,j) present the normalized momentum-resolved emission spectra collected above the lasing threshold for the corresponding Δ_{HV} detunings. The middle panel (Figs. 4.12(k-t)) shows normalized real-space images of lasing measured in H and V polarizations. The excitation spot is marked by a red dashed circle. The maps have been normalized to enhance the visibility of low signal. Based on these results, the lower panel (Figs. 4.12(u-dd)) is plot. Figures 4.12(u,w,y,aa,cc) present overlapped real-space images of both polarizations (with added transparency), while Figures 4.12(v,x,z,bb,dd) expressed them by the S_1 Stokes parameter.

Due to RDSOC coupling, the cavity eigenstates are no longer purely linearly polarized. Thus, in the $(N, N+1)$ regime, instead of using H- and V-mode labels, more descriptive names is used. When Δ_{HV} is in order of several meV and positive (left panel, 4.15 V), RDSOC coupling causes lasing to occur in both modes simultaneously. However, the lasing from mode with a stronger horizontal polarization (at higher energy, ∼2.16 eV) has higher intensity than the lasing from mode with stronger vertical polarization (at lower energy, ∼2.153 eV) (Fig. 4.12(b)). This affect the emission in both polarizations in real space (Figs. 4.12(k,l,u)). On the normalized images, the weaker signal of

one polarization compared to the other manifests as a noisier V image relative to H. This intensity imbalance is clearly visible in the Stokes parameter S_1 distribution (Fig. 4.12(v)), where positive values dominate.

As the detuning Δ_{HV} approaches zero (voltages of 4.05 V and 3.95 V), lasing becomes increasingly localized in two separate valleys (Figures 4.12(d,h)). In real space, this leads to the formation of interference fringes in both polarizations (Figs. 4.12(m,n,q,r,w,aa)), which are in antiphase, signifying the presence of the PSH pattern (Figs. 4.12(x,bb)). The strongest effect occurs at zero detuning (voltage 4.00 V), where the ratio of linear polarizations is equal, and lasing occurs from well-separated valley minima (Figure 4.12(f)). At this point, the fringe contrast is the highest (Figs. 4.12(o,p,y)), and the Stokes parameter S_1 exhibits a clear PSH pattern (Fig. 4.12(z)).

When Δ_{HV} becomes again in order of several meV but, negative (right panel, 3.85 V), lasing occurs from the predominantly horizontally polarized mode, and the two valleys merge (Fig. 4.12(j)). Similar to the 4.15 V case, the real-space signal of both polarizations appears blurred (Figs. 4.12(s,t)), although weak modulated spin texture is still observable (Fig. 4.12(cc)). This is because the lasing mode still weakly interact via RDSOC, as evidenced by the shape of the lasing spectrum. However, in the real-space distribution represented by the Stokes parameter S_1 (Fig. 4.12(dd)), it is clearly visible that, at this detuning, the lasing signal is once again predominantly horizontally polarized.

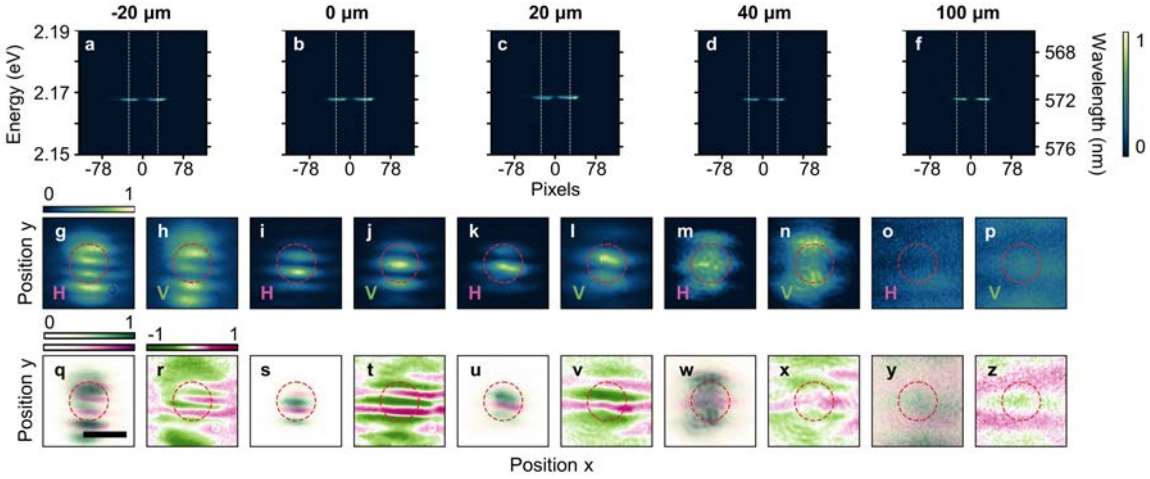

Figure 4.13: **Sample Focus Dependence on the Persistent Spin-Helix.** (a-f) Normalized momentum-resolved emission spectra above the lasing threshold in the RDSOC regime, measured at 4 V, collected at different distances between the sample surface and the microscope objective, as labeled above (with offset). White dashed lines corresponds to ±28 px. (g,i,k,m,o) Corresponding real-space images of horizontally polarized light, and (h,j,l,n,p) vertically polarized light. (q,s,u,w,y) Overlapping signals of both polarizations. (r,t,v,x,z) S_3 Stokes component. The red dashed circle marks the excitation spot. Scale bar (shown on (q) for fixed z_{focus} value): 5 µm.

It is evident that the visibility of the PSH pattern strongly depends on detuning, where even a slight change can blur the image. However, detuning is not the only key parameter in observing PSH properly. As discussed in the Experimental Methods chapter, focusing on the LCMC, which is additionally sandwiched between two glass substrates with a thickness of several hundred micrometers, requires experience and an appropriate optics.

Figure 4.13 presents measurements analogous to those in Figure 4.12, with $\Delta_{HV} = 0$, but varying

the distance z_{focus} between the sample and the detecting microscope objective. The z_{focus} values are indicated at the top of Figure 4.13 and correspond to the difference between an arbitrary reference distance ('offset'), close to the working distance of the detecting objective, that is chosen as 'the correct one', and the measured distance. More colloquially, these measurements show PSH lasing as a function of "focus". Since Δ_{HV} remains unchanged, reflectivity measurements have been omitted, while the remaining panels follow the same scheme as in Figure 4.12.

Since, as demonstrated below, the value of z_{focus} affects both momentum-space and real-space images, the x-axis of the normalized momentum-resolved spectra in Figure 4.13(a-f) is expressed in CCD camera pixels. In the real-space images of Figure 4.13(g-z), to allows the tracking of changes, the scale bar size/camera pixel ratio is fixed and determined for a calibration sample according to the procedure described in the Experimental Methods chapter.

Comparing the separation Q of the lasing valleys (Figs. 4.13(a-f)), it is evident that Q changes slightly as a function of z_{focus}. The estimated Q values in pixels, from left to right, are: 56 px, 52 px, 48 px, 46 px, and 42 px, so for the two extreme values of z_{focus}, the ratio $Q_{-20\mu\text{m}}/Q_{100\mu\text{m}}$ is 1.33. To better visualize this small change, white dashed lines were added at ± 28 px (half of the highest separation value).

In the real-space image (Figs. 4.13(g-z)), the PSH pattern changes significantly with z_{focus}, affecting both the contrast of oscillations and the period d_{PSH}. According to Eq. 38, the relationship between the PSH period and the separation Q is given by $d_{\text{PSH}} = 2\pi/Q$ [14]. For $z_{\text{focus}} = 0$, the polarization fringes are most distinct. However, for other values of z_{focus}, although blurred, they remain visible. The estimated d_{PSH} values, assuming a fixed real-space scale, from left to right, are: 1.66 µm, 2.02 µm, 2.46 µm, 3.25 µm, and 5.44 µm. The ratio of the extreme period values, $d_{\text{PSH},-20\mu\text{m}}/d_{\text{PSH},100\mu\text{m}}$, is 3.26. This discrepancy results from simple geometric optics principles, where improper focusing alters the image size.

Thus, an incorrectly chosen z_{focus} has only a minor impact on estimating the separation Q but significantly affects the estimation of the PSH period d_{PSH} in real space. According to issues described in the Experimental Methods chapter, this may explain why previous studies [4, 5, 14] reported inconsistencies in PSH period estimations between reciprocal and real space. In one study the real-space period was approximately 20% too small, while in others, it was 20% too large. Assuming that $z_{\text{focus}} = 0$ represents the correct focal position, in this study the agreement between the PSH period estimated from the reciprocal space ($d_{\text{PSH,k-space}} = 2\pi/Q = 2\pi/3.10\ \mu\text{m}^{-1} \approx 2.03\ \mu\text{m}$) and that estimated from real space ($d_{\text{PSH,r-space}} = 2.02\ \mu\text{m}$) is remarkably good.

4.4 Summary and Outcome

In this chapter, I presented a continuously tunable laser based on P580-doped LCMC in the weak light-matter coupling regime. The tunability in the visible range reaches nearly 200 meV (50 nm). This tunability enables lasing in the Rashba-Dresselhaus regime, where two orthogonally circularly polarized beams are emitted at different angles and can be triggered by a single pulse of the excitation laser. The interference of these beams results in Persistent Spin-Helix lasing on the sample surface, demonstrating the spin coherence of the system. The spatial profile of the S_3 Stokes component can serve as an effective measure of the inseparability between orbital and polarization degrees of freedom. Additionally, I investigated PSH as a function of the detuning Δ_{HV} and the sample-to-microscope objective distance, explaining the discrepancies in the period values observed in previous studies.

These investigations serve as a starting point for extending the system to the strong light-matter coupling regime, which is presented in the following chapter. Chapters 3-5, dedicated to self-assembled photonic crystals, also include sections discussing lasing in the weak coupling regime

with P580.

The presented tunable lasing device has several important drawbacks. When the liquid crystal is heated with high excitation power (e.g., approximately 20 mW with a continuous-wave laser), it starts to disorder over time, leading to line broadening and a decreasing of effective birefringence (mode splitting Δ_{HV} decreases). In the case of a tightly focused nanosecond laser beam with high power (above approximately 50 mJ/cm^2, though this value depends on the beam spot size and the dye concentration), irreversible defects can locally appear in the liquid crystal, leading to multimode lasing, a phase transition from the nematic to the isotropic state, or, in extreme cases, damaging the Bragg mirrors. Thought, for similar power density, I have also burned holes in silver mirrors from Thorlabs company, so this is not an unusual occurrence. Furthermore, dye photobleaching occurs, and the high intensity nonlinearity leads to significant output power fluctuations, as discussed in Figures 4.6 and 4.9.

These are inherent drawbacks of organic lasers, but with proper optimization of the cavity fabrication process, they can be mitigated or indirectly solved, as for example in dye lasers, by simply changing the position on the sample after photobleaching occurs. The stability issue of the emitter could be resolved by replacing the organic material with a semiconductor quantum well, forming a hybrid structure that combined a VCSEL with LCMC.

The tuning range of the laser can be further extended by constructing a thinner cavity. Additionally, the emission wavelength can be shifted by changing the active medium, as liquid crystals also perform well in the telecom range [29, 30]. This platform can be utilized in quantum communication, where information is encoded through light polarization [160, 161], and its high degree of nonlinearity could be of interest for neuromorphic computing applications [162–164].

Because the relaxation process is not fast enough to preserve the excitation polarization and, in both this and the next chapter, the excitons of the active medium are linearly polarized, lasing in the RDSOC regime always occurs simultaneously, and it is not possible to distinguish which valley will reach the threshold first. Currently, I am working on incorporating a chiral absorber with circular dichroism strong enough [165] that would significantly reduce the lifetime of one of the valleys. The output of such symmetry breaking could be chiral lasing from a single valley on demand and the observation of the Non-Hermitian skin effect [10].

Some high-quality samples exhibit features that suggest the possibility of photon thermalization, similar to what has been observed in photon condensates [77, 141, 166]. Due to the lack of sufficiently systematic studies, this work does not aim to discuss or assume the occurrence of such a phenomenon in dye-doped LCMCs. However, interested readers are referred to Appendix B, where measurements with such spectral features are shown in Fig. 9.10.

5 Nematic Planar Liquid Crystal Optical Microcavity in the Strong Coupling Regime

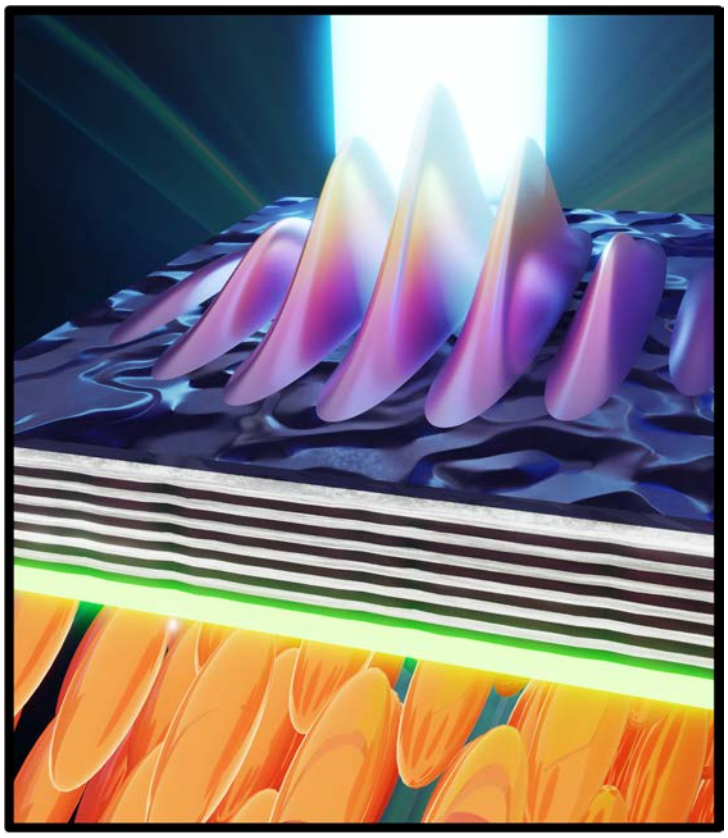

The results presented in this chapter are described in a manuscript currently under review:

M. Muszyński, et al. Observation of a stripe phase in a spin-orbit coupled exciton-polariton Bose-Einstein condensate. arXiv:2407.02406 (2024). [14]

In this chapter, I will present the results obtained for a liquid crystal microcavity in the strong coupling regime. The chapter begins by outlining the numerous technical challenges encountered during this project. Subsequently, evidence of strong light-matter coupling in the system is provided through analysis of the effective mass and observation of polariton branch anticrossing as a function of voltage applied to the sample. Under strong optical excitation, I demonstrate a Bose–Einstein condensate of exciton-polaritons that can be electrically- and polarization-switched. In the Rashba–Dresselhaus regime for polariton condensates, spin–orbit interaction gives rise to a periodic stripe phase and persistent spin helix, as well as spin-dependent propagation of condensates in real space. In single-shot experiments, spontaneous symmetry breaking during condensate formation and superfluid behavior are observed. The simultaneous demonstration of the stripe phase and superfluidity provides experimental evidence for the realization of a supersolid phase of exciton-polaritons at room temperature.

5.1 The Evidence of the Strong Coupling

In the previous chapter, results for LCMCs in the weak coupling regime were presented, where nonlinear processes were interpreted as photonic lasing. In this chapter, I will explore a system in which excitons strongly couple to cavity modes, leading to the formation of exciton-polaritons (hereafter simply referred to as polaritons). A key feature of polaritons, as mentioned in the introduction, is the phase transition to a Bose–Einstein condensate.

Exciton-polaritons interact both with the excitonic reservoir and with each other. These interactions give rise to a wide variety of phenomena, including optical traps and lattices [167–169], reservoir-based computing [104, 164, 170], and formation of solitons [58, 171]. Due to their long coherence times and propagation lengths [66, 172, 173], as well as interactions inherited from their excitonic component, exciton-polariton BECs (and, in many cases, even polaritons below the condensation threshold) offer a versatile platform for studying propagation-driven effects such as superfluidity [81, 174], quantized vortices [80, 175], synthetic gauge fields [176, 177], quantum fluid behavior [178], and many others.

Spin–orbit interactions in semiconductor microcavities open the door to a wide range of rich physical phenomena. This allows for effects such as the optical spin Hall effect [55, 56, 179], the realization of topological insulators [110, 111, 180], and Zitterbewegung [181, 182]. In this context, combining strong light–matter coupling with highly birefringent LCMCs, characterized by TE-TM splitting up to two orders of magnitude larger than in conventional semiconductor cavities, on-demand giant Zeeman splitting, and Rashba–Dresselhaus SOC, is a promising goal. This approach has already been demonstrated in experiments considering the formation of BEC in RDSOC valleys [9, 20], tunable Berry curvature [7], electrically controlled vortices [13, 183], tunable Zitterbewegung and spin precession [16, 19], and the polariton spin Hall effect [17].

Because polariton condensation does not require population inversion, the threshold for condensation is typically two orders of magnitude lower than that of conventional photonic lasing. This makes the platform attractive not only for light-emitting devices but also for photonic applications at room temperature. In such scenarios, strong nonlinearities can be achieved with low input power, and particles interactions provide additional degree of control over system behavior.

In recent years, organic materials have emerged as promising candidates for achieving strong coupling and polariton BECs at room temperature, thanks to their large oscillator strengths and high exciton binding energies. Among these, perovskites have become particularly prominent, enabling demonstrations of effects such as polariton parametric scattering [184] and all-optical propagation switching [185]. However, as mentioned in the previous chapter, room-temperature BECs have also been achieved in a variety of other materials.

Initially, the Polariton Group explored the use of the luminescent protein mCherry [186] to realize room-temperature BEC in LCMCs. Despite initial success, such as observation of nonlinear emission, the material was abandoned because of rapid degradation and surface inhomogeneity. As an alternative, the MeLPPP polymer was adopted and will be the focus of this chapter. MeLPPP has already been used in several advanced photonic devices, including a single-photon switch [187], a polariton transistor [188], and universal all-optical logic gates [189]. Its high saturation density, quantum efficiency and photostability allow single shot measurements that can be repeated a large number of times at a given sample position.

In BECs, spin–orbit coupling can give rise to supersolidity, a unique state of matter in which superfluidity coexists with a periodic spatial modulation of particle density known as the stripe phase, reminiscent of crystalline order. The existence of supersolidity was first proposed in the context of superfluid helium [190], although its experimental confirmation remains challenging [191].

BECs composed of particles with repulsive interactions are also expected to exhibit superfluidity. Several strategies have been developed to break translational symmetry while retaining this superfluid character. Of particular relevance to this thesis is the implementation of Rashba–Dresselhaus SOC in spinor BECs [192,193]. In this scenario, two degenerate condensates with equal and opposite nonzero momenta interfere, giving rise to the stripe phase resulting from coherent superposition.

Alternative approaches include the use of optical lattices, which can be continuously tuned [194]; however, in these systems, the spatial symmetry is imposed externally rather than broken spontaneously. Another pathway involves BECs of atoms with long-range dipolar interactions [195], which naturally form periodic droplet arrays for which clear evidence of supersolid includes measurements of superfluidity [195], estimation of the superfluid fraction [196], and observation of quantized vortices [197] have recently been observed.

In exciton–polariton systems, translation symmetry breaking has been reported via resonant parametric scattering in photonic crystal lattices [198]. Here, interference between the condensate signal and idler states leads to a spatially modulated amplitude of the wave function.

Supersolidity, resulting from the coexistence of superfluid and crystalline features, has thus far been experimentally realized in atomic BECs either via spin–orbit coupling [192, 193] or through dipolar interactions [194, 195]. More broadly, the existence of supersolid phases is anticipated in a variety of quantum systems, ranging from ultracold gases to astrophysical objects such as neutron stars [199].

The spontaneous formation of exciton–polariton BEC [83], driven by strong polariton–polariton interactions, allows it to be treated as quantum fluids of light [178] that can emerge near thermal equilibrium [200]. When combined with the tunability of the modes, including access to the RD-SOC regime, this system provides an exceptionally promising platform for investigating supersolid behavior, especially in the presence of an internal photonic disorder.

Figure 5.1 shows the scheme of the LCMC used in this chapter. As in the previous chapter, it is a planar nematic cavity; however, the light emitter is no longer the P580 dye dispersed in an LC matrix. Instead, emission is provided by 35 nm layers of a π-conjugated methyl-substituted ladder-type poly(-para-phenylene) (MeLPPP) polymer, which are directly spin-coated onto the DBRs. As described in Chapter 3 (Samples section), the DBRs in this case are centered at 490 nm (2.53 eV) and are composed of alternating SiO_2/Ta_2O_5 layers. To enhance the Rabi splitting, two MeLPPP layers were deposited at the electric field antinodes of the cavity mode. To protect MeLPPP from direct contact with the LC, each layer was coated with a 20 nm thick protective Al_2O_3 layer.

The MeLPPP polymer features a relatively stiff molecular backbone due to methylene bridges connecting phenyl rings. This structural rigidity results in high quantum yield and pronounced singlet-related optical transitions. The emission (red) and absorption (black) spectra of MeLPPP on a glass substrate are presented in Figure 5.2(a). The absorption spectrum shows a narrow

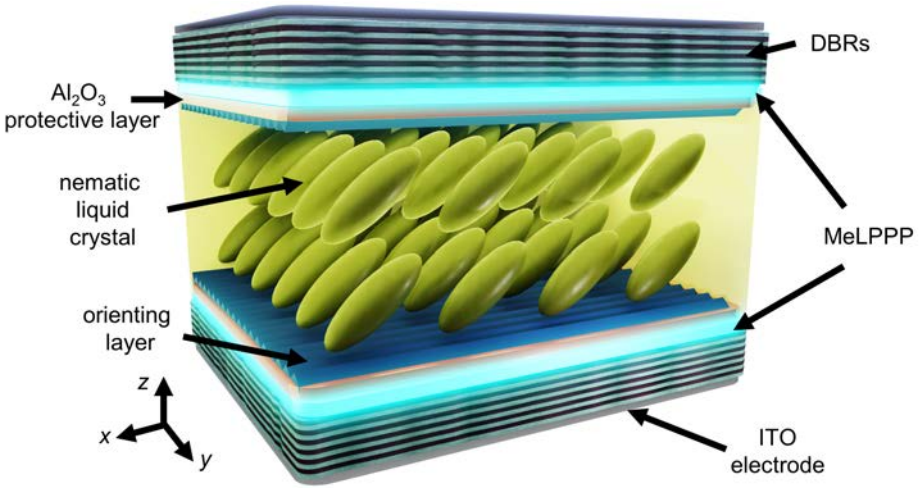

Figure 5.1: **Scheme of the Planar Nematic Liquid Crystal Optical Microcavity in strong coupling regime.** The two blue-emitting layers on top of the DBRs represent the active layers of the MeLPPP polymer, positioned at the electric field antinodes to facilitate strong light-matter coupling.

electronic transition accompanied by a vibronic progression, with excitonic linewidths broadened inhomogeneously to around 60 meV at room temperature.

A simplified MeLPPP energy level diagram, depicting one vibrational sublevel each of the ground and first excited singlet states, is shown in Figure 5.2(b). This scheme includes both upward and downward singlet-singlet transitions. After photoexcitation, the highest excited state $S_{1,1}$ relaxes to the lowest excited level $S_{1,0}$ through internal conversion (IC). According to previous studies [201], IC is the dominant relaxation pathway, effectively limiting the lifetime of hot excitons to below 100 fs.

The main absorption peaks of MeLPPP appear at 2.72 eV (456 nm) and 2.91 eV (426 nm), which correspond to the $S_{0,0} \rightarrow S_{1,0}$ (0–0) and $S_{0,0} \rightarrow S_{1,1}$ (0–1) singlet-singlet transitions, respectively. The emission spectrum closely mirrors the absorption spectrum, with a small Stokes shift of approximately 40 meV. It exhibits a dominant emission peak at 2.68 eV (462 nm), corresponding to the $S_{1,0} \rightarrow S_{0,0}$ singlet (0–0) transition, and a secondary vibronic peak at 2.51 eV (494 nm), associated with the $S_{1,0} \rightarrow S_{0,1}$ (0–1) transition.

Before presenting the core results that demonstrate strong coupling in MeLPPP-LCMCs, I would like to briefly address several technical challenges encountered during the four years of this project. Fabrication of the samples involved significant logistical effort. Each sample underwent a multi-step journey: from MUT (Warsaw, preparation of ITO-coated substrates) to IBM Research (Zurich, deposition of DBRs, spin-coating of MeLPPP, and application of the protective layer), back to MUT (application of orienting layers, cavity assembly, and LC filling), and finally to the UW (spectroscopic measurements, sometimes performed before LC filling, which occasionally required additional MUT to UW transfers).

Further complications included limited material availability, prolonged customs clearance, occasional sample damage during transport, and breakdowns of fabrication equipment, all of which sometimes resulted in delays of several months between sample batches.

Moreover, what initially appeared to be a technologically straightforward goal: to combine two well-established systems, LCMC and MeLPPP, turned out to be significantly more demanding from

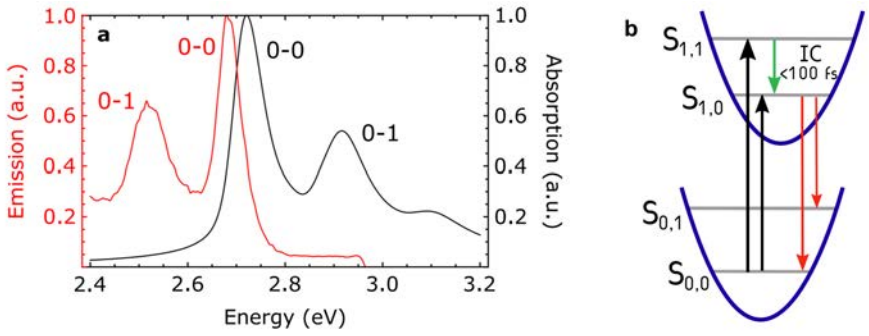

Figure 5.2: **Optical Transitions in MeLPPP.** (a) Absorption and emission spectra of MeLPPP film of 100 nm thickness spin-coated on a glass substrate. The absorption spectrum exhibits two main peaks at 2.91 eV and 2.72 eV. (b) Simplified schematic representation of the polymer's energy structure. Taken from [188].

an engineering perspective than originally anticipated.

Let me list just some of the reasons why many of the fabricated samples (34 in total throughout this project) did not meet the required standards: strong light scattering from certain tested LC mixtures, poor quality in certain batches of DBRs, incorrect cavity thickness, issues with LC capillary action, and difficulties with establishing proper electrical contact. Furthermore, the rubbing process and high temperature involved in fabrication occasionally damaged the Al_2O_3 protective layer and, consequently, the MeLPPP layer. This led to microscopic and macroscopic cracking (see Figure 5.3(a,b)), and delamination.

Samples with damaged MeLPPP occasionally exhibited nonlinear emission (Figure 5.3(c)), however, this was generally attributed to photon lasing or highly localized condensation from defect states. Such effects made it impossible to perform key experiments that required a flat photonic potential and long-range propagation of the condensate. As a result, various LC orienting materials and techniques had to be tested. Even when certain methods showed temporary success, they often proved unsuitable for long-term application. For example, a so-called 'dry rubbing' method allowed for the observation of strong coupling and BEC, but within a few days, the LC orientation deteriorated, leading to mode broadening or even complete disappearance (see Figures 5.3(d,e), which show momentum-resolved reflectivity spectra collected on the same sample one day and two weeks after LC filling, respectively).

The limited number of MeLPPP-coated substrates prevented the systematic step-by-step optimization of the fabrication process. At one point, this led to a situation where, even after obtaining promising results (including BEC and effects suggesting a supersolid phase, which will be presented later in Figure 5.11), a single overlooked modified fabrication parameter prevented the reproduction of a working sample for nearly a year. Despite that the modified samples became stable in time, their exhibited only broad spontaneous emission spectra (Figure 5.3(f)) or photon lasing at high excitation energies.

Eventually, it was decided to perform the entire device assembly process, and, in cases of rapid degradation, also the spectroscopy measurements, in Switzerland. After a week of collaborative efforts between the IBM team and Prof. Piecek's group, a good quality sample was finally reproduced on the last day, Friday at 4 PM. It turned out that the previously overlooked issue was related to the orientation layer material, which had been suppressing the emission; replacing it with PMMA solved the problem. On that same day, with the support of IBM team members, I was able to perform

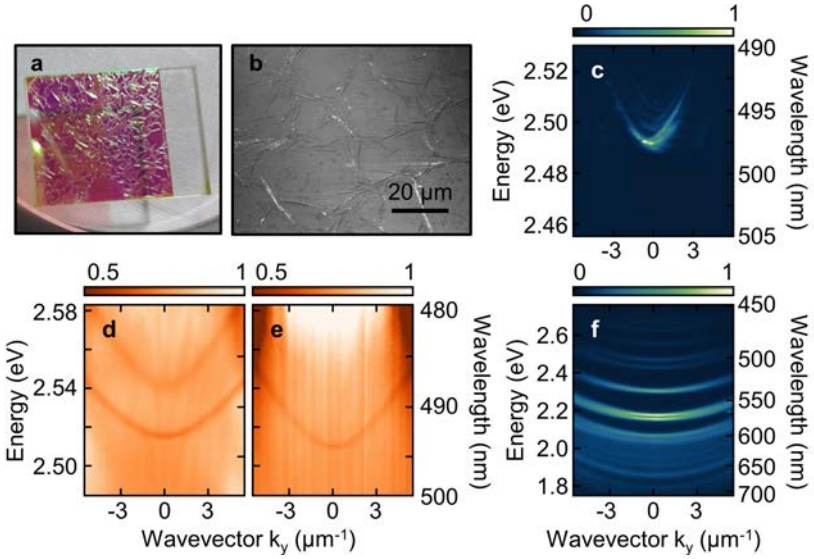

Figure 5.3: **Illustration of Selected Technical Challanges Encountered During the MeLPPP-LCMC Project.** (a) Delamination of the protective layer. (b) Photograph showing microscopic cracks within the LCMC. (c,f) Normalized momentum-resolved emission spectra collected under high excitation energy: (c) example of defect-state lasing; (f) spontaneous emission from degraded MeLPPP withing LCMC. (d,e) Normalized momentum-resolved reflectivity spectra collected (d) one day and (e) two weeks after filling the cavity with liquid crystal.

the coherence measurements and the single-shot experiments demonstrating spontaneous symmetry breaking, presented later in Figs. 5.8 and 5.13.

However, the issue of LC penetration through the protective layer persisted and occurred very quickly. By the time I returned to the laboratory after the weekend, although the condensate was still observable, the photonic potential had degraded to the point where systematic measurements were no longer possible. Currently, the IBM and WAT teams continue to work on resolving this problem. Changing the LC mixture has extended the operational lifetime of the samples to about two weeks. However, all of these difficulties have significantly limited the scope of my experimental investigations.

To claim BEC of exciton-polaritons, one must first demonstrate that the system is in the strong coupling regime. The direct method of confirming strong coupling is by showing the anticrossing between the upper and lower polariton branches in the energy-momentum dispersion relation. However, as mentioned in the previous chapter, in organic materials with strong oscillator strength, high absorption often complicates or prevents observation of the upper polariton branch [20, 124, 133, 202, 203]. In such cases, strong coupling can instead be proven on the basis of the curvature of the lower polariton branch (LPB), supported by theoretical modeling. An effective approach is to observe how the effective mass of the LPB evolves, especially how the branch 'flattens', as a function of the detuning between the cavity mode and the exciton resonance [133, 204], similar to Figure 2.11(a-c).

Figure 5.4 presents normalized momentum-resolved reflectivity spectra of a MeLPPP-LCMC measured under various applied voltages. For clarity, the measurements were collected in horizontal polarization. Due to the wide spectral range and the multimode nature of the cavity, several modes

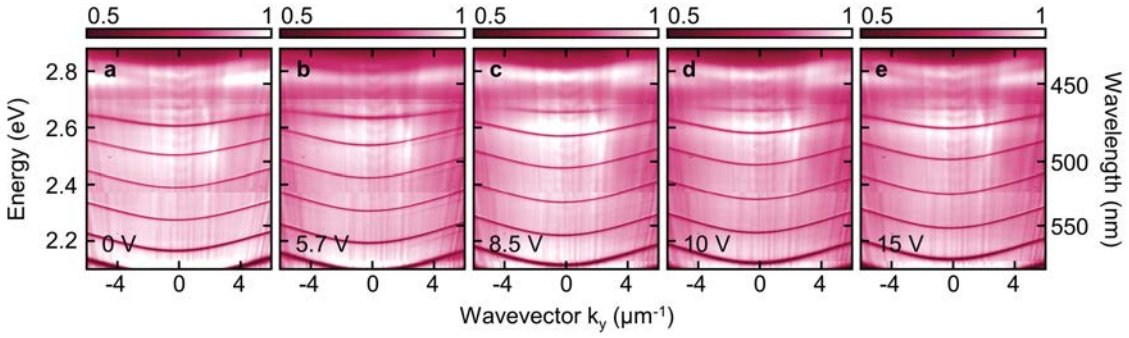

Figure 5.4: **The Influence of Light–Matter Interaction on the Effective Mass of LCMC Modes.** (a–e) Normalized momentum-resolved reflectivity spectra collected in H-polarization over a broad spectral range for different voltages applied to the sample (indicated in the bottom-left). As a result of strong interaction with MeLPPP excitonic resonance centered at $E_x = 2.715$ eV, the mode with an initial energy of approximately 2.6 eV exhibits a pronounced flattening of its dispersion, indicating an increase of the effective mass.

can be observed with different detunings of the excitonic resonance at $E_x = 2.715$ eV.

Initially, in Figure 5.4(a), the curvature of the mode around 2.6 eV does not differ significantly from that of the lower-energy modes. As the detuning decreases with increasing voltage (and increasing cavity mode energy, see Figure 5.4(b)), its effective mass increases, manifested as a flattening of the branch. In Figure 5.4(c), the mode flattens even further and begins to be strongly absorbed at high in-plane wavevectors. Figure 5.4(d) most clearly shows the strong difference in effective mass between two subsequent modes at approximately 2.58 eV and 2.66 eV. Furthermore, the upper polariton becomes visible around 2.78 eV at $|k_y| > 4$ μm^{-1}. In Figure 5.4(e), the mode appears nearly flat, but its intensity becomes weak due to absorption. At around 2.7 eV, an artifact appears due to spectral stitching at the boundaries of the detection window of the spectrometer. However, this occurs at an energy slightly higher than that of the lower polariton mode at the smallest detuning, and thus does not obscure the main effect.

For a more qualitative analysis, similar photoluminescence measurements were performed on different position on the sample. Figures 5.5(a–d) present normalized momentum-resolved emission spectra collected in H polarization for different applied voltages. The spectra were modeled using Hamiltonian (15), shown as solid lines. The color scales are oversaturated to better visualize weak signals. The energy of the vertical mode (depicted as a green line in the model) was determined from measurements in the V polarization (not shown). Due to the use of 3 mm-thick glass substrates, which introduce non-negligible spherical aberrations at high angles, the modeling was limited to an in-plane wavevector range of ±3 μm^{-1} (corresponding to approximately 13° in vacuum at 2.6 eV).

At 4 V (Fig. 5.5(a)), the observed mode structure corresponds to the characteristic spectrum of the Rashba-Dresselhaus regime, where the band curvature is modified by RDSOC (for more details, see Appendix A, Figure 9.7). As the voltage increases, the horizontal mode leaves the regime of strong RDSOC, with its energy approaching the exciton resonance (Figs. 5.5(b–d)). As previously shown in Fig. 5.4, its effective mass changes and can be extracted through modeling. This data analysis was performed by Pavel Kokhanchik (Institute Pascal, CNRS, Clermont-Ferrand), as described in [14], and is shown in Fig. 5.5(e) as the effective mass of the LPB plotted as a function of detuning $E_{\mathrm{LPB}} - E_X$.

To extract Rabi splitting Ω, a Tavis–Cummings model incorporating inhomogeneous exciton

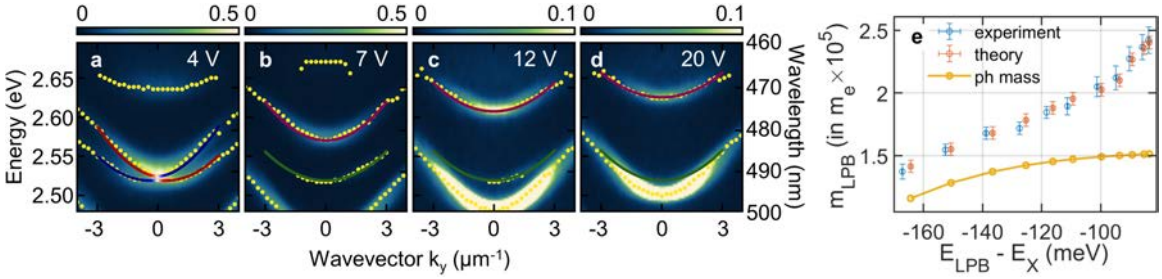

Figure 5.5: **Strong Light–Matter Coupling in LCMC.** (a–d) Normalized momentum-resolved emission spectra collected in H-polarization for different voltages applied to the sample (indicated in the top-right corner of each panel). Within the wavevector range of ± 3 μm^{-1}, the spectra were modeled using Hamiltonian 1, shown as solid lines. Yellow dots indicate the extracted peak maxima. (e) effective mass of LPB as a function of LPB detuning: experimental values (blue dots), results of numerical simulation results (red dots), and the photonic mode masses used in the simulations for each voltage (yellow dots). Data in panel (e) was analyzed and modeled by Pavel Kokhanchik.

broadening was used (see Methods in [14] for details). The energy and mass of the cavity photonic mode (in the absence of excitons) were determined using Berreman simulations and included in the model (yellow points in Fig. 5.5(e)). This photonic mode was coupled to N excitons with a Gaussian energy distribution and a exciton–photon coupling strength $\hbar g = \Omega/\sqrt{N}$. The model thus yields both the energy and the effective mass of the LPB (orange points in Fig. 5.5(e)), from which a Rabi splitting of $\Omega = 93$ meV was extracted. Based on this, the excitonic fraction in LPB was found to be approximately 5.5% in the RDSOC regime (Fig. 5.5(a)), confirming that strong coupling persists under these conditions.

As further evidence of strong coupling, the anti-crossing of two polariton branches as a function of polariton detuning can be demonstrated. This type of evidence is most commonly obtained by changing the cavity length, either by scanning the position on wedge-type cavities [205, 206], or by tuning the voltage applied to a piezo-stage in open cavities [130, 207, 208].

Here, this experiment could also be performed by changing the position on the sample due to the wedge geometry of the cavity. However, it is more convenient and reliable to keep the position fixed and scan the voltage instead. Figure 5.6(a) shows normalized transmission spectra collected at normal incidence as a function of the applied voltage, measured in H polarization, and plotted on a logarithmic scale. Around an energy of 2.7 eV, a clear anti-crossing behavior is observed.

Notably, for voltages around 7.5 V, both polariton branches are simultaneously visible and well separated in energy, excluding the possibility that this effect is caused by a change in the dielectric tensor due to LC molecules reorientation. Figure 5.6(b) presents the corresponding simulation, performed using the Berreman matrix method with the same approach as in Figure 4.4, where the optical response of the MeLPPP excitons was taken from Extended Data Figure 3 in [14].

The results presented in this section provide convincing evidence for the realization of the strong-coupling regime in MeLPPP-LCMC.

5.2 Bose-Einstein Condensation in Liquid Crystal Microcavity

To create a sufficiently high particle density to reach the Bose–Einstein condensation of exciton-polaritons, optical excitation is typically used. Here, excitation was provided by a femtosecond laser tuned to an energy of 2.91 eV ($\lambda = 426$ nm), corresponding to the (0–1) optical vibron-assisted

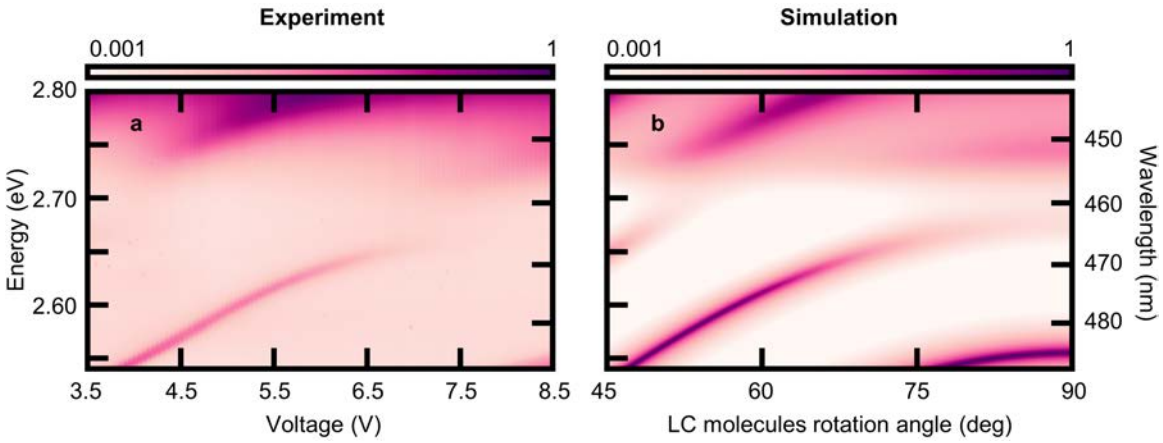

Figure 5.6: **Anticrossing of Upper and Lower Polariton Branches.** (a) Experimental and (b) numerically simulated transmission spectra in H-polarization presented on a logarithmic scale as a function of applied voltage and the corresponding rotation angle of the liquid crystal molecules, respectively. A distinct anticrossing behavior is observed around 7.5 V (corresponding to a rotation angle of approximately 75 degree).

transition shown in Figure 5.2. The polariton modes were tuned to the energy approximately 200 meV below the excitonic resonance, corresponding to an excitonic fraction of approximately 5%.

Figure 5.7(a–c) shows momentum-resolved emission spectra collected at different excitation energy densities at a position on the sample with negative Δ_{HV} detuning. Near the condensation threshold (Fig. 5.7(a)), spontaneous emission occurs from both polariton branches corresponding to the H and V polarizations. Once the threshold is crossed (Fig. 5.7(b)), strong emission from the bottom of the vertical mode at 2.516 eV begins to dominate the spectrum. Doubling the excitation energy density (Fig. 5.7(c)) increases the emission intensity by a factor of approximately 40. Here, in contrast to photon lasing described in the previous section, the emission profile above the condensation threshold is not sharply localized in energy and in-plane momentum. Instead, it resembles the thermalized polariton BEC presented in Fig. 3(c) of [139] and Supplementary Fig. S4(a) of [187], both using MeLPPP as active medium.

Figures 5.7(d,e) present the emission intensity, linewidth, and peak energy as a function of the excitation energy density. For comparison, an additional data point from reflectivity measurements at the same position is included in Fig. 5.7(e). The condensation threshold energy density of approximately 100 $\mu J/cm^2$ is comparable to that reported in previous works where MeLPPP served as the active material [139, 188, 209], and is two orders of magnitude lower than for the P580-LCMC sample in the weak-coupling regime shown in Figure 4.6. Based on the modeling of the previous section, at an exciton–photon detuning of -192 meV, the energy difference between the uncoupled photon mode and the lower polariton branch is equal 11 meV, nearly three times larger than the observed blueshift of 4 meV. This confirms that strong coupling is preserved above the condensation threshold. The observed nonlinear increase in emission intensity, spectral narrowing, and small blueshift all support the conclusion that the results correspond to a BEC of exciton–polaritons.

An essential characteristic of BEC is the presence of long-range phase coherence. Figure 5.8(a) shows a real-space image of the emission collected above the condensation threshold, interfered using a Michelson interferometer with a retroreflected mirror-symmetric copy of the same image. This type

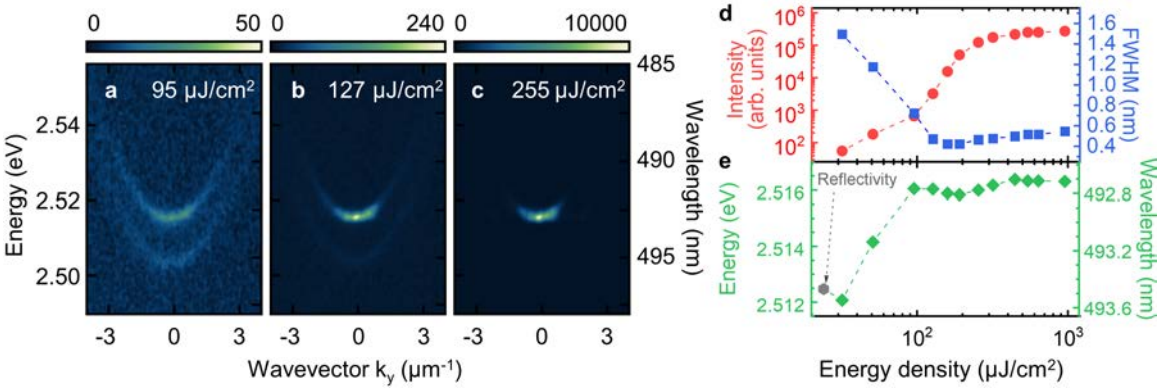

Figure 5.7: **Bose–Einstein Condensation of Exciton-Polaritons at Room Temperature in LCMC.** (a–c) Momentum-resolved emission spectra collected (a) below and (b,c) above the condensation threshold. The excitation pulse energy is indicated in top-right corner. (d) Emission intensity (red dots), spectral linewidth (blue squares), and (e) peak emission energy (green diamonds) as a function of excitation pulse energy density. An additional data point from reflectivity measurements is included in (e) (gray hexagon) for comparison.

of measurement allows spatial mapping of interference fringe visibility and thus provides access to the coherence length, which in this case exceeds 30 μm.

By introducing a delay line in one arm of the interferometer and using pulsed excitation, it is also possible to investigate the evolution of first-order temporal coherence. By delaying the light in one arm with respect to the other by a time Δt, the temporal overlap between the interfering pulses is reduced, leading to a decrease in the visibility of the fringes. By analyzing the intensity contrast, one can determine the temporal coherence time of the condensate. Figure 5.8(b) presents the fringes visibility, extracted using Fourier analysis, as a function of time delay Δt. A Gaussian fit to the data yields a full width at half maximum of 3.2 ps, corresponding to the temporal coherence time of the condensate.

The polarization of the excitation laser can induce non-spontaneous symmetry breaking, even under non-resonant excitation. In MeLPPP, chromophores with dipole moments aligned with the polarization of the excitation laser are selectively excited. If the relaxation of excited particles to the condensate state occurs faster than the depolarization effects caused by energy transfer to differently oriented chromophores, the polarization of the condensate will also be determined by the excitation laser. The pinning of exciton-polariton BEC polarization to pump polarization has already been demonstrated for microcavities with MeLPPP [139].

However, in typical cavities, the TE-TM splitting at small in-plane wavevectors $k_{\parallel}$ is negligible, so even with symmetry breaking through polarized excitation, the resulting emission typically shows different polarizations but identical energies. To lift the degeneracy between polariton modes, one can apply a magnetic field to induce Zeeman splitting [210]. Here, thanks to artificial Zeeman splitting (i.e. detuning Δ_{HV}), which is electrically tunable on demand, I will demonstrate how this additional degree of freedom allows use of MeLPPP-LCMC as a polariton switch to control both the polarization and energy of the BEC with the applied voltage and polarization of the excitation laser.

Figure 5.9 presents normalized momentum-resolved emission spectra collected above the condensation threshold, with the excitation polarization indicated above each column. The measurements

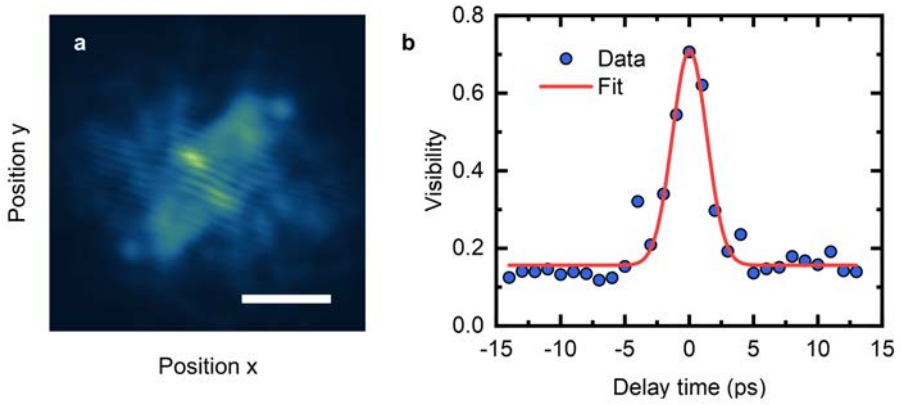

Figure 5.8: **Spatial and Temporal Coherence of Polariton BEC in LCMC.** (a) Real-space image of the interference pattern collected above the condensation threshold at zero delay ($\Delta t = 0$), obtained by superimposing two mirror-symmetric images using a Michelson interferometer. Scale bar: 20 µm. (b) Visibility of the interference fringes (blue dots) as a function of delay time, extracted by 2D Fourier transform and fitted with a Gaussian function (red). Delay time resolution: 1 ps.

were performed at two positions on the sample with different energies of vertically polarized LPB, allowing investigation of both detunings $\Delta_{HV} > 0$ (top row) and $\Delta_{HV} < 0$ (bottom row), while keeping the LPB energies near the efficient vibronic transition (0–1) comparable. Figures 5.9(a–d) were collected at the first position, and Figures 5.9(e,f) at the second.

First, excitation with circular polarization σ^+ (Figs. 5.9(a,d)) will be consider. Because excitons in MeLPPP are linearly polarized, this excitation does not favor a specific condensate polarization. As condensation occurs on the lower-energy LPB, tuning only the applied voltage enables switching between a V-polarized condensate at 2.49 eV when $\Delta_{HV} > 0$ (Fig. 5.9(a)) and an H-polarized condensate at 2.48 eV when $\Delta_{HV} < 0$ (Fig. 5.9(d)).

For linearly polarized excitation, condensation occurs on the polariton branch that matches the pump polarization. In positive detuning ($\Delta_{HV} > 0$), when the sample is excited with V-polarized light (Fig. 5.9(b)), condensation again occurs on the V-polarized branch at 2.49 eV, while H-polarized excitation (Fig. 5.9(c)) leads to condensation on the H-polarized branch at 2.50 eV. The same effect is observed for negative detuning ($\Delta_{HV} < 0$), where the energies of the H and V branches are chosen to mirror the situation in the positive detuning case. In this scenario, V-polarized excitation (Fig. 5.9(e)) results in condensation on the V-polarized branch at 2.50 eV, while H-polarized excitation (Fig. 5.9(f)) leads to condensation on the H-polarized branch at 2.49 eV.

The pump polarization control is effective as long as the detuning Δ_{HV} is not too large (typically up to ∼20 meV). Otherwise, condensation occurs on the polariton branch with energy closer to the vibronic transition energy.

This demonstrates a polariton switch, unique in that it allows control over not only the polarization of the condensate but also its energy via both the polarization of the excitation and the applied electric field.

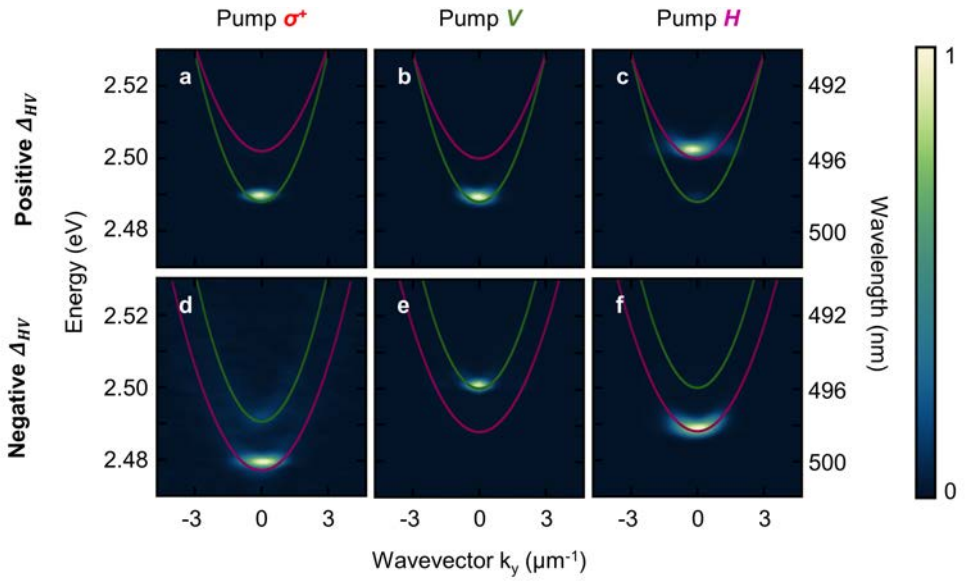

Figure 5.9: **Voltage- and Excitation-Polarization-Tunable BEC.** (a–f) Normalized momentum-resolved emission spectra collected above the condensation threshold. The excitation polarization is indicated at the top; the upper row corresponds to positive, and the lower row to negative Δ_{HV} detunings. (a,d) Under σ^+ excitation, condensation occurs in the lower-energy, linearly polarized lower polariton branches. (b,c,e,f) For linearly polarized excitation, condensation takes place in the polariton branch with the same polarization as the excitation beam. Solid lines represent the Stokes vector component S_1 obtained from modeling using Hamiltonian (15) (violet indicates positive values, green indicates negative values).

5.3 Room-Temperature Supersolid Phase and Spin-Dependent Propagation

This section presents the results of condensation in the RDSOC regime, leading to the formation of a supersolid phase of the exciton-polariton BEC. In the beginning, the multi-shot experiment, analogous to the measurements discussed in the previous section, performed with a 500 Hz excitation laser repetition rate, will be considered.

The scheme of realization of the supersolid phase in an LCMC system in a strong coupling regime is shown in Figure 5.10. Non-resonant excitation creates a reservoir of hot excitons that relax into exciton-polariton states in two RDSOC valleys shifted in momentum space to $\pm k_0$. The resulting BECs at these two minima spontaneously acquire phase factors $\Phi_{1,2}$ and inherit the polarization properties of each valley: strong circular and weaker vertical polarization components. The linear polarization component interferes, generating a density modulation pattern of polaritons in a real space with a spatial period of π/k_0. Since the relative phase $\Phi_1 - \Phi_2$ of the condensates determines the position of the interference maxima, each experimental realization exhibits a spatial shift that decreases contrast in the multi-shot experiment.

Figure 5.11(a) shows normalized momentum-resolved emission spectra collected above the condensation threshold, without an applied voltage. In this case, both linearly polarized polariton branches are well-separated in energy. Figure 5.11(d) presents the total emission intensity in real

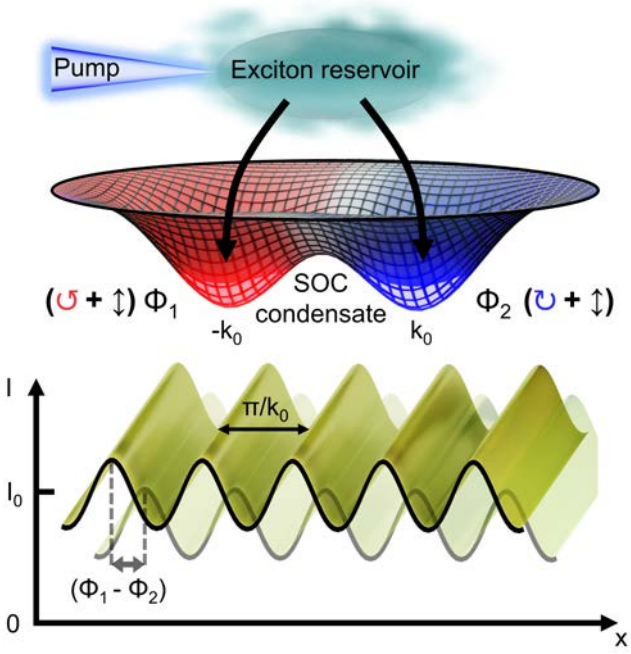

Figure 5.10: **The Scheme of the Realization of the Supersolidity in a Strongly Coupled LCMC.** Particles from the excitonic reservoir, created via non-resonant pumping, relax and condense in both RDSOC valleys. The condensates at the $\pm k_0$ dispersion minima acquire a relative phase Φ and inherit the polarization properties of the respective valleys. The linear polarization components interfere in real space, forming a stripe-phase pattern, with maxima positions determined by the phase difference $\Phi_1 - \Phi_2$.

space. Due to the presence of photonic disorder, bright speckles appear on a nearly homogeneous background with a size of approximately 25 µm, comparable to the excitation spot size. Since condensation occurs at the bottom of the vertically polarized mode, the condensate emission in the real space is also strongly vertically polarized, as shown in Figure 5.11(g), expressed by the Stokes parameter S_1. The Fourier transform of the total intensity of the real-space emission is shown as the dashed line on a logarithmic scale in Figure 5.11(j) and indicates the absence of spatial periodicity.

When a voltage of 7.6 V is applied to the sample, the system enters the RDSOC regime with small detuning $\Delta_{HV} = -1.3\,\text{meV}$ (Figure 5.11(b)), resulting in two minima at $\pm k_0 \approx 1\,\mu\text{m}^{-1}$. Using the Hamiltonian 1 to model the data (solid lines in Figures 5.11(a,b)) yields the SOC constant $\alpha = 2.7\,\text{meV} \cdot \mu\text{m}$. Based on this Hamiltonian, the wavevector of the minima is given by:

$$k_0 \approx \frac{2M\hbar^2\alpha^2 - \hbar^2\Delta^2}{4\alpha^2}. \tag{39}$$

The eigenstates at both minima exhibit elliptical polarization, with opposite circular polarization degrees and equal linear polarization components. From Hamiltonian 1 the following analytical expression for the degree of linear polarization S_1 can be derived:

$$S_1 = \frac{\Delta + \gamma k_p^2}{4\alpha^2 k_0^2 + (\Delta + \gamma k_0^2)^2}, \tag{40}$$

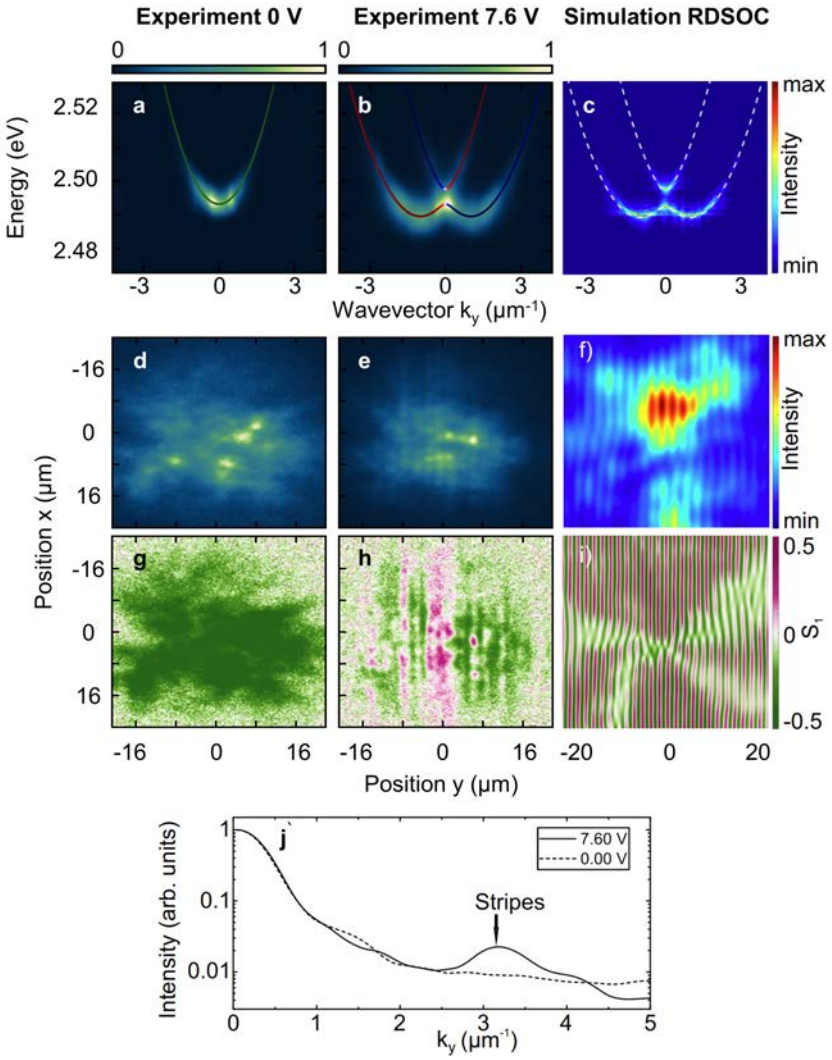

Figure 5.11: **Room-Temperature Supersolid Phase of Polariton–Exciton BEC in LCMC.** Multiple-shot emission measured above the condensation threshold at 0 V (left column), in the RDSOC regime at 7.6 V (middle column), and numerically simulated with presence of RDSOC (right column). (a–c) Normalized momentum-resolved spectra of the total emission. (a) Condensation from a single, vertically polarized valley, and (b,c) in two RDSOC valleys shifted in reciprocal space. Solid and dashed lines represent modelling using Hamiltonian 1. (d–f) Real-space total emission: (d) no stripe pattern is observed, (e, f) presence of a stripe phase indicating supersolid state. (g–i) Real-space emission expressed by the Stokes parameter S_1. (g) Dominant vertical polarization without the PSH pattern, (h,i) emergence of the PSH. (j) Fourier transform of the experimental real-space intensity from panels (d,e), with the diffraction peak corresponding to the stripe pattern indicated. Simulations and analysis shown in panels (c,f,i,j) were performed by Pavel Kokhanchik, Dmitry Solnyshkov, and Guillaume Malpuech from the Institute Pascal, CNRS, Clermont-Ferrand.

The value obtained from Eq. (40), $S_1 = 0.23$, is in reasonable agreement with the experimentally measured value of 16%.

As in the previous chapter, condensation in both valleys leads to interference between circularly polarized components (approximately 80%), resulting in the formation of a persistent spin helix, shown in Figure 5.11(h). Similarly, interference between linearly polarized components (16–18%) leads to the emergence of density stripes in the total polariton density, visible as vertical fringes in Figure 5.11(e), which shows the total real-space emission. Here, as in the zero-voltage case, photonic disorder causes additional spatial speckles.

The period of both the polarization and the density modulations is equal to π/k_0. The presence of density stripes is confirmed in Figure 5.11(j) (solid line), where a pronounced peak at $k_y = 2k_0 = 3.1\,\mu\text{m}^{-1}$ shows reasonable agreement with the value expected from direct momentum-resolved measurements, taking into account the discrepancy in the PSH period discussed in the previous chapter, further increased by the use of a 3 mm glass substrate.

The experimental contrast of the density stripes, estimated through Fourier analysis, is 2.2%, whereas for the polarization stripes it reaches 40%. This difference arises from the nature of the multi-shot experiment, where hundreds of realizations reduce the contrast due to shot-to-shot variations, and from the difference in the circular and linear polarization degrees of the condensates. This phenomenon will also be addressed later in the context of single-shot experiments.

The observation of the stripes in multi-shot experiment is possible because of the phase-locking mechanisms between condensates in the two valleys. The most efficient phase-locking mechanism originates from the inhomogeneous spatial gain profile imposed by the Gaussian shape of the non-resonant excitation spot. The stripe maxima appear preferentially in regions where the gain is strongest. However, it should be emphasized that this pump-induced gain profile is not the origin of the stripe formation itself, but rather determines their preferred spatial positioning.

Another intriguing effect known in polariton physics, which can also be observed experimentally here, is the occupation by the condensate not only of the dispersion minima but also of the negative mass state at $k = 0$. At the position of the localized non-resonant excitation, a repulsive potential of hot excitons and polaritons is generated. Polaritons with positive effective mass (at the dispersion minima) are repelled from the excitation spot [79], while polaritons with negative mass (at $k = 0$ of the lowest polariton branch) are effectively attracted to the pump [106, 211], resulting in enhanced emission intensity, as clearly seen in Figure 5.11(b).

The simulations performed by Pavel Kokhanchik, Dmitry Solnyshkov, and Guillaume Malpuech use a hybrid Boltzmann–Gross-Pitaevskii equation incorporating non-resonant excitation, finite lifetime, energy relaxation, saturation gain [212], spin-anisotropic polariton–polariton interactions, and disorder, are shown in Figures 5.11(c,f,i). Details of the model and the parameters used can be found in the Methods section in [14]. In the momentum-resolved spectra in Figure 5.11(c), condensation occurs at multiple energies due to the non-equilibrium nature of the polariton condensate [200]. Similarly to the experiment, the condensate populates both the dispersion minima and the negative-mass state at $k = 0$. The simulations in Figures 5.11(f,i) also reproduce the density stripes and the persistent spin helix, respectively.

The previous discussion focused on the total polariton density and the degree of linear polarization. For circular polarizations, RDSOC leads to a strong spatial separation of spin-polarized condensates. Figure 5.12(a) shows the momentum-space image expressed by the S_3 Stokes parameter in the RDSOC regime, corresponding to the measurements in Figs. 5.11(b,e,h). Since the condensate occupies the minima of valleys that are elliptically polarized (mainly circular), its polarization inherits this character, as seen in Figure 5.12(a).

In real space, in the absence of applied voltage (Figure 5.12(b)), the degree of circular polarization is nearly zero and within the noise level. In contrast, in the RDSOC regime (Figure 5.12(c)), a spatial

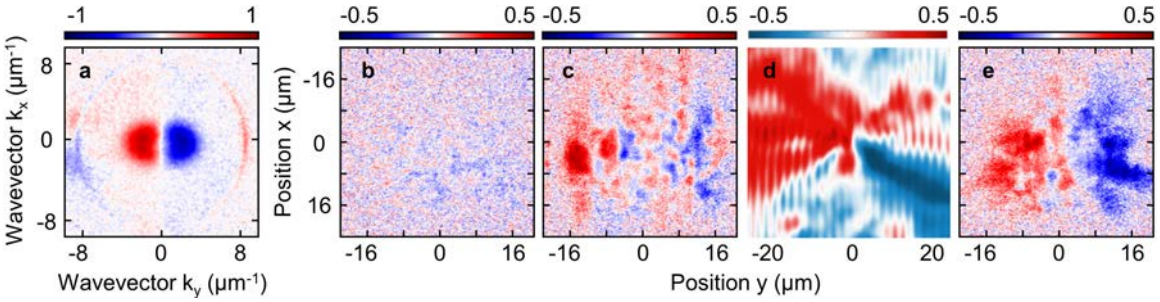

Figure 5.12: **Spin-Dependent Propagation of BEC in the RDSOC Regime.** (a) Momentum-space emission and (b–d) real-space emission expressed by the S_3 Stokes parameter, collected above the condensation threshold at the position shown in Figure 5.11. Panel (b) shows the 0 V condition, while (a,c,d) correspond to the RDSOC regime. (e) Real-space image acquired at a different position on the sample in RDSOC regime. Panels (a–c,e) present experimental data, whereas the simulation in panel (d) was performed by Pavel Kokhanchik, Dmitry Solnyshkov, and Guillaume Malpuech.

separation of condensates with opposite circular polarization becomes visible and is reproduced by simulations (Figure 5.12(d)). This effect stems from the fact that condensates at the RDSOC valley minima acquire not only distinct spin (polarization) properties but also nonzero and opposite momentum. Consequently, this leads to spin-dependent propagation of the condensates in real space, which can be turned on and off on demand.

This effect is even more clearly visible in Figure 5.12(e), which also presents a real-space image above the condensation threshold, expressed by the S_3 Stokes component in the RDSOC regime, but taken at a different position on the sample.

The results of single-shot measurements of one linear polarization component are presented in Figure 5.13. To minimize pump pinning, a larger excitation spot of 30 μm was used compared to multiple-shot experiments. A single linear polarization component is expected to follow the same spatial pattern as the density stripes, but with a much higher contrast due to the much stronger circular components. This high contrast makes the stripes observable even in single-shot experiments, where the signal-to-noise ratio is close to the detection limit.

The spontaneous symmetry breaking associated with the random relative phase between the two counter-propagating components is illustrated in Figures 5.13(a,b), which show two particular single-shot images with visibly displaced stripe patterns. The white dashed lines in Figure 5.13(a) mark the stripe maxima, which appear to be clearly shifted in Figure 5.13(b). This displacement results from two factors: (i) the random choice of relative phase and (ii) the formation of domains with different relative phases, which can give rise to topological defects such as vortices. These vortices emerge spontaneously during the condensation process via the Kibble–Zurek mechanism [213, 214]. In atomic supersolids, vortices have recently been generated by rotating the condensate [197].

Figures 5.13(c,d) show an example of such a topological defect, which appears as a dislocation in the stripe pattern in a particular single-shot image (Fig. 5.13(c)), and as a vortex in the corresponding phase map extracted from the Fourier transform (Fig. 5.13(d)). The random nature of the relative phase is further confirmed by the histogram in Figure 5.13(e), built from over 500 single-shot realizations.

Due to this phase randomness, the integration of multiple shots, as in Figure 5.11, necessarily reduces contrast. In the limit of an infinite number of pulses, the contrast vanishes, while for a large but finite number N, it decreases as $1/\sqrt{N}$ (see SI Section 6 in [14] for details). This scaling behavior

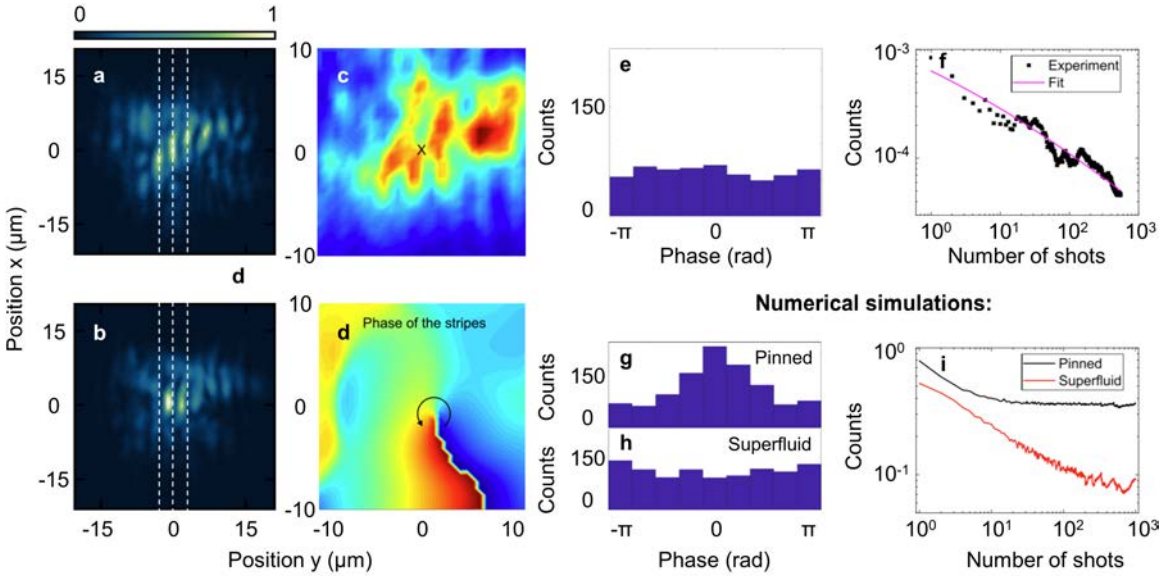

Figure 5.13: **Spontaneous Symmetry Breaking and Superfluidity Evidence in Single-Shot Experiments.** (a,b) Two single-shot images of condensate emission at 2 P_{th} collected with a linear polarizer placed in front of the camera. White dashed lines serve as guides for the eye, indicating fringe shifts caused by spontaneous symmetry breaking (random phase). (c) Fringes pattern exhibiting a dislocation, with its position marked with a cross. (d) Phase map extracted from the fringe pattern, revealing a vortex singularity. (e) Histogram of phase values from the fringes pattern, demonstrating a near-uniform distribution. (f) Reduction of fringe contrast due to averaging over multiple shots. The contrast decreases as $1/\sqrt{N}$ for large N. (g,h) Histograms of theoretically calculated phase values for the fringe patterns in the pinning (g) and superfluid (h) regimes. (i) Theoretically calculated fringe contrast in the absence of interactions (black) and in the superfluid regime (red). Simulations and analysis of the experimental results in panels (e–i) were performed by Pavel Kokhanchik, Dmitry Solnyshkov, and Guillaume Malpuech.

is confirmed in Figure 5.13(f), where the black dots show the experimental contrast extracted from single-shot images, and the red curve is a theoretical fit showing a very good agreement.

Due to the relatively slow power-law decay, the contrast after 500 realizations is reduced by approximately one order of magnitude, consistent with the multi-shot result shown in Figure 5.11 (observed: 2%; expected: 20%).

A key feature of these observations is that the stripe positions appear fully insensitive to the disorder potential present in the cavity plane. This behavior is characteristic of superfluid stripes (i.e. a supersolid phase), which are robust against elastic scattering. Figures 5.13(g–i) present simulations supporting this interpretation. Figure 5.13(g) shows that for non-interacting particles, the relative phase distribution is non-uniform (exhibiting preferred values), and the contrast does not decay significantly with the number of shots (Fig. 5.13(i)). In contrast, when interactions are included with strengths comparable to the amplitude of the disorder, the phase becomes random (Fig. 5.13(h)) and the contrast decays following the expected power-law behavior.

The observation of density stripes exhibiting superfluid behavior represents the first realization of a supersolid phase at room temperature.

5.4 Summary and Outcome

In this chapter, I presented a liquid crystal optical microcavity integrated with an organic polymer MeLPPP in the strong light-matter coupling regime. After an initial discussion of the technical challenges encountered during the project, the evidence for strong coupling in the system was provided based on the analysis of the change in the effective mass of the lower polariton branch and the observation of an anti-crossing as a function of applied voltage. Subsequently, Bose-Einstein condensation of exciton-polaritons was demonstrated, where the condensation threshold is two orders of magnitude lower than in samples in the weak coupling regime. Measurements of the spatial and temporal coherence of the condensate were presented, showing a coherence length that exceeds 30 µm and a coherence time of 3.2 ps.

Then a polariton switch based on artificial Zeeman splitting, which can be tuned on demand, was presented. In this device, both the polarization and the energy of the condensate can be controlled by the applied external electric field and the polarization of the excitation laser.

In the RDSOC regime, the non-equilibrium condensate simultaneously occupies the negative-mass state at $k = 0$, which is a signature of the repulsive interaction with the excitonic reservoir, and the two degenerate minima of the dispersion. Real-space distributions of total intensity and polarization reveal the presence of stripes. In single-shot experiments, the position of the polarization stripes randomly varies between condensate realizations, indicating spontaneous breaking of the translational symmetry. The robustness of this process with respect to the intrinsic disorder potential of the structure, along with the detection of quantum vortices, confirms the superfluid behavior of the stripe phase, thereby demonstrating the supersolid nature of the observed state.

The realization of Bose-Einstein condensation of exciton-polaritons in a liquid crystal microcavity at room temperature opens a range of intriguing possibilities that are not accessible in the weak coupling regime. The demonstration of a polariton switch in such a system represents a significant step forward in the rapidly developing field of polariton-based transistors [188, 215, 216] and, more broadly, logic devices [120, 189, 217, 218] operating at room temperature. The additional control parameters, as well as the spin degree of freedom, can significantly expand the functionality of such devices.

Furthermore, the demonstrated long coherence length and the spin-polarized directional propagation of condensates, which can be interpreted as a spin current, suggest that this platform may find applications in various photonic devices, such as spin-dependent photonic couplers or photonic circuits. Importantly, the spin current can be switched on and off on demand, which is not straightforward in many systems (for example, those exhibiting the optical spin Hall effect resulting from TE-TM splitting).

From the perspective of fast logic operations, a major drawback of LCMC in general is the sub-millisecond time response of liquid crystals. To overcome this limitation, an alternative tunable medium with high birefringence and faster switching times would be required; however, to the best of my knowledge, no such material is currently available. Moreover, the samples still suffer from rapid degradation over time. In my view, this issue is purely engineering-related and will hopefully be resolved in the near future through the combination of an appropriate LC mixture and protective layer. Other challenges, such as scattering induced by the LC and the photobleaching typical of organic materials, also need to be addressed before this technology can be considered for real-world applications. Despite these limitations, from the standpoint of fundamental research, it offers a promising platform for studying a single condensate or multiple condensates in optical lattices under synthetic magnetic fields.

The realization of a supersolid phase of a BEC of exciton-polaritons at room temperature marks a significant milestone in the field, which has so far been predominantly explored in ultracold atomic

systems [192–197]. Due to the relatively fast degradation of the samples used, several important effects still need to be systematically studied, for example, the dependence of the supersolid period on detuning. On already degraded samples, consistent results could not be obtained. Hovewer, the observation of density stripes in the total polariton density, a key signature of the supersolid phase, was achieved in at least three independent samples, confirming the reproducibility of the effect. Currently, further studies of this phase are underway in the IBM Research group using single-shot experiments. These include investigations of the Kibble–Zurek mechanism and the dependence of the number of generated quantum vortices on excitation power and distance from the pump center. Their findings further support the interpretation of the results presented here.

It is worth noting that both preprints reporting the observation of a supersolid phase in polariton BECs [14, 219] appeared simultaneously. One of them [198] has already been published, despite lacking direct evidence of superfluidity or spontaneous symmetry breaking. Recently, another group published a preprint claiming the observation of a supersolid phase in an LCMC in the strong coupling regime [22], where the formation of density stripes occurs via scattering into neighboring modes. This highlights the rapidly growing interest in this topic and the competitive nature of current research. The manuscript presenting the results discussed in this chapter is still under peer review.

These studies open new perspectives for exploring quantum fluids of light in the presence of spin–orbit coupling and beyond, including in topologically non-trivial systems, both Hermitian and non-Hermitian.

6 One Dimensional Self-Organizing Photonic Potential - Uniform Lying Helix

The results presented in this chapter have been published in:

M. Muszyński, et al. Electrically Tunable Spin-Orbit Coupled Photonic Lattice in a Liquid Crystal Microcavity. *Laser & Photonics Reviews* **18**, 2400794 (2024). [15]

In this chapter, I will present a one-dimensional, self-assembled photonic structure that forms on macroscopic scale. It is based on a chiral liquid crystal in the uniform lying helix (ULH) phase, embedded within a liquid crystal optical microcavity, where it acts as an in-plane periodic photonic potential. This potential leads to the formation of distinct band structures for two orthogonal linear polarizations of light. These band structures can be dynamically and precisely tuned using an external electric field.

When the liquid crystal is tilted within the plane of the cavity, a spin-orbit coupling emerges between bands of different polarizations and parities in the (N, N) regime, referred to as interband spin-orbit interaction (ISOC).

Additionally, I will present polarization-conserving lasing, light propagation perpendicular to the periodic structure, and various types of topological defects. One particular type of defect exhibits change of the ISOC sign and features a state that potentially possesses nontrivial topological properties.

6.1 Polarized Tunable Photonic Band Structures

In the previous two chapters, I discussed a translationally invariant nematic LCMC. The following two chapters will focus on cases where a periodic photonic potential of different dimensionalities is introduced into the LCMC.

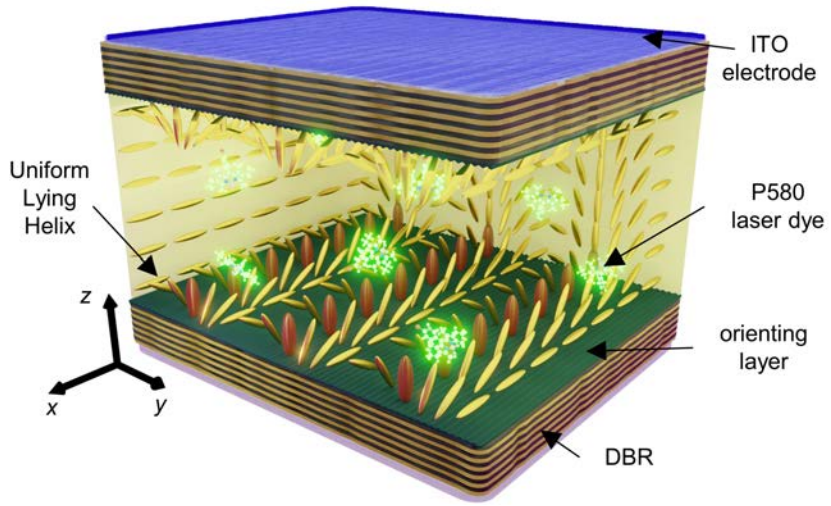

Figure 6.1: **ULH Texture Inside an Optical Microcavity.** Scheme of the dye-doped optical microcavity with an embedded stabilized ULH structure. The rows of molecules with vertically oriented directors are colored in red to indicate the lattice period.

Figure 6.1 presents a scheme of the ULH-LCMC structure, which will be discussed in this chapter. The cavity design resembles that of Chapter 4 (Figure 4.1), with the P580 dye dispersed in LC mixture at a concentration of 1% and the system is in the weak light-matter coupling regime.

The cavity is filled with a nematic liquid crystal and a chiral dopant, which induces a helical twist in the LC matrix, forming a supramolecular helical structure with a helical pitch (double period p) on the order of several micrometers [220, 221]. When the boundary surfaces of the LCMC induce the homeotropic anchoring, they impose a topological frustration that produce a Uniform Lying Helix,

with the helical axis aligned parallel to the substrate.

The confinement ratio C defines the relationship between the cavity thickness d and the helical pitch p: $C = \frac{d}{p}$. In this study, by tuning the chiral dopant concentration, C was kept within the range of 1.85 to 2.75. This plays a crucial role in achieving a well-ordered periodic ULH with a small period of 1-4 µm while also reducing the number of dislocations.

Microcavity photons experience a potential defined by the effective refractive index obtained by averaging along the z-axis. The periodic modulation of the effective refractive index along the y-direction results in the formation of a one-dimensional photonic crystal for light within the visible spectrum. To highlight this periodicity, in Figure 6.1, rows of molecules with the same orientation of the LC director (and thus stripes where the effective refractive index remains constant) are colored red.

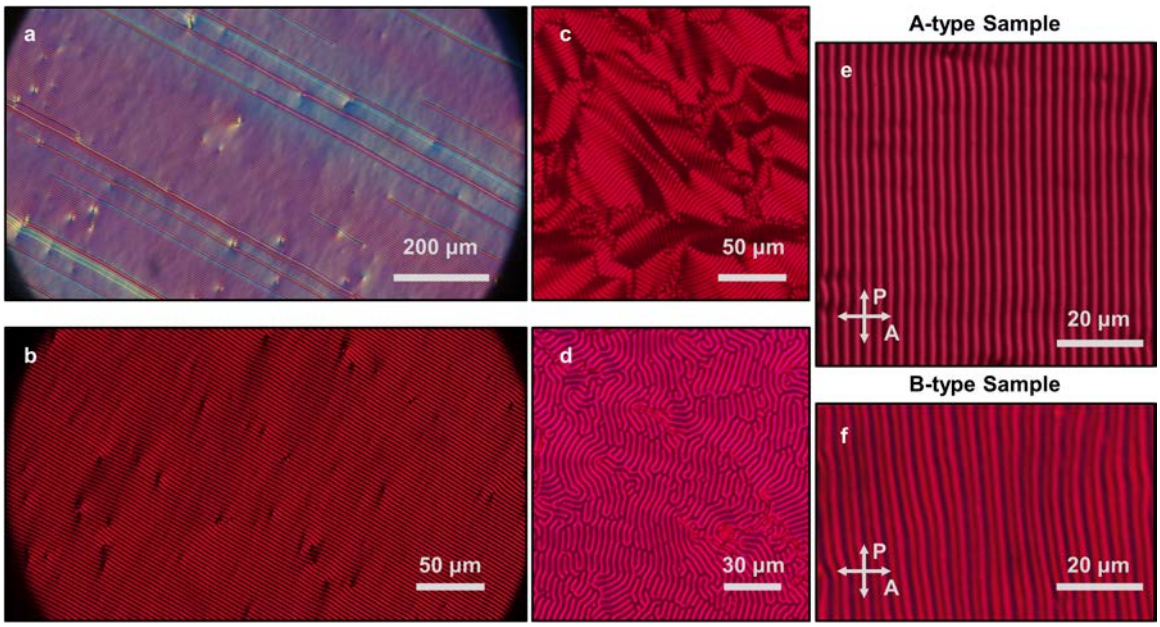

Figure 6.2: **Polarized Optical Microscopy Images of Various ULH Textures.** Well-ordered ULH in a large area (a) inside a glass cell, and (b) inside a microcavity. (c,d) Textures of ULH with varying sizes of well-organized regions. (e) POM image of standard (non-tilted) A-type ULH. (f) POM image of B-type (tilted) ULH. Arrows indicate polarizer and analizer alignment. Photographs by Eva Oton (MUT).

Figure 6.2 presents polarized optical microscope (POM) images of various ULH textures obtained for samples with different fabrication parameters. In such images, the color corresponds to the phase shift of transmitted light, providing insight into the spatial orientation of the LC director. Figure 6.2(a) was taken with low magnification through a glass cell (without DBRs) containing a well-aligned ULH structure. It can be observed that over a macroscopic area of hundreds of micrometers, well-oriented stripes are formed, corresponding to the modulation of the refractive index. Similarly, a well-ordered macroscopic structure can be obtained within a microcavity, as shown in Fig. 6.2(b). Due to the higher magnification, the ULH stripes are clearly distinguishable.

POM images collected on cavity samples are typically two-colored. The black regions (absence of light) correspond to situations where polarized light passes through the LC oriented either parallel

or perpendicular to the polarizer axis (it does not experience retardation and is extinguished by the analyzer). In contrast, the red regions correspond to light that has undergone phase retardation and can thus be transmitted. The red color dominates the image because, unlike cells without DBRs, light is filtered by the cavity, and primarily high transmission through the Bragg modes on the long-wavelength side of the stopband is visible.

Depending on sample preparation (liquid crystal mixture, cavity thickness, quality of the orienting layer, etc.), the ULH structure may be well-ordered over a smaller areas, forming domains with different orientations (Fig. 6.2(c)) or small regions resembling LC fingerprints (Fig. 6.2(d)). Additionally, the elastic constants and viscosity of the nematic host play a crucial role in the stable distribution of the director.

Two types of samples were studied: A-type Samples (Fig. 6.2(e)) and B-type Samples (Fig. 6.2(f)), which differ in the liquid crystal used (LC2091* and E7, respectively), leading to different internal molecular tilt. A-type Samples show equidistant stripes and do not exhibit additional tilting of the LC molecules, whereas B-type Samples show a dimerized stripes pattern, indicating the presence of additional LC molecule tilting. More details on this will be shown in the Interband Spin-Orbit Interaction section.

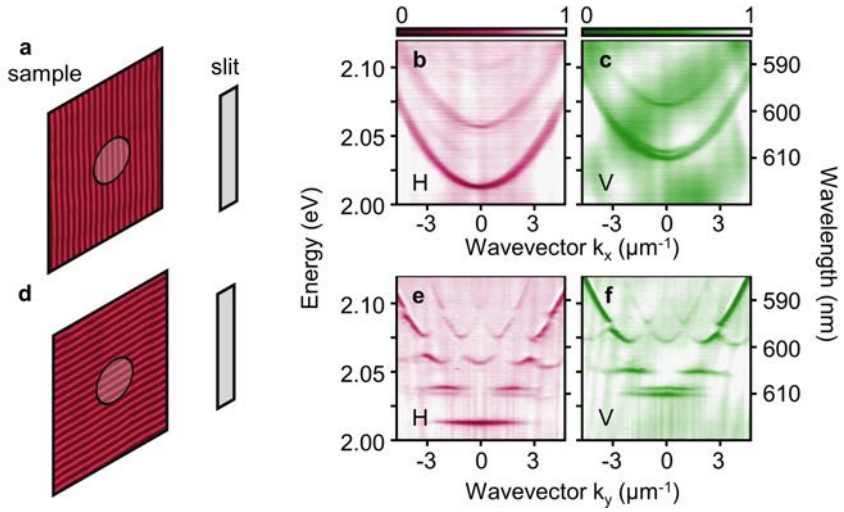

Figure 6.3: **Band Structure Along and Perpendicular to the ULH Period.** (a) Scheme of the experimental configuration with the periodic potential aligned along the spectrometer slit. (b,c) Corresponding normalized momentum-resolved reflectivity spectra, showing no band gaps in horizontal and vertical polarization, respectively. (d) Scheme of the experimental configuration with the periodic potential perpendicular to the spectrometer slit. (e, f) Corresponding spectra in horizontal and vertical polarization, respectively. The periodic modulation of the refractive index leads to the appearance of photonic bands and band gaps.

Since the photonic potential created by ULH is periodic in one direction, the image observed along the k_x or k_y directions (which can be measure, for example, by changing the orientation of the sample relative to the slit) will differ. Figure 6.3 presents an example of such an experiment, where the upper panel shows the results of normalized momentum-resolved reflectivity spectra measured for H and V polarizations along k_x (periodicity along the slit, schematically shown in Fig. 6.3(a)) and along k_y (periodicity perpendicular to the slit, Fig. 6.3(d)).

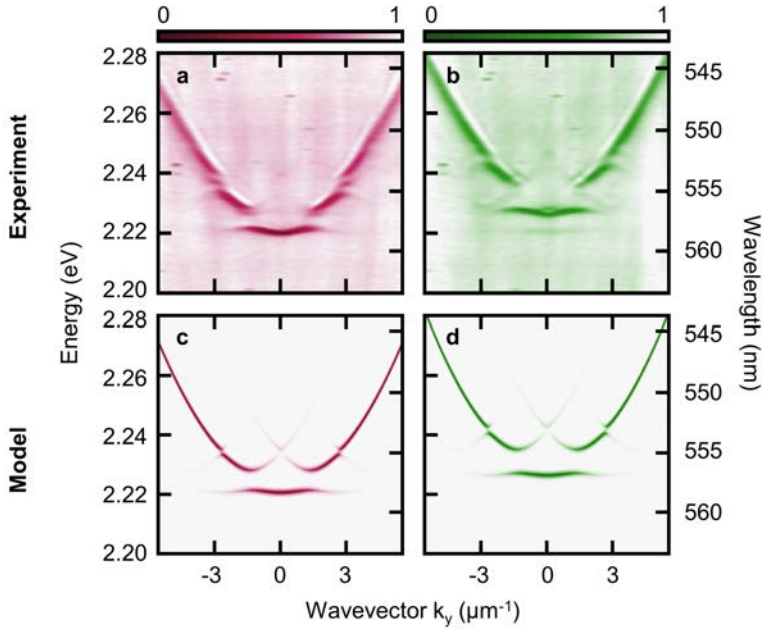

Figure 6.4: **Band Structure of ULH-LCMC A-type sample.** (a,b) Experimental normalized momentum-resolved reflectivity spectra measured along the k_y direction for horizontal and vertical polarization, respectively. (c,d) Corresponding simulations based on Hamiltonian (41).

Along k_x (thus $k_y = 0$), the observed bands in both polarizations are continuous, shifted in energy relative to each other, and multiple bands appear within the spectral window. Spectra measured along k_y (and $k_x = 0$) provide information on the nature of those bands. Here, for both H and V polarizations (Fig. 6.3(e,f), respectively), a very distinct band structures with photonic band gaps are visible. The lowest states are very flat (indicating a large effective mass), which signifies a deep localizing potential, whereas higher bands (such as the d-bands and above) exhibit noticeable curvature, indicative of lattice interaction.

To distinguish bands in both polarizations, I will use uppercase letters for polarization and subscripts for orbitals (e.g., H_s refers to the s-band in H polarization). Comparing the energy of the bands along k_x and k_y, it is evident that the higher bands in the k_x direction result from the periodicity of the potential in k_y direction. For instance, the continuous bands in H polarization in Fig. 6.3(b) at approximately 2.06 eV and 2.10 eV correspond to the H_d and H_g bands, with wavefunction distribution peaks at both $k_x = 0$ and $k_y = 0$.

The additional splitting of the H_p and V_s bands arises due to interband spin-orbit coupling, which will be introduced in the following section (these measurements were performed on a B-type sample).

One of the advantages of wedge-type ULH-LCMC is that the periodic texture formed across an entire macroscopic sample with multiple domains (as shown in Fig. 6.4), results in different photonic potentials with varying depths and periods (as the ULH period is directly related to the thickness of the cavity through the confinement ratio C). This property makes ULH an excellent platform for studying various photonic potentials without the need to prepare multiple samples.

Figure 6.4(a,b) presents the normalized momentum-resolved reflectivity spectra along k_y (from now on, all spectra in this chapter will be presented along k_y) for H and V polarizations, respectively,

for an A-type sample (without molecular tilt). The photonic potential was chosen to be shallow enough for the s-states to form a bands, as is evident from their curvature. Unlike in Fig. 6.3 (or in the next Figure 6.5), the energy gap between the s and p bands in the V polarization is larger than in the H polarization. This system thus provides a unique opportunity to study band structures that due to the polarization-dependent photonic potentials not only differ for the two linear polarizations, but can also swap their characteristics.

In general case, an effective Hamiltonian describing the cavity modes of two polarizations H and V in the polarization-dependent periodic potential created by the ULH, expressed in the (H, V) basis in real space, reads:

$$H_{cont} = \begin{pmatrix} -\frac{\hbar^2}{2m_H}\frac{\partial^2}{\partial y^2} + \frac{A_H}{2}[1-\cos(2qy)] - \frac{\delta}{2} & -2i\alpha\frac{\partial}{\partial y} \\ -2i\alpha\frac{\partial}{\partial y} & -\frac{\hbar^2}{2m_V}\frac{\partial^2}{\partial y^2} + \frac{A_V}{2}[1-\cos(2qy)] + \frac{\delta}{2} \end{pmatrix}, \tag{41}$$

where $\hbar$ is the reduced Planck constant, m_H, m_V are the effective masses for two orthogonally polarized cavity modes, δ is the linear birefringence, $q = 2\pi/p$, and p is the pitch of the ULH. $A_{H,V}$ are the potential amplitudes for H and V polarizations. The coefficient α describes the SOC resulting from the optical activity, which is zero for A-type sample.

Using the Hamiltonian (41) and the finite difference method, the experimental results were successfully modeled with good agreement (Figures 6.4(c,d)). It assume that the potential period for both polarizations is the same and equals 2.35 µm (corresponding to a pitch of 4.7 µm). The other modeling parameters are: $\delta = 5$ meV, $m_H = 2.42 \times 10^{-5} m_0$, $m_V = 2.24 \times 10^{-5} m_0$, $A_H = 6.9$ meV, $A_V = 8.2$ meV.

Changing the position on the sample is one way to modify the periodic potential. However, a more practical approach—allowing for systematic control of the band structure—is the application of an electric voltage. Let us first consider how an applied electric field should microscopically affect the ULH molecules.

The director distribution in the absence of an external voltage naturally consists of a perfectly aligned ULH along the y axis, with superimposed director fluctuations around this ideal orientation (Figure 6.5(a)) [222]. The effective refractive index distribution, obtained by averaging along the z axis for both polarizations, is shown in Figure 6.5(c) in the form of effective refractive index ellipses. The analysis is simplified by considering only the refractive index distribution for the perpendicular direction. This assumption is justified by the small incidence angles of the probe light and the excellent qualitative agreement with experimental results.

Notably, only the H polarization (pink, along the x axis) exhibits a periodic variation of the refractive index, whereas the V polarization (green, along the y axis) remains constant. This results in energy gaps present only for the H polarization and a continuous dispersion for the V polarization, as illustrated in the right part of Figure 6.5(a).

When a non-zero voltage (AC) is applied, the molecules inside the microcavity reorient according to the dielectric effect [223, 224]. This induces a spatially non-uniform suppression of thermal fluctuations and a spatially non-uniform realignment of the average (fluctuation-free) director orientation (Figure 6.5(a-d)). As a result, the refractive index contrast gradually increases for both polarizations, deepening the photonic potentials, opening a gap for the V polarization, and further increasing the existing gap for the H polarization (Figure 6.5(d)). Additionally, the narrowing of the trapping potential (middle region in Figure 6.5(c,d)) shifts the modes toward higher energies. A more detailed description is provided in Section I.A of [225].

The normalized momentum-resolved reflectivity spectra confirm these expectations. Without an applied voltage (Figure 6.5(e,h)), a band gap is visible only for the H polarization, while the

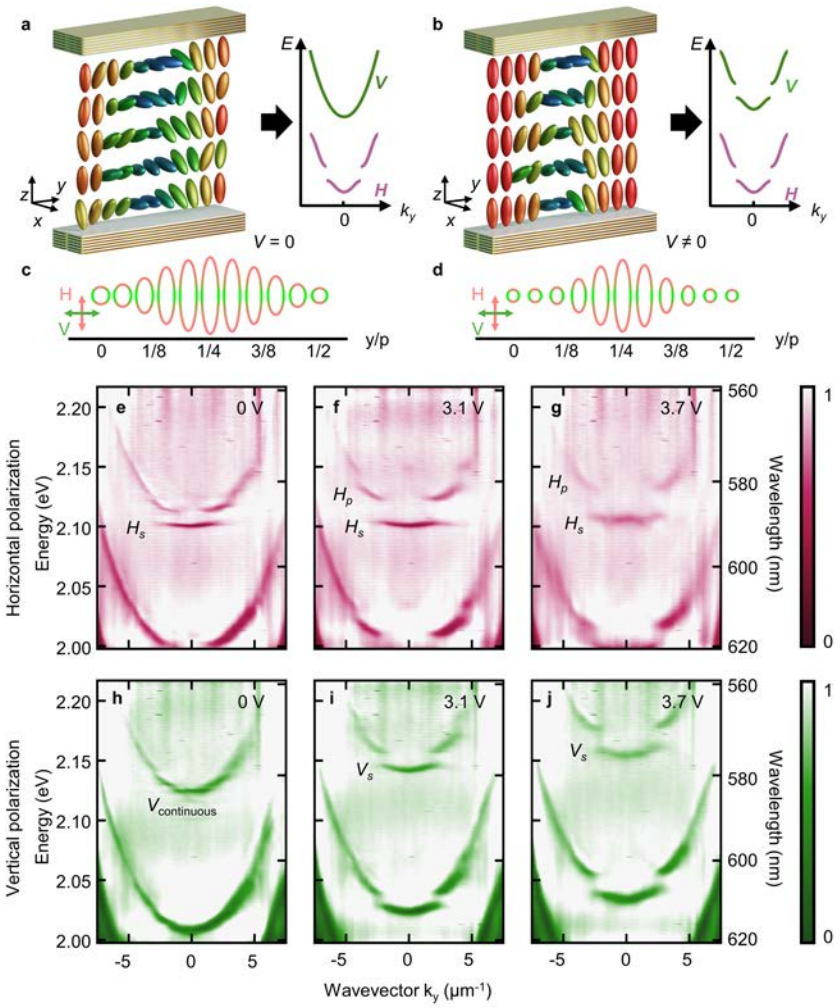

Figure 6.5: **Tunable Band Structure.** Illustrative representation of the LC director arrangement inside the microcavity and the corresponding schematic dispersion relations for the horizontal (H, pink) and vertical (V, green) modes: (a) at zero voltage and (b) at non-zero voltage. Effective refractive index ellipses for H and V polarizations, showing periodic dependence along the ULH axis y over half pitch p, obtained by averaging the director distributions shown in (a) and (b) along the microcavity axis z for (c) zero voltage and (d) non-zero voltage. Momentum-resolved reflectivity spectra of (e–g) horizontally and (h–j) vertically polarized band structures measured for different voltages (indicated in the top-right corners) applied to the A-type sample.

V polarization spectrum remains gapless (within the spectrometer resolution and line broadening). The symmetric H_s band is observed in the H polarization at $E \approx 2.1$ eV.

Under an applied voltage, an energy gap emerges in the V polarization as well (Figure 6.5(i,j)), increasing from 0 meV at 0.0 V to 20 meV at 3.7 V. Additionally, the entire band structure in the V polarization shifts toward higher energies. The gap for the H polarization also increases, from 12 meV at 0.0 V to 25 meV at 3.7 V (Figure 6.5(f,g)). Besides the symmetric s-band, another gap

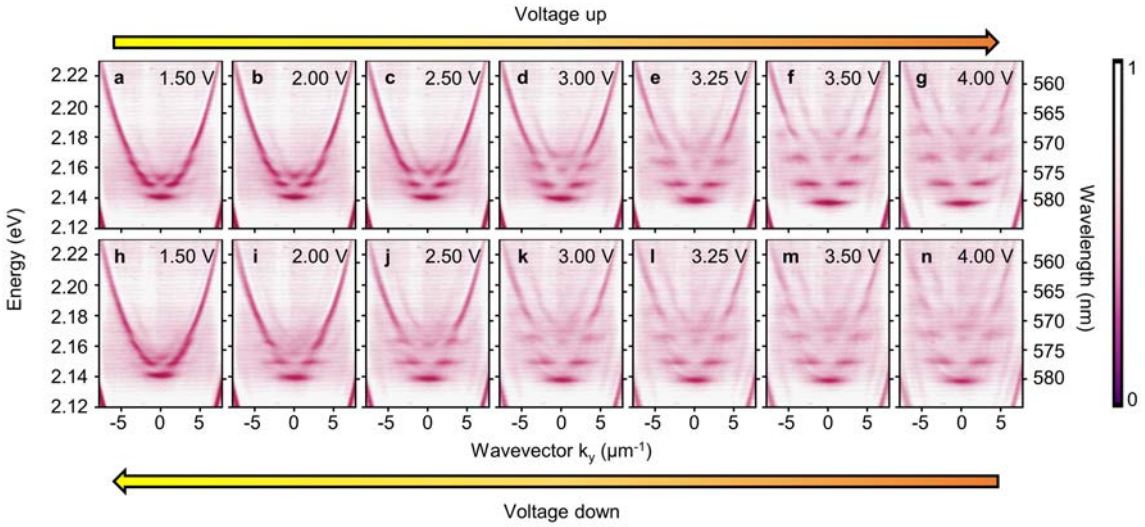

Figure 6.6: **Tunability of the Horizontally Polarized Band Structure.** Normalized momentum-resolved reflectivity spectra measured for (a-g) increasing and (h-n) decreasing voltage. The voltage values are indicated in the top-right corners, and the voltage scan directions are shown with arrows.

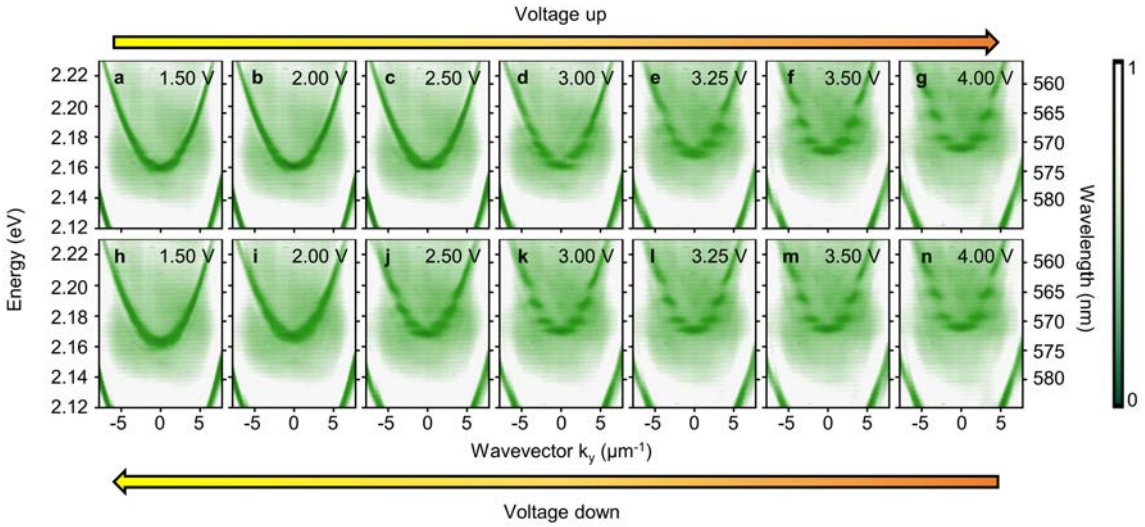

Figure 6.7: **Tunability of the Vertically Polarized Band Structure.** Normalized momentum-resolved reflectivity spectra measured for (a-g) increasing and (h-n) decreasing voltage. The voltage values are indicated in the top-right corners, and the voltage scan directions are shown with arrows.

opens at higher energies (around 2.14 eV), forming an additional antisymmetric H_p band.

To further demonstrate the reversible tunability of both H and V band structures, Figure 6.6 and Figure 6.7 present a complete voltage cycle, first increasing the voltage (top rows of both figures)

and then decreasing it (bottom rows) at a second position on the sample. The results reveal precise control and multiple band gap openings in both polarizations. The gap-opening process is fully reversible, as liquid crystal director fluctuations recover once the applied voltage is removed - at 1.5 V, both at the beginning and end of the cycle, the band structure shows no significant change. Therefore, it has demonstrated that A-type samples exhibit on-demand reconfigurability of the band structures.

6.2 Interband Spin-Orbit Interaction

In the previous section, the strong optical activity of the cholesteric LC helix in A-type Sample was suppressed by the presence of the cavity, preserving inversion symmetry [225]. As a result, in the Hamiltonian (41), α—and consequently the off-diagonal coupling terms between the H and V modes—were equal to zero. This allowed both band structures to be treated independently. However, when inversion symmetry is broken, the two linear polarizations should couple via an antisymmetric SOC term, which, in simplest approximation, is linear. To investigate the impact of broken inversion symmetry on the band structures of ULH-LCMC, this section presents results for B-type Sample, where the effective refractive index possesses a non-zero component along the y direction.

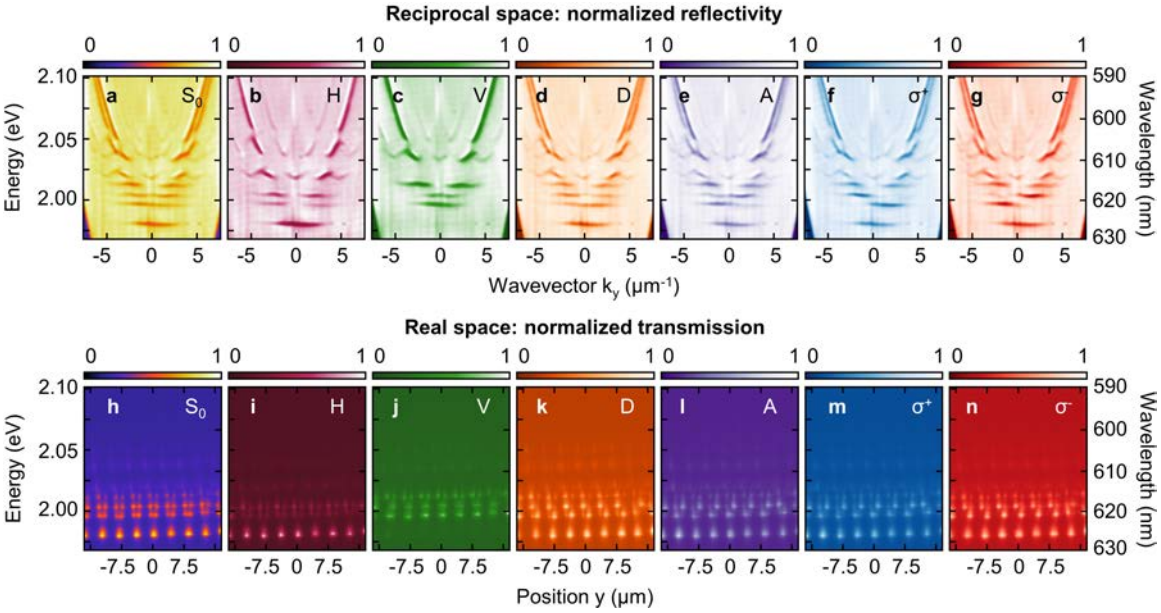

Figure 6.8: **Polarization Properties of B-Type Sample Band Structure.** Normalized momentum-resolved reflectivity spectra measured for (a) total intensity (S_0 Stokes component), (b) horizontal, (c) vertical, (d) diagonal, (e) antidiagonal, (f) σ^+, and (g) σ^- polarization. (h-n) Corresponding spatially-resolved transmission spectra.

Figure 6.8 presents normalized momentum-resolved reflectivity spectra (top panel) and spatially-resolved transmission spectra (bottom panel) collected for total intensity and three pairs of orthogonal polarizations on Sample B. The total intensity momentum-resolved spectrum in Figure 6.8(a) reveals well-separated bands with shapes similar to those in Figure 6.3. However, the band structure

exhibits an unusual ladder of states, particularly the presence of two flat bands around 2 eV. To understand this, it is essential to compare the band structures for H and V polarizations.

Starting with horizontal polarization (Fig. 6.8(b)), the lowest symmetric band, H_s, appears around 1.98 eV. At approximately 2 eV, where the antisymmetric H_p band would be expected, two bands with minima at $k_y = 0$ are observed instead. At higher energies (2.025 eV and above), additional bands appear, resembling the expected d-band (2.025 eV) and f-band (2.04 eV).

In the V polarization (Figure 6.8(c)), the lowest band appears to split around 2 eV, while higher-energy bands follow a more conventional band structure, consistent with the results from previous section. This suggests an interaction between the H_p and V_s bands.

The D and A spectra (Figures 6.8(d,e)) resemble the total intensity S_0, as they represent the sum of H and V polarizations. However, the intensity distribution of the mixed states becomes particularly intriguing in circular polarizations (Figures 6.8(f,g)). The alternating pattern observed in these mixed states strongly indicates the presence of coupling.

Figures 6.8(h-n) show the spatially-resolved spectra. By comparing the energies between the top and the bottom panels, one can determine the real-space distribution of the bands. The alternating pattern seen in Figures 6.8(f,g) is clearly visible not only in P and M polarizations but also in D and A polarizations (Figures 6.8(k-n)).

Since the SOC term is an odd function of k, it only couples bands of different parity. This coupling leads to the emergence of new mixed states. For instance, in the case of the symmetric V_s band and the antisymmetric H_p band, this interband spin-orbit interaction (ISOC, to distinguish it from the SOC between continuous modes in a planar cavity) generates new mixed bands with a quadrupolar circular polarization pattern, as schematically illustrated in Figure 6.9(a).

In this regime, one can take a step further and derive from the continuous Hamiltonian (41) a tight-binding Hamiltonian describing the ISOC between two bands (Details on the derivation and explicit expressions can be found in Section IV [225].

The corresponding tight-binding Hamiltonian reads:

$$H = \begin{pmatrix} E_{H_p} - 2t_{pp}\cos\left(k_y p/2\right) & -i\alpha\left[t_{sp,0} - 2t_{sp,1}\cos\left(k_y p/2\right)\right] \\ c.c. & E_{V_s} - 2t_{ss}\cos\left(k_y p/2\right) \end{pmatrix}, \tag{42}$$

where E_{H_p} and E_{V_s} are the onsite energies of H_p and V_s, respectively. The parameters t_{pp} and t_{ss} represent the nearest-neighbor couplings between the p states of H and the s states of V, respectively, $t_{sp,0}$ and $t_{sp,1}$ correspond to the onsite and nearest-neighbor couplings between H_p and V_s (ISOC terms), respectively. All coupling parameters are derived from the Hamiltonian (41) (including the ISOC terms) using standard perturbation theory based on the s and p states of a harmonic oscillator.

The tight-binding Hamiltonian advantage over the general continuous Hamiltonian is that since it considers only the two bands, its size is reduced to 2×2, making it easier to predict results from the included terms and significantly faster the computations.

The momentum-resolved spectra of the Hamiltonian (42), expressed in terms of the Stokes parameters S_1 and S_3 ($S_2 = 0$ everywhere) in the limit of strongly localized modes ($\alpha t_{sp,1},\ t_{ss},\ t_{pp} \ll \alpha t_{sp,0}$), are shown in Figures 6.9(b,c), respectively. To confirm the theoretical prediction, Figures 6.9(d-f) present the Stokes components S_1, S_2, and S_3 based on the experimental results in Figures 6.8(b-g). A good agreement between experiment and theory is observed, particularly in the characteristic quadrupolar pattern of S_3.

Furthermore, Figures 6.9(g,i) illustrate a model beyond the tight-binding approximation, based on a semi-analytical solution of Maxwell's equations [226]. This approach utilizes the Fourier decomposition coefficients of the dielectric tensor of the cavity material as fitting parameters (details can be found in Section V [225]). Although this method allows for highly accurate reconstruction of the entire band structure, it requires consideration of multiple modeling parameters.

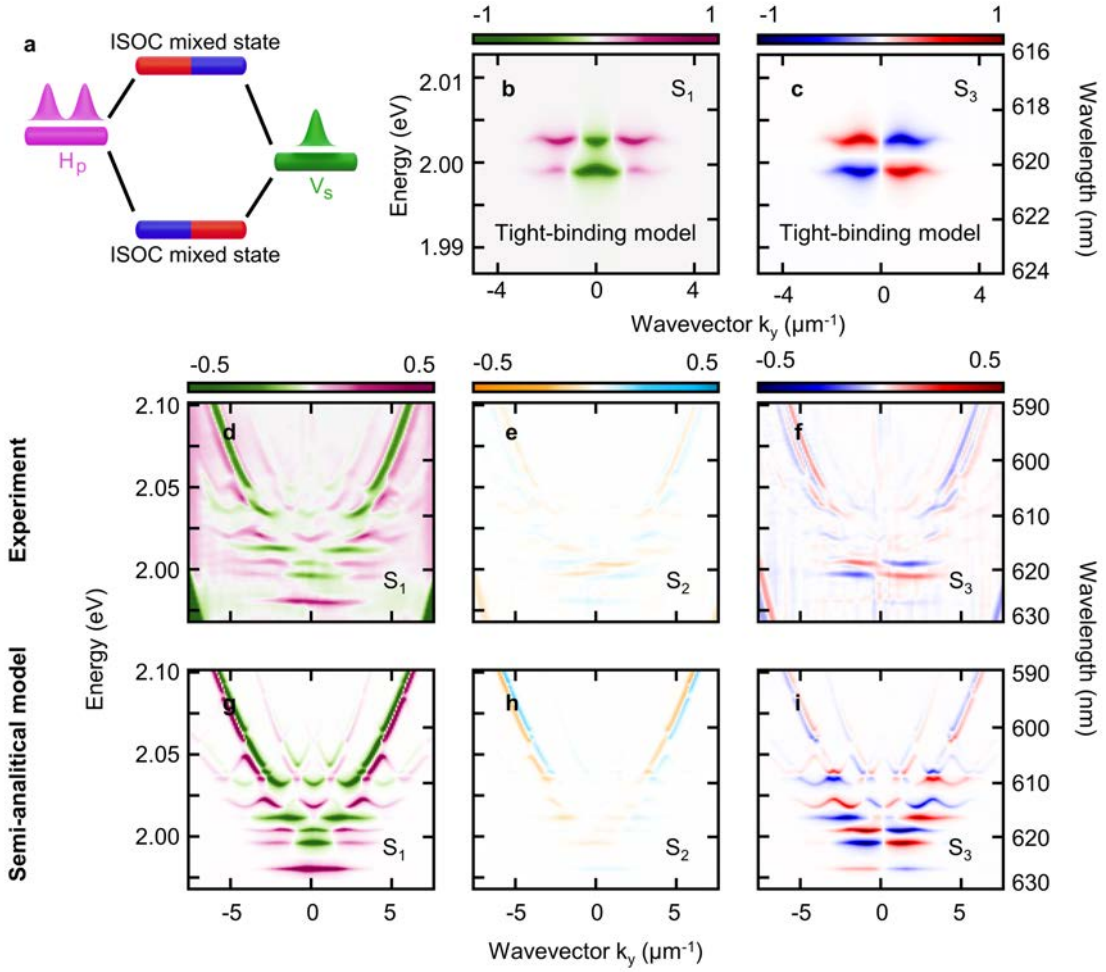

Figure 6.9: **Interband Spin-Orbit Coupling in ULH LCMC.** (a) A scheme of hybridization. *sp*-hybridized bands obtained from the tight-binding Hamiltonian (3) with colors corresponding to (b) S_1 and (c) S_3 Stokes parameters ($S_2 = 0$ everywhere). (d-f) Experimental momentum-resolved reflectivity spectra expressed by Stokes parameters S_1, S_2, and S_3, respectively. (g-i) Corresponding semi-analytical model. ISOC-mixed eigenstates appear near 2.0 eV as a result of coupling between the *p*-band of horizontal polarization and the *s*-band of vertical polarization. Calculations in (b,c) were performed by Pavel Kokhanchik, and calculations in (g–i) were performed by Przemysław Oliwa.

The H_p and V_s bands are not the only bands of opposite parity present in the spectrum, so ISOC is expected to couple other bands as well, as predicted by Figure 6.9(i). Depending on the photonic potential (which defines coupling constants and detunings), the interaction strength varies for different bands. In the studied samples, the H_p and V_s bands most frequently exhibited strong ISOC. However, as demonstrated in Figure 6.12(b,h,n) (which will be discussed later), the semi-analytical model predictions that other pairs of bands with opposite parity can couple via ISOC are correct.

Since the experimental measurements were performed in reflectivity configuration, and the cavity mode depth (due to LC scattering and other losses) reaches at most several dozen percent, determining accurate Stokes parameter values (and thus its contrast) in reflectivity is challenging. It requires a sophisticated normalization method or the subtraction of inhomogeneous background signals, which might heavily distort the spectrum. One can see that in Figures 6.8(f,g) the ISOC mixed states appear nearly completely circularly polarized, yet the contrast of the Stokes parameter S_3—which should reach unity (Figure 6.9(f))—is not as high as, for example, in real-space transmission data (Figure 6.10(f)). Transmission measurements also have drawbacks, such as typically broader linewidths, but do not require such a complicated normalization. However, based on the experience gained during my PhD, if I were to repeat these measurements (or advise future experimentalists), I would recommend measuring reciprocal space of LCMC using white-light transmission, as is already done in the next chapter.

Previously, it was mentioned that B-type samples exhibit broken inversion symmetry. Figure 6.10(a) presents the director distribution of ULH within such cavities proposed by Pavel Kokhanchik that fulfills this assumption, based on two main observations.

Firstly, the POM images obtained for the B-type sample (Figure 6.2(f)) correspond very well to the numerically simulated ones found in the literature (Fig. 7 in [227]) for the tilted ULH molecular distribution. Both POM images exhibit a dimerized pattern, characterized by bright (red) lines splitting into pairs separated by wide dark zones.

At the same time, the POM image for the A-type sample obtained in the experiment (Figure 6.2(e)) closely matches the POM image for a standard (non-tilted) ULH director distribution taken from [227]. Notably, neither of these images show a dimerized pattern. This comparison confirms a key difference between the director distributions in A-type and B-type samples: the director distribution is tilted in B-type samples but remains unperturbed in A-type samples.

Secondly, the director distribution shown in Figure 6.10(a) phenomenologically describe the key experimental findings. These principal observations include: the presence of ISOC, the presence of a periodic potential for both polarizations even at zero voltage, and the spatial coincidence of potential minima and maxima for both polarizations, as confirmed by real-space spectroscopy in Figure 6.10(d). The proposed director distribution explains these features as follows. As demonstrated in Section IV of [225] through Maxwell's equation solutions, and in Section I.B of [225] via symmetry analysis, ISOC can only emerge when the helix is combined with a molecular tilt produced by rotation around the x-axis. The coincidence of potential maxima for both polarizations implies that molecules must predominantly align along the z-axis at these spatial positions (edges of the distribution in Figure 6.10(a), represented by vertical red ellipsoids). Similarly, the coincidence of potential minima for both polarizations requires that molecules deviate significantly from the z-axis, resulting in increased effective in-plane refractive index components along both x and y directions (middle of the distribution in Figure 6.10(a), depicted as tilted and rotated ellipsoids in green and blue). Wide dark lines in the POM image (Figure 6.2(f)) correspond to potential maxima (edges of the director distribution in Figure 6.10(a)), whereas each pair of bright red lines corresponds to a potential minimum (middle of the distribution in Figure 6.10(a)). Finally, the homeotropic anchoring condition ensures that the director orientation remains vertical (red ellipsoids) near the cavity mirrors.

From a fabrication perspective, both A- and B-type samples were prepared using the same temperature protocol for ULH growth, explaining their similar pitch values. However, A-type sample A was fabricated using the nematic host LC2091*, whereas B-type sample utilized E7. These two liquid crystals exhibit vastly different viscosities. Since the mixture undergoes flow within the cavity during ULH growth, the viscosity of the nematic host plays a crucial role in stabilizing the director distribution. After examining multiple nematic hosts, it was found that the viscosity difference in

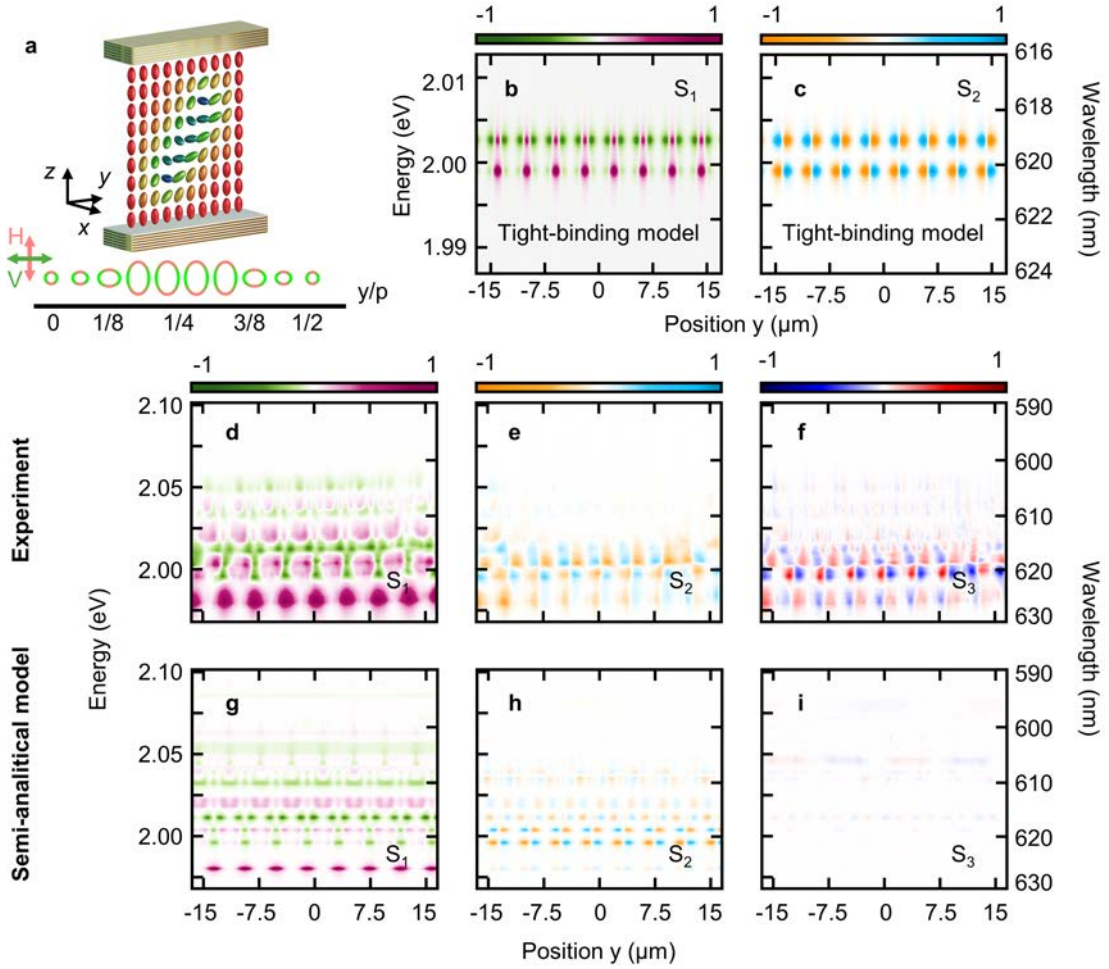

Figure 6.10: **Spatially-Resolved Spectra of B-Type ULH-LCMC Sample.** (a) (top) Illustration of the LC director distribution inside the microcavity and (bottom) effective refractive index ellipses. Spatially-resolved spectra obtained from the tight-binding Hamiltonian (Eq. 2) with colors corresponding to (b) S_1 and (c) S_2 Stokes parameters ($S_3 = 0$ everywhere). (d–f) Experimental spatially-resolved transmission spectra expressed by the Stokes parameters S_1, S_2, and S_3, respectively. (g–i) Corresponding semi-analytical model. Calculations in (b, c) were performed by Pavel Kokhanchik, and calculations in (g–i) were performed by Przemysław Oliwa.

E7 affects the flow dynamics during ULH growth, inducing a pretilt in the director configuration that is absent in the LC2091-based A-type sample.

The Stokes parameters of the spatially-resolved spectrum are shown in Figure 6.10(b-i), following a similar panel arrangement as in Fig. 6.9. The lowest energy states in Figures 6.10(d,g) reveal the spatial periodicity of the refractive index, corresponding to half of the ULH pitch. A checkerboard pattern, similar to that observed in Figure 6.9(f), appears in the Stokes parameter S_2 (Figure 6.9(c,e,h)) for *sp*-hybridized states at energies around 2 eV, further confirming the presence of ISOC.

In the tight-binding model, $S_3 = 0$ in real space, since the polarization component S_3 in real space corresponds to S_2 in momentum space (and vice versa). This behavior is also observed in the semi-analytical model, where S_3 in real space is nearly zero, just like in momentum space in Figure 6.9(h). However, in the experiment, the S_3 component in real space is surprisingly strong, suggesting interactions with different cavity modes. This discrepancy arises from the fact that the cavity is multimodal, a factor that neither the tight-binding nor the semi-analytical model accounts for. The second reason is the non-zero k_x components probed by light (excitation beam has a finite size in reciprocal space due to the finite aperture of the excitation objective). These components can lead to couplings in circular polarizations [225], whereas both models assume only normal incidence.

It is crucial to emphasize the fundamental difference between SOC in a planar cavity and ISOC in ULH-LCMC. In contrast to the previous chapters and earlier studies on SOC in birefringent cavities, where the opposite parity of states was satisfied by coupling even and odd H and V modes [2, 228], here, the cavity modes share the same parity (the (N, N) regime). Consequently, in a planar cavity, SOC would not be observable. The required odd-parity coupling is instead achieved through band quantization—two modes of the same parity form symmetric and antisymmetric bands, which then undergo ISOC interactions.

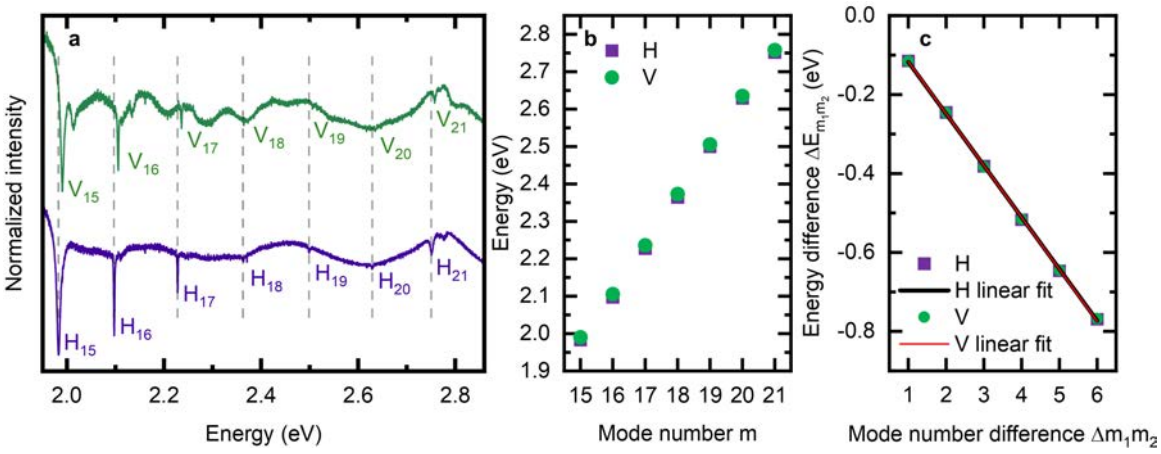

Figure 6.11: **Determination of the Photonic Mode Number and LCMC Regime.** (a) Normalized reflectivity spectra measured at normal incidence for horizontal (purple) and vertical (green) polarization, plotted with an offset. Gray dashed lines indicate the peak positions of the horizontal modes for comparison. (b) Peak position as a function of mode number for both polarizations. (c) Energy difference between the 15th and subsequent modes versus mode number difference. Black and red lines represent linear fits to the data for horizontal and vertical polarization, respectively. The analysis clearly demonstrates that the results are obtained in the (N, N) regime.

To confirm that the system is indeed in the (N, N) regime, Figure 6.11(a) presents normalized reflectivity spectra for H (violet) and V (green) polarizations at normal incidence, measured over a broad spectral range covering nearly the entire stopband for the B-type sample (waterfall plot). Gray dashed lines indicate the energies of the H modes. Wherever the V modes are sufficiently deep, one can see that their energy is consistently shifted by a similar value relative to the H modes. Figure 6.11(b) shows the energies of the H and V modes as a function of the determined mode number. The energies of shallow V modes were extracted from momentum-resolved spectra (not shown), where they were easier to estimate. It is evident that the V mode energy is always higher

than that of the H modes, as expected for the (N, N) regime with minimal detuning Δ_{HV}. The mode numbers were determined using the method described in Section 2.2.3, based on the slope of the linear fit to the difference between the energies of two modes as a function of the difference in the mode numbers (Figure 6.11(c)).

The second evidence distinguishing SOC from ISOC is shown in Appendix A, Figure 9.5, which discusses an artificial one-dimensional photonic lattice made with a focused ion beam combined with a nematic LCMC. Although the microscopic origin of ISOC differs in this case (tilt of the helix versus interactions with modes of higher orders), the resulting effects are similar and arise due to the quantization of bands. Furthermore, this system allows voltage-controlled exploration of two regimes: $(N, N+1)$ and $(N, N+2)$. Notably, only in the $(N, N+2)$ regime does the characteristic quadrupole pattern of ISOC emerge.

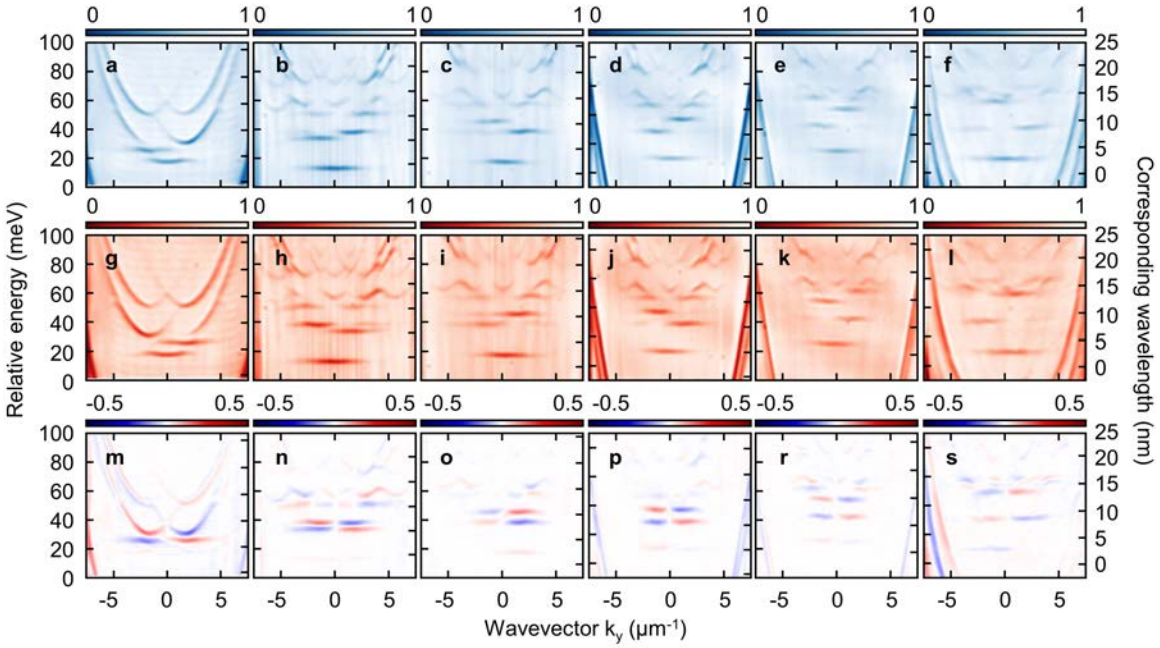

Figure 6.12: Δ_{HV} **Detuning Dependence on ISOC.** Normalized momentum-resolved reflectivity spectra in (a–f) σ^+, (g–l) σ^-, and (m–s) S_3 Stokes parameter measured at different positions on the sample.

Because of the wedge configuration, B-type samples can exhibit different photonic potentials depending on the position on the sample. This variation can affects the ISOC. Figure 6.12 presents normalized momentum-resolved reflectivity spectra measured in σ^+ (top panel), σ^- (middle panel), and both circular polarizations expressed as the Stokes parameter S_3 (bottom panel). The spectra were obtained at different positions on the sample, each corresponding to different photonic potentials, and are arranged in order of increasing separation between the mixed ISOC bands (detuning $\Delta_{H_pV_s}$).

Since the cavity width varies across the sample, the spectra are plotted on a common relative energy scale with an arbitrary offset for each position. It is evident that the effective masses of bands can vary—from shallow potentials, where the s-bands still exhibit noticeable curvature (Figs. 6.12(a,g,m)), to deep potentials with strongly localized flat bands. In each case, the structure

of ISOC spectra for the lowest bands remains the same: no coupling for the lowest band, followed by a quadrupole pattern for the next two mixed bands of opposite symmetry. As expected, as the $\Delta_{H_pV_s}$ increases, the interaction strength decreases (manifested as a decreasing of the Stokes vector S_3 value).

An intriguing observation is that the ISOC sign can also change. For instance, in Figures 6.12(o,s), the higher-energy ISOC-mixed band exhibits a positive Stokes vector value for positive wavevectors, opposite to the behavior observed in other positions. There are two possible mechanisms responsible for this sign change: a change in the $\Delta_{H_pV_s}$ sign (see Appendix A and ISOC control via voltage, Figure 9.5) and a change in the effective director distribution of the LC. In this case, the direction (positive or negative sense) of the molecular tilt of the LC along y from Figure 6.10(a) will determine the sign of ISOC.

A similar effect can be achieved in a planar cavity by changing the chirality of the dopant, causing the LC molecules to align differently under the applied voltage. Alternatively, flipping the sample 180 degrees along the x-axis would yield the same result.

Both mechanisms will have the same result. Regardless of the underlying cause, this dependence of the ISOC sign demonstrates an additional degree of control over the band structure of ULH-LCMC.

6.3 Polarization-Conserving Lasing

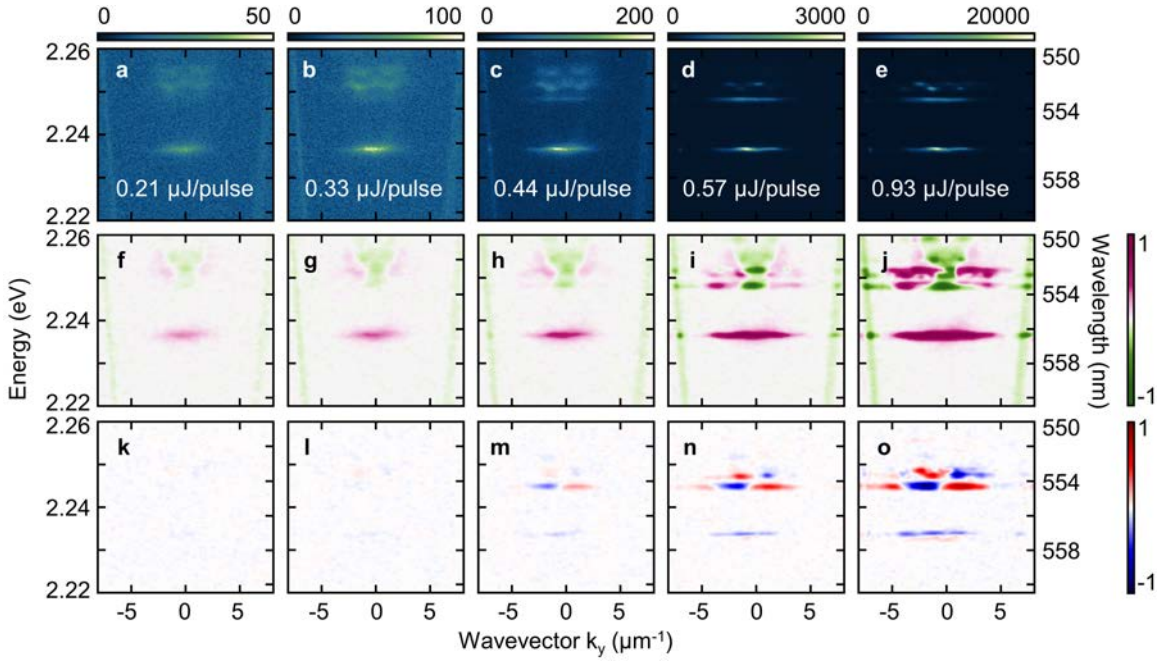

Figure 6.13: **Polarized Lasing from ISOC Mixed States.** (a–e) Momentum-resolved emission spectra collected for different excitation pulse energies, labeled at the bottom. Corresponding spectra expressed by (f–j) S_1 and (k–o) S_3 Stokes parameters.

Since the cavity contains P580 dye, nanosecond excitation allows for the observation of photon lasing in the weak light-matter coupling regime. Figure 6.13 presents momentum-resolved emission

spectra collected for different excitation pulse energies. The top panel shows total intensity spectra, the middle panel express emission in terms of the Stokes vector S_1, and the bottom panel the Stokes vector S_3.

At low excitation energies (Figs. 6.13(a,b)), spontaneous emission from the lattice bands is observed, exhibiting linear polarization consistent with previous reflectivity results for type-B samples (Figs. 6.13(f,g)). The degree of circular polarization is very low (Figs. 6.13(k,l)).

At the lasing threshold (Fig. 6.13(c,h,m)), an increase in emission from the H_s band occurs. Interestingly, the lower ISOC-mixed state at 2.248 eV, which had a weaker spontaneous emission signal compared to other bands, reaches the lasing threshold almost simultaneously with the H_s band. This results in a significant enhancement of its visibility in the Stokes parameter S_3 spectrum (Fig. 6.13(m)).

Further increasing the excitation energy leads to a sudden increase in emission and to reaching the lasing threshold for other bands (Figs. 6.13(d,e)). This also results in high values of the Stokes parameters S_1 and S_3 Stokes parameters (Figs. 6.13(i,j,n,o)), demonstrating that lasing inherits the polarization of the bands.

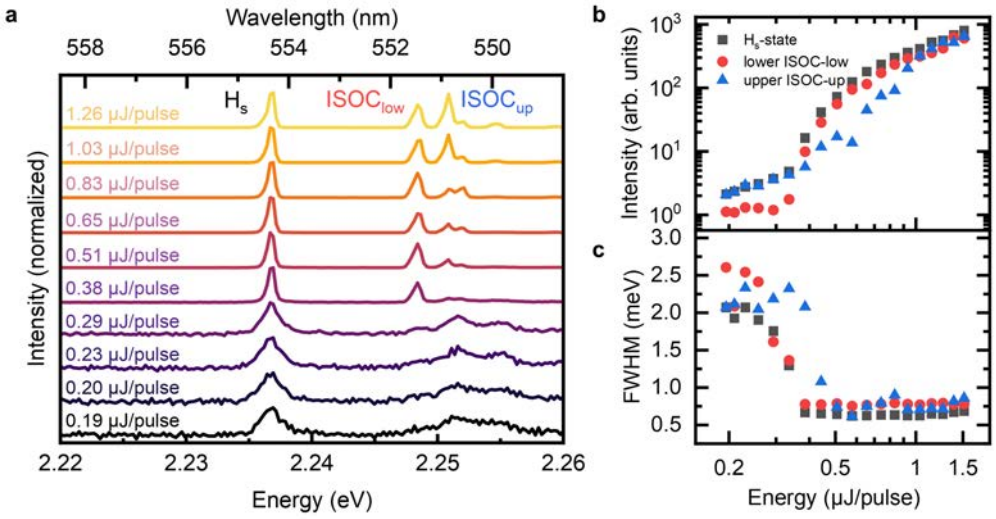

Figure 6.14: **ULH-LCMC Lasing.** (a) Normalized PL spectra, plotted with an offset, collected at normal emission for different excitation pulse energies labeled on the left. Peaks corresponding to the horizontal s-state and the lower and upper ISOC mixed states are indicated as H_s, $\mathrm{ISOC_{low}}$, and $\mathrm{ISOC_{up}}$, respectively. (b) Peak intensity and (c) linewidth as a function of excitation pulse energy for these three peaks, extracted by Lorentzian fitting. Gray squares represent H_s, red circles denote $\mathrm{ISOC_{low}}$, and blue triangles correspond to $\mathrm{ISOC_{up}}$.

To better illustrate lasing in ULH-LMCM, Figure 6.14(a) presents the evolution of normalized spectra collected at normal emission on a waterfall plot, with excitation energy labeled on the left. At the lasing threshold of the two lowest bands (approximately 0.38 μJ/pulse), the linewidth of both bands narrows, and the intensity of the lower ISOC-mixed band ($\mathrm{ISOC_{low}}$) increases significantly compared to the other peaks, similar to what is observed in the momentum-resolved spectra (Fig. 6.13(c)).

Based on Lorentzian fits to the emission peaks, the dependence of intensity (Fig. 6.14(b)) and linewidth (Fig. 6.14(c)) on the excitation pulse energy for the three lowest bands was plotted. The curves corresponding to the H_s band (gray squares) and the lower ISOC-mixed band (red circles) have similar shapes and reach the lasing threshold almost simultaneously. The upper ISOC-mixed band (blue triangles), although more intense than the lower ISOC band in the spontaneous emission regime, reaches the threshold at slightly higher excitation energy (around 0.5 μJ/pulse), and the nonlinear increase in emission intensity is smaller. At high excitation energies (above 1 μJ), all three bands reach saturation with similar intensities.

It is worth mentioning that the presented results correspond to a scenario in which the spectral profile of the high gain of the emitter covers the energy of lasing bands (see Figure 4.8). By controlling the detuning between the gain and a given band (e.g. by changing the position on the wedge-type cavity), it is possible to slightly influence which part of the spectrum reaches the lasing threshold first.

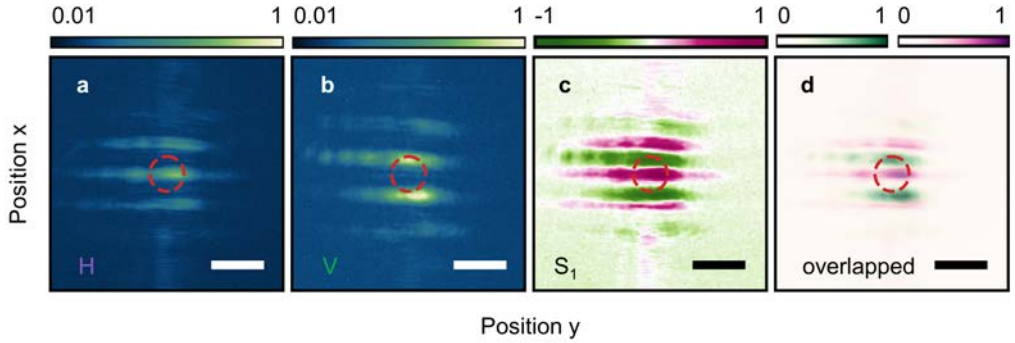

Figure 6.15: **Real-space Lasing Profile Modified by ULH Photonic Potential.** (a, b) Real-space emission collected above the lasing threshold for horizontal and vertical polarization, respectively, plotted on a logarithmic scale. The same signals are (c) expressed by the S_1 Stokes parameter and (d) overlapped, where green corresponds to vertical polarization and purple to horizontal polarization. The red dashed circle marks the excitation spot. Scale bar: 5 μm.

By using this feature of ULH-LCMC, it is possible to achieve lasing that predominantly occurs at the two ISOC-mixed bands. As seen in Figures 6.10(b,d,g), the linear polarization distribution of these bands is modulated in real space.

Figure 6.15 presents real-space images collected above the lasing threshold at such a case, measured in H and V polarizations (Figs. 6.15(a,b), respectively). The intensity profiles of both polarizations form shifted stripe patterns, which, when expressed in the Stokes parameter S_1 (Fig.6.15(c)), create a texture resembling PSH. This effect is evident when both images are overlapped (Fig. 6.15(d)).

This is just one example of how the diversity of photonic potential landscape in ULH-LCMC, combined with a high degree of control, enables the creation of unique polarization lasing patterns.

The proposed device may have applications in light propagation. Liquid crystals are widely used as diffraction optical elements [229–231], and ULH structures also find applications in beam steering and holography [221, 232]. Interestingly, lasing within the cavity also exhibits directional scattering induced by interaction with the periodic potential of ULH.

Figure 6.16 presents four normalized real-space emission images collected above the lasing threshold. These images reveal that in both H-polarization (Figs.6.16(a,b)) and V-polarization (Figs.6.16(c,d)), light jets form along directions perpendicular to the periodicity of the potential, marked by white,

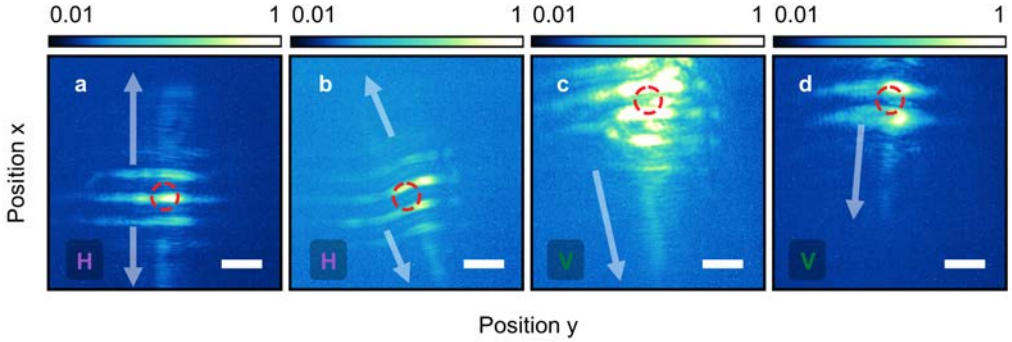

Figure 6.16: **Light Waveguiding Perpendicular to the Periodicity of the ULH-Based Potential.** Real-space emission collected above the lasing threshold for four different positions on the sample for (a, b) horizontal and (c, d) vertical polarization, plotted on a logarithmic scale. White, transparent arrows indicate the light jet formed by diffraction on the periodic potential. The red dashed circle marks the excitation spot. Scale bar: 5 µm.

semi-transparent arrows. Although their intensity is relatively low (the images are shown on a logarithmic scale), the propagation length of these jets significantly exceeds that of homogeneous lasing emission. In Fig. 6.16(c), the jet extends nearly 20 µm from the lasing source, compared to the non-directional lasing area of approximately 8 µm.

This phenomenon presents intriguing possibilities for waveguiding of light or exciton-polaritons, enabling information transfer between latice sites, the formation of supermodes that extend lasing states via multi-spot excitation [233], and selective excitation of specific defects within the ULH structure (see the next section).

6.4 Topological Defects

The results presented in the previous sections were obtained in regions where the ULH texture formed a well-ordered periodic potential for light. However, entire branches of physics explore how defects and the resulting defect states give rise to fascinating phenomena in fields such as photonic crystals [234, 235], semiconductors [236], magnetic systems [237, 238], superconductivity [239], and many others.

In liquid crystals, a wide range of topological defects is well-documented [39, 40], leading to intriguing physical effects, like the generation of optical phase singularities [240], random lasing [241], and a cascade of spontaneous symmetry breaking [242]. Moreover, liquid crystal defects offer an interesting platform for simulating biological and cosmological phenomena [243, 244].

In the next section and throughout the following chapter, several topological defects that emerge within the ULH structure will be presented.

In the previous chapters, samples was excited using pulsed lasers, which allow for high peak energy over short timescales, enabling lasing thresholds to be reached while minimizing heat deposition. The use of a focused *cw* laser with high power density allows for *in-situ* creation a localized defect that acts as a photonic trap for light.

Figure 6.17 illustrates the trap-creation process using a *cw* laser ($\lambda = 532$ nm, power of 160 µW and a beam diameter of approximately 2 µm) on a A-type sample. Figures 6.17(a,b) show real-space white-light reflectivity images of the sample surface before and after 30 seconds of laser illumination, respectively. The weak contrast in the images results from high NA detecting objective and the use

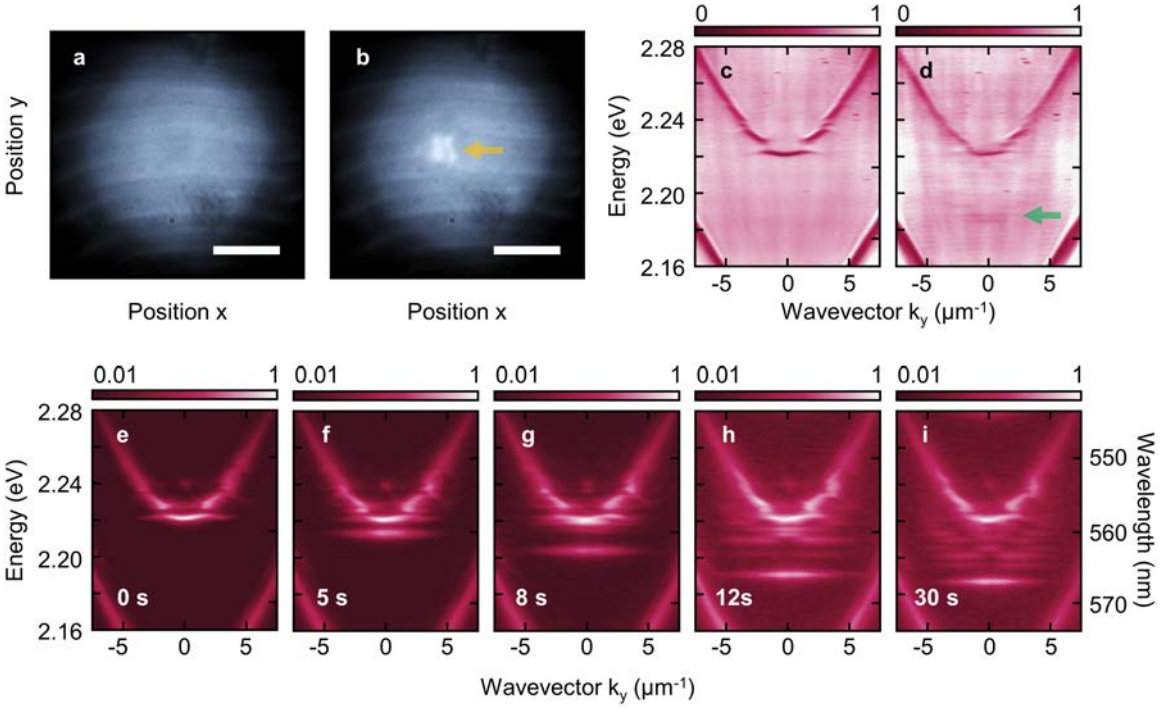

Figure 6.17: **On-Demand *In Situ* Formation of a 0D Photonic Trap by *cw* Laser.** (a,b) Real-space reflectivity images before and after illumination, respectively. The yellow arrow marks the created defect. Scale bar: 10 μm. Normalized momentum-resolved reflectivity spectra (c) before and (d) after illumination. The green arrow marks localized states. (e–i) Momentum-resolved spontaneous emission spectra collected for different illumination times, labeled in the bottom left corner, plotted on a logarithmic scale. Data collected for horizontal polarization.

of unpolarized light. Before laser illumination, a uniform ULH stripe pattern is observed, whereas after light exposition, a defect comparable in size to the laser spot appears.

Normalized momentum-resolved reflectivity spectra collected in H polarization (Figs. 6.17(c,d)) confirm these observations. Before illumination, a well-defined band structure with H_s and H_p bands is visible. After laser exposure, the bands become distorted (as the white-light reflectivity spot of approximately 10 μm mostly probing the defect), but the presence of localized states around 2.185 eV can be observed.

These localized states become more evident in *cw*-PL measurements, which can also be collected during the laser illumination process. Figures 6.17(e-i) present the evolution of localized states in normalized momentum-resolved emission spectra in H polarization after different illumination times. Initially (Fig. 6.17(e)), the PL and reflectivity spectra are very similar. After a few seconds (Fig. 6.17(f)), the first flat localized state appears below the H_s band. As illumination time increases (Figs. 6.17(g,h)), the energy of the localized state decreases, and additional localized states emerge, indicating a deepening potential well. After 30 seconds (Fig. 6.17(i)), the energy separation between the H_s band and the lowest localized state reaches approximately 38 meV, with multiple localized states clearly visible.

This method does not create as well-defined potentials as electron beam litography, direct write

litography (see Appendix A) or photo-patterning of the alignment layer, but it presents a complementary technique. Its advantages include the ability to generate a localization potential *in situ* on an already fabricated photonic structure at a precisely defined position, and through real-time monitoring during illumination, achieving a desired potential depth. When combined with the directional scattering effects described in the previous chapter, this approach offers an interesting possibility for light propagation control, where the localization potential could be created along the path of a previously observed light jet.

The above method concerns artificially created photonic traps. Now, various types of self-organizing defects in ULH will be presented. Figure 6.18 shows different POM images of such defects in glass cells (Figs. 6.18(a,d,f)) as well as inside the cavity (Figs. 6.18(b,c,e)), although there is no reason to expect that the cavity itself affects the formation of defects.

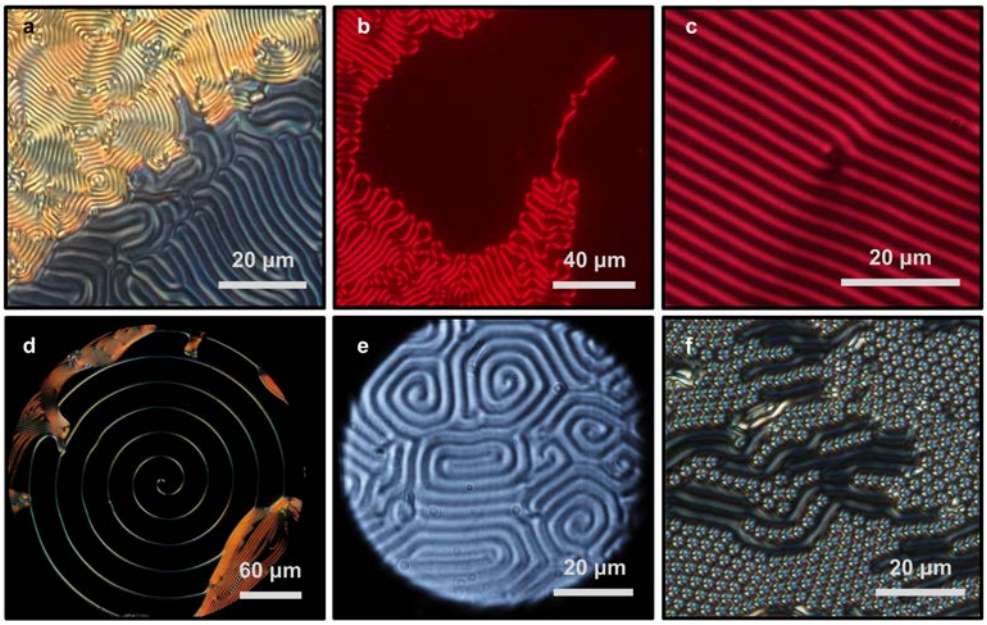

Figure 6.18: **Polarized Optical Microscopy Images of Various Defects in ULH Textures.** (a) Boundary between two regions with different ULH thicknesses. (b) Loosely packed ULH and a single stripe surrounded by isotropic LC. (c) Fork-like dislocation in a well-ordered ULH structure. (d) Liquid crystal torons in a ULH surrounding. (e) Liquid crystal spiral. (f) Tightly packed ULH spirals. Photographs (a-d,f) by Eva Oton.

Figure 6.18(a) presents a boundary where there is a sudden change between two different ULH periods. In the upper left region, the ULH period is approximately twice as small as in the lower right region. Such boundaries are likely related to a sudden step in cavity thickness.

A single straight ULH stripe can be found at the boundary of well-oriented ULH. In this case, ULH becomes increasingly loosely packed, sometimes forming a single stripe surrounded by isotropic LC (Fig. 6.18(b)). Such a stripe can serve as a single, one-dimensional optical trap without the interactions with neighboring stripes.

Figure 6.18(c) presents a fork-like dislocation in the periodic ULH structure. Since the spatially varying birefringence of the LC texture leads to the formation of a synthetic magnetic field (see the next chapter), this type of structure is predicted to host discrete optical states analogous to Landau

levels of charged particles in a uniform magnetic field. Despite initial attempts to observe synthetic Landau levels in fork-like dislocations, I discontinued these studies after successfully observing the similar effect in LC torons.

Zero-dimensional liquid crystal defects with different topological charges, such as torons or hopfions [245, 246], which can differ in the number of helical twists inside the defect [247], are a type of LC droplet with sizes on the order of single micrometers. They can exist as isolated traps or form entire triangular lattices of different filling factor, which tend to be highest when, as in Fig. 6.18(f), they are surrounded by ULH stripes. The following chapter is entirely dedicated to these structures.

Liquid crystal spirals (Fig. 6.18(d)) consist of single ULH stripes that wind or unwind under applied voltage, with their center pinned to a substrate defect. By changing the voltage, it is possible to control the speed and direction of winding/unwinding, and observe this process in real-time. Due to their large size, I do not see an obvious photonic application for them in LCMC, apart from studying isolated ULH stripes.

When fully winded, LC spirals form a stable structure, as shown in Fig. 6.18(e). These tightly packed ULH stripes can take on the shape of classical Archimedean-like spirals or more rectangular Ulam-like patterns, depending on surrounding. By aligning the edge of a rectangular spiral along the spectrometer slit, results similar to those of a well-oriented ULH structure from previous sections of this chapter can be obtained. At the center of such a structure, a defect forms—a ULH stripe that is either wider or narrower than the neighboring stripes (see the center of the middle spiral in Fig. 6.18(e)). The difference in stripe width leads to a different energy of the states in the center of the spiral [248].

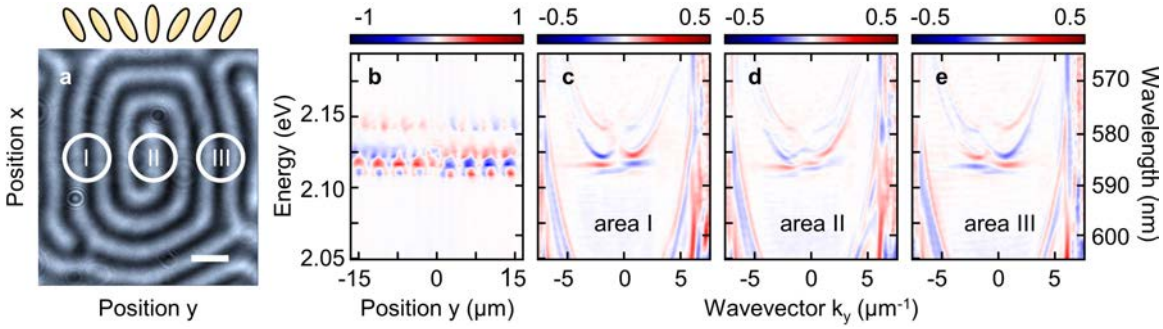

Figure 6.19: **Change of ISOC Sign Within a ULH Spiral.** (a) Real-space image of a ULH spiral with three measurement areas marked. Scale bar: 5 μm. The inset at the top schematically depicts effective refractive index ellipses for a cross-section of the spiral. (b) Spatially resolved transmission spectra expressed by the S_3 Stokes parameter, measured along the y-direction of the ULH spiral. (c–e) Momentum-resolved reflectivity spectra expressed by the S_3 Stokes parameter, measured at the three areas marked in (a).

The varying width of the middle stripe is not the only intriguing property of spirals in ULH-LCMC. Since spirals can be observed in B-type samples, the ULH stripes exhibit a similar modulation of the effective refractive index in space as shown in Fig. 6.10(a). This leads to the appearance of ISOC. However, during the formation of the spiral, the ULH stripes bend in xy plane, finally resulting in a structure where the refractive index distribution differs on the left and right sides relative to the center of the spiral. This is schematically illustrated in the top inset of Fig. 6.19(a), which depicts the effective refractive index distribution in the yz-plane at a cross-section of the spiral along the y-direction. The tilted ellipses do not represent the exact arrangement of individual molecules but

serve as a schematic representation of the effective alignment of the group of LC molecules, as if each ellipse effectively represents the whole molecular arrangement of Fig. 6.10(a).

Figure 6.19(b) presents spatially resolved transmission spectra of the cross-section of the spiral from Fig. 6.19(a) along the y-direction, expressed by the S_3 Stokes component. Mixed ISOC states with an energy of approximately 2.12 eV exhibit a non-zero S_3 value. It is evident that while the Stokes parameter S_3 is not well-defined at the center, comparing S_3 values for positive and negative y-values reveals the change of ISOC sign.

To confirm this position-dependent ISOC sign, momentum-resolved reflectivity spectra were measured at three areas marked with white circles in Fig. 6.19(a) and are expressed by a Stokes parameter S_3 in Figs. 6.19(c-e). While the dispersion in the center of the spiral (region II, Fig. 6.19(d)) appears distorted, measurements in region I (Fig. 6.19(c)) and region III (Fig. 6.19(e)) clearly show a flipped quadrupole of the mixed states, proving the sign change of ISOC.

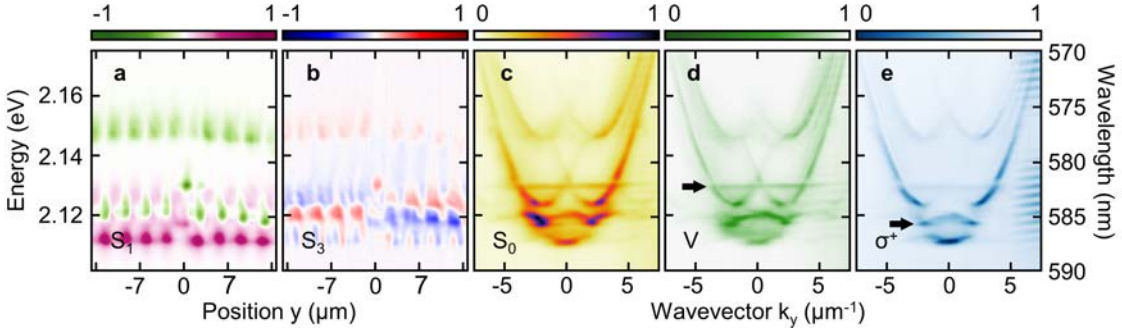

Figure 6.20: **Localized States Within the ULH Spiral.** Spatially resolved transmission spectra expressed by (a) S_1 and (b) S_3 Stokes components. Normalized momentum-resolved reflectivity spectra for (c) total intensity, (d) vertical polarization, and (e) σ^+ polarization. For clarity, in panels (d,e), black arrows indicate states localized at the center of the spiral.

By controlling the energy of the bound states within the ULH-LCMC spiral [248], it is possible to achieve a situation where both states are energetically well separated from the ULH bands. Real- and reciprocal-space measurements were performed on a such position, as shown in Figure 6.20.

In the spatially resolved spectra expressed by the Stokes component S_1 (Fig. 6.20(a)), the presence of two states at $y = 0$ with orthogonal linear polarizations is evident: a state with vertical polarization at an energy of 2.130 eV and a state with horizontal polarization at 2.117 eV. Meanwhile, the spectrum of Stokes parameter S_3 (Fig. 6.20(b)) confirms that these states are located at the center of the spiral, where the ISOC sign changes.

Momentum-resolved reflectivity spectra reveal that these two states exhibit different dependence on the wavevector. In the total intensity spectrum (Fig. 6.20(c)), the localized state with higher energy and V polarization appears completely flat, while the intensity distribution of the lower-energy H-polarized state forms two distinct spots at non-zero wave vectors. These states are better visible when analyzed in separate polarizations: the flat state in V detection polarization (Fig. 6.20(d)) and the two spots in σ^+ polarization, where part of the ISOC-mixed bands signal is filtered out by the polarization detection setup (Fig. 6.20(e)).

A theoretical study is currently in progress, suggesting that at an interface where the sign of SOC changes, a topologically protected state can appear. The current interpretation of this theoretical results indicates that to be topologically nontrivial, this state should form at an energy between two mixed ISOC states. However, before this interpretation was known, I began investigating whether

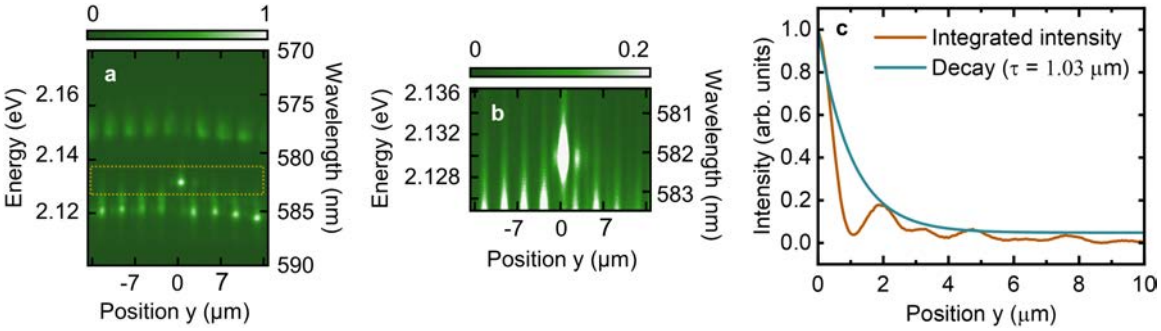

Figure 6.21: **Possible Topologically Non-Trivial State as a Consequence of ISOC Sign Change.** (a,b) Normalized spatially resolved transmission spectra in vertical polarization, with (b) zoomed in and oversaturated for enhanced visualization of the localized state. (c) Integrated intensity over a 1.5 meV energy range across the localized state (brown curve) and fitted with an exponential decay to the intensity peak maxima (cadet blue) with $\tau = 1.03$ μm.

the states within the ULH-LCMC spiral could exhibit topologically nontrivial properties.

One way to demonstrate that an edge state is topologically nontrivial is to show that its intensity decays exponentially in space [99, 249]. Figure 6.21 presents the normalized spatially resolved spectrum from Fig. 6.20(a), but only in V polarization. A yellow dashed rectangle marks a part of the spectrum, which is magnified in Fig. 6.20(b) and oversaturated to enhanced visibility. In this oversaturated map, aside from the state in the center, additional decaying side peaks are visible. Figure 6.20(c) shows a plot of the integrated intensity across 1 meV cross-section of this state as a function of position y. The data is fitted with an exponentially decaying function, yielding a decay constant of $\tau = 1.03$ μm with good agreement.

Experimental results do not provide a clear answer as to whether the observed states are topologically nontrivial, so this subject requires more systematic studies, cleaner spectra, interference measurements, and appropriate theoretical claims to confirm this hypothesis. However, the exponentially decaying intensity and the shape of the states in reciprocal space within energy gaps suggest optimistic prospects. Even if not due to the ISOC sign flip, the interaction between the H and V sublattices may result in the boundary states observed at the spiral's center being topologically protected.

6.5 Summary and Outcome

In this chapter, I presented a self-organized periodic photonic potential based on ULH-LCMC doped with a laser dye. By modifying the growth parameters, the resulting potential landscape can be tailored into various forms, remains well-oriented over a macroscopic area, and allows for significantly faster and simpler fabrication compared to traditional photonic structure manufacturing techniques.

The presence of a periodic potential based on birefringent liquid crystals leads to the formation of two distinct band structures with photonic band gaps for two orthogonal linear polarizations of light. A key advantage of ULH-LCMC is the high degree of dynamic and precise tunability of the band structure via an external electric field. I presented band evolution for both polarizations, including the opening of higher-order photonic band gaps and demonstrated that the voltage-tuning process is reversible. Additionally, the explanation of the observed effects through a microscopic model of LC molecules orientation was provided.

For two different types of samples, I show that the band structures can either be completely independent (A-type samples) or coupled by interband spin-orbit interaction (B-type samples). These coupling is present due to band quantization by the photonic potential. ISOC affect bands of different parity, enabling coupling in the (N, N) regime, unlike in planar microcavities. A LC molecules orientation model for B-type samples was proposed, which, when applied as an effective potential in simulations, corresponding well with experimental results. Furthermore, it was shown that the coupling strength can be controlled by detuning between the ISOC-mixed bands.

Optical excitation can bring ULH-LCMC in a nonlinear regime, leading to photonic lasing that inherit the polarization of the bands. In real space, the periodicity of the structure causes directional scattering of the lasing emission up to approximately 20 µm from the excitation spot.

A range of topological defects in ULH-LCMC has been presented, from artificially created defects using a *cw* laser—where the potential depth can be *in situ* controlled via illumination time—to various naturally occurring defects. A special case involves LC spirals, exhibiting a position-dependent ISOC sign. At the center of such a defect, localized states with orthogonal polarization emerge, possessing differing dispersion relation. It was propose that these states can exhibit topologically nontrivial properties.

The fabrication of photonic structures is typically time-consuming and requires expensive techniques. The method presented here is both fast and simple—the time required by LC to fill the oriented cell with a size of square centimeters, prepared using well-known LCD technology methods, is in order of several minutes. Furthermore, unlike structures created by conventional methods, where lattice parameters are fixed, ULH-LCMC offers a high degree of tunability without the need to fabricate new samples. It is worth mentioning that another tuning parameter—the temperature—is widely used to control the properties of liquid crystals, but has not been explored in this work.

The exploration of polarization properties in standard photonic lattices is limited—most photonic lattices exhibit only weak TE-TM coupling [56] or artificially introduced anisotropy through additional birefringent layers [181]. However, in ULH-LCMC, due to high birefringence of LC, the polarization-related degrees of freedom play a much greater role, enabling band coupling and control over this coupling (see Appendix A, where a one-dimensional chain created by focused ion beam is combined with birefringence inside a nematic LCMC).

Comparisons between the spectroscopic experimental results and the numerical simulation approach presented here may also provide valuable insights into the microscopic structure of more exotic periodic systems, extending beyond liquid crystals. Although this is a complex task, it could represent a significant step toward a deeper understanding of the microscopic orientation in self-organizing photonic crystals, based on, e.g., DNA [250] or nanoparticle complexes [92], which could potentially be embedded into an optical microcavity.

The phenomena related to topological defects presented in this work are only preliminary results in this area. Further experiments are necessary to confirm whether the observed states indeed exhibit nontrivial topological properties. If so, the presence of topologically protected edge states, which manifest through many exciting effects [98,111,180,251], combined with SOC, will open many interesting pathways.

From a technical standpoint, one challenge is sample stability—excessive voltage can lead to sample degradation. Furthermore, some samples exhibited degradation over time: while they appeared perfectly ordered immediately after fabrication, the order decreased after a few days. However, this is an engineering issue that can be resolved through optimization of the preparation process. In particular, some samples stored for more than three years still exhibit excellent properties, suggesting that appropriate fabrication parameters exist and can be achieved.

The ULH-LCMC presented in this chapter is an interesting photonic platform, combining a self-organized, tunable periodic photonic potential with strong polarization properties and lasing. The

unique features of this system—including control over band coupling, ISOC and potential topological states— opens new research directions in optical microcavities and liquid crystal photonics.

7 Two Dimensional Self-Organizing Photonic Potential - Torons

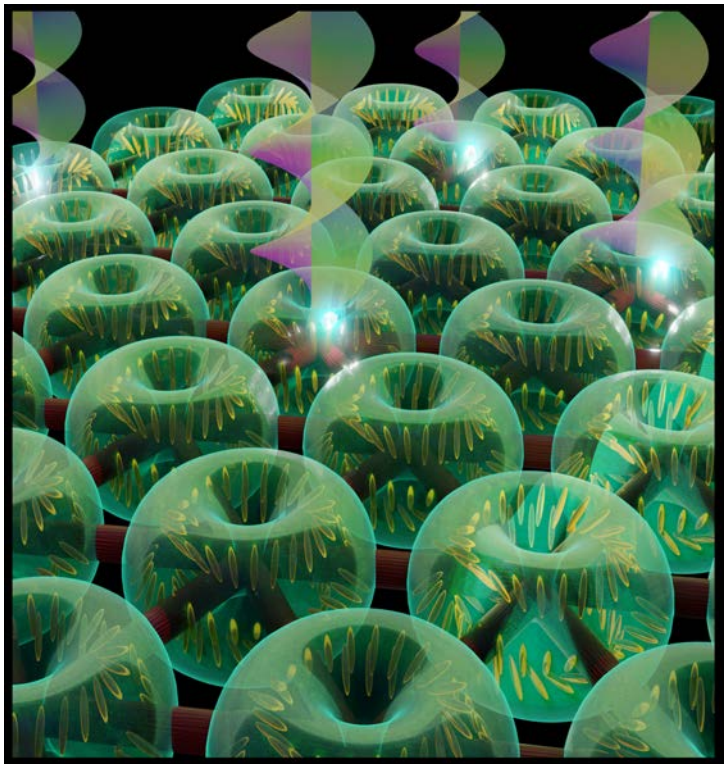

The results presented in this chapter are currently being prepared for publication as:

M. Muszyński, et al. Ground state orbital angular momentum lasing from liquid crystal torons.

In this chapter, I will present the results concerning a dye-doped liquid crystal optical microcavity with topological defects embedded in the liquid crystal matrix, known as torons. Torons act as zero-dimensional optical traps with a spatially dependent synthetic magnetic field. The unusual energy ladder of the confined states in such traps is characterized in both real and momentum space, along with their peculiar polarization properties.

Next, I will demonstrate two nearly equivalent methods of tuning the toron size: by changing the position along a wedge-type sample and by applying an external electric field. The unusual dependence of the energies of the two lowest confined states as a function of the trap size is supported by numerical simulations, which further suggest the possibility of a topological phase transition occurring in the regime of very small torons.

Emission measurements reveal that lasing from the ground state in both circular polarizations carries a non-zero orbital angular momentum of opposite sign. From the perspective of classical non-Abelian gauge field theory, these allow the interpretation of the toron ground state as a synthetic Landau level.

Finally, I will present results for a two-dimensional triangular lattice of torons and an attempt to integrate the system with MeLPPP.

7.1 Polarization Properties of Liquid Crystal Torons Embedded in a Microcavity

In 1992, it was demonstrated that light beams carrying optical vortices (topological phase singularities in electromagnetic fields [252]) also possess quantized orbital angular momentum (OAM) [253]. This discovery opened up a wide range of possibilities in optical communication and manipulation [254]. Today, the terms vortex beam and OAM beam are often used interchangeably, although there is no general one-to-one correspondence between phase vorticity and OAM [255]. Typically, vortex beams carrying OAM are non-ground-state solutions of the paraxial wave equation, characterized by a phase factor of the form $e^{il\varphi}$ in the plane transverse to the beam axis, where φ is the polar angle and l is an integer known as the topological charge. Due to their helical wavefronts, such beams carry an intrinsic [256] and longitudinal [257] OAM equal to $\hbar l$. Due to the formal similarity between the paraxial wave equation and the Schrödinger equation, vortex beams provide a convenient platform for emulating vortex dynamics in quantum fluids of light [178].

Various techniques have been developed to generate vortex beams with OAM, such as imprinting the desired phase profile on an incident beam using bulk optics [27]. However, these methods are typically not tunable or scalable and often require high fabrication precision. A distinct form of angular momentum is the spin angular momentum (SAM), which is associated with the polarization of light [24] and can couple to the OAM under appropriate conditions.

One approach to realizing on-chip OAM lasers involves etching planar semiconductor microcavities to create photonic molecules. In such configurations, states with a given value of OAM form a degenerate quadruplet because of the polarization (spin) degree of freedom. This degeneracy can be partially lifted by SOC [96], and fully lifted via spin-anisotropic interactions induced by optical pumping, enabling OAM-selective lasing [258].

Non-zero OAM states can also be engineered using gauge fields, such as emergent magnetic fields that give rise to Landau-level-like quantization [259]. This topic lies at the intersection of topological photonics [260], where many topologically protected states can be interpreted within the gauge field formalism [261]. In particular, SOC terms can sometimes be interpreted as effective gauge potentials [262]. These gauge fields are often non-Abelian, offering access to richer physics beyond conventional Abelian fields [263–265].

Liquid crystals, with their rich variety of topological defects [246, 266], have been used to couple

SAM with intrinsic (vortex-induced) OAM, for example, in devices such as q-plates [267], forked edge dislocations [268], and nematic droplets [269]. More recently, laser emission of vector beams, which exhibit spatially varying polarization and zero OAM, has been demonstrated from self-assembled topological LC defects confined within optical microcavities [270].

In the previous chapter, a one-dimensional photonic potential was considered, in which birefringence, and the corresponding synthetic magnetic field, varied along only one in-plane direction. In this chapter, I will focus on a zero-dimensional confining potential that, in contrast to conventional photonic traps, features built-in birefringence varying along both in-plane directions of the cavity. This anisotropic birefringence leads to a ground state carrying non-zero OAM.

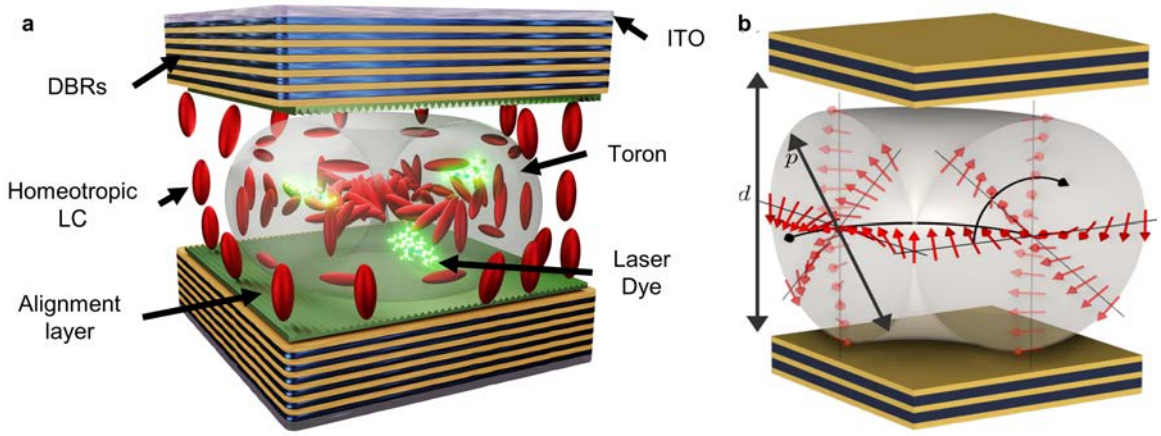

Figure 7.1: **Chiral Nematic Liquid Crystal Torons in an LCMC.** (a) Scheme of a dye-doped optical microcavity with an embedded toron structure. The semi-transparent gray shell illustrates the approximate boundary of the toron. (b) Sketch of the LC director distribution of a single toron. Panel (b) was prepared by Daniel Bobylev (CNRS).

Figure 7.1 presents schematic diagrams of the sample investigated in this chapter, which contains chiral nematic liquid crystal torons embedded within an optical microcavity. Figure 7.1(a) shows the overall structure of the device, which is similar to the ULH-LCMC discussed in the previous chapter. As before, a homeotropically oriented LC matrix doped with P580 laser dye is placed between two DBRs. The key difference here lies in the regions where the orienting layer induces structural frustration, leading to the spontaneous formation of chiral topological defects known as torons. Figure 7.1(b) schematically illustrates the distribution of the LC director (red arrows) within a toron, where d denotes the local cavity thickness and p is the pitch of the supramolecular helical structure.

The diameter of a toron is determined by the condition $d = p$ (where the diameter is equal to the double pitch), while the filling factor and spacing between torons are influenced by both the elastic properties of the LC and the imposed boundary conditions, e.g. cavity thickness, orienting layer material, and the surrounding environment. In fact, as shown in Figure 6.18(f), ULH can coexist with torons in some samples, and its close proximity may lead to tightly packed toron assemblies.

Figure 7.2 shows three POM images of torons inside a glass cell. In Figure 7.2(a), taken at low magnification, numerous well-separated torons can be seen over a large area. The dark regions between them correspond to the homeotropically oriented LC. Figure 7.2(b) shows a higher magnification image, where the characteristic donut-like shape of a toron becomes evident, with a 'hole'

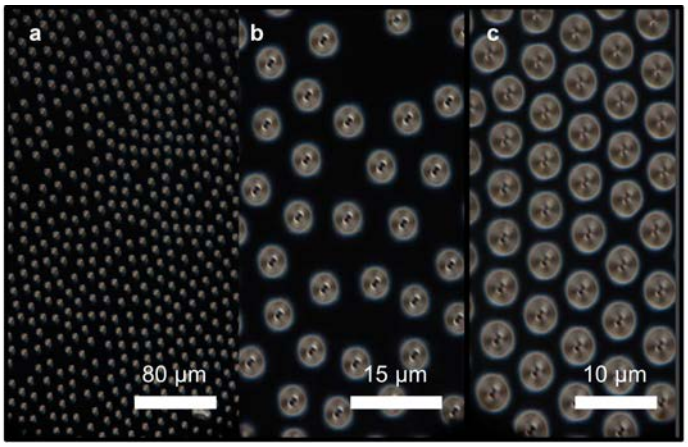

Figure 7.2: **POM Images of Torons in a Glass Cell for Different d/p Ratios.** Photographs of well-separated torons taken at (a) low (b) higher magnification. (c) Densely packed torons forming a triangular lattice. Photographs by Eva Oton.

in the center and a radial distribution of the LC director around it, as illustrated in Figure 7.1(b). When the separation between the edges of neighboring torons exceeds approximately their pitch, they can be considered non-interacting. With an appropriate choice of LC mixture, cavity thickness, and fabrication conditions, torons can self-organize into tightly packed clusters that form a regular triangular lattice, as shown in Figure 7.1(c).

The non-interacting toron acts as a photonic trap, similar to micropillars or mesas, forming a binding potential and a series of localized optical states with some unusual optical properties. To investigate this peculiar energy ladder, polarization-resolved tomography of reciprocal-space transmissions of a single toron with diameter of 4 µm were performed. The normalized momentum-resolved spectrum is shown in Figure 7.3(a), with ground and first excited states marked by green and black arrows, respectively. Unlike conventional trapping potentials, the ground state at 2.119 eV exhibits a minimum intensity at $k_x = 0$.

Figures 7.3 (b-d) and (e–g) present the isoenergetic planes in reciprocal space for the Stokes parameters S_0, S_1, and S_2 for the first excited state and the ground state, respectively. A comparison of the total intensity distributions (Figures 7.3(a,e)), reveals a key difference. While the ground state exhibits a radially symmetric donut-like intensity profile, the first excited state features a central maximum intensity at normal incidence. The saturated outer ring observed in wavevectors greater than 3 μm^{-1} is associated with transmission through cavity modes in the area surrounding the toron. Due to the strong TE-TM splitting induced by the birefringence of the LC, the linear polarization pattern of the S_1 component (Figures 7.3(c,f)) for these cavity modes forms a characteristic double quadrupole, which remains independent of energy. For localized states, the S_1 distribution also forms a quadrupole pattern. However, because of the rotating director of the LC molecules inside the toron and the resulting LT splitting, this quadrupole is rotated with respect to those of the cavity modes. Furthermore, the quadrupoles of the two lowest-energy states are rotated by 90 degrees relative to each other. Complementary results are obtained for diagonal polarizations (Figures 7.3(d,g)), where the S_2 quadrupole is rotated by 45 degrees relative to S_1.

Figures 7.3(h–n) show simulation results performed by Daniel Bobylev. The effective stationary Schrödinger equations used for the qualitative theoretical analysis of the considered system are

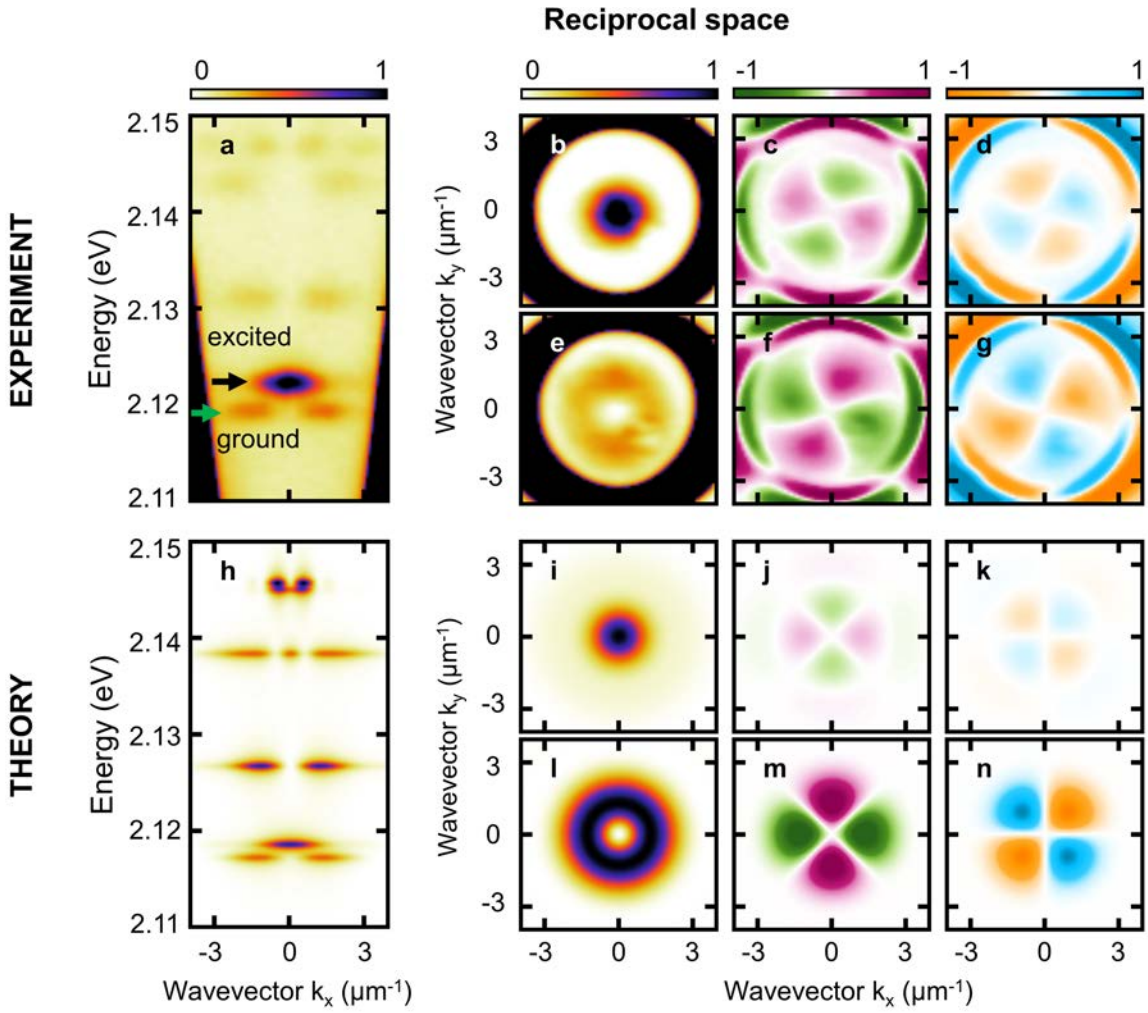

Figure 7.3: **Polarization Properties of a Single Toron Embedded Inside an LCMC in Reciprocal Space.** (a–g) Experimentally measured and (h–n) theoretically calculated Stokes parameters. (a,h) Momentum-resolved transmission spectra, with black and green arrows indicating the energies of the two lowest-energy states. (e–g, l–n) Stokes parameters S_0, S_1, and S_2 corresponding to the ground state, respectively. (b–d, i–k) Stokes parameters S_0, S_1, and S_2 corresponding to the excited state, respectively. Theoretical calculations were performed by Daniel Bobylev.

derived from the time-harmonic macroscopic Maxwell's equations. Specifically, the wave equation for the electric field

$$\nabla \times \nabla \times \mathbf{E} - \frac{\omega^2}{c^2}\hat{\varepsilon}(\mathbf{r})\mathbf{E} = 0\,,$$

with the permittivity tensor $\hat{\varepsilon}(\mathbf{r})$ defined by the liquid crystal director field $\mathbf{d}(\mathbf{r})$ and the principal

values $\varepsilon_{o,e}$ ($\Delta\varepsilon = \varepsilon_e - \varepsilon_o > 0$) as $\varepsilon_{ij} = \varepsilon_o^2\,\delta_{ij} + (\varepsilon_e^2 - \varepsilon_o^2)\,d_i d_j$, is transformed into

$$\left\{\left[\frac{-\hbar^2}{2m}\nabla^2 - \frac{\hbar\omega}{2}\left(\varepsilon_o + \Delta\varepsilon\frac{d_x^2+d_y^2}{2}\right)\right]\sigma_0 - \frac{\hbar\omega}{2}\Delta\varepsilon d_x d_y\sigma_1 - \frac{\hbar\omega}{2}\left(\Delta\varepsilon\frac{d_x^2-d_y^2}{2}\right)\sigma_3\right\}\psi = \frac{-\hbar^2 k_z^2}{2m}\psi\,,$$

provided the slowly-varying medium and paraxial approximations are valid: $\nabla(\nabla\cdot\mathbf{E}) \approx 0$, $\mathbf{E}(x,y,z) \approx (\psi_x(x,y),\psi_y(x,y),0)\;e^{-i\,k_z z} = \psi\;e^{-i\,k_z z}$. The latter conditions are achieved by considering high cavity mode numbers at optical frequencies, which are well-localized within the optical trap.

The simulations reproduce the experimental results very well, with the exception of an additional rotation of the polarization patterns of the localized states relative to the cavity modes.

The real-space distribution of the Stokes components is shown in Figures 7.4, based on polarization-resolved tomography of the same single toron, as in the previous figure. The panel arrangement follows the same scheme as in Fig. 7.3. Similarly to reciprocal space, the normalized spatially resolved spectra reveal that the ground state exhibits a minimum intensity at the center of the toron. The intensity profiles for both lowest-energy states (Figures 7.4(b,e)) show a radially symmetric donut shape, with an additional central maximum appearing in the excited state. As in reciprocal space, the linear polarization patterns of both states form quadrupole structures (Figures 7.4(c,d,f,g)). Interestingly, in contrast to reciprocal space, these quadrupoles do not exhibit any relative rotation between ground and first excited states.

Numerical simulations in real space, performed using the same method as previously, are shown in Figures 7.4(h–n). In Figure 7.4(i), which presents the total intensity of the excited state, no central maximum is observed, unlike in the experiment. In my view, this central maximum is an experimental artifact, likely related to the sample being slightly out of focus. As in the simulations, the correct intensity distribution of the excited state should exhibit a donut-like shape, similar to that of the ground state. However, the simulations do not correctly reproduce the S_2 polarization component in real space, where the quadrupole is rotated by 90 degrees compared to the experimental data.

These results demonstrate that a single toron acts as a 0D photonic trap which, because of the spatially rotating LC molecules, features an unusual ladder of states. The ground state has circular symmetry, a Laguerre–Gaussian-like intensity profile with a non-zero l number, and a quadrupole-like polarization pattern in both real and reciprocal space.

7.2 Tunability of the Photonic Trap Size

In this section, the dependence of the toron energy level structure on its size is investigated. The proposed device offers two methods for tuning the toron size. Since the diameter of the toron depends on the thickness of the cavity ($p = d$), a wedge cavity allows torons of varying sizes to form at different positions on the sample. The second method involves applying an external electric field that dynamically compresses the toron.

Due to the signal-to-noise ratio in transmission measurements of single torons with small sizes (below 3 μm) being close to the detection limit, the measurements in this section were performed on well-isolated torons in groups. Since the torons within the detection spot are very similar, such measurements can be reliably performed at the cost of slight spectral line broadening.

First, the results obtained for torons located at different positions across the sample are presented. Figures 7.5(a–g) show real-space images of various groups of torons, with diameters gradually decreasing from approximately 7 to 2.6 μm. Figures 7.5(h–n) display the corresponding normalized momentum-resolved transmission spectra. Since the different toron groups correspond to different

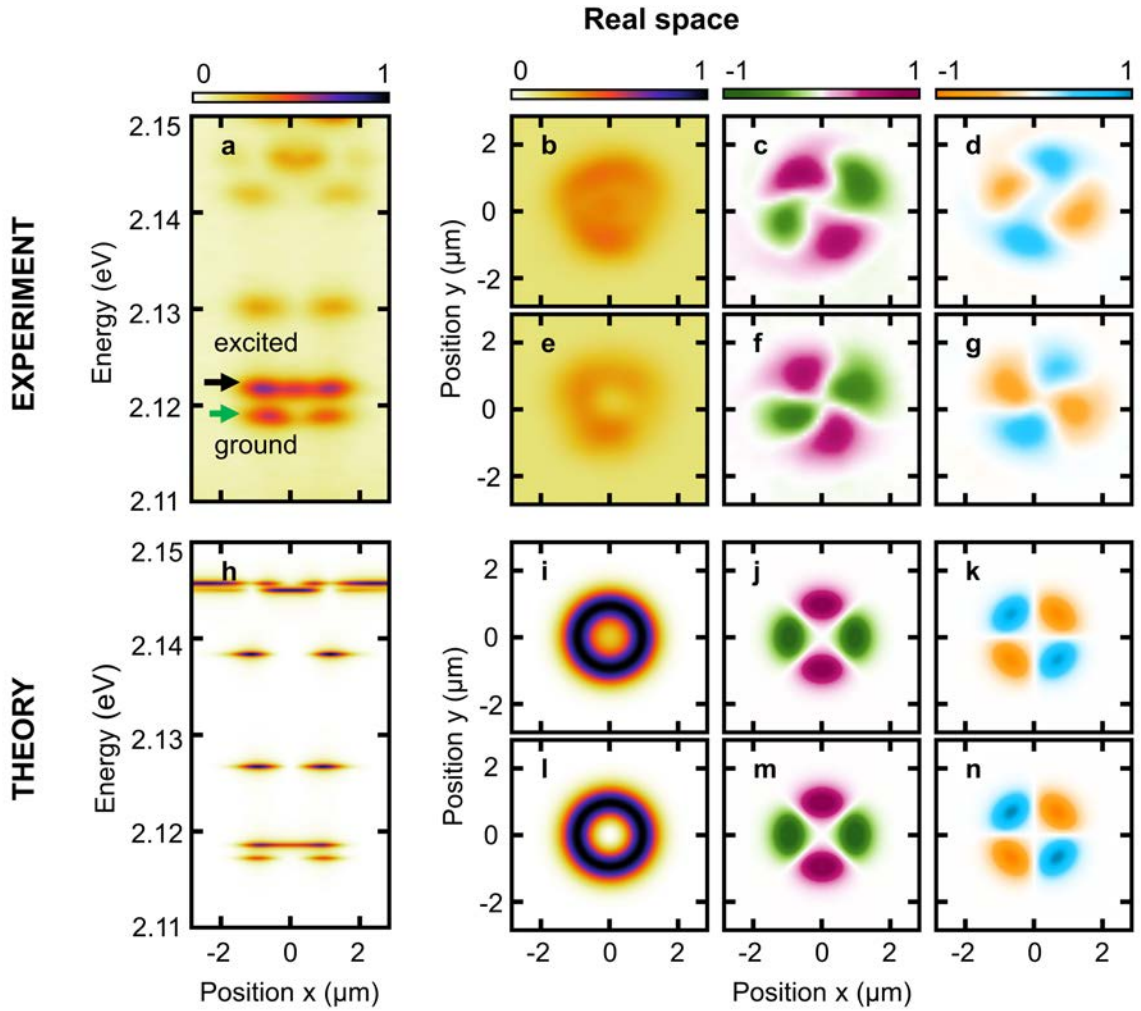

Figure 7.4: **Polarization Properties of a Single Toron Embedded Inside an LCMC in Real Space.** (a–g) Experimentally measured and (h–n) theoretically calculated Stokes parameters. (a,h) Spatially resolved transmission spectra, with black and green arrows indicating the energies of the two lowest-energy states. (e–g, l–n) Stokes parameters S_0, S_1, and S_2 corresponding to the ground state, respectively. (b–d, i–k) Stokes parameters S_0, S_1, and S_2 corresponding to the excited state, respectively. Theoretical calculations were performed by Daniel Bobylev.

cavity thicknesses d (ranging from 3.5 to 1.3 μm, according to the relation that the toron diameter equals twice the pitch p), this change strongly affects both the energies of the cavity modes and the energies of the localized toron states. However, it should not significantly impact the relative energy separation between the states. Therefore, for clarity, a relative energy scale is used in which 0 meV corresponds to the minimum energy of the planar cavity mode.

For the largest measured torons (Fig. 7.5(h)), the dispersion shows many localized states, consistent with a simple quantum well model for a wide potential. The ground and first excited states follow the same order and characteristics as in Fig. 7.3(a), although they are less energetically sepa-

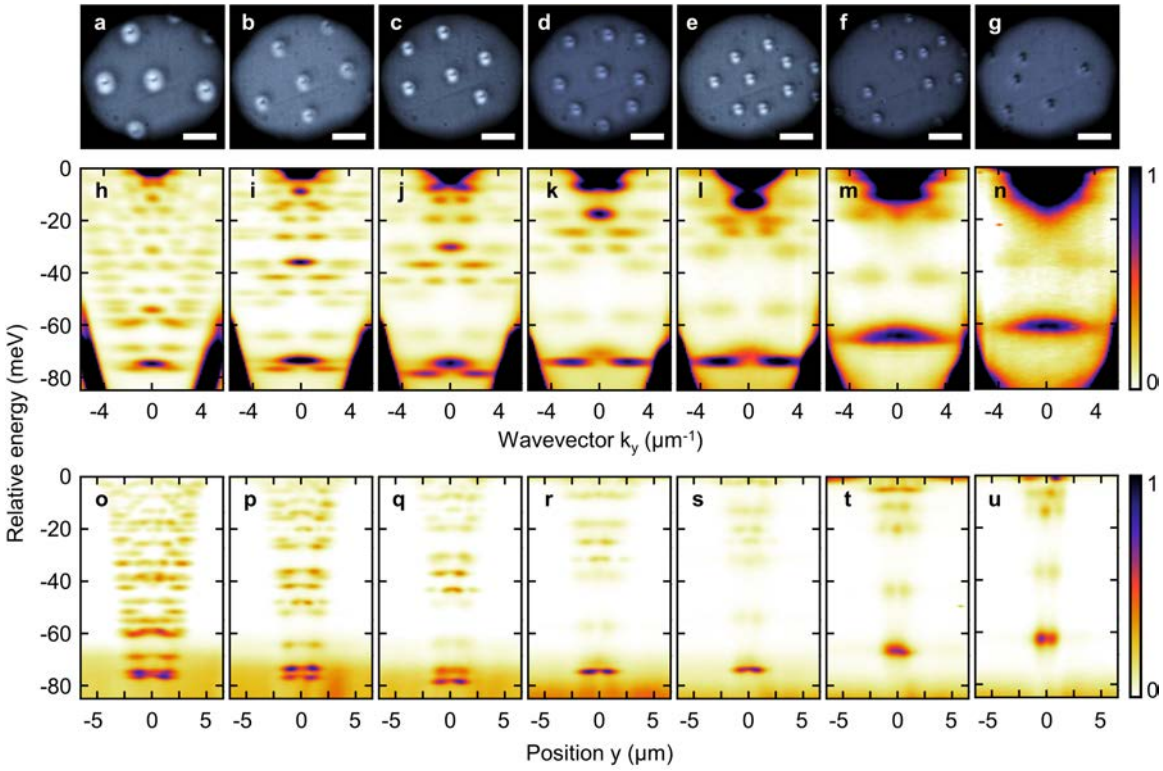

Figure 7.5: **Position-Dependent Size of Photonic Traps.** (a–g) Real-space transmission images of non-interacting torons collected at different positions on the sample. Scale bars: 10 μm. Normalized to maximum intensity of two lowest states (h–n) momentum- and (o–u) spatially resolved transmission spectra corresponding to the same positions. The relative energy values are referenced to the bottom of the planar mode dispersion.

rated. As the diameter of the toron decreases (Figs. 7.5(i,j)), the number of localized states gradually reduces, and the energy and spacing of the higher excited states increase, as expected.

Interestingly, in Fig. 7.5(i), the two lowest-energy states exhibit a counterintuitive trend: their energies decrease even as the trap size becomes smaller. As the size of the trap continues to decrease (Figs. 7.5(d–n)), all states exhibit a blueshift. Notably, the relative intensity of the first excited state, which dominates the spectrum for large torons, becomes weaker as the trap size reduces (Figs. 7.5(k,l)), while the ground state starts to dominate. Furthermore, in the regime of very small torons, the energy separation between the two lowest states unexpectedly decreases, almost disappearing for the smallest torons (Fig. 7.5(n)), in contrast to the simple quantum well intuition.

Figures 7.5(o–u) present the corresponding normalized spatially-resolved spectra. These results show a gradual reduction in the trap size and an increased spatial localization of the states, consistent with the trends observed in reciprocal space.

Figure 7.6(a,b) shows the energies of the four lowest-energy states and the energy separations between each pair of neighboring states as a function of the diameter of the toron, respectively. These plots confirm the trends observed in the previous figure. For the second and third excited states (red and blue triangles), the energy increases monotonically, following an approximately quadratic

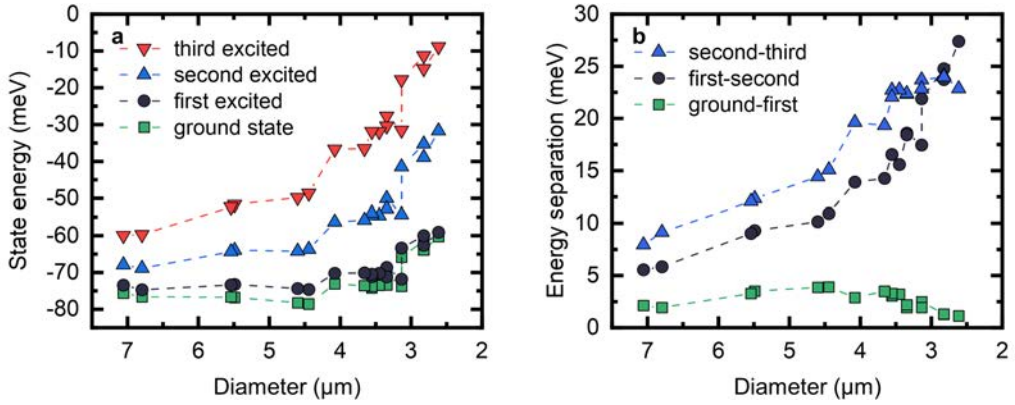

Figure 7.6: **Influence of Trap Size on the Energy of Bound States for Torons Confined at Different Positions with Varying Cavity Width** d**.** (a) Energies of the four lowest localized states and (b) energy separation between consecutive states as a function of toron diameter.

dependence, as expected. In contrast, for the ground and first excited states (black circles and green squares), a slight dip in energy appears around a toron diameter of approximately 4.5 μm, observed in two distinct toron groups. The energy separation plot further emphasizes the differing behavior of the two lowest states. While the separations between the second and third (blue squares), and the first and second (black circles) excited states increase as the diameter of the toron decreases, the separation between the ground and first excited states (green squares) initially increases, then begins to decrease near 4.5 μm.

To more precisely study the unusual energy dependence of the two lowest-energy toron states, toron size was tuned with an external voltage. This method allows for finer control over diameter changes while probing the same group of torons.

Figures 7.7(a–e) present real-space transmission images of several torons under varying applied voltages (AC), showing a gradual decrease in diameter from approximately 6.1 μm to 3.1 μm as the voltage increases. While the torons generally remain in fixed positions, occasional lateral shifts are observed (e.g. the two torons on the left in Fig. 7.7(a)), although most remain unaffected.

As with the position-dependent tuning method, voltage-induced changes in size have a strong effect on the energy spectrum, as seen in the momentum-resolved transmission spectra (Figures 7.7(f–j)). Since the surrounding planar region of the cavity, which forms the potential barrier of the trap, features homeotropic LC alignment, the cavity mode energy remains constant, and no relative energy scale is needed. The trends observed here are consistent with those found in spatial tuning. For larger torons, the first excited state exhibits the highest intensity, which gradually decreases as the toron diameter decreases. Notably, both the energy of the ground state and the energy separation between the two lowest states reach a maximum at a diameter of approximately 4.3 μm. For the smallest torons, the energy levels exhibit a 'normal' ordering, with only the lowest-energy state, lacking the characteristic donut-like shape, is visible. Attempts to observe torons with even smaller diameters were unsuccessful due to either insufficient signal-to-noise ratio or damage caused by an applied voltage, which led to complete homeotropic alignment of the LC.

In the measurements where the toron diameter was tuned using voltage, the effects observed in Figure 7.6 are clearly confirmed. The plots of the ground and first excited state energies, together with their energy separation, extracted by fitting the Lorentzian curve, are shown in Figures 7.8(a,b), respectively. The energies of both lowest states initially decrease with decreasing trap size, before

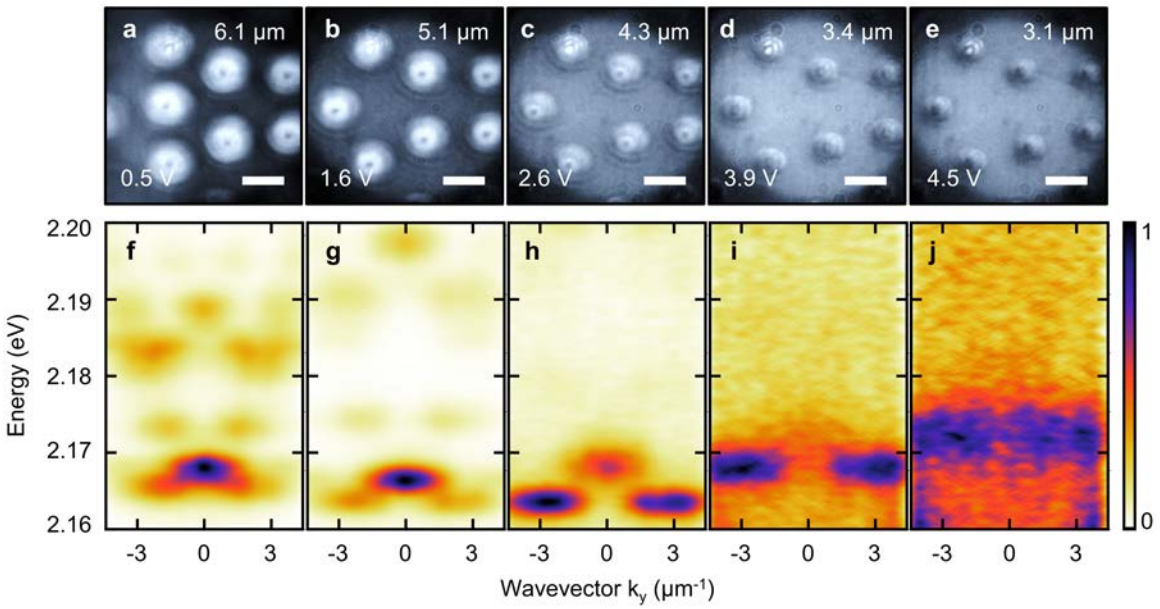

Figure 7.7: **Voltage-Dependent Size of Photonic Traps.** (a–e) Real-space transmission images of non-interacting torons recorded at different applied voltages (indicated in the bottom-left). Estimated toron diameters are labeled in the top-right; scale bar: 5 µm. (f–j) Corresponding normalized momentum-resolved transmission spectra for the voltages shown in panels (a–e).

starting to increase. However, for the excited state this turning point occurs at a slightly larger diameter, around 5 µm, and additionally exhibits a secondary dip below 4 µm. In the energy sep-

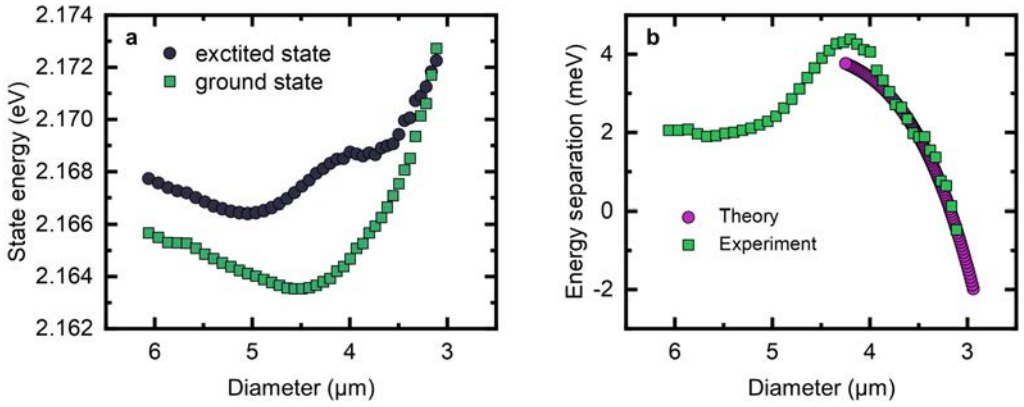

Figure 7.8: **Influence of Trap Size on the Energy of Bound States for Different Applied Voltages.** (a) Extracted energies of the ground state (green squares) and the first excited state (black circles) as a function of the toron diameter. (b) Energy separation between these two states, obtained experimentally (green squares) and from theoretical simulation (purple circles). Theoretical calculations was performed by Daniel Bobylev.

aration plot (Fig. 7.8(b)), a well-defined peak centered on a diameter of 4.3 μm suggests that the evolution of these states is governed not only by photonic confinement, but also by an additional coupling mechanism. When the trap reaches its smallest size, the energy separation becomes negative, indicating an inversion on the order of the two states. The possibility of such a transition is predicted by the theoretical model used in the previous section, and its results are shown as purple circles in Figure 7.8(b). It is worth noting that voltage tuning of torons, similarly to ULH, is reversible as long as the applied voltage does not exceed the threshold that either erases the toron or causes it to drift. Furthermore, while voltage tuning produces macroscopic effects similar to those of position-dependent tuning, it microscopically changes the orientation of LC molecules in a different way. Consequently, the specific toron sizes at which particular effects emerge may differ depending on the tuning method.

7.3 Lasing with Orbital Angular Momentum

The donut-like shape of the total intensity profile and quadrupolar linear polarization distribution is often a signature of a phase singularity underlying the orbital angular momentum [271]. The LC mixture used in the sample contains a laser dye, which allows lasing to be achieved from a single toron state and the investigation of its phase properties.

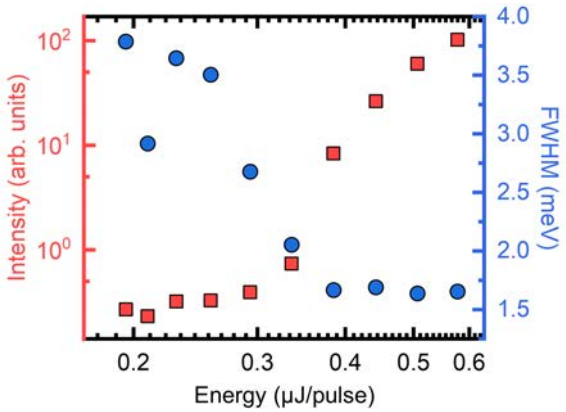

Figure 7.9: **Ground-State Lasing of Toron-LCMC**. Emission peak intensity (red squares) and spectral linewidth (blue circles) as a function of excitation pulse energy, extracted by Lorentzian fitting.

Figure 7.9 presents the intensity and linewidth of the ground state emission from a single toron as a function of the excitation pulse energy. Similarly to previous chapters, a clear threshold behavior is observed, characterized by a nonlinear increase in emission intensity and a narrowing of the emission linewidth, confirming the photonic lasing.

Figures 7.10(a) and 7.10(b) show the momentum-resolved emission spectra of a single toron below and above the lasing threshold, respectively. Below the threshold, the strongest signal originates from microcavity modes in the region surrounding the toron. The spectrum has been partially saturated to also reveal weaker spontaneous emission from several toron states, including the ground state at approximately 2.16 eV. Above the threshold, the emission signal is dominated by the ground state lasing emission with the minimum intensity at $k_x = 0$. The superimposed lasing signals from multiple non-interacting torons in the real-space (Figure 7.10(c)) with horizontal (pink) and vertical (green) polarization form a quadrupole pattern rotated with respect to the xy axes, consistent with

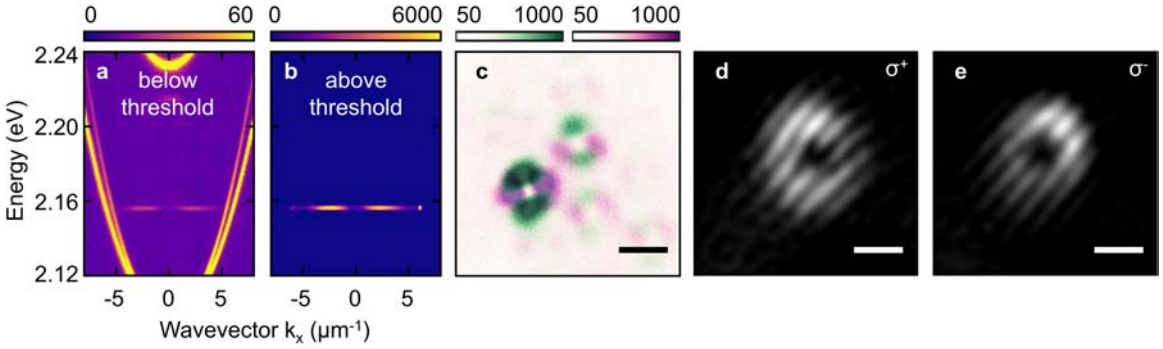

Figure 7.10: **Lasing with Orbital Angular Momentum.** Momentum-resolved photoluminescence spectra measured (a) below and (b) above the lasing threshold. (c) Real-space image of the overlapped horizontally H (pink) and vertically V (green) polarized lasing signals from multiple torons (logarithmic scale). Scale bar: 3 μm. (d,e) Interference patterns collected for σ^+ and σ^- polarizations, respectively. The fork-like patterns with opposite orientations indicate the presence of orbital angular momentum with opposite signs for the two circular polarization states. Scale bars: 1.5mix μm.

the transmission measurements in Figure 7.4(f). Notably, the intensity profile of each toron exhibits a minimum in the center, a characteristic feature of light carrying OAM. To further verify the presence of phase singularities, interferometric measurements of the lasing signal from a single toron were performed in σ^+ and σ^- polarizations (Figures 7.4(d,e)). The resulting fork-like interference patterns - which are mirrored for opposite polarizations - indicate that lasing from the ground state carries OAM with opposite signs in two orthogonal circular polarizations.

The confirmation of OAM in the ground state, along with the state inversion transition described in the previous section, has interesting implications. For the smallest toron sizes, where the energy ladder follows a trivial ordering, the ground state carries zero OAM in both spin components. As the toron diameter increases, a topological transition occurs, characterized by the inversion of state ordering [272–274]: the ground state becomes the one with non-zero OAM, with opposite values in the two spin components. It is in this topologically nontrivial regime that all the observations presented above were made.

The non-zero OAM of the ground state can also be interpreted from the point of view of the classical non-Abelian gauge field theory [262]. The spatially-dependent birefringence can be seen as a varying non-Abelian gauge potential, giving rise to an effective gauge field. This field acts on spin currents similarly to the Lorentz force, resulting in cyclotron orbits. From this perspective, the OAM states observed in this system resemble Landau levels emerging from a non-Abelian analog of a magnetic field.

7.4 Two-Dimensional Self-Organized Lattice of Torons

The results discussed so far have concerned well-separated torons, treated as zero-dimensional photonic traps. As shown in Figure 7.2(c), under appropriate conditions, torons can self-organize into well-ordered lattices, most commonly with a triangular geometry. When the spacing between torons becomes sufficiently small, interactions between their bound states lead to the formation of a band structure, analogous to that observed in ULH-LCMC in Chapter 6.

An example of a densely packed, self-organized toron lattice is shown in Figure 7.11(a). As

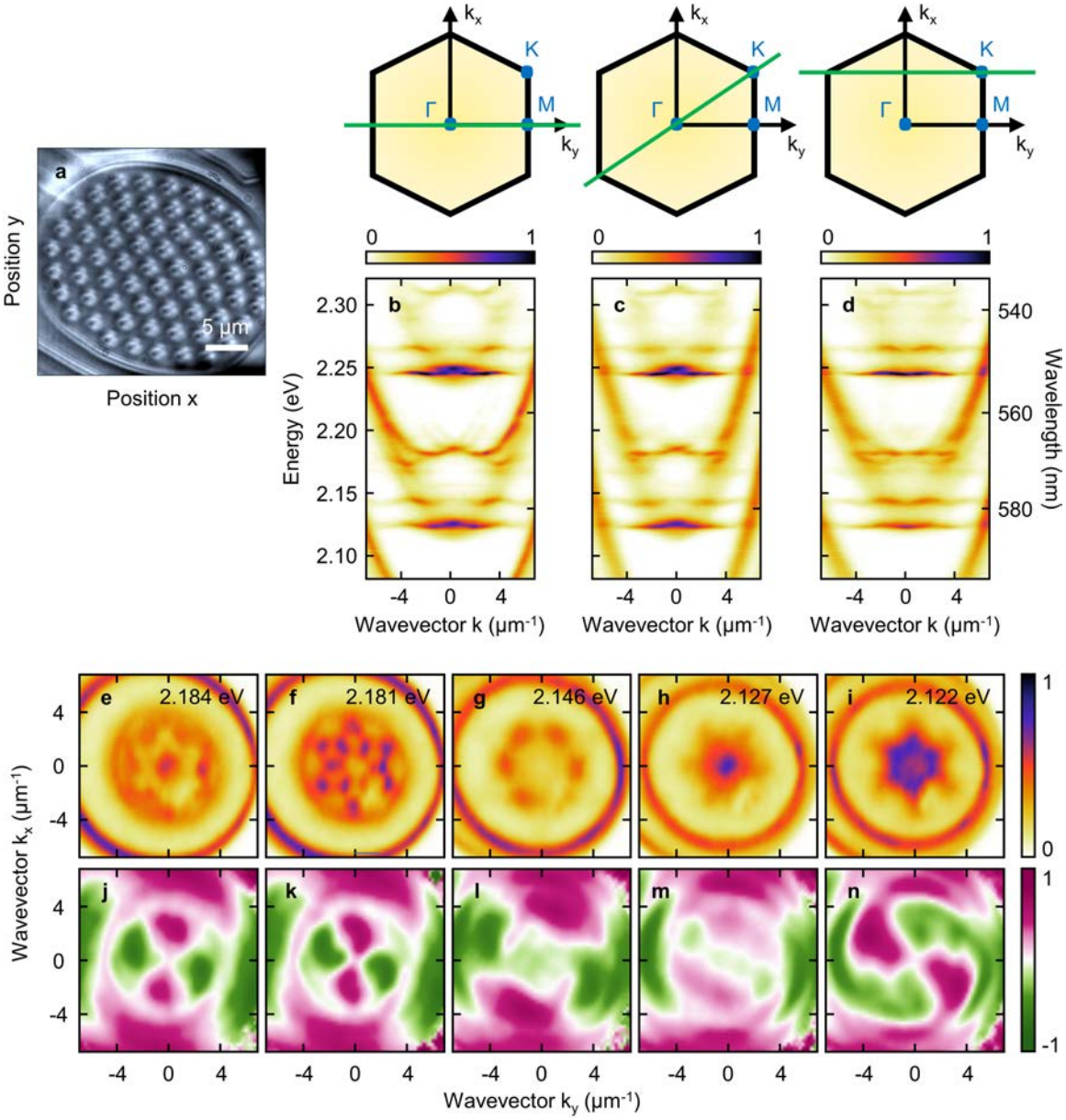

Figure 7.11: **Two-Dimensional Photonic Lattice Based on Liquid Crystal Torons.** (a) Real-space transmission image of densely packed torons. (b–d) Cross-sections of normalized momentum- and energy-resolved transmission tomography through selected critical points in reciprocal space. The directions of the cross-sections are indicated in the inset at the top of each panel. Selected isoenergetic planes (energy indicated in the top-right) represented by Stokes parameters: (e–i) S_0 and (j–n) S_1, demonstrating symmetry and interactions within the lattice.

previously mentioned, the presence of ULH stripes (or disclination loops) in close proximity can assist (although not strictly required) in achieving high toron packing density. In this case, torons are also confined within a loop formed by ULH.

Polarization- and momentum-resolved tomography was performed on the tightly packed lattice, as shown in Figures 7.11(b–n). Figures 7.11(b–d) present normalized total intensity cross-sections along selected high-symmetry directions in reciprocal space, with the directions indicated in the Brillouin zone schemes above each panel. To highlight key spectral features, the energy range has been extended to include two cavity modes; therefore, the two lowest-energy bands, located at approximately 2.25 eV and 2.13 eV, are both shown. In all three directions, the formation of photonic bands with a well-pronounced curvature is clearly visible: originating from the second excited states (around 2.145 eV) and the ground states (around 2.13 eV). Due to limited resolution, it remains uncertain whether the first excited state also forms a band; however, for the higher-energy part of the band structure (2.25 eV), a clear separation is observed between this state and the band formed by the ground states.

Figures 7.11(e–i) show normalized isoenergetic planes of total intensity at selected energies. The resulting patterns display the symmetry characteristic of a triangular lattice (with minor imperfections due to lattice inhomogeneity), providing further evidence of interactions between neighboring torons.

Figures 7.11(j–n) present the corresponding isoenergetic planes expressed by the S_1 Stokes component. The quadrupolar character of the linear polarization patterns is preserved within the lattice, and, as in the case of isolated torons, the quadrupoles corresponding to different bands are rotated by 90 degrees with respect to one another (e.g., Figures 7.11(j,n)).

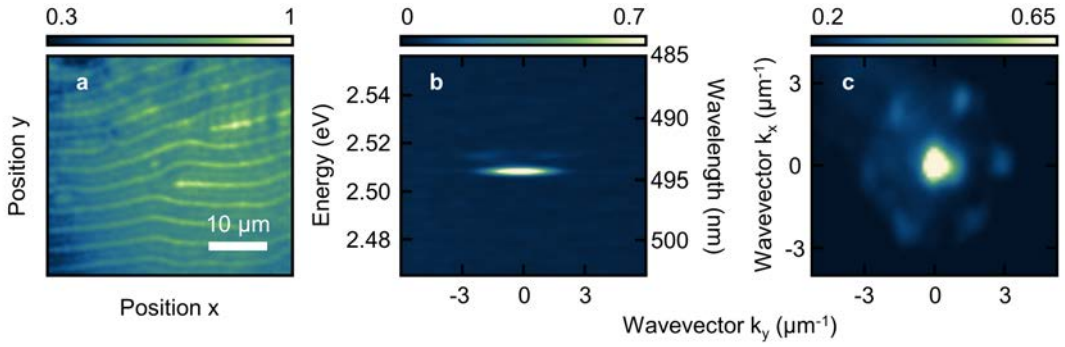

Figure 7.12: **Self-Organizing Photonic Potentials in LCMC Combined with MeLPPP.** (a) Normalized spatially-resolved spontaneous emission from an ULH-LCMC. (b) Normalized momentum-resolved emission spectrum above the lasing threshold from a single ULH stripe. (c) Normalized momentum-space lasing from a triangular lattice of torons.

All results presented for self-organized photonic potentials discussed in Chapters 6 and 7 concern the weak light–matter coupling regime. Despite several attempts to integrate ULH and torons with MeLPPP, various technological challenges extensively discussed in Chapter 5, prevented obtaining conclusive evidence for strong coupling or Bose–Einstein condensation. Nevertheless, in the interest of completeness, Figure 7.12 presents the results of efforts to observe these effects in the integrated structure.

Figure 7.12(a) shows real-space spontaneous emission from a MeLPPP–ULH–LCMC device. The image reveals that, even with MeLPPP as a light emitter, well-oriented ULH and various types of dislocations can form. However, the broad emission linewidth and low quality of the cavity modes

(not shown) did not allow a reliable characterization of these samples. On individual ULH stripes, similar to those shown in Fig. 6.18(b), nonlinear emission from localized states was observed (see Figure 7.12(b)). Owing to the absence of strong coupling signatures and a threshold approximately two orders of magnitude higher than that reported for BEC in Chapter 5, this emission is most likely attribute to photonic lasing rather than condensation.

Similar limitations were encountered with the MeLPPP–toron–LCMC samples. Nonlinear emission was again observed, including from well-ordered toron lattices, e.g. Figure 7.12(c) shows emission above the threshold in momentum space with well-pronounced triangular symmetry. However, this phenomenon is also interpreted as photonic lasing rather than BEC.

In my view, achieving BEC in localized states or photonic bands formed by self-organized structures in such devices remains a realistic goal but will require further optimization of the sample fabrication process.

7.5 Summary and Outcome

In this chapter, the results of a device integrating a dye-doped optical microcavity with liquid crystal torons in the weak light–matter coupling regime were presented. Well-isolated single torons were investigated, acting as zero-dimensional photonic traps with a peculiar ladder of photonic states. The polarization properties of the ground state, which exhibit a donut-like symmetry, and the first excited state were characterized both in real and reciprocal space. Consistent results on tuning the toron size and its effect on the energy spectrum were presented using two independent methods: by changing the position on the sample and applied voltage. These results revealed nontrivial behavior of the energies and energy separation of the two lowest states. In a certain range of trap sizes, the energy of both states decreased with decreasing toron size, contrary to the intuitive behavior expected for standard potential wells. Furthermore, when the toron became very small, an inversion of the two lowest states was observed, attributed to a topological transition of the ground state: from a regime with nonzero orbital angular momentum to a typical s-symmetric state.

The presence of OAM in the ground state was confirmed through interferometric measurements of lasing from a single toron. It was demonstrated that for two opposite circular polarizations of light, the OAM values are nonzero and have opposite sign. Based on these results, the ground state in the topologically nontrivial regime was interpreted as an optical analogue of the Landau level. This Landau level emerges because of a spatially varying synthetic magnetic field originating from the position-dependent birefringence inside the toron, which acts on spin (polarization) currents analogously to a Lorentz force.

Finally, results on self-organized two-dimensional toron lattices were presented. Their photonic band structures were shown to inherit both the symmetry of the lattice and the characteristic polarization features of individual torons.

The results presented in this chapter demonstrate that self-organizing materials can successfully form two-dimensional, interacting photonic lattices. This opens a path toward employing other self-assembled structures within optical microcavities as periodic photonic potentials. An open question is whether self-assembled lattices with symmetries other than triangular, easily achievable through alternative methods (see Appendix A), can also be realized. Beyond the demonstrated 0D and 2D cases, torons can self-organize into one-dimensional chains surrounded by ULH stripes (see Figure 6.18(f)). Although such configurations have not yet been studied in LCMCs, they are expected to give rise to band structures characteristic of 1D lattices. In fact, theoretical investigations currently underway by my collaborators suggest that toron chains may support topologically protected states. Although current simulation parameters indicate that the required toron sizes and overlaps are not experimentally accessible in self-assembled chains, I do not exclude the possibility that techniques

for generating or manipulating torons on demand [275, 276], or electrically controlled flows [277], could achieve the necessary geometry.

Torons represent just one type of topological defect in liquid crystals, along with hopfions, skyrmions, heliknotons, and others [278, 279], which exhibit both Abelian and non-Abelian gauge field characteristics. Embedding such defects into optical microcavities could lead to non-trivial topological transitions and novel phenomena related to spin propagation.

One experiment I aimed to demonstrate, but was unable to perform due to fabrication issues with new toron-lattice samples (the previous sample used for the results in Figure 7.11 degraded, and newly fabricated samples, for unknown reasons, failed to form lattices packed densely enough with well-defined bands), involved voltage-tuning of the band structure. Since the applied voltage reduces the toron size by nearly half (see Figure 7.8), I expect that in a 2D lattice this would decrease the orbital overlap of localized photonic states, thereby allowing control over the interaction strength between lattice sites. In different types of photonic potentials integrated with microcavities, voltage tuning allows control over distinct parameters: in ULH–LCMC, it changes the potential depth; in single toron–LCMC, it sets the potential size; in toron–LCMC lattices, it modulates the orbital overlap; and in FIB–LCMC (see Appendix A, Figure 9.6), it tunes the energy of the entire band structure. With currently available toron–LCMC lattice samples, I was only able to switch between an interacting-lattice regime and a non-interacting one. Systematic measurements that gradually reduce band hybridization have yet to be performed. If a sample comparable in quality to that in Figure 7.11 can be reproduced, I see no reason why such an experiment would not succeed. Furthermore, these measurements could allow for clear separation of the two lowest-energy bands, facilitating a more detailed investigation of their properties.

Because of the size of several micrometers, torons are also promising from an application perspective as microlasers with OAM. An interesting direction for future research is the study of lasing properties, including OAM, that originate from the lowest band of a toron lattice.

Another application of toron–LCMC systems, currently being explored by my collaborators, is their use to capture single-photon emitters. It is predicted that only one or two such emitters could be located within a single toron.

The challenge of integrating ULH–LCMC and toron–LCMC systems into the strong light–matter coupling regime remains unresolved.

8 Three Dimensional Self-Organizing Photonic Potential - Blue Phase

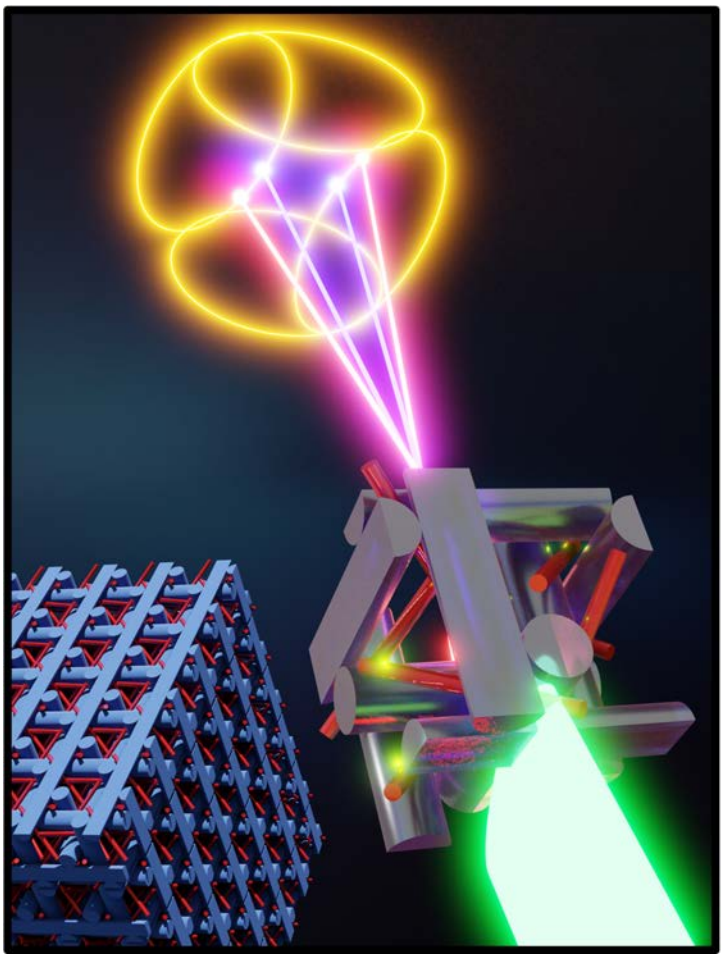

The results presented in this chapter are described in a manuscript currently under review:

E. Oton, M. Muszyński, et al. Directional Lasing from a 3D Blue Phase Photonic Crystal.

In this chapter, I will present results on a three-dimensional, self-organizing monocrystalline photonic crystal based on dye-doped blue phase liquid crystal (I). Most of the findings focus on the monocrystalline blue phase without the presence of a cavity. I will discuss visible-range light diffraction phenomena observed in this structure, known as Kossel patterns, along with their polarization properties. Furthermore, I will demonstrate how angle-resolved optical tomography can be employed to experimentally reconstruct a three-dimensional map of Kossel patterns, in agreement with numerical simulations.

Next, I will present results on directional circularly polarized lasing from the Kossel patterns, where the polarization and intensity of the lasing are strongly influenced by the excitation geometry. I will also demonstrate the feasibility of exfoliating a thin film of dye-doped blue phase (I) and show results from embedding the monocrystalline blue phase (I) inside an optical microcavity, including cavity mode splitting and double-threshold lasing.

8.1 Diffraction and Polarization Properties of Blue Phase

The blue phase (BP) is a liquid crystal phase discovered in 1888 by the botanist Friedrich Reinitzer and the physicist Otto Lehmann [280], based on the observation of two distinct melting points. Its name originates from the blue iridescence observed when the phase was first seen in a crystal extracted from the root of a carrot. This effect arises from selective light reflection - blue phase forms a three-dimensional photonic crystal with a lattice constant on the order of hundreds of nanometers, leading to the appearance of a photonic band gap. Although modern techniques allow precise tuning of the stopband in the range from ultraviolet to the entire visible spectrum [49], the historical name 'blue phase' has been preserved. Interestingly, science historians consider the discovery of BP to be the first documented observation of liquid crystals [281].

Typically, blue phase liquid crystals emerge in a very narrow temperature range, on the order of just a few degrees Celsius, between the chiral nematic (cholesteric) and the isotropic phase. There are three main types of BP, each with a different crystallographic symmetry, ordered by increasing temperature: blue phase (I) (BPI) with body-centered cubic symmetry, blue phase (II) (BPII) with simple cubic symmetry, and BPIII, which is amorphous. The microscopic structure of blue phase (III) remains unclear, although several theoretical models have been proposed [282, 283]. The lattice constant for BPI and BPII is generally in the range of approximately 200–300 nm. In this thesis, the discussion will focus almost exclusively on BPI.

From an application perspective, blue phases, due to their submillisecond response times, have been suggested as promising media for various technologies, including LCDs [284, 285], tunable color devices [286], tunable lasers [287–289], gas, strain, temperature and humidity sensors [46–50], and adaptive lenses [290, 291].

A characteristic feature of the BP is its optical isotropy on the macroscopic scale: it does not exhibit birefringence, in contrast to most liquid crystal phases. Despite this, BP remains strongly optically active. This behavior comes from its microscopic arrangement. Given the typical lattice size for blue phases, a single unit cell contains approximately 10^7 molecules, making the determination of the microscopic structure of molecules significantly difficult.

In typical chiral liquid crystal phases, such as CLC or ULH, the dominant molecular arrangement is the simple twist. In this configuration, molecules twist around a single axis (perpendicular to their long axis). This allows for continuous molecular alignment throughout the three-dimensional space without introducing dislocations.

In contrast, blue phases are composed of a more complex arrangement called the double twist helix, in which the molecules twist around two perpendicular axes (see Figure 8.1(a)). Since the double twist is most stable in the center and becomes weaker as it spreads radially, it results in the

formation of stable cylindrical areas known as double-twist cylinders (Figure 8.1(b)).

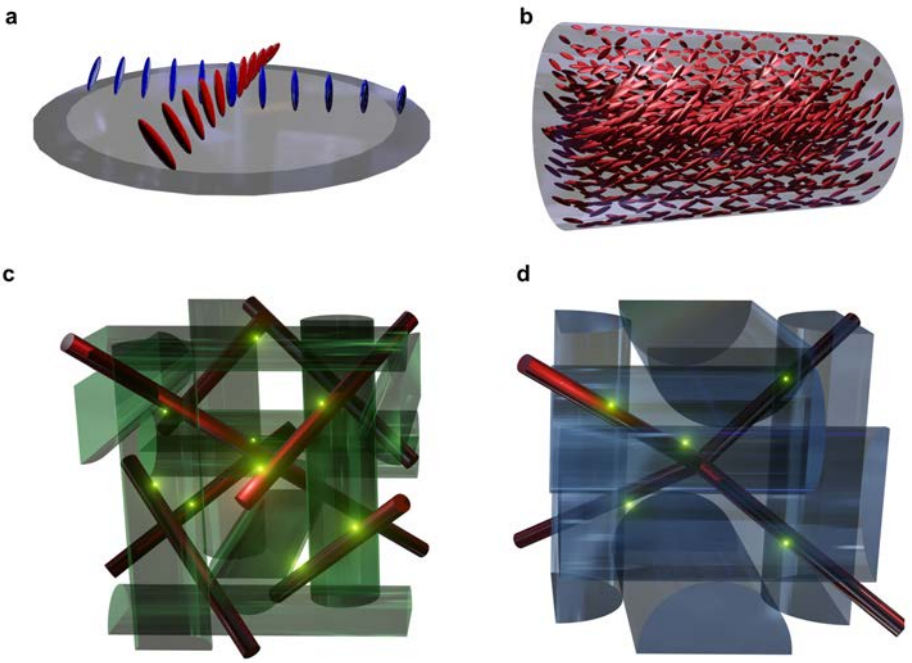

Figure 8.1: **Blue Phase Liquid Crystal as a 3D Self-Organizing Photonic Crystal.** (a) Cross-sectional view of a double-twist cylinder showing the local orientation of LC director. (b) Schematic of a full double-twist cylinder. Elementary unit cells of woodpile-like structures forming (c) blue phase (I) (body-centered cubic) and (d) blue phase (II) (simple cubic).

These cylinders self-organize into a woodpile-like structure. The unit cells of BPI and BPII are illustrated in Figure 8.1(c,d), respectively, where the double-twist cylinders are schematically represented by semi-transparent green (BPI) and blue (BPII) regions.

Unlike a simple twist structure, a double-twist configuration cannot continuously fill a three-dimensional space without formation of the defects. As a result, a network of defects—so-called disclination lines—emerges in the regions between the cylinders (indicated as red rods in Figs. 8.1(c,d)). The coexistence of these defects with the double-twist cylinders is responsible for the narrow temperature range in which blue phases exist. The local twisting force must overcome the tendency to a global defect-free configuration. Depending on which tendency dominates, the system stabilizes either into a blue phase or to a chiral nematic phase. Blue phases are often described as frustrated systems, in which locally stable structures give rise to competing interactions, preventing the realization of a global ground state. To achieve light emission and lasing, BP measured in this thesis is doped with different luminescent dyes. These emitters are schematically represented as glowing green dots in Figs. 8.1(c,d).

To extend the temperature range over which the BP remains stable, several techniques have been developed, including the polymerization of monomers and LCs in disclination lines [292, 293] and the incorporation of gold nanoparticles [294, 295]. These methods allow stabilization over temperature ranges as wide as several tens of degrees Celsius, in contrast to the typical 0.5–2°C range. Such a structure is sometimes referred to as polymer-stabilized BPs (PSBPs) However, one of the main

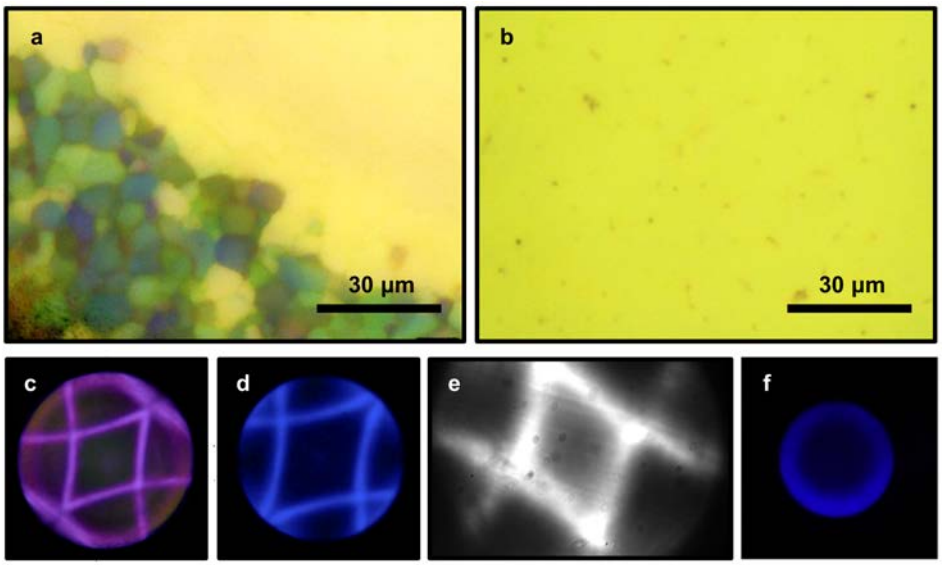

Figure 8.2: **Monocrystalline Blue Phase.** POM images of (a) the boundary between polycrystalline platelets and a monocrystalline blue phase region, and (b) a large-area monocrystalline Blue Phase (I). (c–f) Kossel patterns obtained using monochromatic light source with wavelength λ of (c,e) 405 nm and (d) 450 nm for BPI, (e) 450 nm for BPII. Photographs (c,d,f) were taken by Eva Oton (MUT) using a conoscopic microscope, while (e) was collected on rotated sample using the experimental setup shown in Figure 3.3.

challenges that remains in practical applications is the limited size of the well-oriented crystal. BP naturally tends to form in polycrystalline platelet structures (see Figure 8.2(a)), where individual crystals are only a few micrometers in size.

To fabricate large monocrystalline BP, a variety of techniques have been used, including photopatterning [296], the use of orienting layers [297], temperature gradients [298], long lasting application of electric fields [299] and microstructure confinement [300]. In this work, macroscopic BP monocrystals (over the entire LC cell), shown in Figure 8.2(b), were obtained using the method described in [117], which based on a simple surface treatment that induces weak anchoring. The monocrystalline BP is essential for realizing directional lasing over macroscopic areas, as will be demonstrated later in this chapter.

Because the blue phase forms a three-dimensional photonic crystal with a lattice period on the order of hundreds of nanometers, it is possible to observe diffraction of visible light from its crystallographic structure. For diffraction to occur, the following Bragg condition must be satisfied:

$$\lambda = \frac{2na}{\sqrt{h^2 + k^2 + l^2}} \cos(\theta) \tag{43}$$

where λ, n, and a denote the wavelength of incident light, the average refractive index (assumed to be 1.6 [117]), and the lattice constant, respectively, h, k, and l are the Miller indices and θ is the Bragg angle. The characteristic diffraction patterns (see Figure 8.2(c)) that arise are known as Kossel (or Kikuchi) patterns and can be observed in the back focal plane of the microscope objective. In standard microscopes, a Bertrand lens is used to image the reciprocal space, analogous to the k-space lens in the experimental setup shown in Figure 3.2.

Kossel patterns provide direct evidence of the crystal symmetry, confirming the presence and quality of BP, and allows for the determination of lattice parameters and orientation. Since the diffraction condition in Eq. 43 depends on λ, the probing wavelength influences the size and shape of the Kossel patterns, as shown by comparing Figs. 8.2(c,d), measured for incident light at 405 nm and 450 nm, respectively, for BPI in the [110] orientation (that is, the crystal axis [110] aligned along the observation direction). Rotating the sample within the plane of the LC cell (along the [110] axis) leads to a rotation of the Kossel patterns, as demonstrated in Figure 8.2(e), measured using the rotational sample holder in the Polariton Laboratory setup. Other differences between the patterns, beyond their rotation, are due to the different experimental configurations, including differences in the numerical apertures of the microscope objectives and magnifications used.

In general, any rotation of the sample around an axis other than the observation direction will result in a change in the relative arrangement of the Kossel lines. Furthermore, the Kossel patterns differ for the simple cubic lattice of BPII: instead of the characteristic diamond-like structure observed for BPI, BPII in the [100] orientation exhibits a ring-like diffraction pattern (Figure 8.2(f)), corresponding to an isoenergetic plane of the stopband along this crystallographic direction.

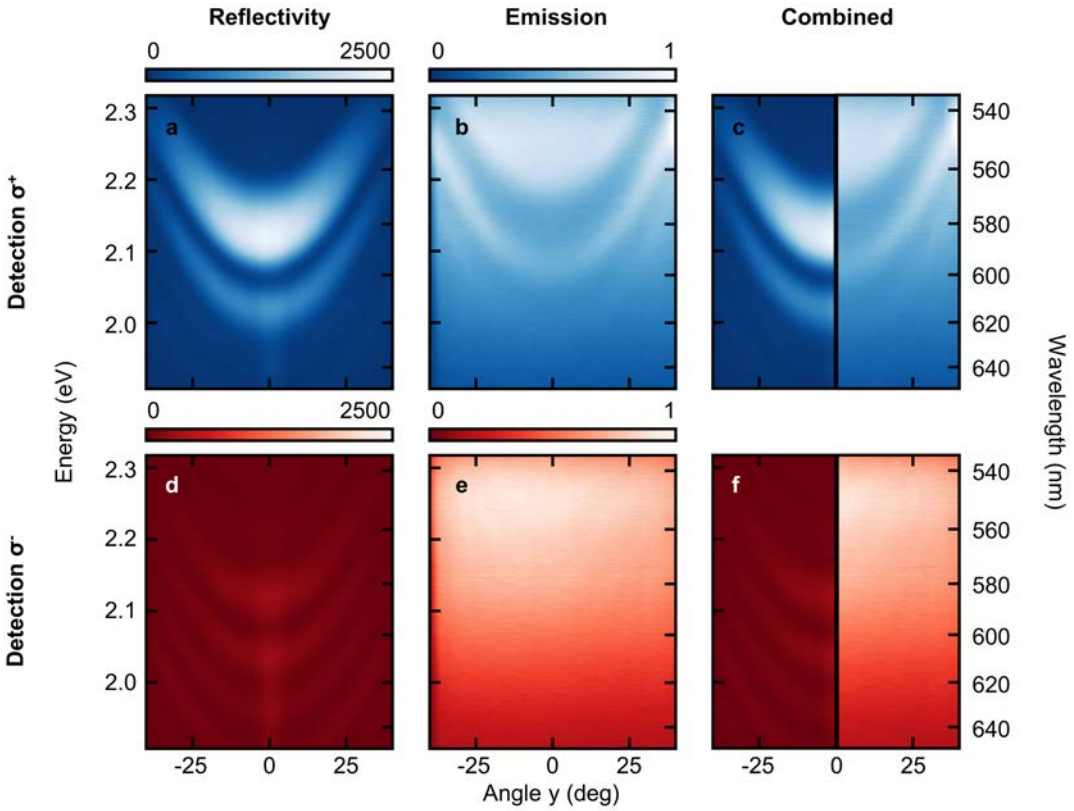

Figure 8.3: **Selective Photonic Band Gap of Monocrystalline Blue Phase (I).** Angle-resolved (a,d) reflectivity spectra, (b,e) normalized emission spectra, and (c,f) the combination of both. The top row corresponds to σ^+, and the bottom row to σ^- detection polarization. For reflectivity measurements, the color scale is normalized to the maximum intensity observed in the σ^+ polarization.

Each Kossel line corresponds to a stopband (photonic band gap) oriented according to the diffrac-

tion conditions for specific crystallographic planes. For a BP sample with a known orientation (determined from for example Kossel pattern analysis or TEM images [301]), and knowing the energy of the particular stopband center, one can determine the lattice constant a using Eq. 43. Because of the microscopically chiral structure of BP, the band gaps themselves exhibit strong polarization-dependent properties.

Figure 8.3 presents angle-resolved spectra of BPI with [110] orientation (from this point onward, only this orientation of BPI will be considered), doped with P580 dye. In Figure 8.3(a), showing the reflectivity measurement for circular polarization σ^+ (matching the chirality of the BP), a distinct stopband is visible, approximately 100 meV wide and centered at normal incidence around 2.14 eV. In the corresponding emission measurement (Fig. 8.3(b)), since the dye molecules are embedded within the photonic crystal, the collected light is suppressed within the stopband spectral region, resulting in significantly reduced emission intensity compared to the signal outside the band gap. At the edges of the stopband, a slight enhancement of emission is observed, associated with an increased photonic density of states (this will be discussed in more detail in the section on Directional Lasing). The effect of the stopband is clearly visible in the combined reflectivity and emission maps shown in Figure 8.3(c).

In contrast, the influence of the stopband is negligible for the opposite circular polarization. To illustrate this, the maximum intensity scale in the σ^- reflectivity measurement (Fig. 8.3(d)) has been fixed to the same value as in Fig. 8.3(a). Only a periodic signal in energy is observed, originating from the Fabry-Pérot etalon effects inside the LC cell. Incidentally, by analyzing the free spectral range of these parabolas, one can determine the cell thickness d, and thus the number of unit cells of BP between the substrates. For this cell, $d \approx 3.8$ µm, corresponding to 11 lattice constants. The normalized emission spectrum for the σ^- polarization (Fig. 8.3(e)) shows a uniform intensity distribution, so in the combined map (Fig. 8.3(f)), the presence of the stopband is not noticeable.

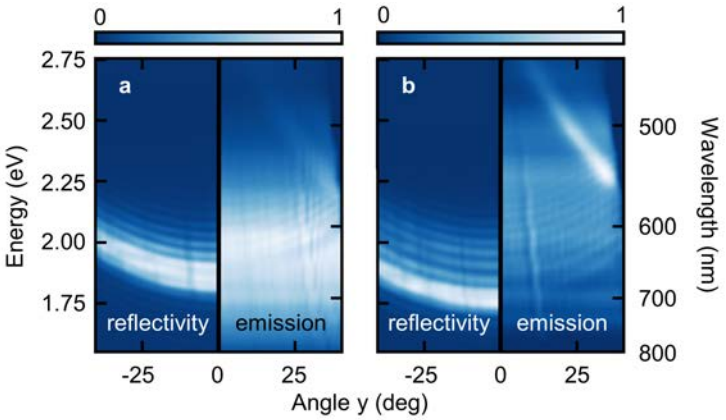

Figure 8.4: **Tunability of Optical Properties in Blue Phase (I).** Normalized, combined angle-resolved reflectivity and emission spectra for two different samples: (a) a sample with a smaller lattice constant doped with Coumarin 540, designed to spectrally match the peak emission with the photonic band gap; and (b) a sample with a larger lattice constant doped with Coumarin 522, prepared to match the emission maximum with one of the Kossel lines.

By controlling the helical twisting power of the LC mixture, as described in [117], it is possible to tune the lattice constant and orientation of monocrystalline BP, achieving lattice parameters for BPI(110) ranging from 170 nm up to nearly 400 nm [117]. The second degree of freedom in

controlling the emission from BP is the choice of dye. Figure 8.4 shows the combined reflectivity (left side of each panel) and emission (right side of each panel) spectra for two samples differing in these parameters, measured in σ^+ polarization for better contrast.

Based on the stopband center (approximately 1.86 eV), the sample presented in Figure 8.4(a) has a lattice constant $a = 293$ nm and is doped with Coumarin 540 laser dye. One can observe that the emission maximum of the dye overlaps with the edge of the photonic stopband. This spectral overlap is utilized in blue phase band-edge lasing [287, 288, 302]. In emission measurement, an additional enhanced signal appears as the line, stretching from 2.75 eV (at normal emission) down to 2.25 eV (at the aperture limit). This feature is, in fact, an enhanced emission occurring at the edge of a different stopband originating from a crystallographic plane distinct from the one responsible for the main stopband at 1.86 eV (associated with the [110] direction). Thus, this line represents one of the cones of light whose isoenergetic cross-section forms a Kossel pattern. Although the origin of both stopbands is the same (diffraction on 3D photonic crystal), their appearance in angle-resolved spectroscopy depends on the direction of observation. For simplicity in the following discussion, these angle-resolved cross-section through the cones of light will also be referred to as Kossel lines.

By selecting a different dye, the emission can be tuned to a particular Kossel line. Figure 8.4(b) shows the results for a sample with a lattice constant $a = 310$ nm, doped with Coumarin 522, whose emission maximum is shifted toward shorter wavelengths. Due to this spectral matching, a much more pronounced enhancement of emission at the Kossel line edge can be observed.

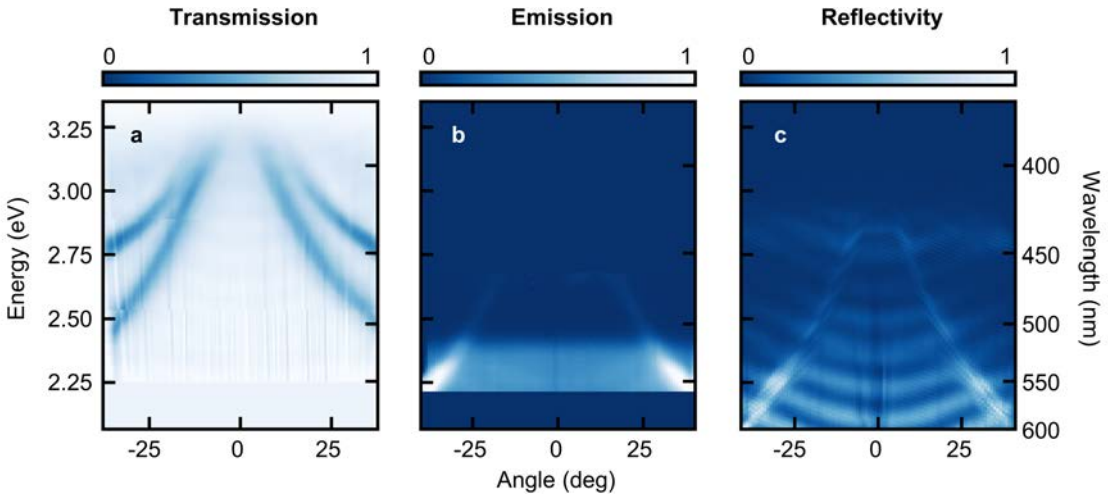

Figure 8.5: **Comparison of Three Experimental Configurations for Kossel Pattern Measurements in Angle-Resolved Spectroscopy.** Normalized (a) transmission, (b) emission, and (c) reflectivity spectra measured on different samples.

Angle-resolved spectroscopy is a powerful tool for observing Kossel lines. Typically, Kossel patterns are studied using relatively narrow-band light — broader sources, such as LEDs with linewidths of hundreds of nanometers, cause the patterns to blur and merge. The method presented here allows for the use of polychromatic light (in reflectivity, transmission, and even emission configurations), providing access to a diffraction pattern with many wavelengths simultaneously. Furthermore, this method enables simultaneous investigation of the dependence of stopband energy on angle, without the need to physically rotate the detector or sample, as required in previous approaches [303]. Figure 8.5 presents a comparative overview of these three experimental configurations on three different

samples (hence the different shapes of the Kossel lines), all measured in σ^+ polarization.

In Figure 8.5(a), normalized white-light transmission is shown. In this configuration, Kossel lines (with the sample rotated to reveal four lines) appear as spectral regions of reduced intensity: incident light that satisfies the Bragg condition is diffracted away and thus not transmitted, whereas other rays pass through the sample to the detector.

In emission measurements (Figure 8.5(b)), similar to what was shown in Figure 8.4, the dye embedded within the BP structure is excited by a laser and emits light. Rays that do not meet the Bragg condition are emitted isotropically, while those that do satisfy it undergo multiple internal reflections and are eventually emitted from the Kossel line edges, appearing as an enhanced intensity compared to the background isotropic emission.

Finally, in reflectivity measurements (Figure 8.5(c)), the Kossel lines manifest as non-zero signal superimposed on the background etalon fringes.

The results discussed above allow for the observation of angle-resolved Kossel lines but do not yet provide Kossel patterns in the form typically used in the liquid crystal community (i.e., reciprocal space images). To achieve this, one can perform 3D angle- and energy-resolved tomography. Figure 8.6 presents the result of transmission tomography in σ^+ polarization, shown from different perspectives. For clarity, Figures 8.6(a-e) display only selected isoenergetic planes stack together, although the actual spectral resolution of the method is higher and is limited only by the spectrometer's resolution.

In the highest-energy layer, it can be seen that by combining the angle-resolved spectra, a diamond-shaped Kossel pattern is reconstructed. Rotating the entire 3D map is equivalent to an experimental rotation of the sample. This can be useful for determining the conditions for directional lasing fixed by excitation laser geometry discussed in the next section.

Figures 8.6(f-j) and 8.6(k-o) present cross-sections along two orthogonal directions, fixed with respect to the reader's perspective. This allows to observe how the angle-resolved Kossel lines evolve as the sample is rotated — for example, to identify the angular conditions under which four lines are visible (e.g., in Figure 8.6(m)) versus when only two lines are observed (e.g., in Figure 8.6(f)), and estimate how these conditions change the overlap between Kossel lines and gain profile of the dye.

Obtaining three-dimensional angle- and energy-resolved tomography of BP allows for the observation and analysis of Kossel patterns for any wavelength of incident light in the visible spectrum. Figure 8.7 presents selected normalized momentum-space images from Fig. 8.6, for the energies indicated in the top right corner of each panel. Below each experimental panel, the corresponding simulated Kossel patterns are shown, based on the method described in [304, 305]. The modeling relies on an orthographic projection of cones of light determined by the Bragg condition for given reciprocal lattice vectors. In the simulation, a constant refractive index $n = 1.6$ was assumed. The extracted value of the lattice constant was 297 nm, which shows good agreement with the lattice constant determined for this sample based on Eq. 43 for the photonic band gap along the [110] direction, where $a_{110} = 302$ nm. In the simulation panels of Figs. 8.7(h,m), the Kossel lines associated with specific crystallographic planes are additionally labeled.

It is worth highlighting some further advantages of this method. First, it allows to obtain many Kossel patterns for different wavelengths using a single light source. Typically, a single LED allows the acquisition of only one Kossel pattern, so multiple LEDs with different central wavelengths are used. However, because of their broad spectral linewidth, the resulting Kossel patterns with relatively wide lines are available for crystallographic structure analysis. In contrast, here the Kossel lines are significantly narrower (since patterns form for well-defined wavelengths filtered by the spectrometer), and the number of Kossel patterns that can be compared with the simulation is much larger. One could propose using a tunable laser source instead, but in my experience, coherent light sources

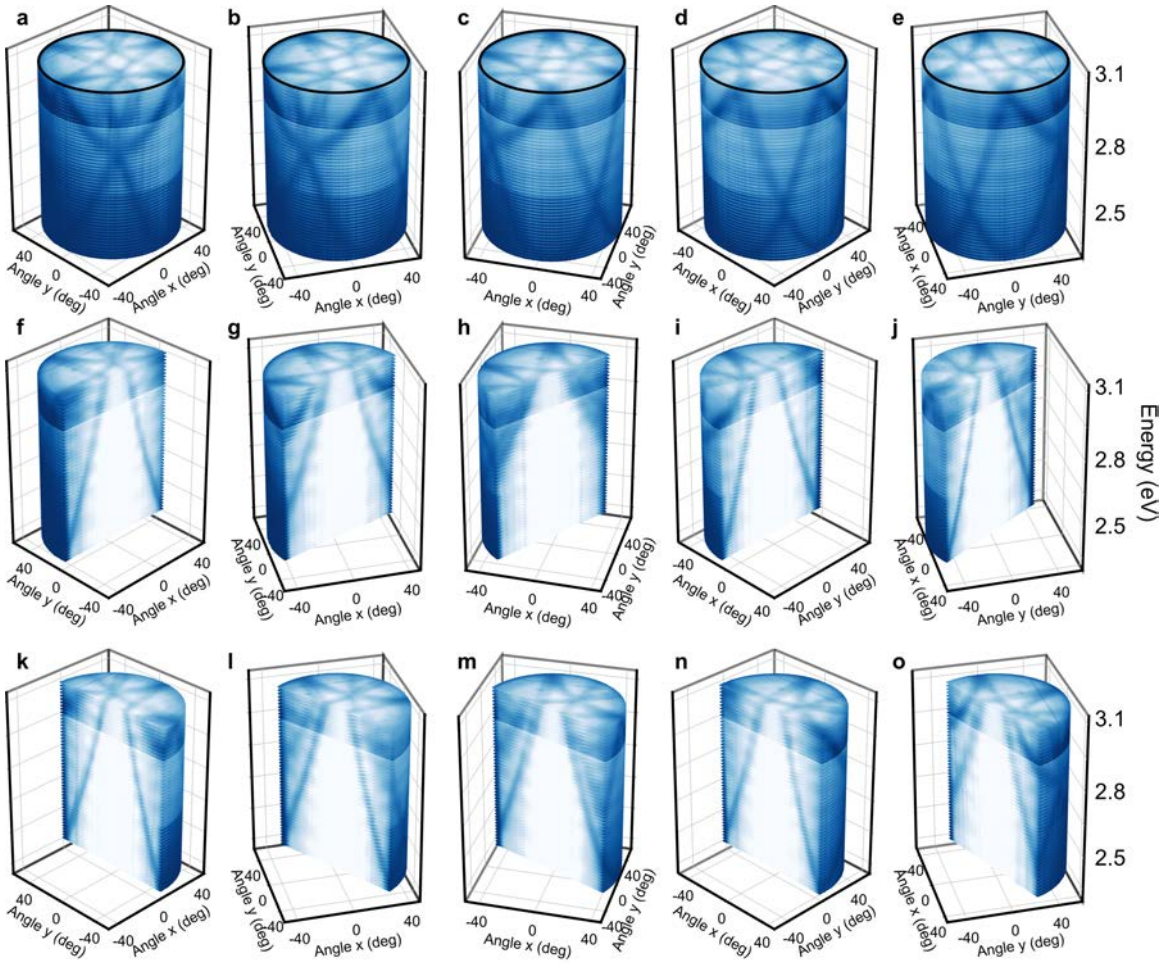

Figure 8.6: **Experimental 3D Reconstruction of Kossel Patterns via Polarization-Resolved Angle- and Energy-Resolved Transmission Tomography.** (a–e) Normalized three-dimensional Kossel pattern maps, shown at rotation angles of sample frame of 0°, 30°, 60°, 90°, and 120° with respect to the viewer. (f–j) and (k–o) corresponding cross-sections taken along two perpendicular directions, highlighting the internal structure of the reconstructed patterns.

produce additional interference speckles that blur the image. These advantages make this method more precise and promising for use in devices such as direction-sensitive stress sensors based on BP elastomers [50, 306, 307].

An interesting property of crystals is crystal twinning, which refers to the situation when two or more adjacent crystals share parts of their crystal lattice at the interface, being related by mirror reflection or other symmetry operation [308]. In blue phases, this effect can also occur as a result of energy minimization during frustrated self-assembly process [309, 310], and the analysis of the Kossel pattern proves to be an excellent method for its characterization. Figure 8.8(a) shows a normalized reciprocal space image from tomography measurements of a sample exhibiting crystal twinning, along with a modeled Kossel pattern (Fig. 8.8(b)). Based on the simulation, it can be seen

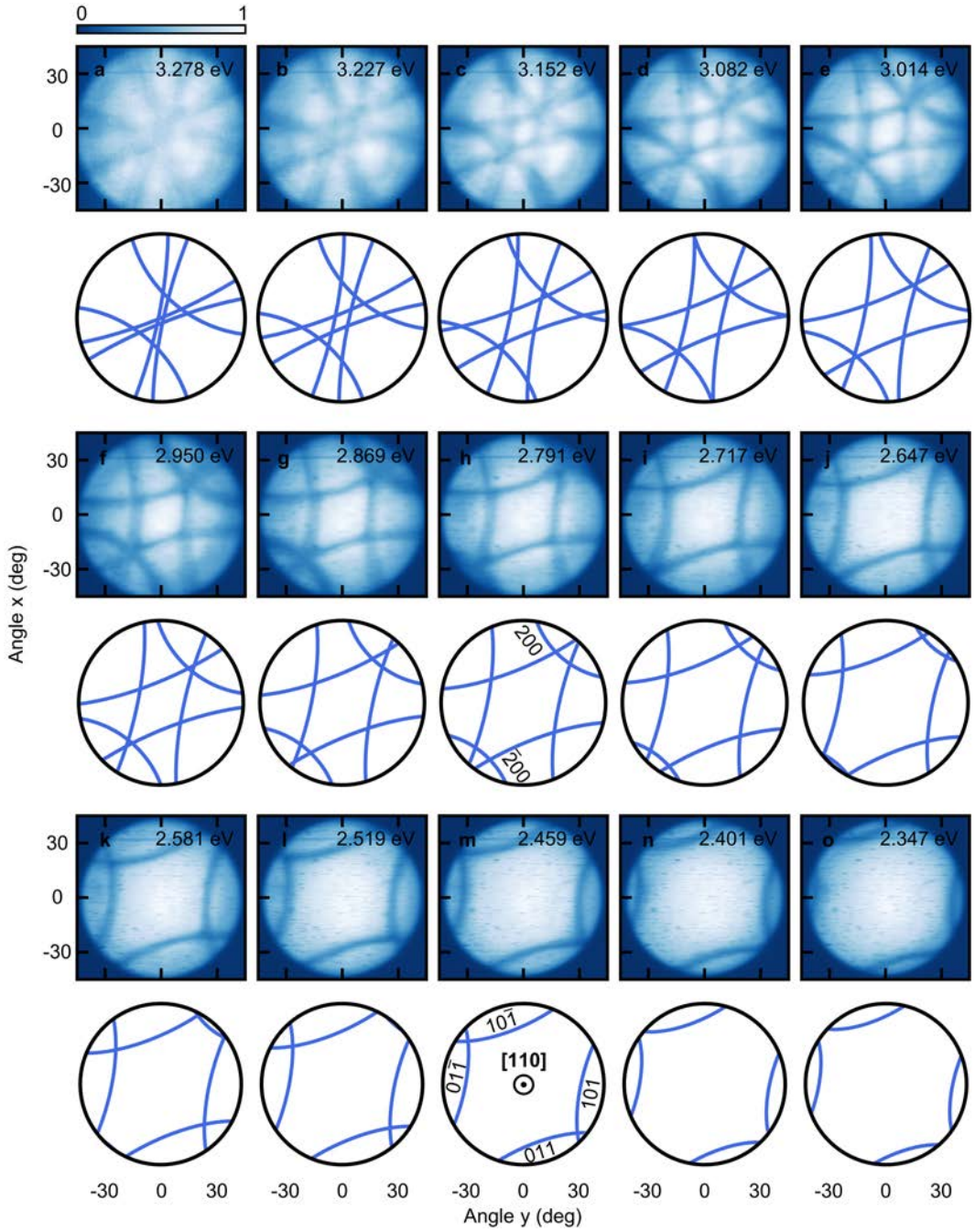

Figure 8.7: **Observation of Kossel Patterns at Arbitrary Energies.** Isoenergetic planes extracted from Figure 8.6 (top rows) for selected energies (indicated in the top-right corners of each panel), shown alongside the corresponding simulated patterns (bottom rows).

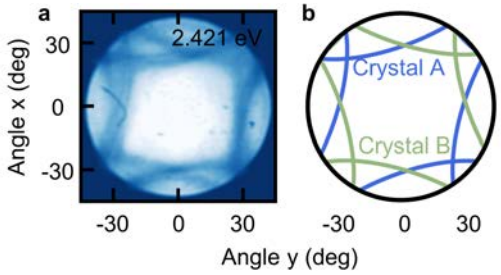

Figure 8.8: **Blue Phase Twinning.** (a) Isoenergetic reciprocal space image of a twinned Blue Phase I crystal. (b) Simulated Kossel patterns corresponding to the twinned crystal structure.

that the coexisting crystals A and B are rotated by 90 degrees relative to each other. Twinned blue phase crystals can also occur at other relative orientations [310], and angle-resolved tomography appears to be a promising technique for the precise characterization of this phenomenon.

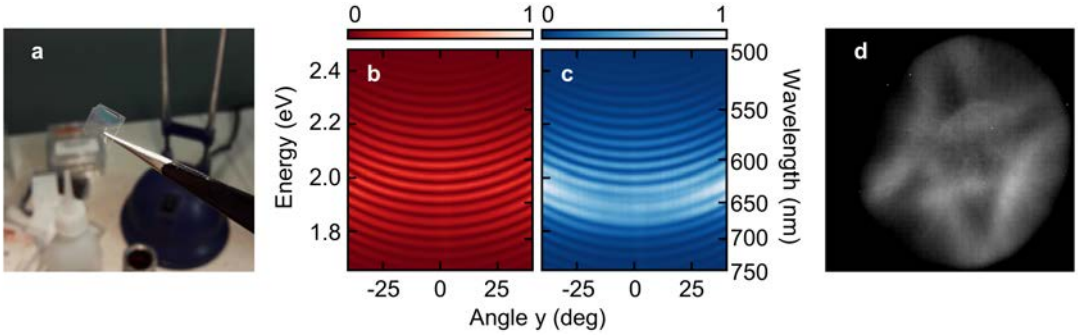

Figure 8.9: **Exfoliated Thin Film of Stabilized Blue Phase (I).** (a) Photograph of a macroscopic thin film of BPI. (b–c) Normalized angle-resolved reflectivity spectra for (b) σ^+ and (c) σ^- polarizations, showing a selective photonic band gap centered around 1.9 eV. (d) Kossel pattern measured from the thin film, confirming its 3D photonic crystal structure.

Another interesting possibility offered by dye-doped monocrystalline polymerized BPI structures is their exfoliation into freestanding thin films [49,50,306]. Figure 8.9(a) shows a photograph of such an exfoliated film held by tweezers, where colorful reflections are associated with selective reflection from the stopband. To confirm this, Figures 8.9(b,c) present normalized angle-resolved reflectivity spectra of the thin film, respectively. In both polarizations, interference fringes due to etalon effects are visible, stronger than those observed for BP confined within a glass cell, because of the higher refractive index contrast. However, a stopband around 1.9 eV appears only in the polarization that matches the handedness of the liquid crystal mixture. To fully confirm the presence of the BP structure in the exfoliated film, the measured Kossel pattern is shown in Figure 8.9(d).

In addition to the previously demonstrated applications of these freestanding films in stress sensing [307,311], chemical solvent detection [306], and photoswitchable bandgaps [312], these structures can also exhibit optically pumped lasing [306, 307, 313]. Therefore, they are a promising platform for Kossel pattern lasing experiments, which will be discussed in the next section.

8.2 Directional Kossel Pattern Lasing

Lasing from dye-doped blue phases has been demonstrated based on two distinct mechanisms. The first mechanism involves random lasing, where, similarly to Anderson localization for electrons, light is confined in closed-loop paths between scattering defects, which act as effective optical cavities. In such systems, optical feedback is achieved without the need for conventional distributed feedback lasers or Fabry–Pérot cavities — no long-range periodically ordered structures or reflective surfaces are required. In the case of blue phase random lasing, the scattering centers are the BP platelets [241, 289], and the resulting laser emission typically exhibits a multi-peak character, with each lasing peak corresponding to a different optical path length within closed loops.

The second mechanism is photonic band edge lasing. This phenomenon occurs in LC phases that possess a periodic structure, and thus exhibit a photonic bandgap. For instance, CLC feature a helical periodicity that gives rise to a Bragg reflection: circularly polarized light with the same handedness as the helix is forbidden from propagating at wavelengths within the photonic bandgap (similar to what is shown in Fig. 8.3). At these energies spontaneous emission is suppressed and the photon group velocity decreases to near zero at the band edge, resulting in an increased photonic density of states, which facilitates mirrorless lasing driven by the band edge effect [314,315]. Lasing phenomena based on this mechanism have also been reported in other chiral LC phases, including the blue phases [286, 288, 315, 316], the chiral smectic phase [317] and the twisted grain boundary phase [318]. Furthermore, lasing tunability can be achieved by changing the stopband energy under external stimuli such as an electric field [319,320], temperature [321,322], or mechanical stress [323].

To the best of my knowledge, lasing from BP structures has so far been demonstrated only under symmetrical excitation geometries (pump spot), without detailed investigation of how excitation geometry influences lasing properties. Typically, lasing was observed at the edges of the stopband, either on the long- or short-wavelength side [287, 324], and along directions aligned with crystallographic planes. Even in cases where multiple stopbands were involved simultaneously [288], the emission direction remained consistent with the periodicity of the crystal. Furthermore, the polarization of the laser emission was found to match the BP structure handedness [316].

In the results presented below, both the excitation geometry and the lasing angular and polarization properties differ from those previously reported.

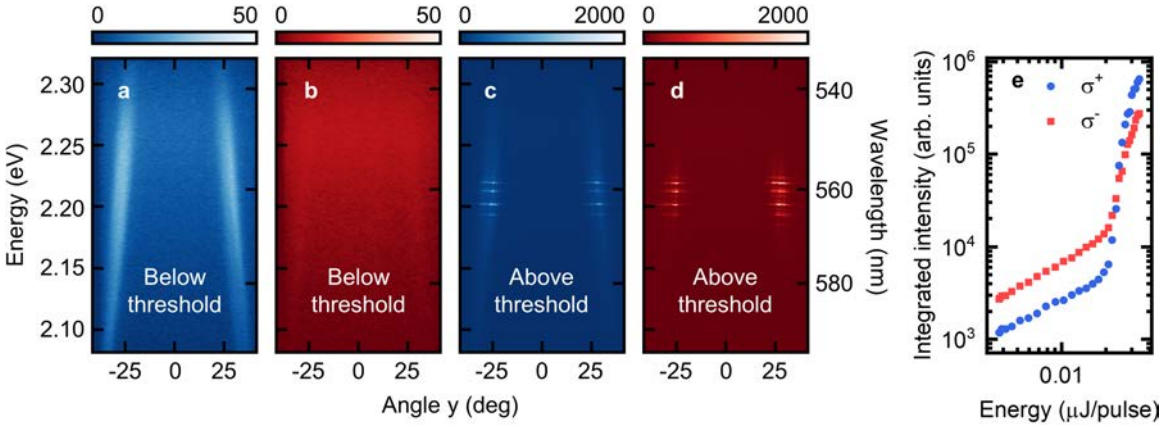

Figure 8.10: **Kossel Pattern Lasing.** Angle-resolved emission spectra collected (a,b) below and (c,d) above the lasing threshold. Panels (a,c) correspond to σ^+, while (b,d) to σ^- detection polarization. (e) Integrated emission intensity as a function of excitation pulse energy for both polarizations.

To extend the photon amplification path and define the lasing directions, the excitation objective from Figure 3.3 was replaced with a cylindrical lens that focused the laser beam into a stripe approximately 1 mm × 50 µm in size. Figure 8.10(a–d) shows the angle-resolved emission spectra of the dye-doped BPI sample excited in this configuration. Figures 8.10(a,b) present results collected below the lasing threshold, detected in σ^+ polarization (matching the handedness of the BP) and σ^- polarization (opposite to the BP handedness), respectively. For comparison, the intensity scale was kept the same for both polarizations. Similarly to what was observed in Fig. 8.3 and Fig. 8.4, spontaneous emission in the polarization that matches the BP handedness is enhanced along the Kossel lines, while for the opposite polarization it remains nearly isotropic. Above the lasing threshold, in the σ^+-polarized photoluminescence spectra (Figure 8.10(c)), narrow lasing peaks appear at a wavelength of approximately 2.2 eV, superimposed on the Kossel lines. Interestingly, these lasing peaks also emerge in the σ^--polarized spectra (Figure 8.10(d)), even though no enhancement of spontaneous emission is observed there.

The plot of integrated intensity within a narrow spectral region around one of the lasing peaks, as a function of excitation pulse energy, shows a clear lasing threshold at approximately 0.23 µJ for both polarizations, as illustrated in Figure 8.10(e).

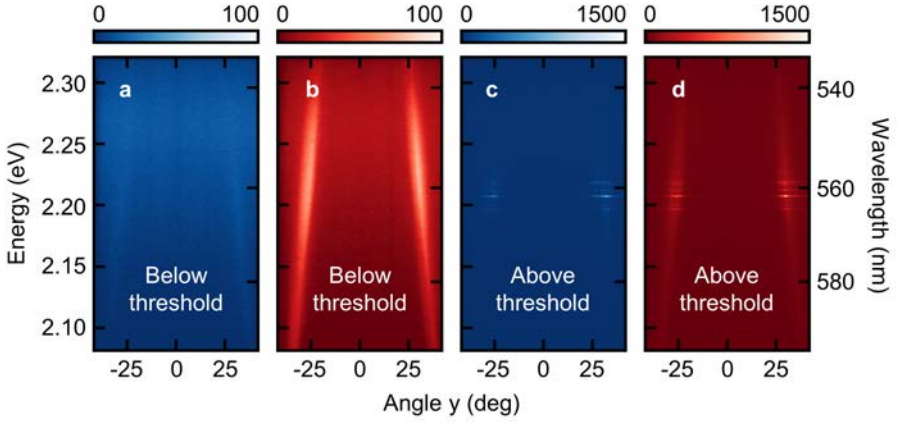

Figure 8.11: **Kossel Pattern Lasing with Opposite Chirality.** Angle-resolved emission spectra collected for different sample with opposite chirality of chiral dopant (a,b) below and (c,d) above the lasing threshold. Panels (a,c) correspond to σ^+, while (b,d) to σ^- detection polarization.

To verify the possibility of achieving lasing with opposite circular polarization properties, a sample with a different chiral dopant, exhibiting the opposite handedness, was investigated. Figure 8.11 shows the angle-resolved photoluminescence spectra measured above the lasing threshold for this sample, detected in both σ^+ and σ^- polarizations. The reversal of circular polarization properties is clearly observed: below the threshold, spontaneous emission is enhanced along the Kossel lines only in the σ^- polarization, whereas above the threshold, lasing peaks appear in both σ^+ and σ^- polarizations.

Because Kossel patterns, which result from diffraction on a periodic structure, rotate with the sample, the lasing emission associated with the BP crystalline structure is also affected. Figure 8.12 presents normalized reciprocal space images measured above the lasing threshold for both circular polarizations and different sample rotation angles. In the top row (Fig. 8.12(a)), a scheme of the experiment is shown. The green arrows indicate the direction of the long axis of the laser excitation stripe, and the angle θ corresponds to the sample rotation relative to this axis, labeled above each

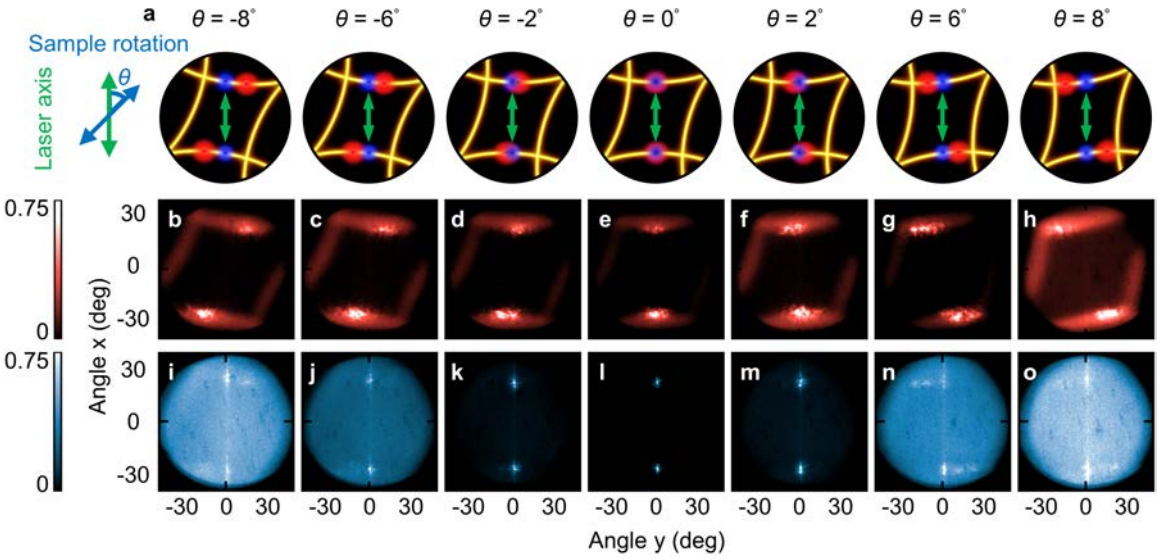

Figure 8.12: **Rotation of Directional Lasing in Kossel Patterns.** The sample rotation angle θ is changed, as schematically shown in the top row. Normalized reciprocal-space emission images collected above the lasing threshold for σ^+ (middle row) and σ^- (bottom row) polarized light. The σ^+ lasing signal follows the rotation of the sample, whereas the σ^- lasing remains fixed relative to the excitation beam position.

column. Additionally, schematic circles illustrate the orientation of the Kossel patterns relative to the laser axis, as well as the positions of the lasing signals in reciprocal space, with red indicating σ^+ and blue indicating σ^- polarizations. The rotation angle $\theta = 0°$ was chosen such that the lasing signals for both polarizations are aligned with the excitation stripe.

The middle row of Figure 8.12 shows measurements with σ^+ detection polarization. Two lasing spots, superimposed on enhanced spontaneous emission along the Kossel lines, are clearly visible. The lasing signal is strongest when the sample is aligned at $\theta = 0°$, which means that the lasing spots are aligned with the excitation stripe. As the sample rotates, both the Kossel pattern and the lasing spots rotate together. Interestingly, the lasing spots rotate in the same direction as the Kossel lines but with an angular displacement approximately three times larger than the actual sample rotation.

The bottom row of Figure 8.12 presents measurements with σ^- detection polarization. Here, lasing is also observed along the directions of the Kossel lines, but the effect of sample rotation is markedly different. At $\theta = 0°$, the two σ^--polarized lasing spots exhibit the strongest intensity and occupy the same positions in reciprocal space as the σ^+ lasing signals — at the intersection points of the Kossel lines with the long axis of the excitation laser stripe. However, the σ^- lasing spots are much more confined in the angle space. Upon sample rotation, the lasing intensity gradually decreases, but unlike the σ^+ case, the σ^- lasing spots do not rotate with the sample; instead, they remain fixed at the original intersection points of the Kossel lines and the laser stripe axis.

To further investigate the evolution of the Kossel patterns lasing behavior, emission measurements were performed as a function of the full sample rotation at a fixed excitation pulse energy. The results are presented in Figure 8.13. Because, as shown in Figure 8.12, lasing in σ^+ polarization rotates at

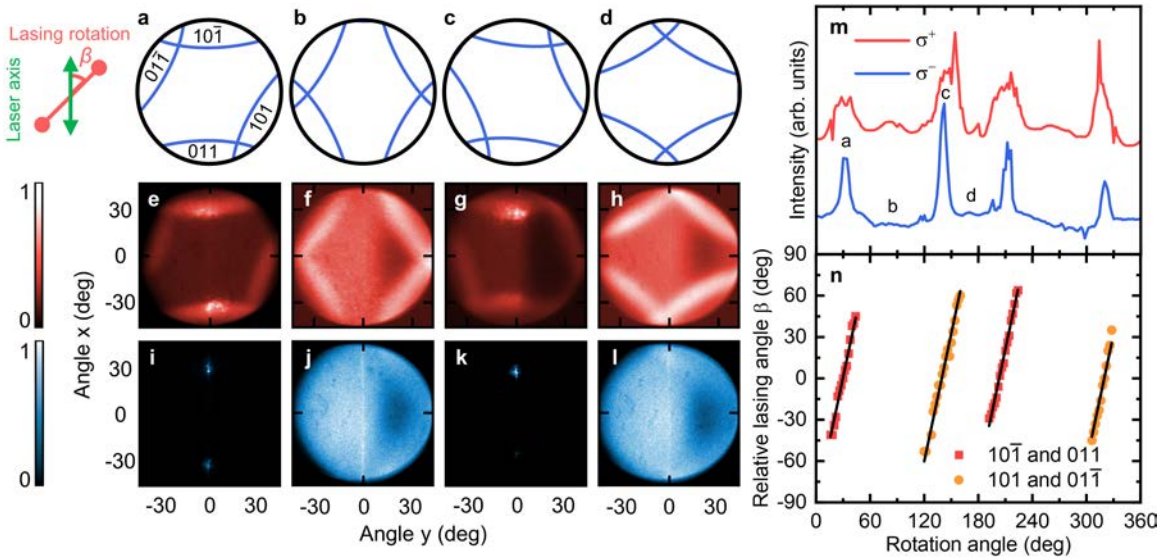

Figure 8.13: **Influence of Sample Rotation on Lasing Intensity.** Reciprocal-space images collected for different sample rotation angles Θ. (a–d) Simulated Kossel patterns for four different sample orientations. Corresponding normalized emission images collected at a fixed excitation energy for (e–h) σ^+ and (i–l) σ^- polarizations. (m) Integrated emission intensity as a function of rotation angle Θ for σ^+ (red) and σ^- (blue) polarizations. (n) Rotation angle of the lasing signal β, measured relative to the excitation laser axis, plotted as a function of Θ for σ^+ polarization. Red and orange points correspond to the Kossel lines where lasing occurs. Black lines represent a global linear fit with a shared slope across all four datasets.

a higher angular rate relative to the sample rotation, an angle β was introduced. This angle defines the orientation in the reciprocal space between the long axis of the laser excitation stripe and the axis determined by the line intersecting the two σ^+ lasing spots (see the inset in the top left corner). For clarity, to ensure that the complete rotation measurement spans the range of 0 to 360 degrees, the offset rotation angle is introduced as $\Theta = \theta + 30°$.

Figures 8.13(a–d) show simulated Kossel patterns for four qualitatively different sample rotation angles, $\Theta = 30°$, 80°, 136°, and 168°, respectively. Figures 8.13(e–h) and Figures 8.13(i–l) present the corresponding measured reciprocal space images of the emission collected with σ^+ and σ^- detection polarizations, respectively. In Figure 8.13(a), the Kossel lines associated with specific crystallographic planes are labeled.

For Figures 8.13(e,i,g,k), the lasing behavior qualitatively resembles the results shown in Figures 8.12(e,l), where in both polarizations the lasing signals appear at the intersections of the laser stripe axis with the Kossel lines. Because this lasing is highly sensitive to the tilt of the sample with respect to the excitation beam, even slight fluctuations during rotation introduce asymmetry between the two lasing points, visible in Figures 8.13(g,k).

As the sample rotates and the tangent of the Kossel lines becomes less perpendicular to the long axis of the laser beam, the lasing signal gradually weakens and eventually falls below the lasing threshold. This is evident in Figures 8.13(j,h,l), where instead of lasing, enhanced spontaneous emission along the Kossel lines (for σ^+ polarization) or a more homogeneous background signal (for

σ^- polarization) is visible. A similar situation might occur in Figure 8.13(f), although no clear evidence is seen due to the numerical aperture limit.

The emission intensities integrated over the selected region for both polarizations as a function of Θ are plotted in Figure 8.13(m). In the analysis, the integration area remained fixed and the σ^+ data set was rotated to consistently integrate the lasing signal (if visible). The measurements corresponding to Figures 8.13(a–l) are indicated with letters. For both polarizations, four distinct intensity peaks are visible, each corresponding to a different Kossel line intersecting the laser stripe axis perpendicularly in reciprocal space. The σ^+ peaks are broader compared to the narrower σ^- peaks, consistent with observations from Figure 8.12, where σ^- lasing was found to be more sensitive to sample rotation and therefore more likely to drop below the lasing threshold.

Figure 8.13(n) shows the manually determined values of the angle β as a function of Θ for the σ^+ polarization, based on measurements where it could be reliably extracted. The lasing signals associated with the same families of crystallographic planes are plotted in red and orange. In contrast, for σ^- polarization (not shown), $\beta(\Theta)$ remains constant at 0 degrees.

For the σ^+ polarization, $\beta(\Theta)$ does not follow a perfectly linear dependence due to the arc-shaped paths of the lasing signals along the Kossel lines. Nevertheless, for each of the four data sets, linear dependences with a common slope (black lines) were fitted. The fitted slope is $a_{\text{fit}} = 3.09 \pm 0.05$, indicating that within the observable lasing range, the σ^+ lasing signals in the BPI [110] orientation rotate at an angular rate approximately three times greater than that of the sample.

These results demonstrate that Bragg diffraction influences the photoluminescence of dye-doped BPs both below and above the lasing threshold, and confirm that the laser emission follows diffraction from the crystal planes. Lasing occurs not only in the σ^+ polarization, matching the handedness of the BP crystal, but also in the σ^- polarization, exhibiting distinct polarization-dependent behaviors. While σ^+ lasing rotates together with the sample, σ^- lasing remains fixed at the intersections of the Kossel patterns with the excitation stripe direction, regardless of the sample rotation.

Although circularly polarized lasing has previously been observed in chiral photonic crystals, the coexistence of two types of lasing with opposite circular polarizations and distinct directionalities relative to the excitation geometry is a puzzling and novel observation. One possible explanation is that this excitation geometry enables the formation of two types of resonators: a one present only for polarization matching the crystal chirality and a second beam-stripe-induced resonator (or reservoir of excitated particles), effective for both polarizations. For σ^+ polarization, the coexistence of both resonators leads to enhanced amplification, effectively resulting in lasing. In contrast, for σ^- polarization, only the beam-stripe resonator is present, and the spontaneous emission distributed along the Kossel pattern — partially depolarized from σ^+, while preserving its momentum — provides the additional energy necessary to cross the lasing threshold.

An alternative interpretation relates to the observation that σ^+ lasing occurs near the arc region of the Kossel lines that are perpendicular to the long axis of the excitation stripe, suggesting the formation of the resonator in between crystal planes. This could also explain why the σ^- lasing, locked to the beam-stripe-induced reservoir, drops below the lasing threshold much more easily than the σ^+ lasing, which tracks the sample rotation.

A complete explanation of the Kossel pattern lasing behavior requires a robust theoretical analysis beyond the scope of this thesis, but I hope that these observations will inspire such future studies.

8.3 Blue Phase in Optical Microcavity

The considerations discussed so far in this chapter covered blue phases confined within glass cells, without the presence of mirrors. In such a configuration, the three-dimensional periodic structure of the photonic crystal provided an effective resonator; however, light was not treated as an analog

of a massive particle in an additional photonic potential, as in previous chapters. In this section, I present an attempt to integrate blue phase (I) with an LCMC structure (BP-LCMC) to create an analog of a massive particle in a 3D photonic potential, similar to the cases discussed in the chapters on ULH and torons.

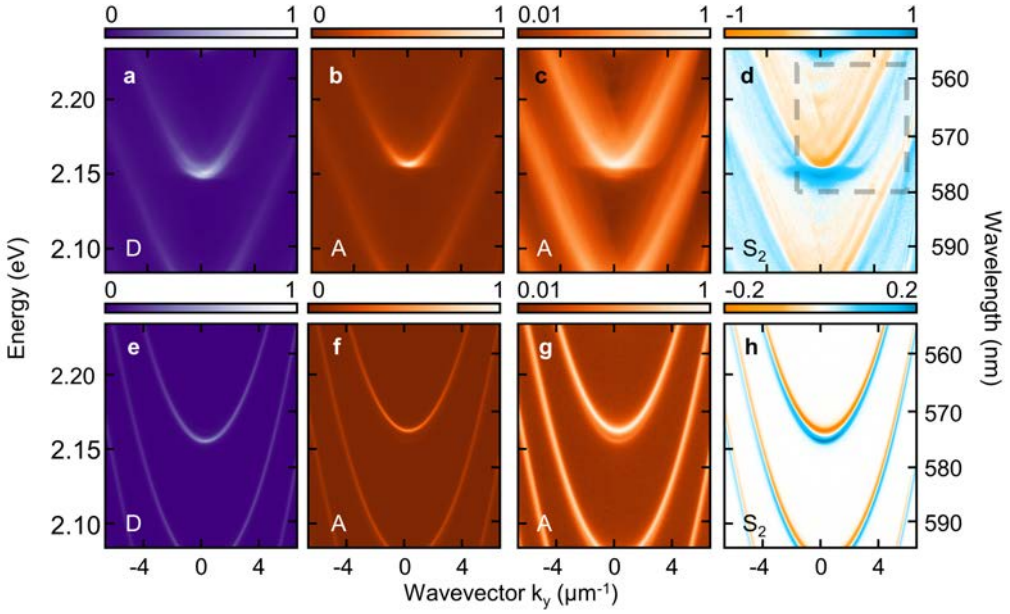

Figure 8.14: **Blue Phase in LCMC as a Candidate for a Self-Organizing Three-Dimensional Photonic Potential for Massive Photons.** Momentum-resolved emission spectra collected for (a,e) diagonal, (b,c,f,g) antidiagonal polarizations, and (d,h) represented by the Stokes parameter S_2. Data in the top row were acquired using *cw* laser excitation, while the bottom row corresponds to pulsed excitation. Panels (c,g) are shown on a logarithmic intensity scale. The dashed transparent rectangle on (d) marks a region with features resembling zone-folded bands; however, based on comparison with the pulsed excitation results, these are attributed to experimental artifacts.

Figure 8.14 shows the angle-resolved emission spectra of dye-doped BP-LCMC excited with a *cw* laser (top row) and a nanosecond pulsed laser (bottom row). Comparing the spectra for diagonal and antidiagonal polarizations (Figures 8.14(a,b), respectively), one can observe small energy splitting between broad spectral cavity modes. The spectrum for antidiagonal polarization is shown again on a logarithmic scale in Figure 8.14(c), where this broadening of the lines is clearly visible. Expressing these spectra using the Stokes parameter S_2 (Figure 8.14(d)), one can observe that the broadened modes form features resembling multiple parabolas shifted in wavevector, as expected for a weakly interacting periodic lattice. One well-visible parabola is indicated by the dashed gray rectangle. Comparison of the wavevector value at its energy minimum, k_y=2.5 μm^{-1}, with the expected value of about 10 μm^{-1} for typical large-period BPI structures (around 300 nm), shows that these parabolas do not originate from neighboring Brillouin zones.

Comparing these results with experiments using pulsed excitation (Figures 8.14(e-h)), it is evident that although the mode splitting between D and A polarizations remains present, the line broadening and additional parabolic features in the S_2 Stokes parameter spectrum are experimental artifacts,

likely attributed to thermal effects associated with *cw* excitation.

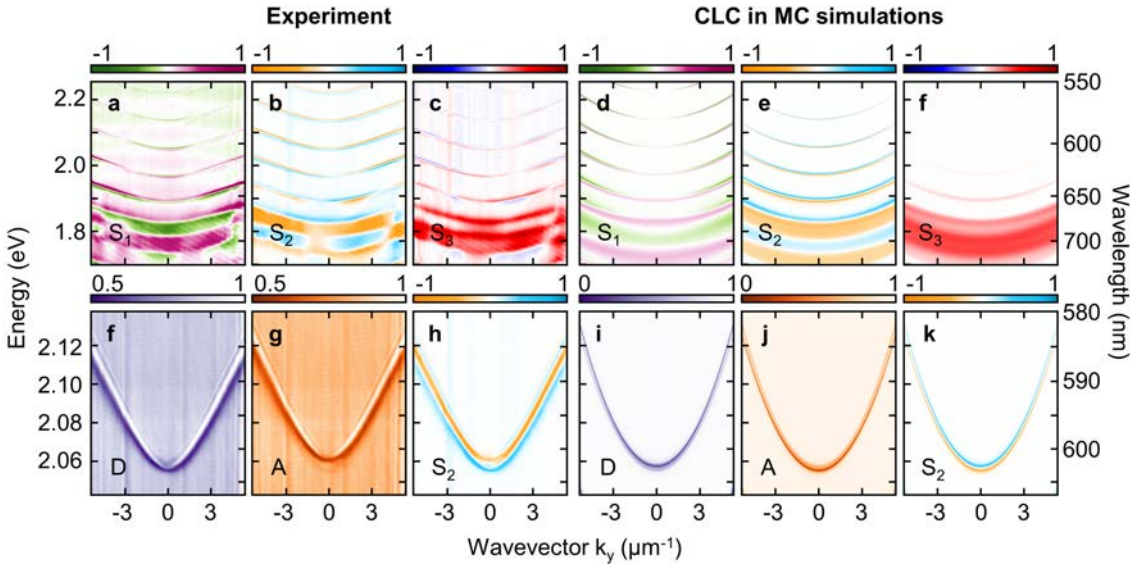

Figure 8.15: **Comparison Between BP-LCMC Experiment and CLC-LCMC Model.** (a–c) Experimental momentum-resolved reflectivity spectra over a broad spectral range for the BP-LCMC sample, expressed by the Stokes parameters S_1, S_2, and S_3, respectively. (d–f) Corresponding simulations using the Berreman transfer matrix method for a cholesteric liquid crystal embedded in the cavity instead of the blue phase. (f–k) The same data presented over a narrower spectral range for (f,i) diagonal, (g,j) antidiagonal polarizations, and (h,k) the S_2 Stokes parameter.

Although the additional parabolic features are experimental artifacts, the mode splitting between the D and A polarizations is a result of the presence of the BP inside the cavity. Simulating such a microscopically complex system is typically difficult, however, the main optical properties of this system can be obtained using a simple model of a CLC embedded inside a cavity.

Figures 8.15(a-c) show the experimental momentum-resolved reflectivity spectra of the BP-LCMC expressed by the Stokes parameters S_1, S_2, and S_3, respectively, over a broad spectral range, while Figures 8.15(d-f) present corresponding Berreman matrix method simulations for a CLC embedded in a cavity. In the experiment, in addition to the cavity modes, a strongly circularly polarized BP stopband is observed around 1.8 eV. The simulation assumes $n_e = 1.55$, $n_o = 1.48$, a CLC helical pitch of 465 nm, and 19 pitches within the cavity. These parameters yield a good agreement with the experiment in terms of the free spectral range of cavity modes, the stopband energy, and its spectral width.

Figures 8.15(f-h) show the data from panel Fig. 8.15(b) in diagonal, antidiagonal polarizations, and expressed as the Stokes parameter S_2 over a narrow spectral range, together with the corresponding simulation results (Figures 8.15(i-k)). It can be seen that the mode splitting in linear polarizations is also reproduced by the simulation. However, the mode polarizations are swapped compared to the experiment, and despite various attempts to recreate proper polarization texture by changing simulation parameters, such as the effective birefringence, polarization of incident light, or the energy separation of the cavity and Bragg modes (which indeed affect the mode polarization degree and the splitting) — I was not able to achieve simultaneous agreement with the experiment for both the polarization of modes and the BP stopband. This discrepancy is most likely due to the

microscopic structure of the BP, which is not captured by the simple model.

Despite these limitations, it is evident that as long as the effects of periodicity in the other spatial directions do not play a significant role (i.e., no additional bandgaps open within the modes), the optical properties of BP-LCMC can be effectively simulated using the much simpler model of a CLC embedded in a cavity.

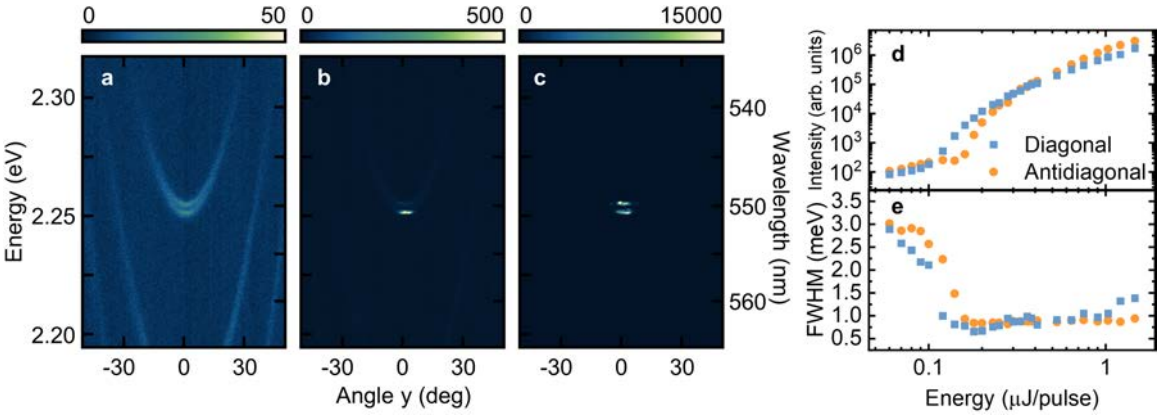

Figure 8.16: **Double-Threshold Dual Lasing from BP-LCMC.** (a–c) Momentum-resolved emission spectra collected at different excitation pulse energies: (a) below, (b) above the first, and (c) above the second lasing threshold. (d) Integrated emission intensity and (e) spectral linewidth as functions of excitation pulse energy for diagonal (azure) and antidiagonal (orange) polarizations. A noticeable difference in lasing threshold between the two polarizations is observed.

This mode splitting can be utilized to realize double-threshold dual lasing. Figure 8.16(a-c) shows momentum-resolved emission spectra collected for different pulsed excitation energies, using the microscope objective excitation (geometry from Figure 3.3). Below the lasing thresholds (Figure 8.16(a)), two equally intense parabolic dispersions are visible. As the excitation pulse energy increases, lasing occurs first at the bottom of the lower-energy parabola (diagonally polarized). Upon further increasing the excitation energy, lasing also emerges in the second mode at higher energy (antidiagonally polarized).

The emission intensity and linewidth dependence for both modes as a function of the excitation pulse energy are shown in Figures 8.16(d,e), respectively. It can be seen that the lasing characteristics of both modes are fairly similar; however, there is a clear difference around the lasing thresholds: lasing in diagonal mode starts at a pulse energy of 0.12 μJ (single-mode lasing regime), while the threshold for the antidiagonal mode is reached at 0.18 μJ/pulse (dual lasing regime).

8.4 Summary and Outcome

In this chapter, I presented the angle-resolved optical and polarization properties of monocrystalline polymer-stabilized dye-doped blue phase (I) with [001] orientation. Because of the chirality of the BP structure, the resulting photonic bandgaps in this three-dimensional photonic crystal are strongly circularly polarized. As a result, light rays with one circular polarization satisfying the Bragg condition cannot propagate through the crystal but can instead be amplified at the band edge, whereas the opposite polarization remains unaffected by the stopband. The emission spectrum can be tuned to match specific diffraction conditions by selecting an appropriate emitter and LC

mixture. Using angle- and energy-resolved tomography, I experimentally mapped the stopbands along different directions (Kossel patterns) and reproduced them through simulations. In addition, I presented the effects of twinning in BPs and the results of exfoliating freestanding thin films.

Using an excitation geometry that distinguishes specific directions, I demonstrated directional Kossel pattern lasing, which, unusually for chiral materials, exhibits lasing in both circular polarizations. These two lasing types display different behaviors upon sample rotation: lasing with polarization matching the BP chirality rotates along the Kossel lines at an angular rate approximately three times grater than the physical rotation of the sample, whereas lasing with opposite polarization remains fixed at the intersection of the direction distinguished by the excitation beam and Kossel lines. I proved that these effects are related to the BP chirality by demonstrating the swapping of the lasing properties in a sample with opposite chirality.

Finally, I presented results for a microcavity with embedded BPI. Because of the relatively small lattice constant, the sample did not exhibit a significant influence of the three-dimensional photonic potential on the photonic modes. Instead, the observed splitting of linear modes could be successfully reproduced using a simple model of a CLC embedded inside a cavity. This mode splitting was then utilized to realize double-threshold dual lasing.

The continuation of the results presented in this chapter may take several interesting directions. To my knowledge, here it is the first experimental realization of a full 3D map of Kossel patterns, which provides access to many isoenergetic planes and cross-sections along arbitrary directions. This method, combined with directional Kossel pattern lasing featuring different behaviors for the two opposite circular polarizations on a freestanding thin BP film or elastomer, could be employed as a novel type of sensor. Because lasing in one polarization is insensitive to sample rotation (and thus less sensitive to shape changes in the Kossel pattern), while the other is strongly sensitive, such a sensor could probe anisotropic strain of the crystal lattice in response to various external stimuli.

It would also be interesting to investigate Kossel pattern lasing in BPI crystals with different orientations, in BPII, or in BPs exhibiting twinning. These experiments may help develop theoretical explanations for the observed phenomena, particularly the mechanism responsible for the generation of lasing polarization opposite to the crystal chirality. Currently, I am also involved in a project in which a quasi-monocrystalline blue phase crystallizes on a radially photoaligned surface. In this configuration, changing the position on the sample results in the rotation of the lattice orientation and, consequently, the rotation of the Kossel pattern lasing. This underscores the unique role of the BP photonic crystal structure in directing lasing, offering potential applications in systems requiring polarized directional emission.

The question of observing a three-dimensional self-assembled photonic potential in LCMC systems remains open. At present, blue phase structures, because of their relatively small lattice constants with respect to visible light wavelengths, do not appear to be good candidates. Cavities designed for shorter light wavelengths is not a good solution, since organic materials exhibit strong absorption in the UV range. However, achieving BP lattice constants above 400 nm is currently not feasible, and to obtain similar photonic band structures in the visible range — as demonstrated, for example, in ULH — the lattice period would need to be around one micron. New materials featuring larger lattice constants may offer a solution.

Another interesting idea would be to attempt to integrate blue phase structures with active materials exhibiting circular optical transitions, such as chiral perovskites [325]. Strong coupling between excitons and circularly polarized Kossel lines would be exciting from the perspective of chiral optics.

9 Summary

In this thesis, I have presented a novel platform that integrates massive photons confined in optical microcavities, spin-orbit coupling arising from the high birefringence of liquid crystals, strong light-matter interactions by embedded light emitters, and a variety of engineered photonic potentials. Due to mathematical analogy, such a system can be regarded as a photonic analogue of solid-state crystals. Confinement within the cavity imparts an effective mass to photons. When polarization and the spatial distribution of the light field are interpreted as forms of angular momentum of light, the birefringent medium gives rise to a synthetic magnetic field, enabling various forms of spin-orbit coupling, analogous to electronic spin-orbit interaction and the Zeeman effect. In the strong coupling regime, the resulting exciton-polariton quasiparticles interact both with the medium and with each other, with interaction strengths several orders of magnitude greater than those of weakly coupled photons. The introduction of zero-dimensional traps and periodic lattice potentials within the cavity further endows these quasiparticles with properties akin to those of electrons bound in atoms or propagating through a crystalline lattice. All of these phenomena occur at room temperature and can be dynamically tuned with an external electric field, making this platform not only a versative tool for fundamental studies with controllable parameters but also a promising candidate for future photonic applications.

These photonic quasiparticles, as constructed in this work, possess a range of unique properties that give rise to the physical phenomena described throughout this thesis. Owing to the light-matter interaction, the resulting nonlinear and coherent emission can manifest either as photon lasing in the weak coupling regime or as a Bose-Einstein condensate in the strong coupling regime. The energy of both phenomena can be precisely tuned using various parameters, such as the applied electric field to cavity electrodes or the polarization of the excitation beam. This tunability enables the realization of lasing or condensation within the Rashba-Dresselhaus spin-orbit coupling regime, where two phase-coherent emission sources emerge in the minima of two circularly polarized valleys that are separated in momentum space. Furthermore, these emission states inherit the spin properties of their respective valleys, leading to the formation of a spin current in real space and the appearance of an optical persistent spin helix in the nonlinear regime.

Because of the interactions between exciton-polaritons in the Bose-Einstein condensate phase, the system exhibits superfluidity. This superfluid behavior is evidenced by the observation of quantum vortices formed via the Kibble-Zurek mechanism and the emergence of a random condensate phase resulting from spontaneous symmetry breaking. The presence of a non-zero linear polarization component causes interference between condensates formed in both valleys in the Rashba-Dresselhaus spin-orbit coupling regime, leading to a periodic modulation of particle density, known as the stripe phase. This modulation, analogous to the spatial ordering in atomic crystals, combined with the superfluid nature of the condensate, is a hallmark of a supersolid phase. This work presents the first complete demonstration of a supersolid phase realized with exciton-polaritons and, importantly, the first observation of such a phase at room temperature. These results have already sparked further research efforts, both in other groups [22] and among my collaborators, who are now investigating the dynamics of quantum vortices and the Berezinskii–Kosterlitz–Thouless transition.

The self-organized photonic potentials investigated in the later part of this thesis exhibited distinct optical properties depending on the chosen liquid crystal phase, either localizing light or acting as photonic lattices of various dimensionalities. Employing the uniform-lying helix phase as a one-dimensional photonic potential allowed for precise and reversible tuning of photonic band gaps in the resulting band structures, which differed for two orthogonal linear polarizations of light. Tilting the liquid crystal molecules within the cavity plane caused these two band structures, independent in the untilted case, to interact via bands of opposite parity, an effect referred to as interband spin-

orbit coupling. Under optical excitation, the system exhibits lasing that preserves the angular and polarization properties of the coupled photonic bands.

A variety of topological defects in such self-assembled structures can potentially give rise to intriguing physical phenomena. In one case, within uniform-lying helix spirals, the sign of the interband spin-orbit coupling changes across the defect, potentially enabling the formation of a topologically protected state. Another class of defects, explored in an entire chapter of this thesis, are liquid crystal torons. Their unique microscopic structure, featuring a spatially rotating liquid crystal texture, gives rise to spatially varying birefringence, effectively acting as a non-Abelian gauge potential. This leads to a ladder of localized optical states inside the toron with nontrivial properties. The ground state exhibits a Laguerre–Gaussian-like intensity profile with a non-zero orbital quantum number l, and a quadrupole-like polarization pattern observable in both real and reciprocal space. Lasing from this state carries non-zero orbital angular momentum, with opposite signs for the two circular polarizations.

Furthermore, because of interactions between the localized modes, the spectral tuning with toron size shows an unexpected behavior: the energies of the two lowest states initially decrease even as the trap size is reduced. At very small sizes, a transition occurs from a nontrivial regime, where the ground state shows Laguerre–Gaussian-like symmetry, to a trivial one with a conventional ordering of localized states. In the nontrivial regime, the ground state can be interpreted as a photonic analogue of the Landau level in a synthetic magnetic field. It was also demonstrated that torons can serve as building blocks for two-dimensional triangular lattices, where their localized states hybridize into photonic bands that preserve their polarization properties.

Studies of blue phase liquid crystals in the absence of an optical microcavity revealed lasing behavior associated with Kossel diffraction patterns, which were highly sensitive to the geometry of the excitation beam. Notably, the lasing emission exhibited polarization not only matched with the intrinsic chirality of the liquid crystal matrix but also, unexpectedly, of opposite handedness. Furthermore, the angular emission profiles of these two polarization components behave differently depending on the orientation of the blue phase crystal lattice relative to the excitation geometry.

From the perspective of the liquid crystal research community, a novel method for investigating Kossel patterns was introduced, based on three-dimensional angle- and spectrally-resolved tomography. This technique offers deeper insight into the detailed structure of the photonic crystal lattice. When blue phase I was incorporated into an optical microcavity, splitting of the cavity modes accompanied by a dual-threshold lasing behavior was observed.

In the Appendix A, additional possibilities for structuring the liquid crystal microcavity using arbitrarily shaped photonic potentials are presented. These configurations enable not only the reproduction of effects observed in self-organized structures but also the realization of novel phenomena that can be uniquely achieved with this method.

In each of the proposed photonic structures, an applied electric field allows for the tuning of a different structural parameter: the diameter of zero-dimensional traps (individual torons), the potential depth (ULH), the orbital overlap (toron lattices), and the energy of entire bands (in lattices fabricated using focused ion beam in combination with the nematic LCMC). Collectively, these phenomena demonstrate that the proposed platform not only serves as a versatile photonic simulator for exploring solid-state physics analogues but also opens pathways to new directions in photonics.

A wide variety of liquid crystal phases and topological defects exist (also beyond the conventional rod-like molecular structures), each exhibiting distinct symmetries. When integrated into a microcavity, these phases can generate different Abelian and non-Abelian gauge fields. The integration of engineered photonic potentials within LCMC in strong light-matter coupling, particularly above the Bose-Einstein condensation threshold, remains an open challenge and has yet to be demonstrated

experimentally. Nevertheless, the growing interest from other polariton research groups suggests that such investigations may soon emerge, potentially revealing non-trivial topological phenomena as well as both Hermitian and non-Hermitian physics.

To conclude this thesis, I would like to point out an interesting (albeit entirely non-scientific!), analogy between supersolids and liquid crystals. Just as liquid crystal media embody a paradox by combining the order of a solid with the fluidity of a liquid, supersolids similarly merge the characteristics of crystalline order with those of a superfluid. Although there is no direct physical connection between these two phenomena, the symbolic resemblance is quite charming, especially in the context of this work, where the main theme is the construction of analogies between light and matter.

Appendices

Appendix A: LCMC Structured by Focused Ion Beam

This section presents results obtained with nematic LCMCs featuring photonic potentials patterned using a focused ion beam. As discussed earlier, compared to self-organized photonic potentials in liquid crystals, this fabrication method requires advanced equipment and is relatively slow. However, it offers excellent precision and control over the structural parameters, as well as different results with electric field tuning. The purpose of this appendix is to highlight the similarities and differences between structures obtained via these two methods. It also presents the technical details of structure patterning and characterization, which I hope will be useful to my younger colleagues in the future.

The first step of the selected fabrication method involves the micropatterning of glass substrates coated with a 20 nm thick ITO layer. To remove the charge accumulation caused by gallium ion bombardment, an additional electrical contact between the electrode and the sample holder was employed, an essential step for achieving high-quality structures.

As I began to work on this technique with almost no prior experience, a substantial amount of effort was devoted to the calibration and optimization of the resulting structures. An additional challenge was the multi-step device assembly process, which was carried out across two institutions: structure patterning at the UW, mirror deposition at the MUT, AFM characterization at UW, cavity assembly at MUT, characterization of air-filled cavities at UW, LC filling at MUT, and final spectroscopic measurements at UW. Consequently, the time intervals between subsequent completed devices often spanned one or two months.

During the optimization phase, two different shapes of individual mesas were tested as building blocks for the lattices: a Gaussian profile (defined by bitmap input) and a cylindrical profile (defined using the built-in FIB patterning tool).

Figure 9.1 presents SEM images of example structures, including a square lattice, a graphene-like (honeycomb) lattice, two SSH chains with different parameters, and a Lieb lattice, all patterned into an ITO electrode using a Gaussian shape profile. The structures were fabricated using a Helios NanoLab 600 (FEI Company). Despite minor defects related to substrate contamination, the images demonstrate the high precision of this fabrication method. The use of Gaussian profiles provides greater flexibility in lattice design, particularly allowing lattice sites to be placed sufficiently close to each other, a requirement for observing topological states in the SSH chain, for instance.

The next step involves characterizing the patterned structures using AFM. Although the FIB system provides calibrated milling times for certain reference materials (such as silicon), it does not offer such a calibration for ITO or SiO_2. Therefore, a dedicated calibration must be performed under the specific patterning conditions, including the ion beam current and acceleration voltage.

There are two primary methods for controlling the milling depth when using a loaded bitmap: (1) by setting a nominal depth based on calibrations with known materials, which is applied globally across the entire structure, and (2) by modulating the 8-bit bit depth values (ranging from 0 to 255). The second method allows shaping the vertical profile of individual features. Interestingly, in the system used here, the resolution of the bitmap also influences the milling depth. Hence, following systematic calibration, I would recommend keeping a constant bitmap resolution.

To optimize the patterning parameters and better understand the resulting structure profiles, AFM scans were performed on a test mesa array both before (Figure 9.2(a)) and after (Figure 9.2(b)) deposition of the DBR.

The patterned matrix consists of mesas with nominal FWHM ranging from 1 µm (bottom row) to 5 µm (top row), in 1 µm increments. The bit depth value at the center of each mesa varies from 50 (left side of the matrix) to 250 (right side), in steps of 50. Milling was performed with a

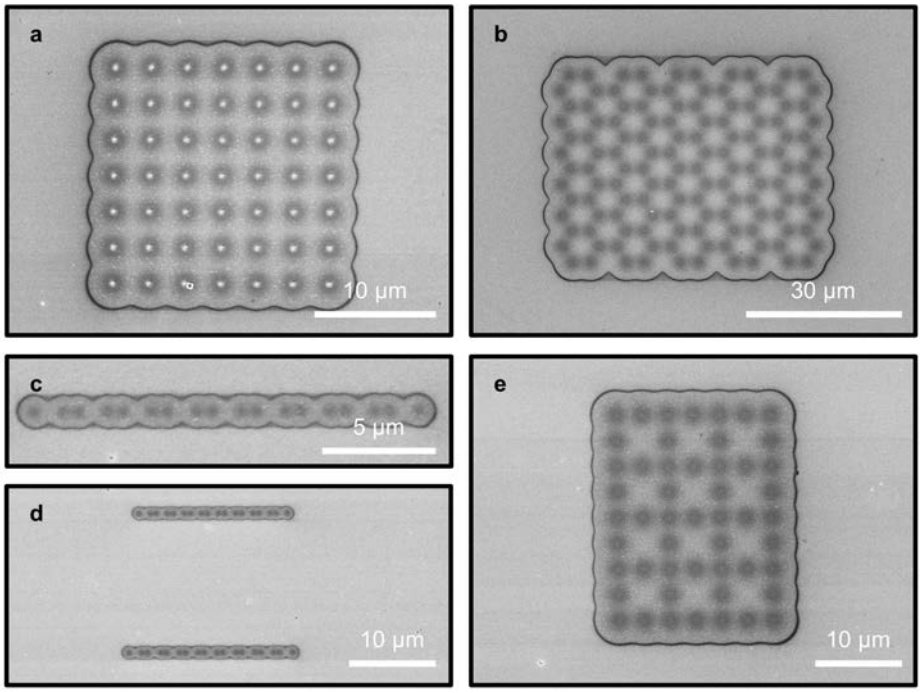

Figure 9.1: **Artificial Photonic Lattices in LCMC Structured with Focused-Ion Beam.** Scanning electron microscope images of various one- and two-dimensional photonic lattices fabricated in LCMC using focused-ion beam: (a) square lattice, (b) graphene lattice, (c,d) topologically non-trivial Su-Schrieffer–Heeger chains shown at low and high magnification, respectively, and (e) Lieb lattice.

beam current of 46 pA and an acceleration voltage of 30 kV. A lower beam current allows for higher patterning precision. The nominal milling depth was set to 120 nm, which, based on the software scaling, corresponds to an expected maximum depth of approximately $120\ \text{nm} \times 250/255 \approx 117$ nm, and a minimum depth of about 23 nm.

Figures 9.2(c-e) present AFM line profiles along selected rows of the matrix, marked by arrows in Fig. 9.2(a). The blue curves correspond to the profiles before DBR deposition, and the red curves after. First, it is evident that the structures are significantly shallower before DBR coating than the nominally set values, indicating the need for independent calibration when patterning in different materials.

In addition, the milling depth also depends on the FWHM of the mesas. Interestingly, the narrowest mesas yield the deepest etching (see Figure 9.2(e)). A distinct depth discontinuity is observed around -10 nm, where the central part of the mesa becomes significantly deeper than the edges. This effect is particularly pronounced in the widest mesas (Figure 9.2(c)), and is also visible in the SEM image in Figure 9.1(a). Similar behavior has been observed during the fabrication of other deeper structures. It is suspected that this jump is associated with complete removal of the ITO layer and the onset of milling into the underlying glass substrate, which appears to be etched more efficiently.

If this were the case, one would expect the jump to occur at around -20 nm (the nominal thickness of the ITO layer). Therefore, the discrepancy may arise from an AFM calibration offset,

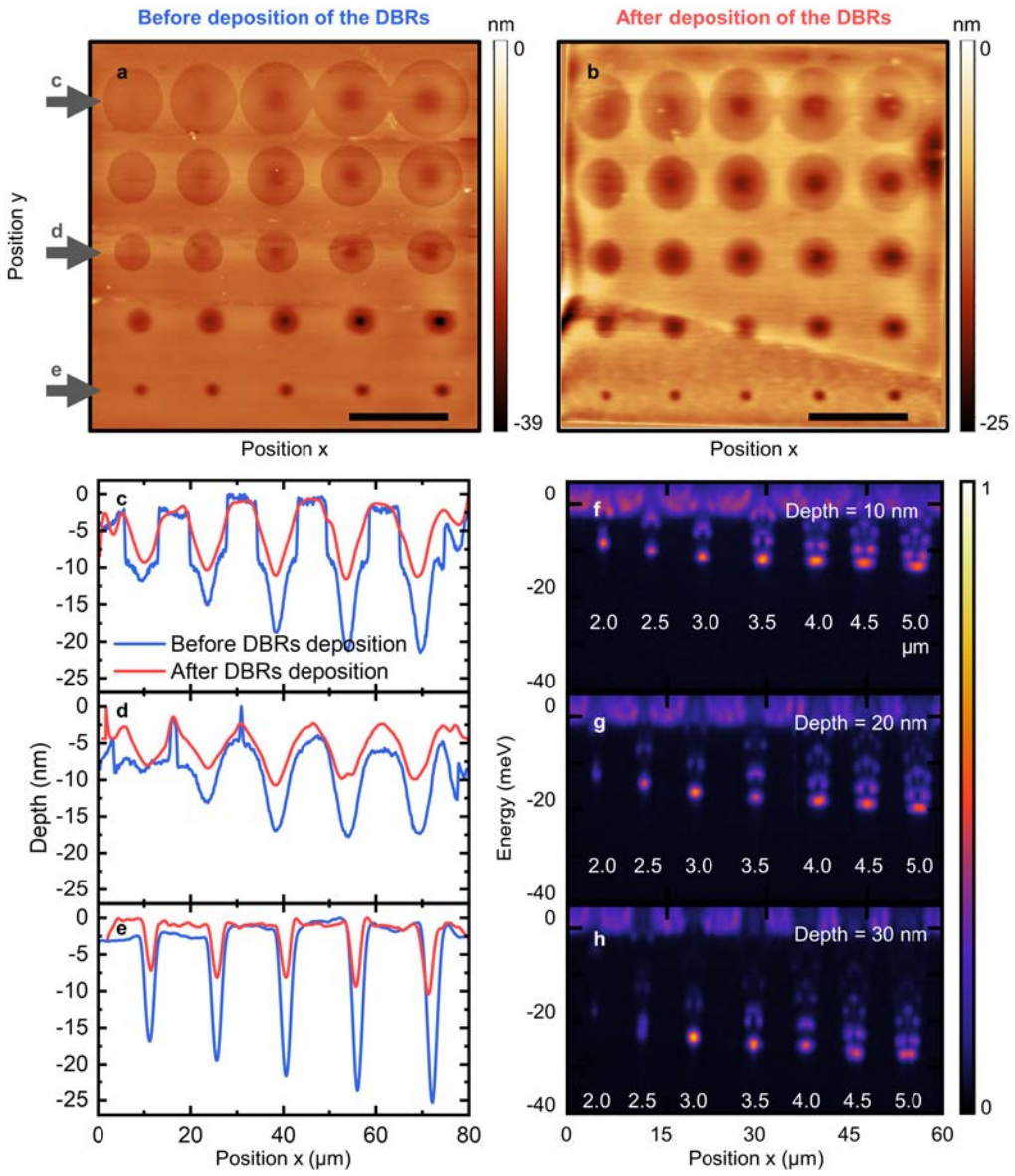

Figure 9.2: **FIB-LCMC potential characterization.** AFM measurements of a structured glass substrate coated with an ITO layer and patterned with a matrix of Gaussian mesas, (a) before and (b) after DBR deposition; scale bar: 20 μm. (c,d,e) Cross-sections along the profiles marked with arrows in (a). (f–h) Spatially resolved transmission spectra along the rows of cylindrical mesas with varying diameters (in μm, indicated below each mesa). The nominal milling depths are (f) 10 nm, (g) 20 nm, and (h) 30 nm.

an inaccurate value of the ITO thickness, or a different origin of the effect itself. However, after DBR deposition (red curves), the mesa profiles become smoother, and this depth discontinuity disappears, while the overall mesa depth is significantly reduced. The resulting profile can be considered, to

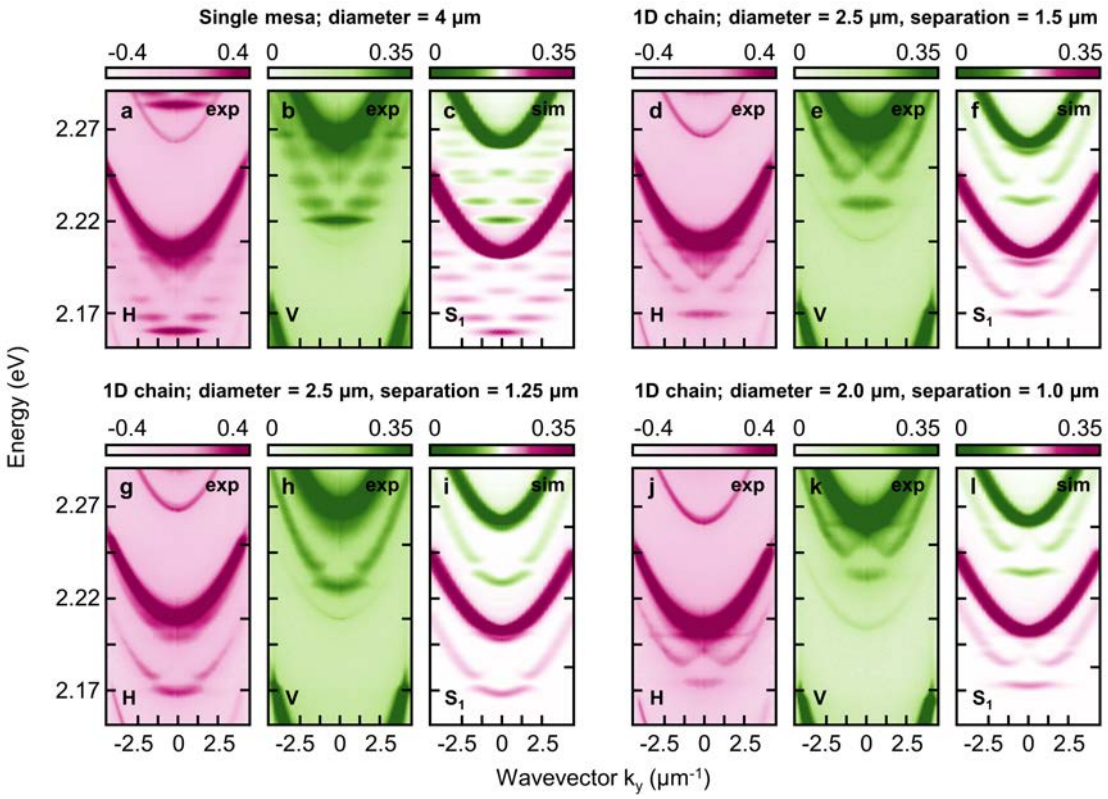

Figure 9.3: **Optical properties of FIB-LCMC structures.** Momentum-resolved spectra of (a–c) a single mesa and (d–l) three one-dimensional chains of mesas, with their geometrical parameters indicated above each data set. Experimental transmission spectra measured in (a,d,g,j) H polarization, (b,e,h,k) V polarization, and (c,f,i,l) calculated and represented by the Stokes parameter S_1.

a first approximation, as the actual potential landscape and can be used as input for numerical simulations of these structures using, e.g., the finite difference operator method.

After the cavity is assembled using a second unstructured symmetric mirror and filled with LC, spectroscopic measurements allow for the observation of spatially localized states. Figures 9.2(f–h) show three rows of isolated mesas (distinct from those presented in Figs. 9.2(a–e)) etched with cylindrical profiles and nominal milling depths of 10 nm, 20 nm, and 30 nm, respectively, plotted as a function of mesa diameter, as indicated in the plots. It is important to note that the two milling methods (bitmap input and in-built software patterning) result in significantly different actual structure depths for the same nominal milling values. Therefore, each method requires an independent calibration. The data demonstrate how changes in the width and depth of the potential profiles influence both the number and the energies of the localized states.

Figure 9.3 presents momentum-resolved transmission spectra measured for selected FIB-LCMC structures, along with a comparison to modeling results obtained using a two-dimensional finite difference method. All structures were etched with cylindrical profiles to a nominal depth of 30 nm. The experimental results are described by the following effective Hamiltonian written in a linear basis:

$$H = \left(E_0 + \frac{\hbar^2 k_x^2}{2m_x} + \frac{\hbar^2 k_y^2}{2m_y} + A(x,y) \right) \sigma_0 + \left(\Delta_{HV} + \delta_x k_x^2 + \delta_y k_y^2 \right) \sigma_z + \delta_{xy} k_x k_y \sigma_x + 2\alpha k_y \sigma_y, \quad (44)$$

where $E_0 = (E_H + E_V)/2$ is mean energy of H and V modes, m_x and m_y are the effective masses on x and y directions, respectively, $A(x,y)$ is the position-dependent photonic potential amplitude, Δ_{HV} is detuning between H and V modes, δ_x, δ_y and δ_{xy} are TE-TM splitting terms, and α is RDSOC constant.

The same simulation parameters were used for all cases (except the potential term $A(x,y)$), with $\hbar^2/2m_x = 3.09$ meV $\cdot$ μm^2, $\hbar^2/2m_y = 3.02$ meV $\cdot$ μm^2, $\Delta_{HV} = 30$ meV, $\delta_x = -0.073$ meV$\cdot$μm^2, and $\delta_y = -0.514$ meV$\cdot$μm^2. Since only the k_y direction was analyzed and no external voltage was applied (i.e., no RDSOC was present), $\delta_{xy} = 0$ and $\alpha = 0$.

Figures 9.3(a–c) show the spectra of a single mesa with a diameter of 4 μm, measured in H and V polarizations, and the corresponding simulation expressed by the Stokes parameter S_1, respectively. Both the experimental data and simulations reveal the non-dispersive nature of the localized states in both polarizations. To accurately reproduce the spectral features, in the simulations a narrower mesa profile of 2.8 μm was assumed. This discrepancy can be attributed to partial narrowing of the etched profile during the DBR deposition process.

Figures 9.3(d–l) present the spectra and corresponding simulations for three one-dimensional chains, measured along their respective axes. The diameters of the individual nodes and the center-to-center separations are indicated above each set of panels. The formation of energy bands by coupled localized states is clearly visible. Once again, good agreement with the simulations is observed, although this required assuming node diameters 15–30% smaller than those nominally etched by FIB. Specifically, for the simulations shown in Figs. 9.3(f,i,l), the assumed node diameters were 1.9 μm, 1.7 μm, and 1.7 μm, respectively.

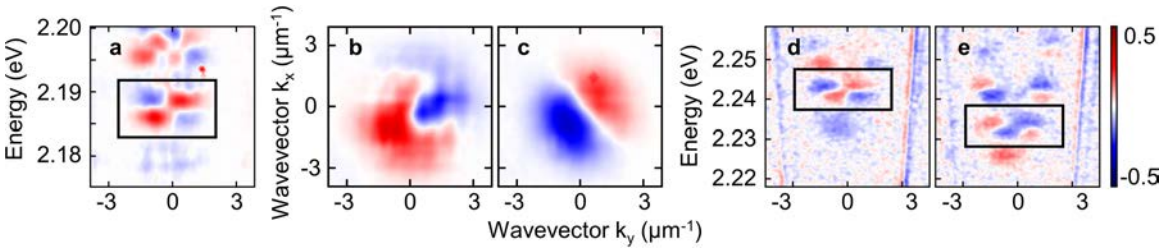

Figure 9.4: **Interband Spin–orbit Coupling in an Artificial 0D Photonic Trap Embedded in Nematic LCMC.** (a) Momentum-resolved transmission spectrum at zero $\Delta_{H_s V_p}$ detuning. (b,c) Momentum-space images of the lower and upper ISOC-like mixed states, respectively. (d,e) Momentum-resolved transmission spectra measured on a thicker sample, for detunings $\Delta_{H_s V_p} = 0$ and $\Delta_{H_p V_s} = 0$, respectively. All panels are presented in terms of the S_3 Stokes parameter. Black rectangles mark the zero-detuned subbands with strong ISOC.

Since nematic LCMC allows for a different type of voltage tuning compared to ULH-LCMC, where only the H mode energy is tunable in the first case, while energies of both H and V modes change in the second case, FIB-LCMC offers greater flexibility for studying interactions between states of different polarizations. Figure 9.4 presents ISOC-like phenomena observed in a single cylindrical mesa.

Figure 9.4(a) shows momentum-resolved transmission spectra expressed by the Stokes parameter S_3 at zero $\Delta_{H_sV_p}$ detuning in the $(N, N{+}2)$ regime. A characteristic quadrupolar pattern emerges between the H_s and V_p states, similar to that observed in ULH-LCMC. The isoenergetic planes obtained from momentum-resolved tomography for the lower and upper ISOC-mixed states are shown in Figures 9.4(b,c), respectively. These reveal a circular polarization separation in the momentum space, rotated by 45° with respect to the rubbing direction, and opposite for the two mixed states.

Because the first sample was too thin to achieve zero detuning for $\Delta_{H_pV_s}$, a thicker sample was fabricated. Unfortunately, it exhibited poorer LC alignment, which decreased the quality of the spectra. However, measurements analogous to those in Figure 9.4(a) are presented in Figures 9.4(d,e), corresponding to detunings $\Delta_{H_sV_p} = 0$ and $\Delta_{H_pV_s} = 0$, respectively. As previously observed in ULH-LCMC, coupling different localized states can lead to a reversal in the sign of the ISOC. However, in this case, such a sign change can be achieved at the same position on the sample only by tuning the applied electric field.

I refer to this effect as an ISOC-like phenomenon because, although it yields the same polarization pattern and emerges from the coupling between states of opposite parity within cavity modes of the same parity, the underlying physical mechanisms differ. In ULH-LCMC, ISOC arises as a result of the optical activity of the liquid crystal helix. In contrast, in the FIB-LCMC, optical activity is absent, and the coupling between localized states occurs indirectly through interaction with higher-order modes, mediated by the non-Hermitian nature of the system. A theoretical approach describing this phenomenon is currently under development.

It is also important to emphasize that this effect is highly sensitive to the lifetimes of the coupled states. In cavities where the LC alignment is poor and the linewidth of the H modes significantly broadens when electric field is applied, while the linewidth of the V modes remains nearly constant, observing this effect becomes very challenging or even impossible.

The observation of ISOC-like phenomenon is also possible in chains of multiple mesas, if the RDSOC and spectrometer slit are oriented perpendicular to the chain axis (see Figure 9.5(a) for the experimental configuration and a corresponding SEM image of the chain). In this orientation, similar to the case of a single mesa, the bands of both polarizations exhibit a nearly flat dispersion in momentum-resolved spectra along k_y.

Figure 9.5(b) shows the Stokes parameter S_3 as a function of the applied voltage for an in-plane wavevector of $\pm 2.05\ \mu\text{m}^{-1}$, corresponding to cross-sections through the p-bands (negative wavevectors shown in the upper panel, positive in the lower panel). Within the voltage ranges marked by dashed rectangles, the bands undergo anticrossings accompanied by a flip in circular polarization.

Figures 9.5(c–h) present momentum-resolved transmission spectra at voltages corresponding to the resonance of the s- and p-bands of both modes at two different detunings, for the S_0, S_1, and S_3 Stokes parameters. The observed polarization patterns, particularly the ISOC sign flip, are consistent with the results obtained for single mesas and ULH-LCMC.

A qualitatively different scenario emerges in the $(N, N{+}1)$ regime (Figures 9.5(i–o)). Here, because of the differing parities of the planar cavity modes, the strongest spin-orbit coupling occurs between bands of the same parity. As a result, unlike the $(N, N{+}2)$ regime, the transition between positive and negative detuning does not lead to a reversal of the circular polarization state of the interacting bands (Figure 9.5(i)). This behavior is clearly reflected in the momentum-resolved spectra (Figures 9.5(j–o)), where the quadrupolar structure in the S_3 Stokes parameter remains unchanged in sign for both detuning (Figures 9.5(j) and 9.5(o), respectively).

Since a chain with identical parameters was also patterned along the RDSOC direction (see Figure 9.6(a)), a similar experiment can be performed by observing the band structure along the chain.

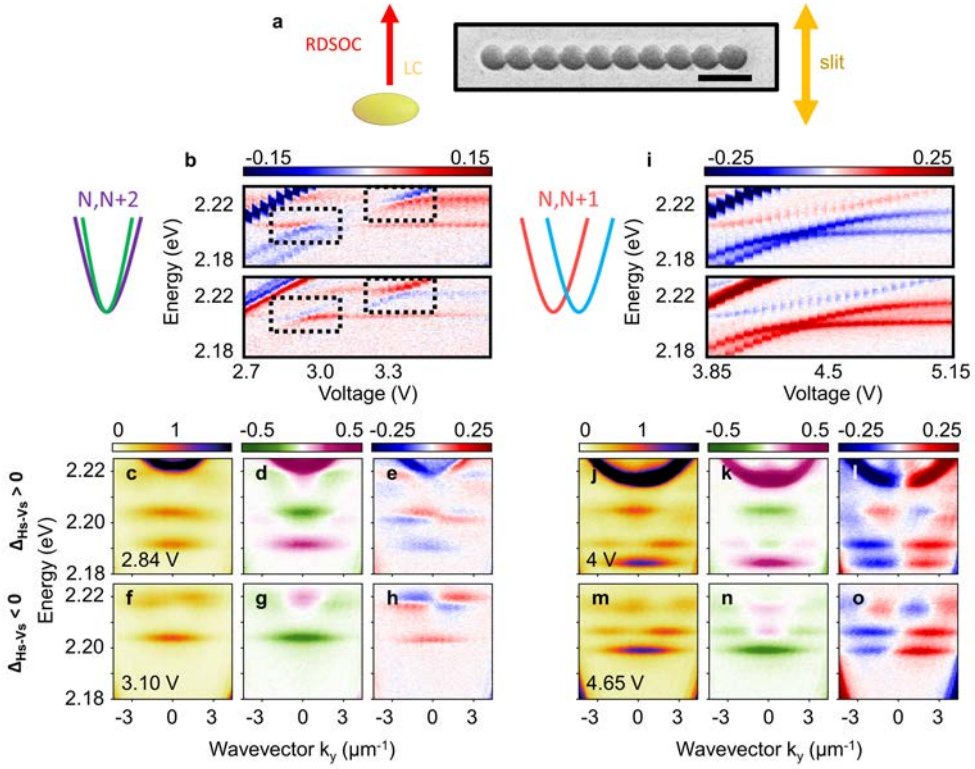

Figure 9.5: **Spin–Orbit–Coupled Band Structure perpendicular to the 1D chain.** (a) Schematic showing the relative orientation of LC molecules, the direction of RDSOC, the 1D chain (SEM image), and the spectrometer slit. Scale bar: 5 µm. (b) Stokes parameter S_3 plotted as a function of energy and applied voltage at fixed momentum $k_y = \pm 2.05$ µm^{-1}, measured in the $(N, N+2)$ regime. The dashed rectangle highlights the voltage range where intersubband spin–orbit coupling (ISOC) becomes visible. (c–h) Corresponding momentum-resolved transmission spectra for Stokes parameters S_0 (c,f), S_1 (d,g), and S_3 (e,h). Rows indicate the detuning between the H_s and V_p bands: (c–e) positive, and (f–h) negative. (i–o) Analogous results in the $(N, N+1)$ regime. Applied voltages for each measurement are indicated in the bottom-left corners of the S_0 panels.

Figure 9.6(b) presents the Stokes parameter S_1 as a function of the applied voltage at normal incidence in the $(N, N+2)$ regime. The strong signal observed in the upper left corner corresponds to the H mode of the planar cavity region surrounding the chain. A voltage-independent signal with a positive Stokes vector value of around 2.15 eV originates from the lowest band of the vertically polarized mode V_s, while the lowest band of the horizontally polarized mode H_s exhibits tunability, changing its energy from 2.12 eV to 2.17 eV within the voltage range of 2.7 V to 3.1 V. In particular, in this regime, the two bands cross each other.

Figures 9.6(c–k) show momentum-resolved spectra of the Stokes parameters S_0, S_1, and S_3 for three different detunings $\Delta_{H_p-V_s} = 0$ (Figs. 9.6(c-e)), $\Delta_{H_s-V_s} = 0$ (Figs. 9.6(f-h)), and $\Delta_{H_s-V_p} = 0$ (Figs. 9.6(i-k)). Across all detuning values, the Stokes parameter S_3 does not exhibit a significant contribution, so the ISOC is not present for a bands. I attribute this to higher inhomogeneity in the chain compared to the single mesa, which causes this very sensitive to linewidth effect to be lost.

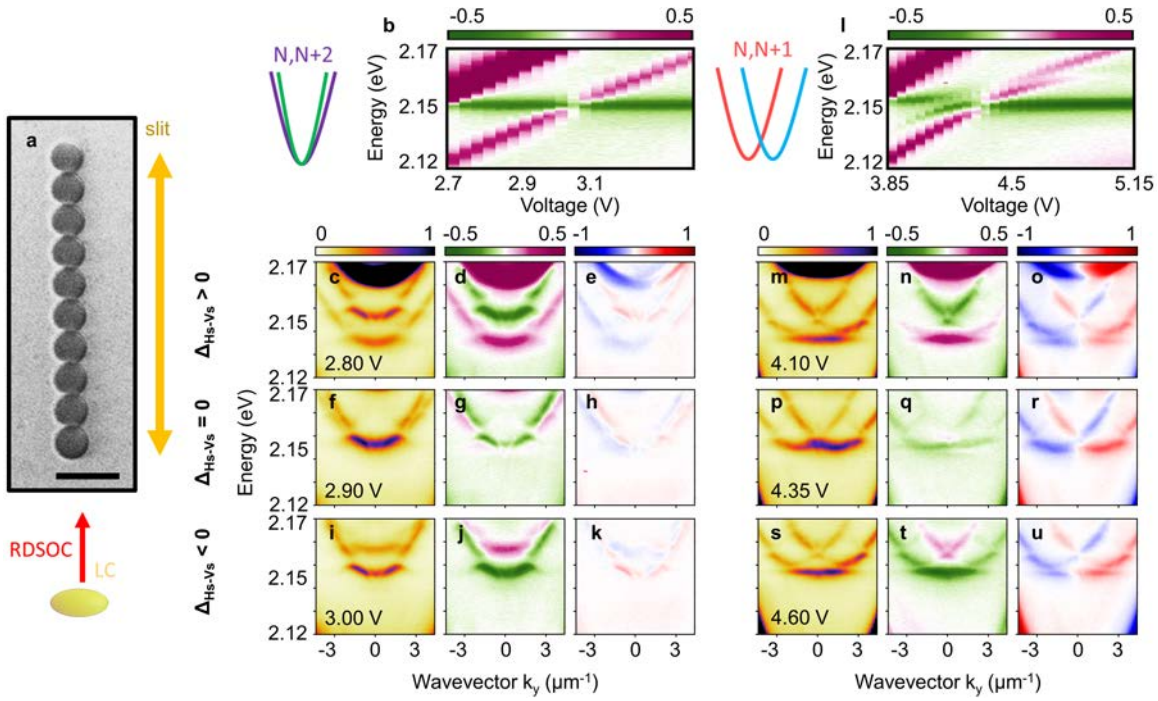

Figure 9.6: **Spin-Orbit-Coupled Band Structure of a 1D Chain.** (a) Scheme of the relative orientation between the LC molecules, RDSOC direction, 1D photonic chain (SEM image), and the spectrometer slit. Scale bar: 5 μm. (b) Stokes parameter S_1 as a function of energy and voltage for $k_y = 0$ μm^{-1}, measured in the $(N, N+2)$ regime. (c–k) Stokes components of momentum-resolved transmission spectra: S_0 (c,f,i), S_1 (d,g,j), and S_3 (e,h,k), for three different detunings between the H_s and V_s bands—positive (c–e), zero (f–h), and negative (i–k). (l–u) Analogous results for the $(N, N+1)$ regime. The applied voltages for each case are indicated in the lower-left corners of the S_0 panels.

A different behavior is observed in the $(N, N+1)$ regime. Here, RDSOC leads to the formation of an additional band between the H_s and V_s bands, as shown in Figure 9.6(l). The polarization state of this emergent band depends on the detuning, showing vertical polarization for negative $\Delta_{H_s-V_s}$ detuning and horizontal polarization for positive detuning. The momentum-resolved spectra reveal a band tuning behavior in linear polarization similar to that observed in the $(N, N+2)$ regime. For $\Delta_{H_p-V_s}$=0, the lower band is horizontally polarized, while for $\Delta_{H_s-V_p}$=0, it is vertically polarized, and vice versa for the upper band (Figures 9.6(o,u)).

However, a key distinction lies in the shape of the band structure. Due to RDSOC, the bands separate along the k_y direction and change their effective masses, akin to planar cavity modes. In particular, the mixed s-band can achieve an almost flat dispersion for both positive and negative detunings (Figures 9.6(n,t)), whereas for zero detuning (Figure 9.6(q)), its effective mass becomes negative. In the S_3 Stokes component (Figures 9.6(p,s,v)), similar to planar modes, the bands exhibit strong circular polarization, as a result RDSOC.

RDSOC can significantly modify the curvature of energy bands, and therefore must be taken into account when determining quantities such as the effective mass. Figure 9.7 demonstrates how this effect can be used to achieve a change of the sign of the effective mass of bands in a 1D chain.

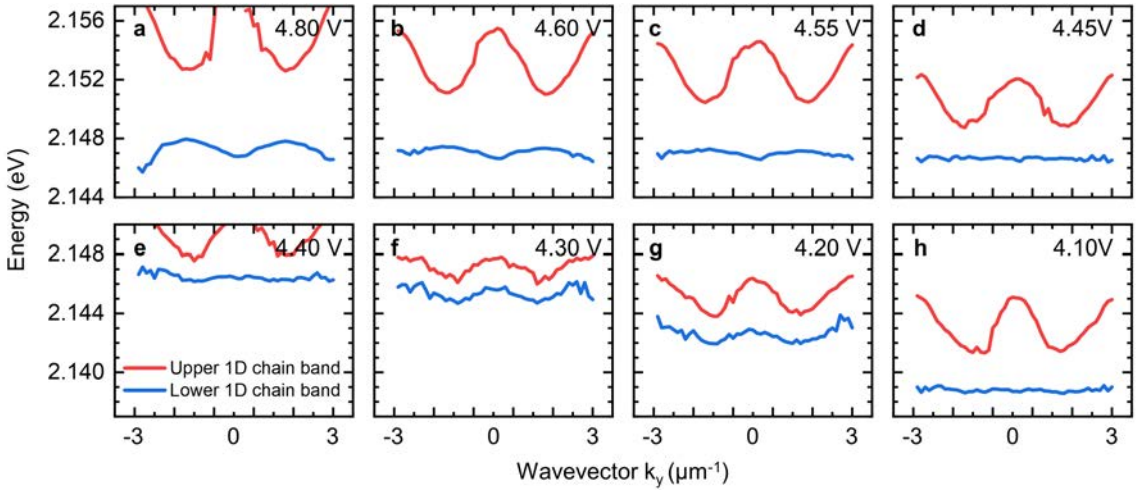

Figure 9.7: **RDSOC Effect on the Effective Mass of 1D Chain Bands.** (a–h) Momentum-resolved spectra extracted by Lorentzian fitting of the transmission data for the two lowest energy bands of a 1D chain, shown for various applied voltages (indicated in the top-right corner of each panel), in the $(N, N+1)$ regime.

Figures 9.7(a–h) show momentum-resolved energy spectra of the two lowest bands, obtained via Lorentzian fitting of transmission spectra, based on the same dataset as in Fig. 9.6(l–u), presented for selected voltages in the $(N, N+1)$ regime.

Note that, in order to simultaneously show a broader tuning range and zoom in on the band structure, the energy scales differ between the upper and lower rows of panels. In Fig. 9.7(a), the lowest (blue) band has a positive curvature at $k_y = 0$. As the voltage is lowered, the energy separation between the two bands decreases (Figs. 9.7(b,c)), leading to a flattening of the lower band, which becomes nearly flat in Fig. 9.7(d)—the energy difference between its maximum and minimum is 0.42 meV, with a standard deviation of 0.10 meV.

Further reduction of the voltage results in strong hybridization between the two bands, both acquiring a characteristic RDSOC-like shape with negative curvature at $k_y = 0$ (Fig. 9.7(f)). As the energy separation increases again, the coupling between the bands weakens, and the lowest band becomes flat once again (Fig. 9.7(h))—the energy difference between the maximum and minimum values is 0.52 meV, with a standard deviation of 0.12 meV.

This analysis demonstrates that through precise tuning, one can engineer a flat band as well as control the sign of the effective mass (positive or negative) at $k_y = 0$ in a one-dimensional chain.

Since FIB provides extensive flexibility in shaping arbitrary photonic potentials, I conclude by presenting examples of two-dimensional square and graphene-like lattices. Figure 9.8 shows momentum-resolved transmission tomography measurements on a square lattice, where the first column corresponds to V polarization without applied voltage, while the remaining three columns were acquired in the RDSOC regime: the second shows the total intensity, and the third and fourth present Stokes parameters S_1 and S_3, respectively. The first row shows momentum-resolved spectra for $k_x = 0$. In V polarization without applied voltage (Figure 9.8(a)), one can clearly distinguish the lowest band and observe relatively narrow linewidths. Upon applying voltage, the spectral lines broaden significantly, likely due to a distorted electric field distribution induced by the patterned electrode structures (discussed further below). The dispersions shown in Figures 9.8(b–d) exhibit

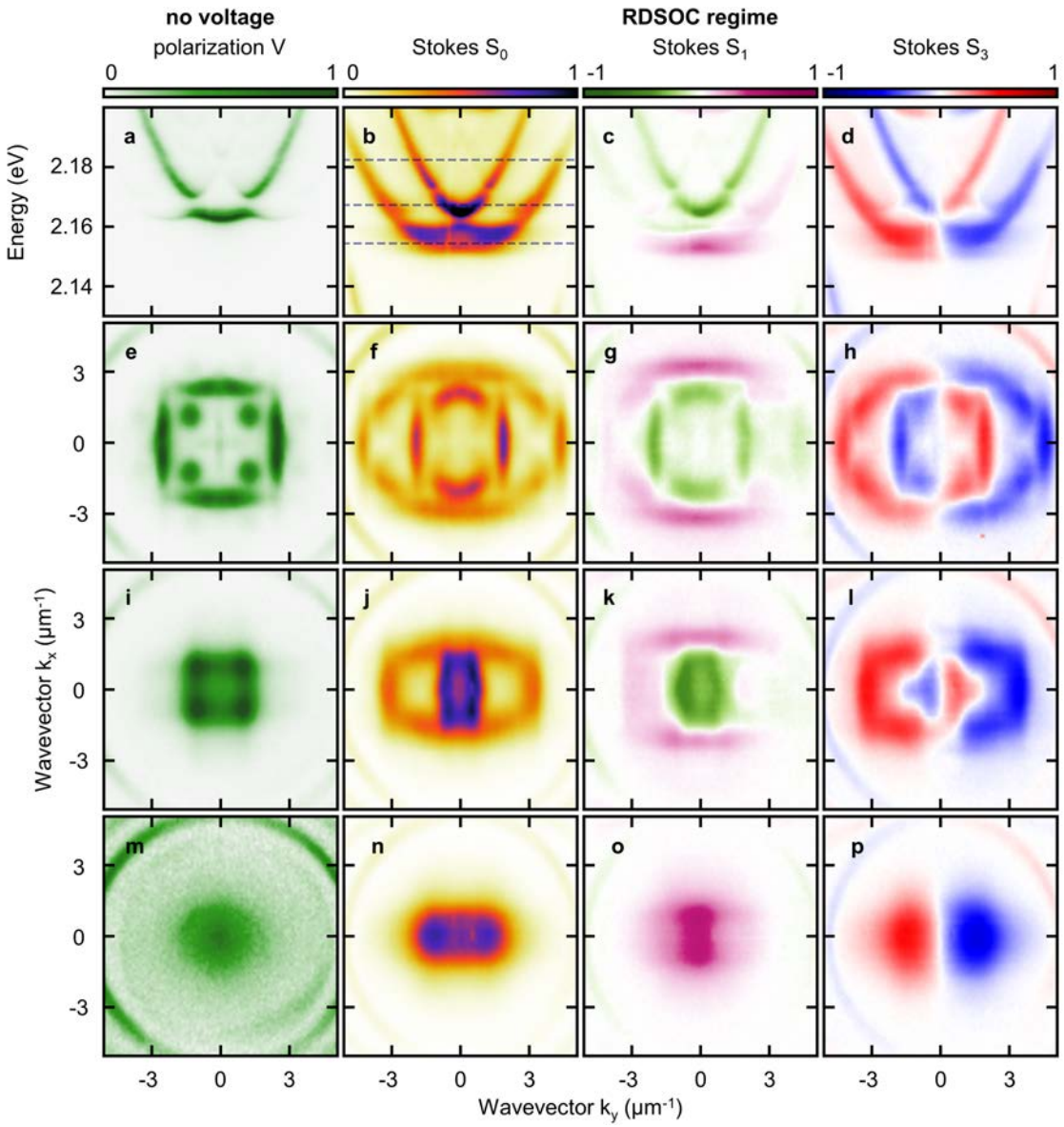

Figure 9.8: **Artificial Photonic Square Lattice in LCMC.** (a–d) Momentum-resolved transmission spectra measured (a) without applied voltage, and (b–d) in the RDSOC regime. The first column corresponds to V-polarized detection, while the second, third, and fourth columns show the S_0, S_1, and S_3 Stokes components, respectively. (e–p) Momentum-space images at selected energies indicated by dashed lines in panel (b): (e–h) 2.182 eV, (i–l) 2.167 eV, and (m–p) 2.154 eV.

RDSOC-modified shapes and a strong circular polarization component. In Figure 9.8(b), selected arbitrary energies are marked with dashed lines, for which the isoenergetic planes are plotted in Figures 9.8(e–p). Without applied voltage, in V polarization, the square symmetry of the lattice is

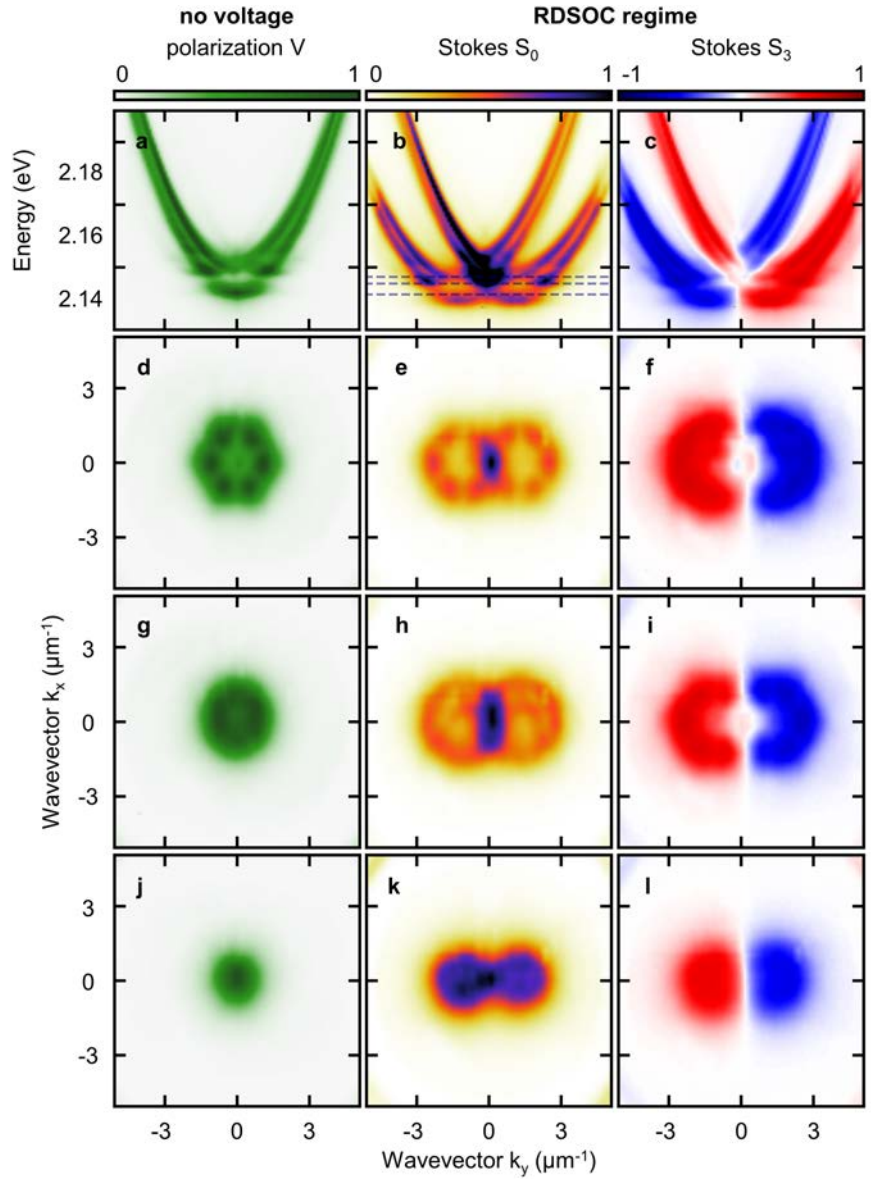

Figure 9.9: **Artificial Photonic Graphene Lattice in LCMC.** (a–c) Momentum-resolved transmission spectra measured (a) without applied voltage, and (b,c) in the RDSOC regime. The first column corresponds to V-polarized detection, while the second and third columns show the S_0 and S_3 Stokes components, respectively. (d–l) Momentum-space images at selected energies indicated by dashed lines in panel (b): (d–f) 2.182 eV, (g–i) 2.167 eV, and (j–l) 2.154 eV.

clearly visible in Figures 9.8(e,i). When voltage is applied, despite the broadening of the spectral lines, the square symmetry remains visible but is strongly modified by RDSOC. Each valley inherits the square lattice symmetry; however, the additional splitting of the valleys along the k_y direction

leads to a non-square momentum-space distribution.

Similar observations can be made for the graphene-like lattice shown in Figure 9.9. The panel layout follows the same convention as in the square lattice case, except that the S_1 column is omitted. Here also, without applied voltage and in V polarization, the sixfold symmetric character of the lattice is clearly visible (Figure 9.9(d)). Under RDSOC, this symmetry is replicated and shifted along the k_y direction for each valley.

As discussed in the context of Fig. 9.2, the step introduced by milling through the ITO/glass interface complicates the precise control over the designed potential profiles. A more critical issue arises in lateral structures larger than 5 µm. The complete removal of the ITO layer beneath such patterns results in the loss of electrical contact, distorting the electric field that controls the LC orientation. Although LC regions above small mesas still exhibit partial tunability owing to field from the surrounding intact ITO and elastic LC forces, in large-scale, deep two-dimensional lattices, voltage tuning becomes nearly impossible. Increasing the ITO thickness is not a good solution, as even partial thinning of the electrode negatively impacts the tunability, and thicker ITO layers introduce optical losses due to absorption.

An alternative approach that I am currently investigating involves direct patterning of the DBR mirror rather than the ITO electrode. Simulations suggest that this should not significantly degrade the cavity's Q-factor. Additionally, charging effects during FIB processing of the dielectric mirror were mitigated by using a sacrificial gold layer, which was deposited prior to milling and subsequently chemically removed. Preliminary AFM characterization of the structures shows promising results, and I am currently awaiting the assembly of the completed cavity for spectroscopic measurements.

I hope that the more than a year-long effort invested in optimizing this fabrication approach will serve as a solid foundation for future PhD students, enabling a wide range of remarkable discoveries within arbitrarily shaped photonic potentials in LCMC. I strongly believe that the combination of effects known from photonic lattices in microcavities and the large birefringence of the liquid crystal medium allowing for dynamic voltage tuning, and the presence of various types of spin-orbit interactions, offers tremendous scientific potential for uncovering new and fascinating physical phenomena.

Appendix B: Miscellaneous

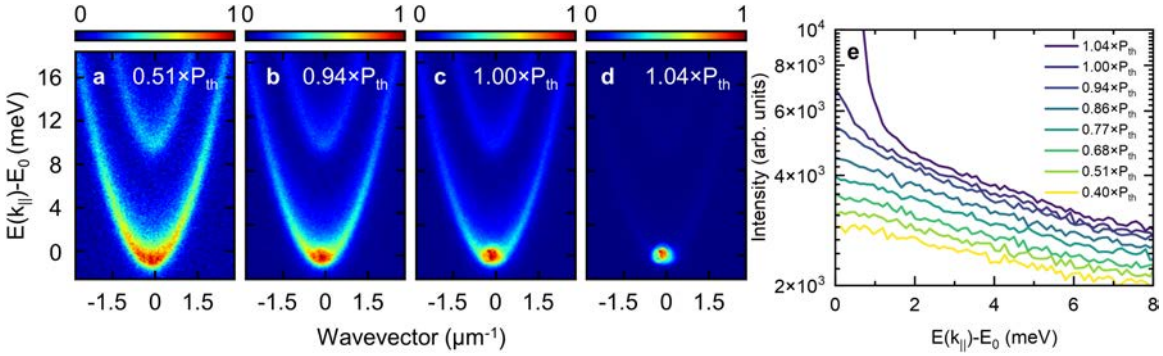

Figure 9.10: **Photon Thermalization in Dye-Doped LCMC.** (a–d) Momentum-resolved and (e) momentum-integrated emission spectra collected at different excitation powers.

Figure 9.10 presents emission measurements performed on a dye-doped nematic P580-LCMC sample in the weak light–matter coupling regime, which potentially exhibits features of photon thermalization [77, 141, 166]. This particular sample had deeper photonic modes (indicating low scattering) and was fabricated using higher-quality mirrors than those discussed in Chapter 4.

Figures 9.10(a–d) show normalized momentum-resolved emission spectra collected at different excitation powers, labeled in the upper right corners of each panel with respect to the threshold power P_{th}. The two visible parabolas correspond to the H and V modes. At excitation powers well below the threshold (Fig. 9.10(a)), spontaneous emission occurs uniformly across the entire parabola. As the excitation power approaches P_{th} (Fig. 9.10(b)), the emission begins to concentrate around the bottom of the mode, with the spectral width gradually narrowing. This leads to a smooth transition at threshold (Fig. 9.10(c)), which contrasts with the abrupt transition of photon lasing observed in Fig. 4.6, and more closely resembles the condensation behavior seen in Fig. 5.7. Above threshold (Fig. 9.10(d)), a slight blueshift of approximately 0.5 meV is observed, and the emission spectrum becomes fully dominated by the signal at the bottom of the parabola.

Figure 9.10(e) shows the integrated emission spectra for various excitation powers. Interestingly, not only below but also at the threshold power ($1.00 \times P_{\mathrm{th}}$), the intensity profile resembles a Bose–Einstein distribution. However, for just slightly higher excitation ($1.04 \times P_{\mathrm{th}}$), the system appears to depart from thermal equilibrium.

These findings may point to the possibility of photon condensation (photon BEC) in this system [77, 141, 166]. However, confirming this phenomenon requires further investigation, for example, detailed measurements of the real-space emission profile near the threshold P_{th}.

Figure 9.11 shows a photo of the experimental spectroscopy setup in the Polariton Group Organic Laboratory. The main optical path, starting from the nanosecond pulsed laser (not shown) and ending at the spectrometer slit, is marked by a green line. Part of important components are marked: (1) CCD camera, (2) spectrometer, (3) Dove prism, (4) detection polarization setup, (5) real-space camera with Wollaston prism mounted in front, (6) second k-space lens and (7) real-space lens mounted on automated translation stages, (8) 50:50 beam splitter, (9) reflectivity white light source, (10) Mach–Zehnder interferometer, (11) cw 405 nm laser, (12) cw 532 nm laser, (13) long-pass filter, (14) 30:70 beam splitter, (15) sample placed between collection and excitation objectives, (16) excitation polarization setup, (17) set of bandpass filters, (18) transmission white light source, (19) beginning of the ns laser beam path, (20) function generator, (21) power meter, (22) automated

Figure 9.11: **Photograph of the Spectroscopy Experimental Setup in Polariton Group Organic Laboratory.** Green lines help trace the main optical path.

optical microscope, and (23) spatial light modulator.

Appendix C: List of Publications

Articles and preprints described within the thesis

1. **M. Muszyński**, P. Kokhanchik, D. Urbonas, P. Kapuściński, P. Oliwa, R. Mirek, I. Georgakilas, T. Stöferle, R. Mahrt, M. Forster, U. Scherf, D. Dovzhenko, R. Mazur, P. Morawiak, W. Piecek, P. Kula, B. Piętka, D. Solnyshkov, G. Malpuech, J. Szczytko, Observation of a stripe phase in a spin-orbit coupled exciton-polariton Bose-Einstein condensate. *arXiv* (2024), arXiv:2407.02406 (under review) [14].
doi:10.48550/arXiv.2407.02406

2. **M. Muszyński**, P. Oliwa, P. Kokhanchik, P. Kapuściński, E. Oton, R. Mazur, P. Morawiak, W. Piecek, P. Kula, W. Bardyszewski, B. Piętka, D. Bobylev, D. Solnyshkov, G. Malpuech, J. Szczytko, Electrically Tunable Spin-Orbit Coupled Photonic Lattice in a Liquid Crystal Microcavity. *Laser Photonics Rev.* **18**, 2400794 (2024). [15]
doi:10.1002/lpor.202400794

3. **M. Muszyński**, M. Król, K. Rechcińska, P. Oliwa, M. Kędziora, K. Łempicka-Mirek, R. Mazur, P. Morawiak, W. Piecek, P. Kula, P. G. Lagoudakis, B. Piętka, J. Szczytko, Realizing persistent-spin-helix lasing in the regime of Rashba-Dresselhaus spin-orbit coupling in a dye-filled liquid-crystal optical microcavity. *Phys. Rev. Appl.* **17**, 014041 (2022). [5]
doi:10.1103/PhysRevApplied.17.014041

Unpublished articles described within the thesis

4. E. Oton, **M. Muszyński**, K. Cyprych, P. Kapuściński, P. Morawiak, M. Popławska, P. Oliwa, J. Myśliwiec, J. Szczytko, W. Piecek, Directional Lasing from a 3D Blue Phase Photonic Crystal. (under review).

5. **M. Muszyński**, D. Bobylev, P. Kapuściński, P. Oliwa, E. Oton, R. Mazur, P. Morawiak, W. Piecek, P. Kula, B. Piętka, D. Solnyshkov, G. Malpuech, J. Szczytko, Ground state orbital angular momentum lasing from liquid crystal torons. (in preparation).

6. **M. Muszyński**, W. Solarska, P. Kapuściński, P. Oliwa, R. Mazur, P. Morawiak, W. Piecek, P. Kula, D. Solnyshkov, G. Malpuech, J. Szczytko, Rashba-Dresseulaus spin-orbit coupling in photonic lattices. (in preparation).

Other articles and preprints not directly related to the thesis

7. R. Mirek, P. Kokhanchik, D. Urbonas, I. Gorgakilas, **M. Muszyński**, P. Kapuściński, P. Oliwa, B. Piętka, J. Szczytko, M. Forster, U. Scherf, P. Morawiak, W. Piecek, P. Kula, D. Solnyshkov, G. Malpuech, R. Mahrt, T. Stöferle, In-situ tunneling control in photonic potentials by Rashba-Dresselhaus spin-orbit coupling. *arXiv* (2024), arXiv:2408.08582 (under review). [18]
doi:10.48550/arXiv.2408.08582

8. P. Oliwa, P. Kapuściński, M. Popławska, **M. Muszyński**, M. Król, P. Morawiak, R. Mazur, W. Piecek, P. Kula, W. Bardyszewski, B. Piętka, H. Sigurðsson, J. Szczytko, Electrically tunable momentum space polarization singularities in liquid crystal microcavities. *Adv. Sci.* **12**, 2500060 (2025). [21]
doi:10.1002/advs.202500060

9. K. Łempicka-Mirek, M. Król, L. De Marco, A. Coriolano, L. Polimeno, I. Viola, M. Kędziora, **M. Muszyński**, P. Morawiak, R. Mazur, P. Kula, W. Piecek, P. Fita, D. Sanvitto, J. Szczytko, B. Piętka, Electrical polarization switching of perovskite polariton laser. *Nanophotonics* **13**(14), 2659–2668 (2024). [20]
doi:10.1515/nanoph-2023-0829

10. **M. Muszyński**, I. Antoniazzi, B. Camargo, Ion-beam-milled graphite nanoribbons as mesoscopic carbon-based polarizers. *Appl. Phys. Lett.* **123**(3) (2023). [326]
doi:10.1063/5.0147673

11. M. Furman, A. Opala, M. Król, K. Tyszka, R. Mirek, **M. Muszyński**, B. Seredyński, W. Pacuski, J. Szczytko, B. Piętka, Inverted optical bistability and optical limiting in coherently driven exciton–polaritons. *APL Photonics* **8**(4), 046105 (2023). [327]
doi:10.1063/5.0136380

12. K. Łempicka-Mirek, M. Król, H. Sigurdsson, A. Wincukiewicz, P. Morawiak, R. Mazur, **M. Muszyński**, W. Piecek, P. Kula, T. Stefaniuk, M. Kamińska, L. de Marco, P. Lagoudakis, D. Ballarini, D. Sanvitto, J. Szczytko, B. Piętka, Electrically tunable Berry curvature and strong light-matter coupling in liquid crystal microcavities with 2D perovskite. *Sci. Adv.* **8**(40), eabq7533 (2022). [7]
doi:10.1126/sciadv.abq7533

13. M. Król, I. Septembre, P. Oliwa, M. Kędziora, K. Łempicka-Mirek, **M. Muszyński**, R. Mazur, P. Morawiak, W. Piecek, P. Kula, W. Bardyszewski, P. G. Lagoudakis, D. Solnyshkov, G. Malpuech, B. Piętka, J. Szczytko, Annihilation of exceptional points from different Dirac valleys in a 2D photonic system. *Nat. Commun.* **13**(1), 5340 (2022). [6]
doi:10.1038/s41467-022-33001-9

14. **M. Muszyński**, H. Teisseyre, K. Sobczak, J. Suffczyński, Stable charged exciton in a ZnO/(Zn, Mg)O quantum well at near room temperature. *Appl. Phys. Lett.* **117**(3), 033102 (2020). [328]
doi:10.1063/5.0016380

15. K. Łempicka, M. Furman, **M. Muszyński**, M. Król, A. Wincukiewicz, K. Rechcińska, R. Mazur, W. Piecek, M. Kamińska, J. Szczytko, B. Piętka, Exciton-polaritons in a tunable microcavity with 2D-perovskite. *Terahertz Science and Applications*, JW4A-66 (2019). [329]
doi:10.1364/isst.2019.jw4a.66

Appendix D: List of Conference Presentations

Invited Presentations

- Optical tomography o momentum-resolved emission of dye-doped monocrystalline blue phase (I), OLC 2021, Optics of Liquid Crystals 2021, 2021, Okinawa, Japan

Oral Presentations

- Two-dimensional self-organized liquid crystal photonic potential based on a lattice of torons in an optical microcavity, ILCC 2024, 29th International Liquid Crystal Conference, 2024, Rio de Janeiro, Brasil
- Self-Assembled Two-Dimensional Lattice of Liquid Crystal Torons as a Potential Landscape for Massive Photons with Spin, 51th "Jaszowiec" International School and Conference on the Physics of Semiconductors, 2024, Szczyrk, Poland
- Tunable band structures coupled by spin-orbit interaction in self-organized photonic potential inside a liquid crystal optical microcavity, META, 13th International Conference on Metamaterials, Photonic Crystals and Plasmonics, 2023, Paris, France
- Liquid Crystal Optical Microcavity with built-in Uniform Lying Helix as a platform for tunable one-dimensional photonic potential with spin-orbit interaction, ECLC, 16th European Conference on Liquid Crystals, 2023, Rende, Italy
- Nonlinear emission of spin-orbit-coupled tunable band structures in self-assembled photonic potential embedded in optical microcavity, EPIC, Excitonics and Polaritonics International Conference, 2023, Singapore
- Persistent spin-helix laser based on liquid crystal optical microcavity, Organic and Hybrid Light Emitting Materials and Devices XXVI, 2022, San Diego, USA
- The room-temperature persistent spin-helix lasing and the spin coherence in the dye-doped liquid crystal optical microcavity, ICSCE-11, 11th International Conference on Spontaneous Coherence in Excitonic Systems, 2022, Burlington, USA
- Realizing Rashba-Dresselhaus lasing in tunable liquid crystal birefringent optical microcavity, ILCC 2022, 28th International Liquid Crystal Conference, 2022, Lisbon, Portugal
- Persistent Spin-Helix and Tunable Laser Operating at Room Temperature Based on Liquid Crystal Optical Microcavity, 50th "Jaszowiec" International School and Conference on the Physics of Semiconductors, 2022, Szczyrk, Poland
- Rashba-Dresselhaus and tunable lasing at room temperature in dye-filled liquid crystal optical microcavities, XXIII Conference on Liquid Crystals, 2021, Karpacz, Poland - Best Oral Presentation Award

Posters

- Spin-Orbit Coupled Tunable Band Structures in a Self-Assembled Photonic Potential within a Liquid Crystal Optical Microcavity, HMF25, 25th International Conference on High Magnetic Fields in Semiconductor Physics, 2024, Warsaw, Poland
- Self-organizing photonic potential with tunable band structures coupled by spin-orbit interaction in birefringent optical cavity, 51th "Jaszowiec" International School and Conference on the Physics of Semiconductors, 2023, Szczyrk, Poland
- Optical properties of dye-doped monocrystalline free-standing blue phase liquid crystal, 49th "Jaszowiec" International School and Conference on the Physics of Semiconductors, 2021, Szczyrk, Poland
- Strong Coupling of Light and Matter Observed in a Tunable Microcavity with 2D-Perovskites at Room Temperature, MRS 2020, 2020 Virtual MRS Spring/Fall Meeting & Exhibit, 2020, Boston, USA
- Tunable Room-Temperature Exciton-Polaritons in a Microcavity Containing 2D-Perovskites, ICSCE-10, 10TH International Conference on Spontaneous Coherence in Excitonic Systems, 2020, Melbourne, Australia
- Exciton-Polaritons in a Tunable Microcavity with 2D-Perovskite, POEM 2019, 2019, Wuhan, China – Best Poster Award
- Large surface epitaxial MoSe2 layers grown on SiO2/TiO2 Bragg mirrors, 48th "Jaszowiec" International School and Conference on the Physics of Semiconductors, 2019, Szczyrk, Poland

Appendix E: Glossary

BEC - Bose-Einstein condensate; BP, BPI, BPII - blue phase, blue phase (I), blue phase (II); CLC - cholesteric liquid crystal; CNRS - Centre national de la recherche scientifique; ISOC - interband spin-orbit interaction; LC - liquid crystal; LCMC - liquid crystal microcavity; nBEC - non-equilibrium Bose-Einstein condensate; MeLPPP - methyl-substituted ladder-type poly(-para-phenylene); MUT - Military University of Technology; OA - optical activity; P580 - pyrromethene 580, organic laser dye; PhCs - photonic crystals; PBGs - photonic bandgaps; PL - photoluminescence; POM - polarized optical microscopy; SOC - spin-orbit coupling; ULH - uniform lying helix; UW - University of Warsaw.

References

[1] Katarzyna Lekenta, Mateusz Król, Rafał Mirek, Karolina Łempicka, Daniel Stephan, Rafał Mazur, Przemysław Morawiak, Przemysław Kula, Wiktor Piecek, Pavlos G Lagoudakis, et al. Tunable optical spin Hall effect in a liquid crystal microcavity. *Light Sci. Appl.*, 7(1):74, 2018.

[2] Katarzyna Rechcińska, Mateusz Król, Rafał Mazur, Przemysław Morawiak, Rafał Mirek, Karolina Łempicka, Witold Bardyszewski, Michał Matuszewski, Przemysław Kula, Wiktor Piecek, et al. Engineering spin-orbit synthetic Hamiltonians in liquid-crystal optical cavities. *Science*, 366(6466):727–730, 2019.

[3] Mateusz Król, Helgi Sigurdsson, Katarzyna Rechcińska, Przemysław Oliwa, Krzystof Tyszka, Witold Bardyszewski, Andrzej Opala, Michał Matuszewski, Przemysław Morawiak, Rafał Mazur, et al. Observation of second-order meron polarization textures in optical microcavities. *Optica*, 8(2):255–261, 2021.

[4] Mateusz Król, Katarzyna Rechcińska, Helgi Sigurdsson, Przemysław Oliwa, Rafał Mazur, Przemysław Morawiak, Wiktor Piecek, Przemysław Kula, Pavlos G Lagoudakis, Michał Matuszewski, et al. Realizing optical persistent spin helix and Stern-Gerlach deflection in an anisotropic liquid crystal microcavity. *Phys. Rev. Lett.*, 127(19):190401, 2021.

[5] Marcin Muszyński, Mateusz Król, Katarzyna Rechcińska, Przemysław Oliwa, Mateusz Kędziora, Karolina Łempicka-Mirek, Rafał Mazur, Przemysław Morawiak, Wiktor Piecek, Przemysław Kula, et al. Realizing persistent-spin-helix lasing in the regime of Rashba-Dresselhaus spin-orbit coupling in a dye-filled liquid-crystal optical microcavity. *Phys. Rev. Appl.*, 17(1):014041, 2022.

[6] Mateusz Król, I Septembre, P Oliwa, Mateusz Kędziora, K Łempicka-Mirek, Marcin Muszyński, Rafał Mazur, Przemysław Morawiak, W Piecek, Przemysław Kula, et al. Annihilation of exceptional points from different Dirac valleys in a 2D photonic system. *Nat. Commun.*, 13(1):5340, 2022.

[7] Karolina Łempicka-Mirek, Mateusz Król, Helgi Sigurdsson, Adam Wincukiewicz, Przemysław Morawiak, Rafał Mazur, Marcin Muszyński, Wiktor Piecek, Przemysław Kula, Tomasz Stefaniuk, et al. Electrically tunable Berry curvature and strong light-matter coupling in liquid crystal microcavities with 2D perovskite. *Sci. Adv.*, 8(40):eabq7533, 2022.

[8] Pavel Kokhanchik, Dmitry Solnyshkov, Thilo Stöferle, Barbara Piętka, Jacek Szczytko, and Guillaume Malpuech. Modulated Rashba-Dresselhaus spin-orbit coupling for topology control and analog simulations. *Phys. Rev. Lett.*, 129(24):246801, 2022.

[9] Yao Li, Xuekai Ma, Xiaokun Zhai, Meini Gao, Haitao Dai, Stefan Schumacher, and Tingge Gao. Manipulating polariton condensates by Rashba-Dresselhaus coupling at room temperature. *Nat. Commun.*, 13(1):3785, 2022.

[10] Pavel Kokhanchik, Dmitry Solnyshkov, and Guillaume Malpuech. Non-Hermitian skin effect induced by Rashba-Dresselhaus spin-orbit coupling. *Phys. Rev. B*, 108(4):L041403, 2023.

[11] Qian Liang, Xuekai Ma, Teng Long, Jiannian Yao, Qing Liao, and Hongbing Fu. Circularly polarized lasing from a microcavity filled with achiral single-crystalline microribbons. *Angew. Chem. Int. Ed.*, 62(9):e202213229, 2023.

[12] Reo Ohkura, Takaya Inukai, Shun Takahashi, Hitoshi Mizuno, Masaaki Nakayama, Yohei Yamamoto, and Kenichi Yamashita. Rashba-Dresselhaus spin-orbit coupling and polarization-coupled luminescence in an organic single crystal microcavity. *arXiv preprint arXiv:2310.06465*, 2023.

[13] Xiaokun Zhai, Xuekai Ma, Ying Gao, Chunzi Xing, Meini Gao, Haitao Dai, Xiao Wang, Anlian Pan, Stefan Schumacher, and Tingge Gao. Electrically controlling vortices in a neutral exciton-polariton condensate at room temperature. *Phys. Rev. Lett.*, 131(13):136901, 2023.

[14] Marcin Muszynski, Pavel Kokhanchik, Darius Urbonas, Piotr Kapuscinski, Przemyslaw Oliwa, Rafal Mirek, Ioannis Georgakilas, Thilo Stöferle, Rainer F Mahrt, Michael Forster, et al. Observation of a stripe phase in a spin-orbit coupled exciton-polariton Bose-Einstein condensate. *arXiv preprint arXiv:2407.02406*, 2024.

[15] Marcin Muszyński, Przemysław Oliwa, Pavel Kokhanchik, Piotr Kapuściński, Eva Oton, Rafał Mazur, Przemysław Morawiak, Wiktor Piecek, Przemysław Kula, Witold Bardyszewski, et al. Electrically tunable spin-orbit coupled photonic lattice in a liquid crystal microcavity. *Laser Photonics Rev.*, page 2400794, 2024.

[16] Evgeny Sedov, Mikhail M Glazov, Pavlos G Lagoudakis, and Alexey V Kavokin. Light-matter coupling and spin-orbit interaction of polariton modes in liquid crystal optical microcavities. *Phys. Rev. Res.*, 6(2):023220, 2024.

[17] Jie Liang, Wen Wen, Feng Jin, Yuri G Rubo, Timothy CH Liew, and Rui Su. Polariton spin Hall effect in a Rashba–Dresselhaus regime at room temperature. *Nat. Photonics*, 18(4):357–362, 2024.

[18] Rafał Mirek, Pavel Kokhanchik, Darius Urbonas, Ioannis Georgakilas, Marcin Muszyński, Piotr Kapuściński, Przemysław Oliwa, Barbara Piętka, Jacek Szczytko, Michael Forster, et al. In-situ tunneling control in photonic potentials by Rashba-Dresselhaus spin-orbit coupling. *arXiv preprint arXiv:2408.08582*, 2024.

[19] Wen Wen, Jie Liang, Huawen Xu, Feng Jin, Yuri G Rubo, Timothy CH Liew, and Rui Su. Trembling motion of exciton polaritons close to the Rashba-Dresselhaus regime. *Phys. Rev. Lett.*, 133(11):116903, 2024.

[20] Karolina Łempicka-Mirek, Mateusz Król, Luisa De Marco, Annalisa Coriolano, Laura Polimeno, Ilenia Viola, Mateusz Kędziora, Marcin Muszyński, Przemysław Morawiak, Rafał Mazur, et al. Electrical polarization switching of perovskite polariton laser. *Nanophotonics*, 13(14):2659–2668, 2024.

[21] Przemysław Oliwa, Piotr Kapuściński, Maria Popławska, Marcin Muszyński, Mateusz Król, Przemysław Morawiak, Rafał Mazur, Wiktor Piecek, Przemysław Kula, Witold Bardyszewski, et al. Electrically tunable momentum space polarization singularities in liquid crystal microcavities. *Adv. Sci.*, page 2500060, 2025.

[22] Xiaokun Zhai, Chunzi Xing, Xinmiao Yang, Xinzheng Zhang, Haitao Dai, Xiao Wang, Anlian Pan, Stefan Schumacher, Xuekai Ma, and Tingge Gao. Electrically tunable nonrigid Moire exciton polariton supersolids at room temperature. *arXiv preprint arXiv:2504.11057*, 2025.

[23] Filippo Cardano and Lorenzo Marrucci. Spin–orbit photonics. *Nat. Photonics*, 9(12):776–778, 2015.

[24] Konstantin Yu Bliokh, Francisco J Rodríguez-Fortuño, Franco Nori, and Anatoly V Zayats. Spin–orbit interactions of light. *Nat. Photonics*, 9(12):796–808, 2015.

[25] Olivier Castany, Cyril Paranthoen, Christophe Levallois, Ahmad Shuaib, Jean-Philippe Gauthier, Nicolas Chevalier, Olivier Durand, Laurent Dupont, and Alain Le Corre. Demonstration of a 34 nm monolithic continuously tunable vcsel at 1.55 μm combined with liquid crystal. In *IPRM 2011-23rd International Conference on Indium Phosphide and Related Materials*, pages 1–4. IEEE, 2011.

[26] Frank J Duarte. *Tunable laser applications*. CRC press, 2008.

[27] Alison M Yao and Miles J Padgett. Orbital angular momentum: origins, behavior and applications. *Adv. Opt. Photonics*, 3(2):161–204, 2011.

[28] Gabriel Molina-Terriza, Juan P Torres, and Lluis Torner. Twisted photons. *Nat. Phys.*, 3(5):305–310, 2007.

[29] Thomas Kleine-Ostmann and Tadao Nagatsuma. A review on terahertz communications research. *J. Infrared, Millimeter, Terahertz Waves*, 32:143–171, 2011.

[30] Carmen Catanescu, L-C Chien, and Shin-Tson Wu. High birefringence nematic liquid crystals for display and telecom applications. *Mol. Cryst. Liq. Cryst.*, 411(1):93–102, 2004.

[31] Jean-Christophe P Gabriel and Patrick Davidson. Mineral liquid crystals from self-assembly of anisotropic nanosystems. *Colloid Chemistry I*, pages 119–172, 2003.

[32] Ian William Hamley. Liquid crystal phase formation by biopolymers. *Soft Matter*, 6(9):1863–1871, 2010.

[33] Teresa E Strzelecka, Michael W Davidson, and Randolph L Rill. Multiple liquid crystal phases of DNA at high concentrations. *Nature*, 331(6155):457–460, 1988.

[34] Dennis Chapman. Liquid crystals and cell membranes. *Ann. N. Y. Acad. Sci.*, 137(2):745–754, 1966.

[35] Frederick Charles Bawden and Norman Wingate Pirie. The isolation and some properties of liquid crystalline substances from solanaceous plants infected with three strains of tobacco mosaic virus. *Proc. R. Soc. Lond. B Biol. Sci.*, 123(832):274–320, 1937.

[36] Steven A Kivelson, Eduardo Fradkin, and Victor J Emery. Electronic liquid-crystal phases of a doped Mott insulator. *Nature*, 393(6685):550–553, 1998.

[37] Harry Coles and Stephen Morris. Liquid-crystal lasers. *Nat. Photonics*, 4(10):676–685, 2010.

[38] Jakub Karcz, Jakub Herman, Natan Rychłowicz, Przemysław Kula, Ewa Górecka, Jadwiga Szydlowska, Pawel W Majewski, and Damian Pociecha. Spontaneous chiral symmetry breaking in polar fluid–heliconical ferroelectric nematic phase. *Science*, 384(6700):1096–1099, 2024.

[39] Maurice Kléman. Defects in liquid crystals. *Rep. Prog. Phys.*, 52(5):555, 1989.

[40] Maurice Kleman and Oleg D Lavrentovich. Topological point defects in nematic liquid crystals. *Philos. Mag.*, 86(25-26):4117–4137, 2006.

[41] Janglin Chen, Wayne Cranton, and Mark Fihn. *Handbook of visual display technology*. Springer Publishing Company, Incorporated, 2011.

[42] Vsevolod Fréedericksz and V Zolina. Forces causing the orientation of an anisotropic liquid. *Trans. Faraday Soc.*, 29(140):919–930, 1933.

[43] Peter J Collings and John W Goodby. *Introduction to liquid crystals: chemistry and physics*. Crc Press, 2019.

[44] Hitesh Khandelwal, Albertus PHJ Schenning, and Michael G Debije. Infrared regulating smart window based on organic materials. *Adv. Energy Mater.*, 7(14):1602209, 2017.

[45] Nobuyuki Tamaoki. Cholesteric liquid crystals for color information technology. *Adv. Mater.*, 13(15):1135–1147, 2001.

[46] De-Shan Hou, Lin Zheng, Dong-Peng Sun, Xuan Zhou, Ji-Liang Zhu, and Wen-Ming Han. Polymer-stabilized blue phase liquid crystal sensor for sensitive and selective detection of organic vapors. *Liq. Cryst.*, 49(2):201–208, 2022.

[47] Yu Yang, Young-Ki Kim, Xin Wang, Michael Tsuei, and Nicholas L Abbott. Structural and optical response of polymer-stabilized blue phase liquid crystal films to volatile organic compounds. *ACS Appl. Mater. Interfaces*, 12(37):42099–42108, 2020.

[48] Yanzhao Yang, Xuan Zhang, Yuanhao Chen, Xiao Yang, Jiazhe Ma, Jingxia Wang, Ling Wang, and Wei Feng. Bioinspired color-changing photonic polymer coatings based on three-dimensional blue phase liquid crystal networks. *ACS Appl. Mater. Interfaces*, 13(34):41102–41111, 2021.

[49] Kushal Bagchi, Tadej Emeršič, José A Martínez-González, Juan J de Pablo, and Paul F Nealey. Functional soft materials from blue phase liquid crystals. *Sci. Adv.*, 9(30):eadh9393, 2023.

[50] F Castles, SM Morris, JMC Hung, Malik Muhammad Qasim, AD Wright, Shabeena Nosheen, SS Choi, BI Outram, SJ Elston, C Burgess, et al. Stretchable liquid-crystal blue-phase gels. *Nat. Mater.*, 13(8):817–821, 2014.

[51] Mikolaj Rogoz, Hao Zeng, Chen Xuan, Diederik Sybolt Wiersma, Piotr Wasylczyk, et al. Light-driven soft robot mimics caterpillar locomotion in natural scale. *Adv. Opt. Mater.*, 4:1689–1694, 2016.

[52] Eli Yablonovitch. Inhibited spontaneous emission in solid-state physics and electronics. *Phys. Rev. Lett.*, 58(20):2059, 1987.

[53] Sajeev John. Strong localization of photons in certain disordered dielectric superlattices. *Phys. Rev. Lett.*, 58(23):2486, 1987.

[54] Alexey V Kavokin, Jeremy J Baumberg, Guillaume Malpuech, and Fabrice P Laussy. *Microcavities*. Oxford university press, 2017.

[55] Alexey V Kavokin, Guillaume Malpuech, and Mikhail M Glazov. Optical spin Hall effect. *Phys. Rev. Lett.*, 95(13):136601, 2005.

[56] Charles Leyder, Marco Romanelli, J Ph Karr, Elisabeth Giacobino, Tim CH Liew, Mikhail M Glazov, Alexey V Kavokin, Guillaume Malpuech, and Alberto Bramati. Observation of the optical spin Hall effect. *Nat. Phys.*, 3(9):628–631, 2007.

[57] Filippo Cardano, Ebrahim Karimi, Sergei Slussarenko, Lorenzo Marrucci, Corrado de Lisio, and Enrico Santamato. Polarization pattern of vector vortex beams generated by q-plates with different topological charges. *Appl. Opt.*, 51(10):C1–C6, 2012.

[58] R Hivet, H Flayac, DD Solnyshkov, D Tanese, T Boulier, D Andreoli, E Giacobino, J Bloch, A Bramati, G Malpuech, et al. Half-solitons in a polariton quantum fluid behave like magnetic monopoles. *Nat. Phys.*, 8(10):724–728, 2012.

[59] P Renucci, Tobias Amand, X Marie, P Senellart, J Bloch, B Sermage, and KV Kavokin. Microcavity polariton spin quantum beats without a magnetic field: A manifestation of Coulomb exchange in dense and polarized polariton systems. *Phys. Rev. B: Condens. Matter*, 72(7):075317, 2005.

[60] Michael S Spencer, Yongping Fu, Andrew P Schlaus, Doyk Hwang, Yanan Dai, Matthew D Smith, Daniel R Gamelin, and X-Y Zhu. Spin-orbit–coupled exciton-polariton condensates in lead halide perovskites. *Sci. Adv.*, 7(49):eabj7667, 2021.

[61] Roman Dąbrowski, Przemysław Kula, and Jakub Herman. High birefringence liquid crystals. *Crystals*, 3(3):443–482, 2013.

[62] B Andrei Bernevig, J Orenstein, and Shou-Cheng Zhang. Exact SU(2) symmetry and persistent spin helix in a spin-orbit coupled system. *Phys. Rev. Lett.*, 97(23):236601, 2006.

[63] Jake D Koralek, Christopher P Weber, Joe Orenstein, B Andrei Bernevig, Shou-Cheng Zhang, Shawn Mack, and DD Awschalom. Emergence of the persistent spin helix in semiconductor quantum wells. *Nature*, 458(7238):610–613, 2009.

[64] Timur Yagafarov, Denis Sannikov, Anton Zasedatelev, Kyriacos Georgiou, Anton Baranikov, Oleksandr Kyriienko, Ivan Shelykh, Lizhi Gai, Zhen Shen, David Lidzey, et al. Mechanisms of blueshifts in organic polariton condensates. *Commun. Phys.*, 3(1):18, 2020.

[65] Yongbao Sun, Yoseob Yoon, Mark Steger, Gangqiang Liu, Loren N Pfeiffer, Ken West, David W Snoke, and Keith A Nelson. Direct measurement of polariton–polariton interaction strength. *Nat. Phys.*, 13(9):870–875, 2017.

[66] Mark Steger, Gangqiang Liu, Bryan Nelsen, Chitra Gautham, David W Snoke, Ryan Balili, Loren Pfeiffer, and Ken West. Long-range ballistic motion and coherent flow of long-lifetime polaritons. *Phys. Rev. B*, 88(23):235314, 2013.

[67] Jie Gu, Valentin Walther, Lutz Waldecker, Daniel Rhodes, Archana Raja, James C Hone, Tony F Heinz, Stéphane Kéna-Cohen, Thomas Pohl, and Vinod M Menon. Enhanced nonlinear interaction of polaritons via excitonic Rydberg states in monolayer WSe2. *Nat. Commun.*, 12(1):2269, 2021.

[68] JJ Hopfield. Theory of the contribution of excitons to the complex dielectric constant of crystals. *Phys. Rev.*, 112(5):1555, 1958.

[69] David M Coles, Niccolo Somaschi, Paolo Michetti, Caspar Clark, Pavlos G Lagoudakis, Pavlos G Savvidis, and David G Lidzey. Polariton-mediated energy transfer between organic dyes in a strongly coupled optical microcavity. *Nat. Mater.*, 13(7):712–719, 2014.

[70] Raphael F Ribeiro, Luis A Martínez-Martínez, Matthew Du, Jorge Campos-Gonzalez-Angulo, and Joel Yuen-Zhou. Polariton chemistry: controlling molecular dynamics with optical cavities. *Chem. Sci.*, 9(30):6325–6339, 2018.

[71] NA Gippius, IA Shelykh, DD Solnyshkov, SS Gavrilov, Yuri G Rubo, Alexey V Kavokin, SG Tikhodeev, and G Malpuech. Polarization multistability of cavity polaritons. *Phys. Rev. Lett.*, 98(23):236401, 2007.

[72] TK Paraïso, Michiel Wouters, Y Léger, F Morier-Genoud, and Benoit Deveaud-Plédran. Multistability of a coherent spin ensemble in a semiconductor microcavity. *Nat. Mater.*, 9(8):655–660, 2010.

[73] Mike H Anderson, Jason R Ensher, Michael R Matthews, Carl E Wieman, and Eric A Cornell. Observation of Bose-Einstein condensation in a dilute atomic vapor. *Science*, 269(5221):198–201, 1995.

[74] Kendall B Davis, M-O Mewes, Michael R Andrews, Nicolaas J van Druten, Dallin S Durfee, DM Kurn, and Wolfgang Ketterle. Bose-Einstein condensation in a gas of sodium atoms. *Phys. Rev. Lett.*, 75(22):3969, 1995.

[75] T Nikuni, M Oshikawa, A Oosawa, and H Tanaka. Bose-Einstein condensation of dilute magnons in $TlCuCl_3$. *Phys. Rev. Lett.*, 84(25):5868, 2000.

[76] JP Eisenstein and Allan H MacDonald. Bose–Einstein condensation of excitons in bilayer electron systems. *Nature*, 432(7018):691–694, 2004.

[77] Jan Klaers, Julian Schmitt, Frank Vewinger, and Martin Weitz. Bose–Einstein condensation of photons in an optical microcavity. *Nature*, 468(7323):545–548, 2010.

[78] David Snoke. Spontaneous Bose coherence of excitons and polaritons. *Science*, 298(5597):1368–1372, 2002.

[79] Esther Wertz, Lydie Ferrier, DD Solnyshkov, Robert Johne, Daniele Sanvitto, Aristide Lemaître, Isabelle Sagnes, Roger Grousson, Alexey V Kavokin, Pascale Senellart, et al. Spontaneous formation and optical manipulation of extended polariton condensates. *Nat. Phys.*, 6(11):860–864, 2010.

[80] KG Lagoudakis, T Ostatnickỳ, Alexey V Kavokin, Yuri G Rubo, Régis André, and Benoit Deveaud-Plédran. Observation of half-quantum vortices in an exciton-polariton condensate. *Science*, 326(5955):974–976, 2009.

[81] Alberto Amo, Jérôme Lefrère, Simon Pigeon, Claire Adrados, Cristiano Ciuti, Iacopo Carusotto, Romuald Houdré, Elisabeth Giacobino, and Alberto Bramati. Superfluidity of polaritons in semiconductor microcavities. *Nat. Phys.*, 5(11):805–810, 2009.

[82] Tim Byrnes, Na Young Kim, and Yoshihisa Yamamoto. Exciton–polariton condensates. *Nat. Phys.*, 10(11):803–813, 2014.

[83] Jacek Kasprzak, Murielle Richard, S Kundermann, A Baas, P Jeambrun, Jonathan Mark James Keeling, FM Marchetti, MH Szymańska, R André, JL a Staehli, et al. Bose–Einstein condensation of exciton polaritons. *Nature*, 443(7110):409–414, 2006.

[84] Vinodkumar Saranathan, Chinedum O Osuji, Simon GJ Mochrie, Heeso Noh, Suresh Narayanan, Alec Sandy, Eric R Dufresne, and Richard O Prum. Structure, function, and self-assembly of single network gyroid (I_{4132}) photonic crystals in butterfly wing scales. *PNAS*, 107(26):11676–11681, 2010.

[85] Annalisa Coriolano, Antonio Fieramosca, Laura Polimeno, Rosanna Mastria, Francesco Todisco, Milena De Giorgi, Luisa De Marco, Aurora Rizzo, Dario Ballarini, Ilenia Viola, et al. Microfluidic-assisted growth of perovskite microwires for room-temperature all-optical switching based on total internal reflection. *arXiv preprint arXiv:2502.15313*, 2025.

[86] Nguyen Ha My Dang, Simone Zanotti, Emmanuel Drouard, Céline Chevalier, Gaëlle Trippé-Allard, Emmanuelle Deleporte, Christian Seassal, Dario Gerace, and Hai Son Nguyen. Long-range ballistic propagation of 80% excitonic fraction polaritons in a perovskite metasurface at room temperature. *Nano Lett.*, 24(38):11839–11846, 2024.

[87] Rahul Jayaprakash, Charles E Whittaker, Kyriacos Georgiou, Onkar S Game, Kirsty E McGhee, David M Coles, and David G Lidzey. Two-dimensional organic-exciton polariton lattice fabricated using laser patterning. *ACS Photonics*, 7(8):2273–2281, 2020.

[88] Julian D Töpfer, Ioannis Chatzopoulos, Helgi Sigurdsson, Tamsin Cookson, Yuri G Rubo, and Pavlos G Lagoudakis. Engineering spatial coherence in lattices of polariton condensates. *Optica*, 8(1):106–113, 2021.

[89] Maciej Pieczarka, Eliezer Estrecho, Sanjib Ghosh, Matthias Wurdack, Mark Steger, David W Snoke, Kenneth West, Loren N Pfeiffer, Timothy CH Liew, Andrew G Truscott, et al. Topological phase transition in an all-optical exciton-polariton lattice. *Optica*, 8(8):1084–1091, 2021.

[90] Joanna M Zajac and Wolfgang Langbein. Structure and zero-dimensional polariton spectrum of natural defects in GaAs/AlAs microcavities. *Phys. Rev. B: Condens. Matter*, 86(19):195401, 2012.

[91] Juan F Galisteo-López, Marta Ibisate, Riccardo Sapienza, Luis S Froufe-Pérez, Álvaro Blanco, and Cefe López. Self-assembled photonic structures. *Adv. Mater.*, 23(1):30–69, 2011.

[92] Zhongyu Cai, Zhiwei Li, Serge Ravaine, Mingxin He, Yanlin Song, Yadong Yin, Hanbin Zheng, Jinghua Teng, and AO Zhang. From colloidal particles to photonic crystals: advances in self-assembly and their emerging applications. *Chem. Soc. Rev.*, 50(10):5898–5951, 2021.

[93] Simon Betzold, Marco Dusel, Oleksandr Kyriienko, Christof P Dietrich, Sebastian Klembt, Jürgen Ohmer, Utz Fischer, Ivan A Shelykh, Christian Schneider, and Sven Höfling. Coherence

and interaction in confined room-temperature polariton condensates with Frenkel excitons. *ACS Photonics*, 7(2):384–392, 2019.

[94] JMea Gerard, D Barrier, JY Marzin, R Kuszelewicz, L Manin, E Costard, V Thierry-Mieg, and T Rivera. Quantum boxes as active probes for photonic microstructures: The pillar microcavity case. *Appl. Phys. Lett.*, 69(4):449–451, 1996.

[95] Darius Urbonas, Thilo Stöferle, Fabio Scafirimuto, Ullrich Scherf, and Rainer F Mahrt. Zero-dimensional organic exciton–polaritons in tunable coupled gaussian defect microcavities at room temperature. *ACS Photonics*, 3(9):1542–1545, 2016.

[96] VG Sala, DD Solnyshkov, I Carusotto, T Jacqmin, A Lemaître, H Terças, A Nalitov, Marco Abbarchi, E Galopin, I Sagnes, et al. Spin-orbit coupling for photons and polaritons in microstructures. *Phys. Rev. X*, 5(1):011034, 2015.

[97] Philippe St-Jean, Victor Goblot, Elisabeth Galopin, A Lemaître, Thomas Ozawa, Luc Le Gratiet, Isabelle Sagnes, Jacqueline Bloch, and Alberto Amo. Lasing in topological edge states of a one-dimensional lattice. *Nat. Photonics*, 11(10):651–656, 2017.

[98] Nicolas Pernet, Philippe St-Jean, Dmitry D Solnyshkov, Guillaume Malpuech, Nicola Carlon Zambon, Quentin Fontaine, Bastian Real, Omar Jamadi, Aristide Lemaître, Martina Morassi, et al. Gap solitons in a one-dimensional driven-dissipative topological lattice. *Nat. Phys.*, 18(6):678–684, 2022.

[99] Rui Su, Sanjib Ghosh, Timothy CH Liew, and Qihua Xiong. Optical switching of topological phase in a perovskite polariton lattice. *Sci. Adv.*, 7(21):eabf8049, 2021.

[100] V Ardizzone, F Riminucci, S Zanotti, A Gianfrate, M Efthymiou-Tsironi, DG Suàrez-Forero, F Todisco, M De Giorgi, D Trypogeorgos, G Gigli, et al. Polariton Bose–Einstein condensate from a bound state in the continuum. *Nature*, 605(7910):447–452, 2022.

[101] Omar Jamadi, F Reveret, Pierre Disseix, François Medard, Joël Leymarie, Alexis Moreau, D Solnyshkov, C Deparis, M Leroux, E Cambril, et al. Edge-emitting polariton laser and amplifier based on a ZnO waveguide. *Light Sci. Appl.*, 7(1):82, 2018.

[102] Bo Zhang, Zhaorong Wang, Sebastian Brodbeck, Christian Schneider, Martin Kamp, Sven Höfling, and Hui Deng. Zero-dimensional polariton laser in a subwavelength grating-based vertical microcavity. *Light Sci. Appl.*, 3(1):e135–e135, 2014.

[103] Na Young Kim, Kenichiro Kusudo, Congjun Wu, Naoyuki Masumoto, Andreas Löffler, Sven Höfling, Norio Kumada, Lukas Worschech, Alfred Forchel, and Yoshihisa Yamamoto. Dynamical d-wave condensation of exciton–polaritons in a two-dimensional square-lattice potential. *Nat. Phys.*, 7(9):681–686, 2011.

[104] Natalia G Berloff, Matteo Silva, Kirill Kalinin, Alexis Askitopoulos, Julian D Töpfer, Pasquale Cilibrizzi, Wolfgang Langbein, and Pavlos G Lagoudakis. Realizing the classical XY Hamiltonian in polariton simulators. *Nat. Mater.*, 16(11):1120–1126, 2017.

[105] Na Young Kim, Kenichiro Kusudo, Andreas Löffler, Sven Höfling, Alfred Forchel, and Yoshihisa Yamamoto. Exciton–polariton condensates near the Dirac point in a triangular lattice. *New J. Phys.*, 15(3):035032, 2013.

[106] Thibaut Jacqmin, Iacopo Carusotto, Isabelle Sagnes, Marco Abbarchi, DD Solnyshkov, Guillaume Malpuech, Elisabeth Galopin, Aristide Lemaître, Jacqueline Bloch, and Alberto Amo. Direct observation of Dirac cones and a flatband in a honeycomb lattice for polaritons. *Phys. Rev. Lett.*, 112(11):116402, 2014.

[107] Sebastian Klembt, Tristan H Harder, Oleg A Egorov, Karol Winkler, Holger Suchomel, Johannes Beierlein, Monika Emmerling, Christian Schneider, and Sven Höfling. Polariton condensation in s-and p-flatbands in a two-dimensional Lieb lattice. *Appl. Phys. Lett.*, 111(23), 2017.

[108] CE Whittaker, Emiliano Cancellieri, PM Walker, DR Gulevich, H Schomerus, D Vaitiekus, B Royall, DM Whittaker, E Clarke, IV Iorsh, et al. Exciton polaritons in a two-dimensional Lieb lattice with spin-orbit coupling. *Phys. Rev. Lett.*, 120(9):097401, 2018.

[109] Naoyuki Masumoto, Na Young Kim, Tim Byrnes, Kenichiro Kusudo, Andreas Löffler, Sven Höfling, Alfred Forchel, and Yoshihisa Yamamoto. Exciton–polariton condensates with flat bands in a two-dimensional Kagome lattice. *New J. Phys.*, 14(6):065002, 2012.

[110] AV Nalitov, DD Solnyshkov, and G Malpuech. Polariton Z topological insulator. *Phys. Rev. Lett.*, 114(11):116401, 2015.

[111] Sebastian Klembt, TH Harder, OA Egorov, K Winkler, R Ge, MA Bandres, M Emmerling, L Worschech, TCH Liew, M Segev, et al. Exciton-polariton topological insulator. *Nature*, 562(7728):552–556, 2018.

[112] Kai Peng, Wei Li, Meng Sun, Jose DH Rivero, Chaoyang Ti, Xu Han, Li Ge, Lan Yang, Xiang Zhang, and Wei Bao. Topological valley Hall polariton condensation. *Nat. Nanotechnol.*, 19(9):1283–1289, 2024.

[113] Kohki Takatoh, Masanori Sakamoto, Ray Hasegawa, Mitsushiro Koden, Nobuyuki Itoh, and Masaki Hasegawa. *Alignment technology and applications of liquid crystal devices*. CRC press, 2005.

[114] Kunihiro Ichimura. Photoalignment of liquid-crystal systems. *Chem. Rev.*, 100(5):1847–1874, 2000.

[115] B Sivaranjini, R Mangaiyarkarasi, V Ganesh, and S Umadevi. Vertical alignment of liquid crystals over a functionalized flexible substrate. *Sci. Rep.*, 8(1):8891, 2018.

[116] Jai Prakash, Akash Kumar, and Shikha Chauhan. Aligning liquid crystal materials through nanoparticles: a review of recent progress. *Liquids*, 2(2):50–71, 2022.

[117] Eva Otón, Hiroyuki Yoshida, Przemysław Morawiak, Olga Strzeżysz, Przemysław Kula, Masanori Ozaki, and Wiktor Piecek. Orientation control of ideal blue phase photonic crystals. *Sci. Rep.*, 10(1):10148, 2020.

[118] Herbert Gross, Frits Blechinger, and Bertram Achtner. *Handbook of optical systems*, volume 1. Wiley Online Library, 2005.

[119] Mathias Schubert. Polarization-dependent optical parameters of arbitrarily anisotropic homogeneous layered systems. *Phys. Rev. B*, 53(8):4265, 1996.

[120] Daniele Sanvitto and Stéphane Kéna-Cohen. The road towards polaritonic devices. *Nat. Mater.*, 15(10):1061–1073, 2016.

[121] Krzysztof Sawicki, Jean-Guy Rousset, Rafał Rudniewski, Wojciech Pacuski, Maciej Ściesiek, Tomasz Kazimierczuk, Kamil Sobczak, Jolanta Borysiuk, Michał Nawrocki, and Jan Suffczyński. Triple threshold lasing from a photonic trap in a Te/Se-based optical microcavity. *Commun. Phys.*, 2(1):38, 2019.

[122] Denis Sannikov, Timur Yagafarov, Kyriacos Georgiou, Anton Zasedatelev, Anton Baranikov, Lizhi Gai, Zhen Shen, David Lidzey, and Pavlos G Lagoudakis. Room temperature broadband polariton lasing from a dye-filled microcavity. *Adv. Opt. Mater.*, 7(17):1900163, 2019.

[123] Ankun Yang, Thang B Hoang, Montacer Dridi, Claire Deeb, Maiken H Mikkelsen, George C Schatz, and Teri W Odom. Real-time tunable lasing from plasmonic nanocavity arrays. *Nat. Commun.*, 6(1):6939, 2015.

[124] Rui Su, Carole Diederichs, Jun Wang, Timothy CH Liew, Jiaxin Zhao, Sheng Liu, Weigao Xu, Zhanghai Chen, and Qihua Xiong. Room-temperature polariton lasing in all-inorganic perovskite nanoplatelets. *Nano Lett.*, 17(6):3982–3988, 2017.

[125] Wenna Du, Shuai Zhang, Jia Shi, Jie Chen, Zhiyong Wu, Yang Mi, Zhixiong Liu, Yuanzheng Li, Xinyu Sui, Rui Wang, et al. Strong exciton–photon coupling and lasing behavior in all-inorganic $CsPbBr_3$ micro/nanowire Fabry-Pérot cavity. *ACS Photonics*, 5(5):2051–2059, 2018.

[126] Jun Wang, Rui Su, Jun Xing, Di Bao, Carole Diederichs, Sheng Liu, Timothy CH Liew, Zhanghai Chen, and Qihua Xiong. Room temperature coherently coupled exciton–polaritons in two-dimensional organic–inorganic perovskite. *ACS Nano*, 12(8):8382–8389, 2018.

[127] Mateusz Król, Karolina Łempicka-Mirek, Katarzyna Rechcińska, M Furman, K Nogajewski, Rafał Mazur, Przemysław Morawiak, W Piecek, W Pacuski, Jacek Szczytko, et al. Universality of open microcavities for strong light-matter coupling. *Opt. Mater. Express*, 13(9):2651–2661, 2023.

[128] Xiaoze Liu, Tal Galfsky, Zheng Sun, Fengnian Xia, Erh-chen Lin, Yi-Hsien Lee, Stéphane Kéna-Cohen, and Vinod M Menon. Strong light–matter coupling in two-dimensional atomic crystals. *Nat. Photonics*, 9(1):30–34, 2015.

[129] Jie Gu, Biswanath Chakraborty, Mandeep Khatoniar, and Vinod M Menon. A room-temperature polariton light-emitting diode based on monolayer WS_2. *Nat. Nanotechnol.*, 14(11):1024–1028, 2019.

[130] Scott Dufferwiel, Stefan Schwarz, Freddie Withers, Aurélien AP Trichet, Feng Li, Maksym Sich, Osvaldo Del Pozo-Zamudio, Casper Clark, Anton Nalitov, Dmitry D Solnyshkov, et al. Exciton–polaritons in van der Waals heterostructures embedded in tunable microcavities. *Nat. Commun.*, 6(1):8579, 2015.

[131] Mateusz Król, Katarzyna Rechcińska, Karol Nogajewski, Magdalena Grzeszczyk, Karolina Łempicka, Rafał Mirek, Sara Piotrowska, Kenji Watanabe, Takashi Taniguchi, Maciej R Molas, et al. Exciton-polaritons in multilayer WSe_2 in a planar microcavity. *2D Mater.*, 7(1):015006, 2019.

[132] Guillaume Malpuech, Aldo Di Carlo, Alexey Kavokin, Jeremy J Baumberg, Marian Zamfirescu, and Paolo Lugli. Room-temperature polariton lasers based on GaN microcavities. *Appl. Phys. Lett.*, 81(3):412–414, 2002.

[133] S Christopoulos, G Baldassarri Höger Von Högersthal, AJD Grundy, Pavlos G Lagoudakis, Alexey V Kavokin, JJ Baumberg, G Christmann, R Butté, E Feltin, J-F Carlin, et al. Room-temperature polariton lasing in semiconductor microcavities. *Phys. Rev. Lett.*, 98(12):126405, 2007.

[134] Tien-Chang Lu, Ying-Yu Lai, Yu-Pin Lan, Si-Wei Huang, Jun-Rong Chen, Yung-Chi Wu, Wen-Feng Hsieh, and Hui Deng. Room temperature polariton lasing vs. photon lasing in a ZnO-based hybrid microcavity. *Opt. Express*, 20(5):5530–5537, 2012.

[135] Long Zhang, Wei Xie, Jian Wang, Alexander Poddubny, Jian Lu, Yinglei Wang, Jie Gu, Wenhui Liu, Dan Xu, Xuechu Shen, et al. Weak lasing in one-dimensional polariton superlattices. *PNAS*, 112(13):E1516–E1519, 2015.

[136] Hassan Alnatah, Shuang Liang, Qiaochu Wan, Jonathan Beaumariage, Ken West, Kirk Baldwin, Loren N Pfeiffer, Man Chun Alan Tam, Zbigniew R Wasilewski, and David W Snoke. Strong coupling of polaritons at room temperature in a GaAs/AlGaAs structure. *arXiv preprint arXiv:2502.12338*, 2025.

[137] Stéphane Kéna-Cohen and SR Forrest. Room-temperature polariton lasing in an organic single-crystal microcavity. *Nat. Photonics*, 4(6):371–375, 2010.

[138] KS Daskalakis, SA Maier, Ray Murray, and Stéphane Kéna-Cohen. Nonlinear interactions in an organic polariton condensate. *Nat. Mater.*, 13(3):271–278, 2014.

[139] Johannes D Plumhof, Thilo Stöferle, Lijian Mai, Ullrich Scherf, and Rainer F Mahrt. Room-temperature Bose–Einstein condensation of cavity exciton–polaritons in a polymer. *Nat. Mater.*, 13(3):247–252, 2014.

[140] Anton Putintsev, Anton Zasedatelev, Kirsty E McGhee, Tamsin Cookson, Kyriacos Georgiou, D Sannikov, David G Lidzey, and Pavlos G Lagoudakis. Nano-second exciton-polariton lasing in organic microcavities. *Appl. Phys. Lett.*, 117(12), 2020.

[141] Maciej Pieczarka, Marcin Gębski, Aleksandra N Piasecka, James A Lott, Axel Pelster, Michał Wasiak, and Tomasz Czyszanowski. Bose–Einstein condensation of photons in a vertical-cavity surface-emitting laser. *Nat. Photonics*, 18(10):1090–1096, 2024.

[142] Katarzyna Rechcińska. *The spin-orbit interaction of light in tunable liquid crystal microcavities.* PhD thesis, University of Warsaw, 2023.

[143] Karolina Łempicka Mirek. *Polarytony ekscytonowe w mikrownękach optycznych z perowskitami.* PhD thesis, University of Warsaw, 2023.

[144] Erwin Buncel and Srinivasan Rajagopal. Solvatochromism and solvent polarity scales. *Acc. Chem. Res.*, 23(7):226–231, 1990.

[145] Lars-Olof Pålsson, Marek Szablewski, Anthony Roberts, Akira Masutani, Gordon D Love, Graham H Cross, David Bloor, Andrew J Kay, Anthony D Woolhouse, Akira Masutani, et al. Orientation and solvatochromism of dyes in liquid crystals. *Mol. Cryst. Liq. Cryst.*, 402(1):43–53, 2003.

[146] Luxottica. Datasheet 05805, 2025. Accessed: 2025-03-24.

[147] Robert E Hermes, Toomas H Allik, Suresh Chandra, and J Andrew Hutchinson. High-efficiency pyrromethene doped solid-state dye lasers. *Appl. Phys. Lett.*, 63(7):877–879, 1993.

[148] Fritz Peter Schäfer. *Dye lasers*, volume 1. Springer Science & Business Media, 2013.

[149] Frank J Duarte and Lloyd William Hillman. *Dye laser principles, with applications*. San Diego, CA (United States); Academic Press Inc., 1990.

[150] OG Peterson, SA Tuccio, and BB Snavely. CW operation of an organic dye solution laser. *Appl. Phys. Lett.*, 17(6):245–247, 1970.

[151] Robert F Kubin and Aaron N Fletcher. Fluorescence quantum yields of some rhodamine dyes. *J. Lumin.*, 27(4):455–462, 1982.

[152] Edward Peter Raynes. Electro-optic and thermo-optic effects in liquid crystals. *Philosophical Transactions of the Royal Society of London. Series A, Mathematical and Physical Sciences*, 309(1507):167–178, 1983.

[153] Svetlana G Lukishova, Andreas C Liapis, Luke J Bissell, George M Gehring, and Robert W Boyd. Single-photon experiments with liquid crystals for quantum science and quantum engineering applications. *Liq. Cryst. Rev.*, 2(2):111–129, 2014.

[154] Jun Li, Sebastian Gauza, and Shin-Tson Wu. Temperature effect on liquid crystal refractive indices. *J. Appl. Phys.*, 96(1):19–24, 2004.

[155] David A Balzarini. Temperature dependence of birefringence in liquid crystals. *Phys. Rev. Lett.*, 25(14):914, 1970.

[156] Jonathan Keeling and Stéphane Kéna-Cohen. Bose–Einstein condensation of exciton-polaritons in organic microcavities. *Annu. Rev. Phys. Chem.*, 71(1):435–459, 2020.

[157] Pavlos G Lagoudakis, MD Martin, Jeremy J Baumberg, Guillaume Malpuech, and Alexey V Kavokin. Coexistence of low threshold lasing and strong coupling in microcavities. *J. Appl. Phys.*, 95(5):2487–2489, 2004.

[158] F. JONES and T. J. REEVE. Orientation of dyes in liquid crystalline media. *J. Soc. Dyers Colour.*, 95(10):352–359, 1979.

[159] Natalia Korolkova and Gerd Leuchs. Quantum correlations in separable multi-mode states and in classically entangled light. *Rep. Prog. Phys.*, 82(5):056001, 2019.

[160] Isaac Nape, Eileen Otte, Adam Vallés, Carmelo Rosales-Guzmán, Filippo Cardano, Cornelia Denz, and Andrew Forbes. Self-healing high-dimensional quantum key distribution using hybrid spin-orbit Bessel states. *Opt. Express*, 26(21):26946–26960, 2018.

[161] Keshaan Singh, Isaac Nape, Wagner Tavares Buono, Angela Dudley, and Andrew Forbes. A robust basis for multi-bit optical communication with vectorial light. *Laser Photonics Rev.*, 17(6):2200844, 2023.

[162] Zilong Zhang, Wei He, Suyi Zhao, Yuan Gao, Xin Wang, Xiaotian Li, Yuqi Wang, Yunfei Ma, Yetong Hu, Yijie Shen, et al. Spatial nonlinear conversion of structured light for machine learning based ultra-accurate information networks. *Laser Photonics Rev.*, 18(6):2301225, 2024.

[163] Dario Ballarini, Antonio Gianfrate, Riccardo Panico, Andrzej Opala, Sanjib Ghosh, Lorenzo Dominici, Vincenzo Ardizzone, Milena De Giorgi, Giovanni Lerario, Giuseppe Gigli, et al. Polaritonic neuromorphic computing outperforms linear classifiers. *Nano Lett.*, 20(5):3506–3512, 2020.

[164] Rafał Mirek, Andrzej Opala, Paolo Comaron, Magdalena Furman, Mateusz Król, Krzysztof Tyszka, Bartłomiej Seredyński, Dario Ballarini, Daniele Sanvitto, Timothy CH Liew, et al. Neuromorphic binarized polariton networks. *Nano Lett.*, 21(9):3715–3720, 2021.

[165] Mateusz Pawlak, Adam Pierzchała, Elie Benchimol, Jacopo Tessarolo, Lukas Rebholz, Marjan Krstić, Benedikt Zerulla, Ivan Fernandez-Corbaton, Tamás Jávorfi, Giuliano Siligardi, et al. Highly dissymmetric circularly polarized luminescence via multimode chirality enhancement in hierarchically ordered liquid crystal films. *Adv. Opt. Mater.*, page 2402483, 2024.

[166] Ross C Schofield, Ming Fu, Edmund Clarke, Ian Farrer, Aristotelis Trapalis, Himadri S Dhar, Rick Mukherjee, Toby Severs Millard, Jon Heffernan, Florian Mintert, et al. Bose–einstein condensation of light in a semiconductor quantum well microcavity. *Nature Photonics*, 18(10):1083–1089, 2024.

[167] A Askitopoulos, H Ohadi, Alexey V Kavokin, Z Hatzopoulos, PG Savvidis, and Pavlos G Lagoudakis. Polariton condensation in an optically induced two-dimensional potential. *Phys. Rev. B: Condens. Matter*, 88(4):041308, 2013.

[168] Sergey Alyatkin, JD Töpfer, Alexis Askitopoulos, Helgi Sigurdsson, and Pavlos G Lagoudakis. Optical control of couplings in polariton condensate lattices. *Phys. Rev. Lett.*, 124(20):207402, 2020.

[169] Eliezer Estrecho, T Gao, Nataliya Bobrovska, Daniel Comber-Todd, Michael D Fraser, Mark Steger, K West, Loren N Pfeiffer, J Levinsen, MM Parish, et al. Direct measurement of polariton-polariton interaction strength in the Thomas-Fermi regime of exciton-polariton condensation. *Phys. Rev. B*, 100(3):035306, 2019.

[170] Alexey V Kavokin, Timothy CH Liew, Christian Schneider, Pavlos G Lagoudakis, Sebastian Klembt, and Sven Höefling. Polariton condensates for classical and quantum computing. *Nat. Rev. Phys.*, 4(7):435–451, 2022.

[171] Alberto Amo, S Pigeon, D Sanvitto, VG Sala, R Hivet, Iacopo Carusotto, F Pisanello, G Leménager, R Houdré, E Giacobino, et al. Polariton superfluids reveal quantum hydrodynamic solitons. *Science*, 332(6034):1167–1170, 2011.

[172] Shaocong Hou, Mandeep Khatoniar, Kan Ding, Yue Qu, Alexander Napolov, Vinod M Menon, and Stephen R Forrest. Ultralong-range energy transport in a disordered organic semiconductor at room temperature via coherent exciton-polariton propagation. *Adv. Mater.*, 32(28):2002127, 2020.

[173] Gaël Nardin, Konstantinos G Lagoudakis, Michiel Wouters, Maxime Richard, Augustin Baas, Régis André, Le Si Dang, B Pietka, and Benoît Deveaud-Plédran. Dynamics of long-range ordering in an exciton-polariton condensate. *Phys. Rev. Lett.*, 103(25):256402, 2009.

[174] Giovanni Lerario, Antonio Fieramosca, Fábio Barachati, Dario Ballarini, Konstantinos S Daskalakis, Lorenzo Dominici, Milena De Giorgi, Stefan A Maier, Giuseppe Gigli, Stéphane Kéna-Cohen, et al. Room-temperature superfluidity in a polariton condensate. *Nat. Phys.*, 13(9):837–841, 2017.

[175] D Sanvitto, Francesca María Marchetti, MH Szymańska, Guilherme Tosi, M Baudisch, Fabrice P Laussy, DN Krizhanovskii, MS Skolnick, Lorenzo Marrucci, A Lemaitre, et al. Persistent currents and quantized vortices in a polariton superfluid. *Nat. Phys.*, 6(7):527–533, 2010.

[176] H Terças, H Flayac, DD Solnyshkov, and G Malpuech. Non-Abelian gauge fields in photonic cavities and photonic superfluids. *Phys. Rev. Lett.*, 112(6):066402, 2014.

[177] Hyang-Tag Lim, Emre Togan, Martin Kroner, Javier Miguel-Sanchez, and Atac Imamoğlu. Electrically tunable artificial gauge potential for polaritons. *Nat. Commun.*, 8(1):14540, 2017.

[178] Iacopo Carusotto and Cristiano Ciuti. Quantum fluids of light. *Rev. Mod. Phys.*, 85(1):299–366, 2013.

[179] Ying Shi, Yusong Gan, Yuzhong Chen, Yubin Wang, Sanjib Ghosh, Alexey V Kavokin, and Qihua Xiong. Coherent optical spin Hall transport for polaritonics at room temperature. *Nat. Mater.*, 24(1):56–62, 2025.

[180] Tomoki Ozawa, Hannah M Price, Alberto Amo, Nathan Goldman, Mohammad Hafezi, Ling Lu, Mikael C Rechtsman, David Schuster, Jonathan Simon, Oded Zilberberg, et al. Topological photonics. *Rev. Mod. Phys.*, 91(1):015006, 2019.

[181] Seth Lovett, Paul M Walker, Alexey Osipov, Alexey Yulin, Pooja Uday Naik, Charles E Whittaker, Ivan A Shelykh, Maurice S Skolnick, and Dmitry N Krizhanovskii. Observation of Zitterbewegung in photonic microcavities. *Light Sci. Appl.*, 12(1):126, 2023.

[182] Evgeny Sedov, Yuri G Rubo, and Alexey V Kavokin. Zitterbewegung of exciton-polaritons. *Phys. Rev. B*, 97(24):245312, 2018.

[183] Xiaokun Zhai, Ying Gao, Xuekai Ma, Chunzi Xing, Xiao Wang, Anlian Pan, Stefan Schumacher, and Tingge Gao. Robust realization of electrically tunable spin-orbit locked vortex pairs in polariton condensates at room temperature. *arXiv e-prints*, pages arXiv–2403, 2024.

[184] Jinqi Wu, Sanjib Ghosh, Rui Su, Antonio Fieramosca, Timothy CH Liew, and Qihua Xiong. Nonlinear parametric scattering of exciton polaritons in perovskite microcavities. *Nano Lett.*, 21(7):3120–3126, 2021.

[185] Jiangang Feng, Jun Wang, Antonio Fieramosca, Ruiqi Bao, Jiaxin Zhao, Rui Su, Yutian Peng, Timothy CH Liew, Daniele Sanvitto, and Qihua Xiong. All-optical switching based on interacting exciton polaritons in self-assembled perovskite microwires. *Sci. Adv.*, 7(46):eabj6627, 2021.

[186] Fedor V Subach, George H Patterson, Suliana Manley, Jennifer M Gillette, Jennifer Lippincott-Schwartz, and Vladislav V Verkhusha. Photoactivatable mcherry for high-resolution two-color fluorescence microscopy. *Nat. Methods*, 6(2):153–159, 2009.

[187] Anton V Zasedatelev, Anton V Baranikov, Denis Sannikov, Darius Urbonas, Fabio Scafirimuto, Vladislav Yu Shishkov, Evgeny S Andrianov, Yurii E Lozovik, Ullrich Scherf, Thilo Stöferle, et al. Single-photon nonlinearity at room temperature. *Nature*, 597(7877):493–497, 2021.

[188] Anton V Zasedatelev, Anton V Baranikov, Darius Urbonas, Fabio Scafirimuto, Ullrich Scherf, Thilo Stöferle, Rainer F Mahrt, and Pavlos G Lagoudakis. A room-temperature organic polariton transistor. *Nat. Photonics*, 13(6):378–383, 2019.

[189] Denis A Sannikov, Anton V Baranikov, Anton D Putintsev, Mikhail Misko, Anton V Zasedatelev, Ullrich Scherf, and Pavlos G Lagoudakis. Room temperature, cascadable, all-optical polariton universal gates. *Nat. Commun.*, 15(1):5362, 2024.

[190] Anthony J Leggett. Can a solid be" superfluid"? *Phys. Rev. Lett.*, 25(22):1543, 1970.

[191] Moses Hung-Wai Chan, RB Hallock, and L Reatto. Overview on solid ^{4}He and the issue of supersolidity. *J. Low Temp. Phys.*, 172:317–363, 2013.

[192] Jun-Ru Li, Jeongwon Lee, Wujie Huang, Sean Burchesky, Boris Shteynas, Furkan Çağrı Top, Alan O Jamison, and Wolfgang Ketterle. A stripe phase with supersolid properties in spin–orbit-coupled Bose–Einstein condensates. *Nature*, 543(7643):91–94, 2017.

[193] Kevin T Geier, Giovanni I Martone, Philipp Hauke, Wolfgang Ketterle, and Sandro Stringari. Dynamics of stripe patterns in supersolid spin-orbit-coupled Bose gases. *Phys. Rev. Lett.*, 130(15):156001, 2023.

[194] Julian Léonard, Andrea Morales, Philip Zupancic, Tilman Esslinger, and Tobias Donner. Supersolid formation in a quantum gas breaking a continuous translational symmetry. *Nature*, 543(7643):87–90, 2017.

[195] L Tanzi, JG Maloberti, G Biagioni, A Fioretti, C Gabbanini, and G Modugno. Evidence of superfluidity in a dipolar supersolid from nonclassical rotational inertia. *Science*, 371(6534):1162–1165, 2021.

[196] Giulio Biagioni, Nicolò Antolini, Beatrice Donelli, Luca Pezzè, Augusto Smerzi, Marco Fattori, Andrea Fioretti, Carlo Gabbanini, Massimo Inguscio, Luca Tanzi, et al. Measurement of the superfluid fraction of a supersolid by Josephson effect. *Nature*, 629(8013):773–777, 2024.

[197] Eva Casotti, Elena Poli, Lauritz Klaus, Andrea Litvinov, Clemens Ulm, Claudia Politi, Manfred J Mark, Thomas Bland, and Francesca Ferlaino. Observation of vortices in a dipolar supersolid. *Nature*, pages 1–5, 2024.

[198] Dimitrios Trypogeorgos, Antonio Gianfrate, Manuele Landini, Davide Nigro, Dario Gerace, Iacopo Carusotto, Fabrizio Riminucci, Kirk W Baldwin, Loren N Pfeiffer, Giovanni I Martone, et al. Emerging supersolidity in photonic-crystal polariton condensates. *Nature*, pages 1–5, 2025.

[199] Elena Poli, Thomas Bland, Samuel JM White, Manfred J Mark, Francesca Ferlaino, Silvia Trabucco, and Massimo Mannarelli. Glitches in rotating supersolids. *Phys. Rev. Lett.*, 131(22):223401, 2023.

[200] J Kasprzak, DD Solnyshkov, Régis André, Le Si Dang, and Guillaume Malpuech. Formation of an exciton polariton condensate: thermodynamic versus kinetic regimes. *Phys. Rev. Lett.*, 101(14):146404, 2008.

[201] Christoph Gadermaier, G Cerullo, Cristian Manzoni, Ullrich Scherf, EJW List, and Guglielmo Lanzani. Dynamics of higher photoexcited states in m-LPPP probed with sub-20 fs time resolution. *Chem. Phys. Lett.*, 384(4-6):251–255, 2004.

[202] Rui Su, Jun Wang, Jiaxin Zhao, Jun Xing, Weijie Zhao, Carole Diederichs, Timothy CH Liew, and Qihua Xiong. Room temperature long-range coherent exciton polariton condensate flow in lead halide perovskites. *Sci. Adv.*, 4(10):eaau0244, 2018.

[203] Shuai Zhang, Qiuyu Shang, Wenna Du, Jia Shi, Zhiyong Wu, Yang Mi, Jie Chen, Fengjing Liu, Yuanzheng Li, Mei Liu, et al. Strong exciton–photon coupling in hybrid inorganic–organic perovskite micro/nanowires. *Adv. Opt. Mater.*, 6(2):1701032, 2018.

[204] Ch Schneider, K Winkler, Michael D Fraser, Martin Kamp, Y Yamamoto, EA Ostrovskaya, and Sven Höfling. Exciton-polariton trapping and potential landscape engineering. *Rep. Prog. Phys.*, 80(1):016503, 2016.

[205] Krzysztof Sawicki, Thomas J Sturges, Maciej Ściesiek, Tomasz Kazimierczuk, Kamil Sobczak, Andrzej Golnik, Wojciech Pacuski, and Jan Suffczyński. Polariton lasing and energy-degenerate parametric scattering in non-resonantly driven coupled planar microcavities. *Nanophotonics*, 10(9):2421–2429, 2021.

[206] Nhung Vu Cam, Md Abdur Rahman, Syed Akhil, Emek Goksu Durmusoglu, Thi Thu Ha Do, Pedro Ludwig Hernandez-Martinez, Corentin Dabard, Deepshikha Arora, Siam Uddin, Golnoush Zamiri, et al. Tunable multiresonant microcavity exciton-polaritons in colloidal quantum wells. *Nano Lett.*, 25(15):6109–6116, 2025.

[207] Mateusz Król, Katarzyna Lekenta, Rafał Mirek, Karolina Łempicka, Daniel Stephan, Karol Nogajewski, Maciej R Molas, Adam Babiński, Marek Potemski, Jacek Szczytko, et al. Valley polarization of exciton–polaritons in monolayer WSe_2 in a tunable microcavity. *Nanoscale*, 11(19):9574–9579, 2019.

[208] Bo Han, Jamie M Fitzgerald, Lukas Lackner, Roberto Rosati, Martin Esmann, Falk Eilenberger, Takashi Taniguchi, Kenji Watanabe, Marcin Syperek, Ermin Malic, et al. Infrared magnetopolaritons in $MoTe_2$ monolayers and bilayers. *Phys. Rev. Lett.*, 134(7):076902, 2025.

[209] Fabio Scafirimuto, Darius Urbonas, Ullrich Scherf, Rainer F Mahrt, and Thilo Stöferle. Room-temperature exciton-polariton condensation in a tunable zero-dimensional microcavity. *ACS Photonics*, 5(1):85–89, 2018.

[210] R Mirek, M Furman, M Król, B Seredyński, K Łempicka-Mirek, K Tyszka, W Pacuski, M Matuszewski, J Szczytko, and B Piętka. Spin polarization of exciton-polariton condensate in a photonic synthetic effective magnetic field. *Phys. Rev. B*, 107(12):125303, 2023.

[211] D Tanese, H Flayac, D Solnyshkov, A Amo, A Lemaître, E Galopin, R Braive, P Senellart, I Sagnes, G Malpuech, et al. Polariton condensation in solitonic gap states in a one-dimensional periodic potential. *Nat. Commun.*, 4(1):1749, 2013.

[212] LP Pitaevskii. Phenomenological theory of superfluidity near the λ point. *Sov. Phys.—JETP*, 8:282, 1959.

[213] Chad N Weiler, Tyler W Neely, David R Scherer, Ashton S Bradley, Matthew J Davis, and Brian P Anderson. Spontaneous vortices in the formation of Bose–Einstein condensates. *Nature*, 455(7215):948–951, 2008.

[214] Dmitry D Solnyshkov, Anton V Nalitov, and Guillaume Malpuech. Kibble–Zurek mechanism in topologically nontrivial zigzag chains of polariton micropillars. *Phys. Rev. Lett.*, 116(4):046402, 2016.

[215] Dario Ballarini, Milena De Giorgi, Emiliano Cancellieri, Romuald Houdré, Elisabeth Giacobino, Roberto Cingolani, Alberto Bramati, Giuseppe Gigli, and Daniele Sanvitto. All-optical polariton transistor. *Nat. Commun.*, 4(1):1778, 2013.

[216] Tingge Gao, PS Eldridge, Timothy Chi Hin Liew, SI Tsintzos, George Stavrinidis, George Deligeorgis, Z Hatzopoulos, and PG Savvidis. Polariton condensate transistor switch. *Phys. Rev. B: Condens. Matter*, 85(23):235102, 2012.

[217] TCH Liew, Alexey V Kavokin, T Ostatnickỳ, M Kaliteevski, IA Shelykh, and RA Abram. Exciton-polariton integrated circuits. *Phys. Rev. B: Condens. Matter*, 82(3):033302, 2010.

[218] TCH Liew, Alexey V Kavokin, and IA Shelykh. Optical circuits based on polariton neurons in semiconductor microcavities. *Phys. Rev. Lett.*, 101(1):016402, 2008.

[219] Dimitrios Trypogeorgos, Antonio Gianfrate, Manuele Landini, Davide Nigro, Dario Gerace, Iacopo Carusotto, Fabrizio Riminucci, Kirk W Baldwin, Loren N Pfeiffer, Giovanni I Martone, et al. Emerging supersolidity from a polariton condensate in a photonic crystal waveguide. *arXiv preprint arXiv:2407.02373*, 2024.

[220] Eva Oton and Estelle Netter. Wide tunable shift of the reflection band in dual frequency cholesteric liquid crystals. *Opt. Express*, 25(12):13314–13323, 2017.

[221] Hari Krishna Bisoyi, Timothy J Bunning, and Quan Li. Stimuli-driven control of the helical axis of self-organized soft helical superstructures. *Adv. Mater.*, 30(25):1706512, 2018.

[222] JL Martinand and G Durand. Electric field quenching of thermal fluctuations of orientation in a nematic liquid crystal. *Solid State Commun.*, 10(9):815–818, 1972.

[223] P Rudquist, L Komitov, and ST Lagerwall. Linear electro-optic effect in a cholesteric liquid crystal. *Phys. Rev. E*, 50(6):4735, 1994.

[224] BJ Broughton, MJ Clarke, AE Blatch, and HJ Coles. Optimized flexoelectric response in a chiral liquid-crystal phase device. *J. Appl. Phys.*, 98(3), 2005.

[225] Marcin Muszyński, Przemysław Oliwa, Pavel Kokhanchik, Piotr Kapuściński, Eva Oton, Rafał Mazur, Przemysław Morawiak, Wiktor Piecek, Przemysław Kula, Witold Bardyszewski, et al. Supplementary information for "Electrically tunable spin-orbit coupled photonic lattice in a liquid crystal microcavity". Available at https://onlinelibrary.wiley.com/doi/10.1002/lpor.202400794, 2024.

[226] Przemysław Oliwa, Witold Bardyszewski, and Jacek Szczytko. Quantum mechanical-like approach with non-hermitian effective Hamiltonians in spin-orbit coupled optical cavities. *Phys. Rev. Res.*, 6(1):013324, 2024.

[227] Zhixuan Jia, Tejal Pawale, Guillermo I Guerrero-García, Sid Hashemi, José A Martínez-González, and Xiao Li. Engineering the uniform lying helical structure in chiral nematic liquid crystals: from morphology transition to dimension control. *Crystals*, 11(4):414, 2021.

[228] Jiahuan Ren, Qing Liao, Feng Li, Yiming Li, Olivier Bleu, Guillaume Malpuech, Jiannian Yao, Hongbing Fu, and Dmitry Solnyshkov. Nontrivial band geometry in an optically active system. *Nat. Commun.*, 12(1):689, 2021.

[229] Peng Chen, Bing-Yan Wei, Wei Hu, and Yan-Qing Lu. Liquid-crystal-mediated geometric phase: from transmissive to broadband reflective planar optics. *Adv. Mater.*, 32(27):1903665, 2020.

[230] Alexander Ryabchun and Alexey Bobrovsky. Cholesteric liquid crystal materials for tunable diffractive optics. *Adv. Opt. Mater.*, 6(15):1800335, 2018.

[231] Avtar S Matharu, Shehzad Jeeva, and PS Ramanujam. Liquid crystals for holographic optical data storage. *Chem. Soc. Rev.*, 36(12):1868–1880, 2007.

[232] Lingli Zhang, Ling Wang, Uma S Hiremath, Hari Krishna Bisoyi, Geetha G Nair, Channabasaveshwar V Yelamaggad, Augustine M Urbas, Timothy J Bunning, and Quan Li. Dynamic orthogonal switching of a thermoresponsive self-organized helical superstructure. *Adv. Mater.*, 29(24):1700676, 2017.

[233] Dmitriy Dovzhenko, Denis Aristov, Lucinda Pickup, Helgi Sigurðsson, and Pavlos G Lagoudakis. Next-nearest-neighbor coupling with spinor polariton condensates. *Phys. Rev. B*, 108(16):L161301, 2023.

[234] John D Joannopoulos, Pierre R Villeneuve, and Shanhui Fan. Photonic crystals: putting a new twist on light. *Nature*, 386(6621):143–149, 1997.

[235] Susumu Noda, Masayuki Fujita, and Takashi Asano. Spontaneous-emission control by photonic crystals and nanocavities. *Nat. Photonics*, 1(8):449–458, 2007.

[236] Hans J Queisser and Eugene E Haller. Defects in semiconductors: some fatal, some vital. *Science*, 281(5379):945–950, 1998.

[237] RA Cowley and WJL Buyers. The properties of defects in magnetic insulators. *Rev. Mod. Phys.*, 44(2):406, 1972.

[238] Yoshinori Tokura and Naoya Kanazawa. Magnetic skyrmion materials. *Chem. Rev.*, 121(5):2857–2897, 2020.

[239] Tom H Johansen. Flux-pinning-induced stress and magnetostriction in bulk superconductors. *Supercond. Sci. Technol.*, 13(10):R121, 2000.

[240] Paul J Ackerman, Zhiyuan Qi, Yiheng Lin, Christopher W Twombly, Mauricio J Laviada, Yves Lansac, and Ivan I Smalyukh. Laser-directed hierarchical assembly of liquid crystal defects and control of optical phase singularities. *Sci. Rep.*, 2(1):414, 2012.

[241] G Strangi, S Ferjani, Valentin Barna, A De Luca, C Versace, N Scaramuzza, and R Bartolino. Random lasing and weak localization of light in dye-doped nematic liquid crystals. *Opt. Express*, 14(17):7737–7744, 2006.

[242] Carsten Krüger, Gunnar Klös, Christian Bahr, and Corinna C Maass. Curling liquid crystal microswimmers: a cascade of spontaneous symmetry breaking. *Phys. Rev. Lett.*, 117(4):048003, 2016.

[243] Isaac Chuang, Ruth Durrer, Neil Turok, and Bernard Yurke. Cosmology in the laboratory: Defect dynamics in liquid crystals. *Science*, 251(4999):1336–1342, 1991.

[244] Sébastien Fumeron and Bertrand Berche. Introduction to topological defects: from liquid crystals to particle physics. *The European Physical Journal Special Topics*, 232(11):1813–1833, 2023.

[245] Paul J Ackerman and Ivan I Smalyukh. Diversity of knot solitons in liquid crystals manifested by linking of preimages in torons and hopfions. *Phys. Rev. X*, 7(1):011006, 2017.

[246] Jin-Sheng Wu and Ivan I Smalyukh. Hopfions, heliknotons, skyrmions, torons and both Abelian and nonabelian vortices in chiral liquid crystals. *Liq. Cryst. Rev.*, 10(1-2):34–68, 2022.

[247] Ivan I Smalyukh, Yves Lansac, Noel A Clark, and Rahul P Trivedi. Three-dimensional structure and multistable optical switching of triple-twisted particle-like excitations in anisotropic fluids. *Nat. Mater.*, 9(2):139–145, 2010.

[248] Joachim Czapiński. *Localization of light on defects in microcavities with built-in uniform lying helix*. PhD thesis, University of Warsaw, 2023.

[249] Ioannis Georgakilas, Rafał Mirek, Darius Urbonas, Michael Forster, Ullrich Scherf, Rainer F Mahrt, and Thilo Stöferle. In-situ tunable, room-temperature polariton condensation in individual states of a 1D topological lattice. *arXiv preprint arXiv:2405.10468*, 2024.

[250] Ling Wang, Augustine M Urbas, and Quan Li. Nature-inspired emerging chiral liquid crystal nanostructures: from molecular self-assembly to DNA mesophase and nanocolloids. *Adv. Mater.*, 32(41):1801335, 2020.

[251] Ling Lu, John D Joannopoulos, and Marin Soljačić. Topological photonics. *Nat. Photonics*, 8(11):821–829, 2014.

[252] P Coullet, L Gil, and F Rocca. Optical vortices. *Opt. Commun.*, 73(5):403–408, 1989.

[253] Les Allen, Marco W Beijersbergen, RJC Spreeuw, and JP Woerdman. Orbital angular momentum of light and the transformation of Laguerre-Gaussian laser modes. *Phys. Rev. A*, 45(11):8185, 1992.

[254] Yijie Shen, Xuejiao Wang, Zhenwei Xie, Changjun Min, Xing Fu, Qiang Liu, Mali Gong, and Xiaocong Yuan. Optical vortices 30 years on: OAM manipulation from topological charge to multiple singularities. *Light Sci. Appl.*, 8(1):90, 2019.

[255] MV Berry and Wei Liu. No general relation between phase vortices and orbital angular momentum. *J. Phys. A: Math. Theor.*, 55(37):374001, 2022.

[256] AT O'neil, I MacVicar, L Allen, and MJ Padgett. Intrinsic and extrinsic nature of the orbital angular momentum of a light beam. *Phys. Rev. Lett.*, 88(5):053601, 2002.

[257] Konstantin Y Bliokh and Franco Nori. Transverse and longitudinal angular momenta of light. *Phys. Rep.*, 592:1–38, 2015.

[258] Nicola Carlon Zambon, Philippe St-Jean, Marijana Milićević, Aristide Lemaître, Abdelmounaim Harouri, Luc Le Gratiet, Olivier Bleu, DD Solnyshkov, Guillaume Malpuech, Isabelle Sagnes, et al. Optically controlling the emission chirality of microlasers. *Nat. Photonics*, 13(4):283–288, 2019.

[259] René Barczyk, L Kuipers, and Ewold Verhagen. Observation of Landau levels and chiral edge states in photonic crystals through pseudomagnetic fields induced by synthetic strain. *Nat. Photonics*, 18(6):574–579, 2024.

[260] Andrew Forbes, Light Mkhumbuza, and Liang Feng. Orbital angular momentum lasers. *Nat. Rev. Phys.*, 6(6):352–364, 2024.

[261] Xiujuan Zhang, Farzad Zangeneh-Nejad, Ze-Guo Chen, Ming-Hui Lu, and Johan Christensen. A second wave of topological phenomena in photonics and acoustics. *Nature*, 618(7966):687–697, 2023.

[262] Pei-Qing Jin, You-Quan Li, and Fu-Chun Zhang. SU(2) × U(1) unified theory for charge, orbit and spin currents. *J. Phys. A: Math. Gen.*, 39(35):11129, 2006.

[263] Seiji Sugawa, Francisco Salces-Carcoba, Abigail R Perry, Yuchen Yue, and IB Spielman. Second Chern number of a quantum-simulated non-Abelian Yang monopole. *Science*, 360(6396):1429–1434, 2018.

[264] Dali Cheng, Kai Wang, Charles Roques-Carmes, Eran Lustig, Olivia Y Long, Heming Wang, and Shanhui Fan. Non-Abelian lattice gauge fields in photonic synthetic frequency dimensions. *Nature*, 637(8044):52–56, 2025.

[265] Bengy Tsz Tsun Wong, Shu Yang, Zehai Pang, and Yi Yang. Synthetic non-Abelian electric fields and spin-orbit coupling in photonic synthetic dimensions. *Phys. Rev. Lett.*, 134(16):163803, 2025.

[266] N David Mermin. The topological theory of defects in ordered media. *Rev. Mod. Phys.*, 51(3):591, 1979.

[267] Lorenzo Marrucci, Carlo Manzo, and Domenico Paparo. Optical spin-to-orbital angular momentum conversion in inhomogeneous anisotropic media. *Phys. Rev. Lett.*, 96(16):163905, 2006.

[268] Junji Kobashi, Hiroyuki Yoshida, and Masanori Ozaki. Polychromatic optical vortex generation from patterned cholesteric liquid crystals. *Phys. Rev. Lett.*, 116(25):253903, 2016.

[269] Etienne Brasselet, Naoki Murazawa, Hiroaki Misawa, and Saulius Juodkazis. Optical vortices from liquid crystal droplets. *Phys. Rev. Lett.*, 103(10):103903, 2009.

[270] Miha Papič, Urban Mur, Kottoli Poyil Zuhail, Miha Ravnik, Igor Muševič, and Matjaž Humar. Topological liquid crystal superstructures as structured light lasers. *PNAS*, 118(49):e2110839118, 2021.

[271] Baiwei Mao, Yange Liu, Hongwei Zhang, Kang Yang, Ya Han, Zhi Wang, and Zhaohui Li. Complex analysis between CV modes and OAM modes in fiber systems. *Nanophotonics*, 8(2):271–285, 2019.

[272] B Andrei Bernevig, Taylor L Hughes, and Shou-Cheng Zhang. Quantum spin Hall effect and topological phase transition in HgTe quantum wells. *Science*, 314(5806):1757–1761, 2006.

[273] M Zahid Hasan and Charles L Kane. Colloquium: topological insulators. *Rev. Mod. Phys.*, 82(4):3045–3067, 2010.

[274] Roman Jackiw and Cláudio Rebbi. Solitons with fermion number 1/2. *Phys. Rev. D*, 13(12):3398, 1976.

[275] Jacques Peixoto, Darian Hall, Dirk J Broer, Ivan I Smalyukh, and Danqing Liu. Mechanical actuation via homeomorphic transformations of topological solitons within polymer coatings. *Adv. Mater.*, 36(2):2308425, 2024.

[276] Taylor H Ware, Michael E McConney, Jeong Jae Wie, Vincent P Tondiglia, and Timothy J White. Voxelated liquid crystal elastomers. *Science*, 347(6225):982–984, 2015.

[277] Hayley RO Sohn and Ivan I Smalyukh. Electrically powered motions of toron crystallites in chiral liquid crystals. *PNAS*, 117(12):6437–6445, 2020.

[278] Haijun Wu, Nilo Mata-Cervera, Haiwen Wang, Zhihan Zhu, Cheng-Wei Qiu, and Yijie Shen. Photonic torons, topological phase transition and tunable spin monopoles. *arXiv preprint arXiv:2412.08083*, 2024.

[279] Gareth P Alexander. Topology in liquid crystal phases. *The role of topology in materials*, pages 229–257, 2018.

[280] Friedrich Reinitzer. Contributions to the knowledge of cholesterol. *Liq. Cryst.*, 5(1):7–18, 1989.

[281] Michel Mitov. Liquid-crystal science from 1888 to 1922: Building a revolution. *ChemPhysChem*, 15(7):1245–1250, 2014.

[282] Oliver Henrich, K Stratford, ME Cates, and D Marenduzzo. Structure of blue phase III of cholesteric liquid crystals. *Phys. Rev. Lett.*, 106(10):107801, 2011.

[283] J Pišljar, S Ghosh, S Turlapati, NVS Rao, M Škarabot, A Mertelj, A Petelin, A Nych, M Marinčič, A Pusovnik, et al. Blue phase III: Topological fluid of skyrmions. *Phys. Rev. X*, 12(1):011003, 2022.

[284] Hirotsugu Kikuchi, Hiroki Higuchi, Yasuhiro Haseba, and Takashi Iwata. 62.2: Invited paper: Fast electro-optical switching in polymer-stabilized liquid crystalline blue phases for display application. In *SID Symposium Digest of Technical Papers*, volume 38, pages 1737–1740. Wiley Online Library, 2007.

[285] Linghui Rao, Zhibing Ge, Shin-Tson Wu, and Seung Hee Lee. Low voltage blue-phase liquid crystal displays. *Appl. Phys. Lett.*, 95(23), 2009.

[286] F Castles, FV Day, SM Morris, DH Ko, DJ Gardiner, MM Qasim, S Nosheen, PJW Hands, SS Choi, RH Friend, et al. Blue-phase templated fabrication of three-dimensional nanostructures for photonic applications. *Nat. Mater.*, 11(7):599–603, 2012.

[287] Sung-Taek Hur, Bo Ram Lee, Min-Jun Gim, Kyung-Won Park, Myoung Hoon Song, and Suk-Won Choi. Liquid-crystalline blue phase laser with widely tunable wavelength. *Adv. Mater.*, 25(21):3002–3006, 2013.

[288] Wenyi Cao, Antonio Munoz, Peter Palffy-Muhoray, and Bahman Taheri. Lasing in a three-dimensional photonic crystal of the liquid crystal blue phase II. *Nat. Mater.*, 1(2):111–113, 2002.

[289] Chun-Wei Chen, Hung-Chang Jau, Chun-Ta Wang, Chun-Hong Lee, IC Khoo, and Tsung-Hsien Lin. Random lasing in blue phase liquid crystals. *Opt. Express*, 20(21):23978–23984, 2012.

[290] Yi-Hsin Lin, Hung-Shan Chen, Hung-Chun Lin, Yu-Shih Tsou, Hsu-Kuan Hsu, and Wang-Yang Li. Polarizer-free and fast response microlens arrays using polymer-stabilized blue phase liquid crystals. *Appl. Phys. Lett.*, 96(11), 2010.

[291] Chao-Te Lee, Yan Li, Hoang-Yan Lin, and Shin-Tson Wu. Design of polarization-insensitive multi-electrode GRIN lens with a blue-phase liquid crystal. *Opt. Express*, 19(18):17402–17407, 2011.

[292] Hirotsugu Kikuchi, Masayuki Yokota, Yoshiaki Hisakado, Huai Yang, and Tisato Kajiyama. Polymer-stabilized liquid crystal blue phases. *Nat. Mater.*, 1(1):64–68, 2002.

[293] Seong-Yong Jo, Sung-Wook Jeon, Byeong-Cheon Kim, Jae-Hyun Bae, Fumito Araoka, and Suk-Won Choi. Polymer stabilization of liquid-crystal blue phase II toward photonic crystals. *ACS Appl. Mater. Interfaces*, 9(10):8941–8947, 2017.

[294] Hiroyuki Yoshida, Yuma Tanaka, Kosuke Kawamoto, Hitoshi Kubo, Tetsuya Tsuda, Akihiko Fujii, Susumu Kuwabata, Hirotsugu Kikuchi, and Masanori Ozaki. Nanoparticle-stabilized cholesteric blue phases. *Appl. Phys. Express*, 2(12):121501, 2009.

[295] Eva Karatairi, Brigita Rožič, Zdravko Kutnjak, Vassilios Tzitzios, George Nounesis, George Cordoyiannis, Jan Thoen, Christ Glorieux, and Samo Kralj. Nanoparticle-induced widening of the temperature range of liquid-crystalline blue phases. *Phys. Rev. E: Stat. Nonlinear Soft Matter Phys.*, 81(4):041703, 2010.

[296] Zhi-Gang Zheng, Cong-Long Yuan, Wei Hu, Hari Krishna Bisoyi, Ming-Jie Tang, Zhen Liu, Pei-Zhi Sun, Wei-Qiang Yang, Xiao-Qian Wang, Dong Shen, et al. Light-patterned crystallographic direction of a self-organized 3D soft photonic crystal. *Adv. Mater.*, 29(42):1703165, 2017.

[297] Misaki Takahashi, Takuma Ohkawa, Hiroyuki Yoshida, Jun-ichi Fukuda, Hirotsugu Kikuchi, and Masanori Ozaki. Orientation of liquid crystalline blue phases on unidirectionally orienting surfaces. *J. Phys. D: Appl. Phys.*, 51(10):104003, 2018.

[298] Chun-Wei Chen, Chien-Tsung Hou, Cheng-Chang Li, Hung-Chang Jau, Chun-Ta Wang, Ching-Lang Hong, Duan-Yi Guo, Cheng-Yu Wang, Sheng-Ping Chiang, Timothy J Bunning, et al. Large three-dimensional photonic crystals based on monocrystalline liquid crystal blue phases. *Nat. Commun.*, 8(1):727, 2017.

[299] Hannah Claus, Oliver Willekens, Olga Chojnowska, R Dąbrowski, Jeroen Beeckman, and Kristiaan Neyts. Inducing monodomain blue phase liquid crystals by long-lasting voltage application during temperature variation. *Liq. Cryst.*, 43(5):688–693, 2016.

[300] Jia-De Lin, Ying-Lung Daniel Ho, Lifeng Chen, Martin Lopez-Garcia, Shun-An Jiang, Mike PC Taverne, Chia-Rong Lee, and John G Rarity. Microstructure-stabilized blue phase liquid crystals. *ACS Omega*, 3(11):15435–15441, 2018.

[301] Eva Otón, Przemysław Morawiak, Katarzyna Gaładyk, José M Otón, and Wiktor Piecek. Fast self-assembly of macroscopic blue phase 3D photonic crystals. *Opt. Express*, 28(12):18202–18211, 2020.

[302] Jie Liu, Yujie Chen, Feng Jin, Jingxia Wang, Tomiki Ikeda, and Lei Jiang. Single-, dual-, triple, and quadruple-wavelength surface-emitting lasing in blue-phase liquid crystal. *Adv. Mater.*, 34(9):2108330, 2022.

[303] Jin Yan, Yuan Chen, Daming Xu, and Shin-Tson Wu. Angular dependent reflections of a monodomain blue phase liquid crystal. *J. Appl. Phys.*, 114(11), 2013.

[304] Richard J Miller and Helen F Gleeson. Lattice parameter measurements from the Kossel diagrams of the cubic liquid crystal blue phases. *J. Phys. II*, 6(6):909–922, 1996.

[305] P Pieranski, E Dubois-Violette, F Rothen, and L Strzelecki. Geometry of Kossel lines in colloidal crystals. *J. Phys.*, 42(1):53–60, 1981.

[306] Yan-Song Zhang, Shun-An Jiang, Jia-De Lin, Po-Chih Yang, and Chia-Rong Lee. Stretchable freestanding films of 3D nanocrystalline blue phase elastomer and their tunable applications. *Adv. Opt. Mater.*, 9(1):2001427, 2021.

[307] Yanqing Chen, Chenglin Zheng, Wenjie Yang, Jing Li, Feng Jin, Wei Zhang, Wentao Sun, Pingli Wang, Laifeng Li, Jingxia Wang, et al. Stretchable blue phase liquid crystal lasers with optical stability based on small-strain nonlinear 3D asymmetric deformation. *Adv. Mater.*, page 2416448, 2025.

[308] John Wyrill Christian and Subhash Mahajan. Deformation twinning. *Prog. Mater Sci.*, 39(1-2):1–157, 1995.

[309] Yuxian Zhang, Hiroyuki Yoshida, SeongYong Cho, Jun-ichi Fukuda, and Masanori Ozaki. In situ optical characterization of twinning in liquid crystalline blue phases. *ACS Appl. Mater. Interfaces*, 13(30):36130–36137, 2021.

[310] Yuxian Zhang, Hiroyuki Yoshida, Fan Chu, Yu-Qiang Guo, Zhou Yang, Masanori Ozaki, and Qiong-Hua Wang. Three-dimensional lattice deformation of blue phase liquid crystals under electrostriction. *Soft Matter*, 18(17):3328–3334, 2022.

[311] Jiajia Yang, Weidong Zhao, Zhou Yang, Wanli He, Jingxia Wang, Tomiki Ikeda, and Lei Jiang. Photonic shape memory polymer based on liquid crystalline blue phase films. *ACS Appl. Mater. Interfaces*, 11(49):46124–46131, 2019.

[312] Tsung-Hsien Lin, Yannian Li, Chun-Ta Wang, Hung-Chang Jau, Chun-Wei Chen, Cheng-Chung Li, Hari Krishna Bisoyi, Timothy J Bunning, and Quan Li. Red, green and blue reflections enabled in an optically tunable self-organized 3D cubic nanostructured thin film. *Adv. Mater.*, 25(36):5050–5054, 2013.

[313] Jiajia Yang, Jie Liu, Bo Guan, Wanli He, Zhou Yang, Jingxia Wang, Tomiki Ikeda, and Lei Jiang. Fabrication and photonic applications of large-domain blue phase films. *J. Mater. Chem. C*, 7(31):9460–9466, 2019.

[314] Myoung Hoon Song, Na Young Ha, Kazuhiro Amemiya, Byoungchoo Park, Yoichi Takanishi, Ken Ishikawa, Jeong Weon Wu, Suzushi Nishimura, Takehiro Toyooka, and Hideo Takezoe. Defect-mode lasing with lowered threshold in a three-layered hetero-cholesteric liquid-crystal structure. *Adv. Mater.*, 18(2):193–197, 2006.

[315] Alfredo Mazzulla, Gia Petriashvili, Mario Ariosto Matranga, Maria Penelope De Santo, and Riccardo Barberi. Thermal and electrical laser tuning in liquid crystal blue phase I. *Soft Matter*, 8(18):4882–4885, 2012.

[316] Shiyoshi Yokoyama, Shinro Mashiko, Hirotsugu Kikuchi, Kiminori Uchida, and Toshihiko Nagamura. Laser emission from a polymer-stabilized liquid-crystalline blue phase. *Adv. Mater.*, 18(1):48–51, 2006.

[317] Masanori Ozaki, Masahiro Kasano, Dirk Ganzke, Wolfgang Haase, and Katsumi Yoshino. Mirrorless lasing in a dye-doped ferroelectric liquid crystal. *Adv. Mater.*, 14(4):306–309, 2002.

[318] Andro Chanishvili, Guram Chilaya, Gia Petriashvili, Riccardo Barberi, Maria P De Santo, Mario A Matranga, and Federica Ciuchi. Lasing in an intermediate twisted phase between cholesteric and smectic a phase. *Appl. Phys. Lett.*, 88(10), 2006.

[319] Seiichi Furumi, Shiyoshi Yokoyama, Akira Otomo, and Shinro Mashiko. Electrical control of the structure and lasing in chiral photonic band-gap liquid crystals. *Appl. Phys. Lett.*, 82(1):16–18, 2003.

[320] Masahiro Kasano, Masanori Ozaki, Katsumi Yoshino, Dirk Ganzke, and Wolfgang Haase. Electrically tunable waveguide laser based on ferroelectric liquid crystal. *Appl. Phys. Lett.*, 82(23):4026–4028, 2003.

[321] Kazuhiro Funamoto, Masanori Ozaki, and Katsumi Yoshino. Discontinuous shift of lasing wavelength with temperature in cholesteric liquid crystal. *Jpn. J. Appl. Phys.*, 42(12B):L1523, 2003.

[322] SM Morris, AD Ford, MN Pivnenko, and HJ Coles. Enhanced emission from liquid-crystal lasers. *J. Appl. Phys.*, 97(2), 2005.

[323] Francesca Serra, Mario Ariosto Matranga, Yan Ji, and Eugene M Terentjev. Single-mode laser tuning from cholesteric elastomers using a "notch" band-gap configuration. *Opt. Express*, 18(2):575–581, 2010.

[324] Jia-De Lin, Shuan-Yu Huang, Hong-Sheng Wang, Shih-Hung Lin, Ting-Shan Mo, Chi-Ting Horng, Hui-Chen Yeh, Lin-Jer Chen, Hong-Lin Lin, and Chia-Rong Lee. Spatially tunable photonic bandgap of wide spectral range and lasing emission based on a blue phase wedge cell. *Opt. Express*, 22(24):29479–29492, 2014.

[325] Sunihl Ma, Jihoon Ahn, and Jooho Moon. Chiral perovskites for next-generation photonics: from chirality transfer to chiroptical activity. *Adv. Mater.*, 33(47):2005760, 2021.

[326] Marcin Muszyński, Igor Antoniazzi, and Bruno Camargo. Ion-beam-milled graphite nanoribbons as mesoscopic carbon-based polarizers. *Appl. Phys. Lett.*, 123(3), 2023.

[327] M Furman, A Opala, M Król, K Tyszka, R Mirek, M Muszyński, B Seredyński, W Pacuski, J Szczytko, M Matuszewski, et al. Inverted optical bistability and optical limiting in coherently driven exciton–polaritons. *APL Photonics*, 8(4), 2023.

[328] M Muszyński, H Teisseyre, K Sobczak, and J Suffczyński. Stable charged exciton in a zno/(zn, mg) o quantum well at near room temperature. *Appl. Phys. Lett.*, 117(3), 2020.

[329] K Łempicka, M Furman, M Muszyński, M Król, A Wincukiewicz, K Rechcińska, R Mazur, W Piecek, M Kamińska, J Szczytko, et al. Exciton-polaritons in a tunable microcavity with 2d-perovskite. In *Terahertz Science and Applications*, pages JW4A–66. Optica Publishing Group, 2019.